

AD-A275 190



MARTIN MARIETTA

MML TR-93-18

**DESIGN, DEVELOPMENT, AND TESTING
OF ADVANCED BRIDGE STRUCTURES**

Final Report

DTIC
ELECTED
FEB 01 1994
S A

Prepared by:

D. McNamara, A. DasGupta, H. Hand, J. Maisano, and C. Arah

Prepared for:
**U.S. Army Belvoir Research, Development
and Engineering Center**
Fort Belvoir, VA 22060-5606

Under Contract No. DAAK70-90-C-0019

Martin Marietta Technologies, Inc.
Martin Marietta Laboratories
1450 South Rolling Road
Baltimore, MD 21227-3848

94-03108



December 23, 1993

REPORT DOCUMENTATION PAGE

1a. REPORT SECURITY CLASSIFICATION Unclassified		1b. RESTRICTIVE MARKINGS None			
2a. SECURITY CLASSIFICATION AUTHORITY N/A		3. DISTRIBUTION/AVAILABILITY OF REPORT			
2b. DECLASSIFICATION/DOWNGRADING SCHEDULE N/A					
4. PERFORMING ORGANIZATION REPORT NUMBER(S) MML TR-93-18		5. MONITORING ORGANIZATION REPORT NUMBER(S)			
6a. NAME OF PERFORMING ORGANIZATION Martin Marietta Corporation Martin Marietta Laboratories	6b. OFFICE SYMBOL <i>(If applicable)</i> STRBE-JBC	7a. NAME OF MONITORING ORGANIZATION U.S. Army Belvoir Research, Development and Engineering Center			
6c. ADDRESS (City, State, and ZIP Code) 1450 South Rolling Road Baltimore Maryland 21227-3898		7b. ADDRESS (City, State, and ZIP Code) Commander Ft. Belvoir, Virginia 22060-5606			
8a. NAME OF FUNDING/SPONSORING ORGANIZATION U.S. Army Belvoir Res., Devel. & Engin. Center	8b. OFFICE SYMBOL <i>(If applicable)</i> STRBE-JBC	9. PROCUREMENT INSTRUMENT IDENTIFICATION NUMBER DAAK70-90-C-0019			
8c. ADDRESS (City, State, and ZIP Code) Commander Ft. Belvoir, Virginia 22060-5606		10. SOURCE OF FUNDING NUMBERS			
		PROGRAM ELEMENT NO.	PROJECT NO.	TASK NO.	WORK UNIT ACCESSION NO.
11. TITLE <i>(Include Security Classification)</i> Design, Development, and Testing of Advanced Bridge Structures					
12. PERSONAL AUTHOR(S) D. McNamara, A. DasGupta, H. Hand, J. Maisano, and C. Arah					
13a. TYPE OF REPORT Final Technical Rpt.	13b. TIME COVERED FROM 5/90 TO 6/93		14. DATE OF REPORT (Year, Month, Day) 1993 December 23		15. PAGE COUNT 184
16. SUPPLEMENTARY NOTATION					
17. COSATI CODES		18. SUBJECT TERMS <i>(Continue on reverse if necessary and identify by block number)</i> Adhesive Bonding, Composite Surface Preparation, Finite Element Analysis, Adhesive Joint Design Guidelines, Structural Epoxy Adhesives, Sealants, Adhesive Testing			
19. ABSTRACT <i>(Continue on reverse if necessary and identify by block number)</i> Three aspects of the application of adhesive bonding to lightweight bridge structures were examined: producing composite surface treatments to reliably bond with epoxy adhesives, developing computer models to optimize adhesive joint design and develop design guidelines, and adapting a high-toughness, low-temperature-curing epoxy adhesive to practical use as a bridge and repair kit adhesive. New testing methods were developed in the composite surface preparation task to assess fracture toughness and environmental durability of composite-to-adhesive bonds. A wide variety of existing and novel surface treatments were examined. Simple mechanical cleaning, such as hand sanding, was shown to be highly effective in providing the basis for strong, tough, and durable bonds. Finite element models of a prototype tubular lap joint indicated that such a joint could be characterized by a few critical parameters, such as diameter, tube thickness, and joint overlap length. Design guidelines were developed using these parameters to allow a designer to determine load bearing capacity, optimum design, and stress-concentration factor (a figure of merit).					
20. DISTRIBUTION/AVAILABILITY OF ABSTRACT <input type="checkbox"/> UNCLASSIFIED/UNLIMITED <input checked="" type="checkbox"/> SAME AS RPT. <input type="checkbox"/> DTIC USERS			21. ABSTRACT SECURITY CLASSIFICATION Unclassified		
22a. NAME OF RESPONSIBLE INDIVIDUAL Mr. Brian Hornbeck			22b. TELEPHONE <i>(Include Area Code)</i> (703) 704-2549		22c. OFFICE SYMBOL STRBE-JBC

19. Design optimization studies included techniques to reduce stress concentrations and equalize load across the entire surface of the joint. Adhesive enhancement studies resulted in the development and limited production of a lower viscosity, repair-kit suitable version of a high toughness, low-temperature-curing epoxy adhesive originally developed on an earlier research program. Studies of potential sealant systems to prevent degradation of epoxy adhesives due to moisture ingress did not identify any suitable sealants. Thus inherent resistance to moisture degradation is a necessity for structural epoxy adhesives. Finally, a center span demonstration article was designed and constructed based on the design guidelines, and utilizing the epoxy adhesive developed under this program. Construction and adhesive preparation details are reported.

Accession For	
NTIS GRA&I	<input checked="" type="checkbox"/>
DTIC TAB	<input type="checkbox"/>
Unpublished	<input type="checkbox"/>
Justification	
By Mr. B. Hornbeck	
Distribution: STRBE-JBC	
Availability: 10/00	
Dist	AVAIL ON 10/00 Special
A-1	

DTIC QUALITY IMPROVEMENT

EXECUTIVE SUMMARY

Adhesive bonding has theoretical advantages for the construction of lightweight structures, such as mobile bridges. However, very little practical use has been made of bonding technology in structural applications. The purpose of this research program was to investigate three areas where lack of understanding has inhibited the adoption of adhesive bonding. The diverse nature of the three areas mandated a multidisciplinary approach that involved chemists and materials scientist from Martin Marietta Laboratories with design engineers from the University of Maryland. As a final proof of overall concept an adhesively bonded center span was constructed for the Light Vehicle/Foot Bridge (LV/FB) that incorporated design features and adhesives developed during this study.

One area of special concentration was developing a reliable technique for bonding organic composite materials. Organic composites (e.g., graphite fiber/epoxies) suffer significant losses of strength and toughness in the vicinity of mechanical fasteners, making them ideal candidates for adhesive bonding. However, very little was known about the reliability of bonds to composite surfaces, and the effect of various surface preparation techniques on bond strength and durability. Based on prior experience with metal bonding surfaces, we expected that traditional mechanical cleaning techniques would be insufficient for highly loaded structural bonds. After extensive investigations of a wide variety of bonding surface treatments, we concluded that simple mechanical cleaning treatments were very effective and reasonably durable. In fact, the more novel treatments were no better and often far worse. In the course of this investigation we have developed test methods for tensile testing, durability testing, and fracture testing that greatly improve the state of the art for composite testing. We concluded that the limiting factor in the use of adhesive bonds with organic composites currently is the brittle nature of the composite matrix material (epoxy) itself, since the ultimate failure mode in every case using a good surface preparation technique was inevitably within the matrix material itself, i.e., a tougher composite matrix would inevitably improve the ability of the adhesive joint to transfer higher loads to the bulk of the composite.

The second area studied was joint design and prediction of the ultimate load-carrying capability of an adhesively bonded joint. Extensive finite element modeling was performed at the University of Maryland to examine the effects of design choices on joint performance. The first accomplishment was to determine the correct failure criteria for

the computer model. Correlations with previously collected test data demonstrated that von Mises' stress was the best predictor of joint performance. A tubular joint that represented the primary load-carrying member of the LV/FB structure was modeled to determine the effect of design changes that sought to reduce stress concentrations and thereby better utilize the entire adhesively bonded area to support the load. A set of design guidelines was developed that incorporated geometric conditions with load levels and optimum design features that enable a designer to confidently specify sizes and performance of a tubular joint. Finally, finite element methods were applied to the design of the demonstration article to guide the final design of the adhesively bonded LV/FB center section.

The third area of study was the refinement of a practical, high performance adhesive based on promising work in a previous program in which we had developed a four (4) day room-temperature-curing, high-toughness epoxy that offered real advantages for structural bonds, particularly between organic composites and metals. However, this adhesive was difficult to mix and apply due to very high viscosity. We explored various ways to reduce the effective viscosity, and have developed an adhesive (3H-F4) that can be dispensed from self-mixing guns. In this form, the adhesive becomes practical for use as a "repair kit" component, as well as much more manageable for production use.

Table of Contents

1.0 Introduction.....	1
1.1 Task I: Bonding to Dissimilar Materials.....	1
1.2 Joint Architecture and Predictive Modeling	2
1.3 Adhesive Enhancement and Repair Kit Development	3
2.0 Bonding of Dissimilar Materials and to Unprepared Surfaces.....	5
2.1 Literature Search	5
2.2 Surface Preparation Screening Tests	6
2.2.1 PATTI Test Configuration - Aluminum Substrates.....	6
2.2.2 PATTI Test Configuration -- Composite Substrates	9
2.3 Post-Processing Surface Treatments	11
2.3.1 Mechanically Cleaned Composite Surfaces	12
2.3.2 Chemical Etching.....	15
2.3.3 Plasma/Corona Discharge.....	16
2.3.3.1 Plasma-Etched Composite Surfaces	17
2.3.3.2 Corona Discharge	21
2.3.3.3 NH₃ Plasma Composite Surface Treatments	24
2.3.4 Metal Surface Deposition	26
2.3.5 Chemical Surface Modification	26
2.3.5.1 Resin Impregnation of a Swelled Composite.....	27
2.3.5.2 Electrodeposition of a Bond Promoter on the Composite Surface	28
2.4 Surface Conditioning Applied During Composite Curing	31
2.4.1 Peel Ply.....	31
2.4.2 Surface Particle Embedding	32
2.4.3 Prepared Metal Surface Embedding	34
2.5 Correlation of PATTI and Lap Shear Tests	38
2.6 Composite Tensile Strength.....	39
2.7 Durability Testing.....	40
2.7.1 Exposed PATTI Tests	40
2.7.2 Wedge Tests.....	42
2.8 Fracture Testing.....	50
2.9 Lessons Learned	54

Table of Contents (continued)

3.0 Joint Architecture and Predictive Modeling	56
3.1 Three-Dimensional Finite-Element Analysis of Quad-Lap Adhesive Joint	57
3.1.1 Analysis	57
3.1.2 Model.....	57
3.1.3 Boundary Conditions.....	60
3.2.1 Results-Aluminum Specimen	60
3.2.2 Results-Steel Specimen	61
3.2 Elastic-Plastic Analysis of Quad-Lap Specimen.....	63
3.3 Failure Criteria	69
3.4 Parametric Studies of Tubular Joint Design - Reducing Edge Effects	75
3.4.1 Finite Element Models	75
3.4.2 Parametric Study Results.....	82
3.4.3 Mesh Refinement	86
3.5 Parametric Studies of Tubular Lap Joints - Joint Length and Overall Geometry	86
3.5.1 Computer Optimization and Confirmation of Parametric Studies	95
3.5.2 Mechanical Tensile Validation Test.....	104
3.6 Design Guidelines.....	105
3.6.1 Aluminum-to-aluminum Adherend Adhesive Joints	109
3.6.2 Graphite/Epoxy Composite-to-Composite Joints	112
3.6.3 Aluminum and Graphite-Epoxy Tubular Adherend Adhesive Joints	116
3.6.4 Use of the Design Guideline Plots: a Design Example.....	119
3.7 LV/FB Design Assistance	123
3.7.1 Global Stress Analysis of Bridge Span	123
3.7.2 Finite Element Analysis	125
3.7.2.1 Three-Dimensional Global Finite Element Analysis of Bridge Span	125
3.7.2.2 Three-Dimensional Local Finite Element Analysis of the Central Portion of Bridge Span.....	127

Table of Contents (continued)

3.7.3 Composite Deck Finite Element Analysis.....	131
3.7.3.1 Results of Case I.....	132
3.7.3.2 Results of Case II.....	132
3.7.3.3 Results of Case III	132
3.7.3.3 Discussion.....	132
3.8 Lessons Learned	140
4.0 Adhesive Enhancement and Repair Kit Development.....	141
4.1 Viscosity Improvements to Adhesive 3H	141
4.2 Cure Acceleration Experiments.....	144
4.3 Stress Relaxation of 3H-F4	145
4.4 Tensile Testing of 3H-F4	148
4.5 Lap Shear Testing of 3H-F4	150
4.6 3H-F4 Adhesive Preparation.....	153
4.6.1 The Bisazodiol Monomer Reaction	153
4.6.2 Part A Production.....	154
4.6.3 Part B Production.....	155
4.7 Vinyl Functional Additions - 3HVT.....	155
4.7.1 Curing of Resin and Film Preparation	156
4.7.2 Mechanical Testing	157
4.8 Field Repair Technology.....	158
4.9 Sealant Investigation.....	159
4.9.1 Preparation of Sealant Films.....	160
4.9.2 Moisture Absorption	161
4.9.3 Moisture Absorption of Coated Adhesives	162
4.9.4 Stress Relaxation.....	165
5.0 Demonstration Model.....	169
5.1. Design Details	169
5.2. Construction Details	172
5.3. P2 Etch.....	175
5.4 Adhesive Application	175
6.0 References.....	177
Appendix A. Prototype MSDS Forms for Adhesive 3H-F4	179
Part A - Resin Base.....	179
Part C - Hardener and Tougheners.....	182

List of Tables

Table 2.1. PATTI Tensile Values for Aluminum Substrates	8
Table 2.2. Bond Strengths to Mechanically Cleaned Composite Surfaces.....	12
Table 2.3. Mechanical Cleaning and Composite Type Effects on PATTI Tensile Strength	14
Table 2.4. Tensile Bond Strengths to Chemically Etched Composite Surfaces	16
Table 2.5. PATTI Tensile Strengths Using Argon Plasma Etched Surfaces	18
Table 2.6. PATTI Strength Values for High Power/Short Time Plasma Etch Surfaces	18
Table 2.7. PATTI Tensile test results for 200 V plasma surface treatments	21
Table 2.8. Tensile Testing of Metalized Composite Surfaces	26
Table 2.9. PATTI Test Results of the Swelled Composite Experiments.....	28
Table 2.10. PATTI Test Results from the Electrodeposition Experiment.....	30
Table 2.11. Tensile Test Results After Surface Morphology Modifications.	34
Table 2.12. PATTI Tensile Tests of Aluminum Cast Composite Surfaces	36
Table 2.13. Hybrid Composite/Aluminum Double Lap-Shear Test Results.	39
Table 2.14. PATTI Tensile Test Strengths on Sanded, Unidirectional Graphite Composite Beams.	40
Table 2.15. Fracture Data from Composite Sandwich CT Specimens	52
Table 3.1. Properties of Adherends and Adhesive	60
Table 3.2. Double-Lap-Shear Validation Test Results -Tensile Strength (psi)	104
Table 3.3. Material Properties of Adherends and Adhesive	112
Table 3.4. Stacking Sequence and Material Properties of Graphite/epoxy Composites Used for Joint Modeling	112
Table 4.1. Adhesive 3H Viscosity and Property Enhancement	143
Table 4.2. Fracture Testing of Lower Viscosity Formulations	144
Table 4.3. DSC Results of Cure Acceleration Experiments	145
Table 4.4. Stress-Relaxation Results for 3H-F4 and 3H.....	148
Table 4.5. Tensile Testing Results of 3H-F4 and 3H	149
Table 4.6. Double Lap Shear Results.....	150
Table 4.7. Neat Adhesive Strip Tensile Strengths as a Function of Mixing Ratio	152
Table 4.8. Tensile Results for Adhesive 3HVT	157
Table 4.9. Stress Relaxation Results: Adhesive 3H Coated with Various Sealants	167

List of Figures

Figure 2.1. Schematic drawing of the PATTI test instrument	7
Figure 2.2. DSC trace of Hercules 3501-6 epoxy showing cure hysteresis.....	10
Figure 2.3. TGA record of a piece of composite prepreg showing weight loss.....	11
Figure 2.4. Optical macrograph of a sanded composite surface.	13
Figure 2.5. PATTI pull stub after testing a woven graphite composite surface.	15
Figure 2.6. Optical micrograph of a unidirectional graphite composite surface after sulfuric acid etching.	17
Figure 2.7. Effect of argon plasma etch on composite surfaces. a) surface after "low power" treatment, and b) surface after "high power" treatment.....	19
Figure 2.8. SEM micrograph of a composite surface after a "short time, high power" argon plasma treatment.	20
Figure 2.9. Electron micrographs of "smooth" composite surfaces plasma etched at 200 V for a) 8 min and b) 18 min.	22
Figure 2.10. SEM of corona-discharge-treated composite surface.	23
Figure 2.11. Specular reflectance spectrum of an argon-plasma-etched composite.....	25
Figure 2.12. Specular reflectance spectrum of an ammonia-plasma-etched composite.....	25
Figure 2.13. Schematic of chemical bond linkage between composite and adhesive.	29
Figure 2.14. Equipment schematic for electrodeposition experiment.	30
Figure 2.15. Scanning electron micrograph of a composite surface after peel-ply removal.	32
Figure 2.16. Optical macrograph of a composite surface with embedded salt crystals and voids.	33
Figure 2.17. Optical macrograph of a composite surface with embedded activated charcoal additions.....	33
Figure 2.18. SEM micrograph of a composite surface after peeling away a sheet aluminum conditioning plate.	35
Figure 2.19. SEM photomicrograph of the oxide surface produced by the aluminum oxide embedding treatment on a composite test specimen.....	37
Figure 2.20. SEM micrograph of a 50 V PAA oxide film impregnated composite bonding surface.	37

List of Figures (continued)

Figure 2.21. Schematic of composite/aluminum double lap-shear specimen.....	38
Figure 2.22. Plots of exposed PATTI tensile strength tests, for sanded and sandblasted composite surfaces.....	41
Figure 2.23. Schematic of the all-composite wedge-test specimen.....	43
Figure 2.24. Schematic of Aluminum/composite hybrid wedge-test specimen.....	45
Figure 2.25. Photograph of wedge-test specimens after testing. Note the extensive crack opening on the specimen in the middle (arrow).....	45
Figure 2.26. Wedge-test results for the all-composite wedge-test specimens.....	46
Figure 2.27. Schematic drawing of the second hybrid aluminum/composite wedge-test specimen.....	47
Figure 2.28. Results of aluminum/composite-sandwich wedge-tests, compared with the ASTM standard phosphoric acid anodized all-aluminum specimen.....	48
Figure 2.29. Wedge-test results of plasma-etched composite specimens.....	49
Figure 2.30. Schematics of the two types of compact tension test specimens used for fracture testing.....	51
Figure 2.31. Optical macrograph of a cross-grain compact tensions specimen after test. The crack front passed through the graphite fiber bundles in the epoxy matrix over more than one-half the total area.....	53
Figure 3.1. Quad-lap specimen geometry, steel specimen. The shaded region indicates the one quarter section used in the finite element model..	58
Figure 3.2. Finite element model of one quarter of the quad-lap specimen.	59
Figure 3.3. Equivalent stress acting on the middle adhesive layer for an aluminum quad-lap specimen.	62
Figure 3.4. Equivalent stress in the middle adhesive layer for a steel quad-lap specimen.	64
Figure 3.5. Elastic-plastic analysis equivalent stress in top layer of a steel quad-lap specimen.	65
Figure 3.6. Elastic-plastic analysis equivalent stress in the middle adhesive layer of a steel quad-lap specimen.	66
Figure 3.7. Elastic-plastic analysis of the bottom adhesive layer in a steel quad-lap specimen.	67

List of Figures (continued)

Figure 3.8. Middle adhesive layer stress at joint failure for the steel quad-lap specimen.....	68
Figure 3.9. Idealized bilinear constitutive model of adhesive for finite element analyses.....	71
Figure 3.10. Comparison between finite element model prediction and experimental results for failure load of the quad-lap specimen.....	73
Figure 3.11. Comparison between finite element predictions and experimental results using nonconventional failure criteria.....	74
Figure 3.12. Finite element model of tubular lap joint (Step 1).....	76
Figure 3.13. FEM model of a Type I taper tubular lap joint (Step 3).....	77
Figure 3.14. FEM model of a Type I tubular lap joint (Step 5).....	78
Figure 3.15. FEM of a Type II tubular lap joint (Step 3).....	79
Figure 3.16. FEM of an exterior ring tubular lap joint (Step 1).....	80
Figure 3.17. FEM of an exterior ring tubular lap joint (Step 5).....	81
Figure 3.18. FEM of a chamfered tubular lap joint (Step 5).....	83
Figure 3.19. Equivalent stress along the middle adhesive layer for Type I taper lap joints.....	84
Figure 3.20. Equivalent stress as a function of distance along a Type II lap joint.....	85
Figure 3.21. Equivalent stress as a function of distance along an exterior ring stabilized lap joint.....	87
Figure 3.22. Equivalent stress as a function of distance for a chamfered lap joint.....	88
Figure 3.23. Maximum von Mises' equivalent stress in the adhesive as a function of the number of elements used in the finite element model.....	89
Figure 3.24. Equivalent stress as a function of position for tubular joints with differing bond lengths.....	90
Figure 3.25. Factors of safety for an untapered tubular lap joint as a function of overlap length-to-wall thickness ratio for aluminum substrates.....	92
Figure 3.26. Stress concentration factor plots as a function of overlap ratio for an untapered aluminum tubular lap joint.....	93
Figure 3.27. Stress concentration factor plots for the adhesive layer as a function of overlap ratio for Type I (solid line) and Type II (dotted line) taper joints.....	94
Figure 3.28. Stress concentration factors in a Type I tapered aluminum lap joint with a 3-in. overlap as a function of degree of taper.....	96

List of Figures (continued)

Figure 3.29. Stress concentration factor plot for a Type I taper aluminum lap joint with a 0.75-in. overlap, as a function of degree of taper.	97
Figure 3.30. Stress concentration factor plot for an untapered tubular aluminum lap joint with a 0.5-in. overlap.....	98
Figure 3.31. Optimum thickness of leading edge of taper-to-tube-thickness ratio as a function of the joint overlap length-to-tube-thickness ratio.	99
Figure 3.32. Schematic diagram of the joint cross section used for the computer optimization study.....	100
Figure 3.33. Computer optimized joint design for an aluminum tubular lap joint with overlap ratio (L/T_0) = 4.1.....	101
Figure 3.34. Computer optimized design for an aluminum tubular lap joint with overlap ratio (L/T_0) = 24.....	102
Figure 3.35. Distance-ratio-to-overlap-ratio optimums for the computer-based designs compared to the parametric study results.....	103
Figure 3.36. Double lap specimen configuration for taper testing.....	104
Figure 3.37. Tubular lap joint geometry and critical dimensions.	106
Figure 3.38. Type II tapered lap joint geometry and critical dimensions.....	107
Figure 3.39. Optimal applied load plot (normalized for adhesive tensile strength) for aluminum-to-aluminum adherends.....	109
Figure 3.40. Threshold overlap ratio for aluminum-to-aluminum adherends.	110
Figure 3.41. Stress concentration factors for aluminum-to-aluminum adherends.	111
Figure 3.42. Optimal applied load plot for composite-to-composite adherends.....	113
Figure 3.43. Threshold overlap ratio for composite-to-composite adherends.	114
Figure 3.44. Stress concentration factors for composite-to-composite adherends.	115
Figure 3.45. Optimal applied load plot for aluminum-to-composite adherends.	116
Figure 3.46. Threshold overlap ratio for aluminum-to-composite adherends.	117
Figure 3.47. Stress concentration factors for aluminum-to-composite adherends.	118
Figure 3.48. Optimal applied load design plot, composite-to-composite tubular lap joints.	120
Figure 3.49. Threshold overlap length design plot, composite-to-composite tubular lap joints.....	121
Figure 3.50. Stress concentration factor plot, composite-to-composite tubular lap joints.	122
Figure 3.51. Simplified bridge span loading.	124

List of Figures (continued)

Figure 3.52. Cross-section of the simplified bridge span.....	124
Figure 3.53. Three-dimensional finite element mesh of one-quarter of the bridge span.....	126
Figure 3.54. Boundary conditions and applied load for one-quarter of the bridge span.....	128
Figure 3.55. Boundary conditions and applied displacements for one-quarter of the bridge span.....	129
Figure 3.56. Explanation of the locations for "Top" and "Bottom" joints in the central bridge span.....	130
Figure 3.57. Configurations of components used for composite deck plate models....	131
Figure 3.58. Contour plot of shear stress, t_{yz} , of the side panel for Case I.....	134
Figure 3.59. Contour plot of adhesive von Mises' stress in the "top" joint for Case I .	135
Figure 3.60. Contour plot of shear stress, t_{yz} , of the side panel for Case II.....	136
Figure 3.61. Contour plot of adhesive von Mises' stress in the "top" joint for Case II.	137
Figure 3.62. Contour plot of shear stress, t_{yz} , of outer side panel in Case III.....	138
Figure 3.63. Contour plot of shear stress, t_{yz} , of inner side panel in Case III.....	139
Figure 4.1. Neat adhesive compact tension specimens.....	142
Figure 4.2. Stress relaxation plot for formulation no. 8, with Jeffamine 400 curative.	146
Figure 4.3. Stress-relaxation plot for adhesive 3H-F4.....	147
Figure 4.4. Stress-strain plot for neat adhesive 3H-F4 specimen.....	149
Figure 4.5. Adhesive applicator gun.....	151
Figure 4.6. Applying 3H-F4 adhesive to double lap shear specimens.	151
Figure 4.7. Lord PAK 50 dispensing and mixing adhesive gun.	159
Figure 4.8. Optical macrograph of test strips used for moisture pickup (top) and stress relaxation (bottom) testing.	160
Figure 4.9. Water absorption weight gain for sealant materials alone.	162
Figure 4.10. Water absorption weight gains for adhesive 3H alone and coated with sealants.....	163
Figure 4.11. Water absorption weight gains for Hysol 9394 adhesive coated with sealants.....	164
Figure 4.12. Stress relaxation curve for 3H adhesive coated with Silaprene M 6792. .	166
Figure 4.13. Stress-relaxation plots of sealant coated 3H.....	168

List of Figures (continued)

Figure 5.1. Box-section design concept for an adhesively bonded interior bay.	169
Figure 5.2. Cross section drawing of deck support structure, original design.....	170
Figure 5.3. Cross section drawing of demonstration article deck support configuration...	170
Figure 5.4. Layout of internal and end stiffeners.	171
Figure 5.5. Inner stiffener bend detail to avoid weld bead.	172
Figure 5.6. Photograph of the completed LV/FB center span demonstration article....	173
Figure 5.7. Close up view of the end of the span, showing the end doubler plate and hinge fittings.....	173
Figure 5.8. Interior view of demonstration article, showing internal stiffeners.....	174

1.0 INTRODUCTION

To meet its defense commitments in the 1990s, the Army must have reliable, maintainable, and durable military bridging. Emerging technologies, such as lightweight organic composites and high-strength materials, offer good prospects for bridge design improvements. However, the properties of these materials cannot be fully utilized until techniques are developed to incorporate them into structures without compromising their integrity. Adhesive bonding, which is the primary candidate for joining such materials into coherent structures, cannot be properly exploited because of inadequacies in such critical areas as preparation techniques for materials bonding, prediction of joint performance, adhesive performance, and testing for bond integrity. Accordingly, the U. S. Army Belvoir Research, Development and Engineering Center funded the research program described in this report to advance bonding technology for application to military bridges. The primary program goal was to design and fabricate an interior bay of the light vehicle/foot bridge (LV/FB) with bonded joints. The design prototype for this bridge is an all-welded aluminum (6061-T6) structure that would benefit greatly from the use of strong, durable bonded joints because this grade of aluminum loses as much as 60 percent of its yield strength through welding.

The research was intended to be applicable to future bridge design, fabrication, and field repair as well. Therefore, the three subtasks were conceived to both advance the state of knowledge about critical areas of application of adhesive bonding technology to bridge design, as well as to support the construction of the demonstration article. The overriding concern in all tasks was to enable bridge designers to confidently incorporate adhesive bonding in future bridges.

1.1 Task I: Bonding to Dissimilar Materials

The aerospace industry has spent over 30 years perfecting bonding techniques for aluminum substrates, with great success. At Martin Marietta Laboratories, we discovered that the primary reason for the excellent performance of aluminum-to-aluminum bonding was the presence of microporosity in the oxide layer found on properly prepared surfaces that could mechanically interlock with a curing adhesive film, forming a strong interface⁽¹⁾. Another crucial discovery was that the durability of the bond, even more than the strength, was related to the presence of this porosity⁽²⁾. Comparatively little research has been done

on organic composite surfaces, and almost none has been directed to bond durability, a critical component of reliability in outdoor bridging. Thus, we concluded that the development of a bonding technique and the means to testing the durability and strength of resulting bonds are critical to the wide-scale use of lightweight composites in bridge designs.

To this end, we decided that a technique featuring microporosity formation on bonding surfaces would be critical for composites, as it was for metals. The conventional techniques for bonding to composite surfaces, sanding and peel-ply conditioning, seemed sure to have significant durability problems, based on the results of metal-to-metal bonding studies. In addition, the tensile strengths reported by previous researchers had generally been quite low, roughly one-third of the strengths routinely obtained for metal bondments.

As the program progressed, however, we were surprised at the excellent performance of sanding and grit-blasting treatments, as evidenced by the good strengths achieved in testing. Despite extensive efforts to find other techniques that offered better performance, sanding proved to be the most consistent, strongest preparation technique. When we extended testing to include durability and fracture properties, we were again surprised that sanding was equal to or superior to other techniques, and entirely satisfactory as a bonding preparation. It also became clear that the weak link in composite bonding was the composite itself. High tensile strength bonds could be made, but the poor fracture performance of the graphite/epoxy composites limited both its strength and durability. Fracture testing resulted in particularly low values, again because of the inherently brittle matrix of the composites.

The ultimate lesson of this task was that the material properties of the composite will always be the limiting factor in bonding performance when used either with themselves or in combination with other materials. A reasonably tough adhesive will always outperform the conventional composite matrix. The current selection of composite matrices, optimized for high-stiffness and high-temperature performance, are poor choices for structural designs.

1.2 Joint Architecture and Predictive Modeling

The intent of this task was to develop techniques that would allow the bridge designer to incorporate adhesive joints into a design with confidence, knowing their reliable performance level. Design techniques that have been developed for welded metal structures are not directly transferable to bonded composite or mixed structures. Uncertain

performance predictions and the experience of premature and unexpected failures have severely impacted the use of these techniques in structural design.

A primary problem with adhesive joining is the stress concentration effect that edges introduce. Since adhesives are inherently brittle, compared to metals, a concentration of strain leads to local overloading and failure that proceeds through the entire joint, rather than local deformation and stress equalization. Thus, the designer cannot confidently predict the failure load of most joint designs, since it is unrelated to the area of the bond, but depends critically on joint geometry. Therefore, a primary goal of this task was to develop joint designs that nearly eliminate the stress concentrations, so simple design formulas can be used to predict the load-bearing capabilities of joints. We focused on an overlapping tubular joint which modeled the critical joint in the LV/FB design, the lower hinge fitting-to-longitudinal extrusion joint.

Finite element computer modeling was extensively used to optimize the design of the overlapping tubular joint and to predict its behavior. Joint design guidelines were developed for aluminum-to-aluminum, composite-to-composite, and aluminum-to-composite adherends of this geometry that cover a wide range of sizes and can be applied to adhesives of any strength. This geometry proved to be a particularly easy one from a stress concentration viewpoint, so the immediate results cannot be generalized to joints of arbitrary geometry; but finite element modeling tools and appropriate failure conditions were developed that can be used to model any prospective design. Indeed, we used these techniques to model and guide the design of the demonstration article.

1.3 Adhesive Enhancement and Repair Kit Development

This task was directed towards developing an adhesive that would be well suited to use in structural bonding, including aluminum, composite and dissimilar substrates, and could be used by field personnel in a repair kit.

In another program with BRDEC⁽³⁾, we developed a low-temperature-curing epoxy formulation that demonstrated all the desirable properties for a structural adhesive—exceptional toughness along with excellent strength and durability. (A low temperature curing adhesive is necessary to avoid significant bonding induced stresses in the adhesive, particularly when dissimilar materials with different thermal expansion coefficients are

used.) However, this formulation was difficult to mix and apply, and we wished to investigate further property improvements. Although we were not able to significantly enhance the properties, we did develop a modified formulation (3H-F4) that is much more "user-friendly" without sacrificing properties. We utilized this formulation, along with self mixing dispensers that are readily adaptable to repair kit use, to construct the demonstration article.

We also investigated the use of sealants designed to prevent moisture transport. Since moisture is the cause of poor adhesive bond durability, primarily due to the poor performance of the adhesive polymer when infused with water molecules, the ability to seal out the moisture should enhance the long-term performance of bonded joints. However, we found that no sealant was effective in preventing moisture infusion, particularly when the sealed adhesive was exposed to moisture under load. Thus reliable adhesive joints will have to depend on the long-term moisture-equilibrium properties of the adhesive itself. This emphasizes the need to choose adhesives, like the one formulated during this program, that can retain a significant fraction of their properties when exposed to moisture.

2.0 BONDING OF DISSIMILAR MATERIALS AND TO UNPREPARED SURFACES

2.1 Literature Search

A thorough literature search uncovered relatively few treatment techniques that offered any advantage for preparing graphite/epoxy surfaces for bonding. All of the reported surface modifications were applied after the composite had been cured. We found no record of research on texturing surfaces during composite cure for bonding purposes.

Studies that focused on chemical or physical modification of surfaces (i.e., solvent cleaning, acid etching, scrubbing, and sanding) consistently found no improvement in bonding.⁽⁴⁻⁶⁾ Similarly, solvent wipe and scrubbing were determined to have relatively little effect on surface cleanliness (i.e., silicon-containing species left over from mold releases, etc., were not much reduced by these surface treatments).^(1,7)

Oxygen plasma treatments were found to be useful for polyimide and epoxy composites⁽²⁾ and sheet molding compound,^(8,9) typically improving bond strength (i.e., lap-shear values) by a factor of two (from 1680 psi to 3220 psi for epoxies)⁽²⁾. Corona discharge treatments also produced similar improvements for epoxies, presumably through a very similar surface modification mechanism.⁽¹⁰⁾ Most authors concluded that the primary benefit of these treatments is the removal of mold release agents and general surface cleaning, rather than surface roughening or formation of chemical bonding sites. As far as we can determine, previous researchers have not tried to optimize surface morphology as a function of surface treatment conditions.

Use of a "peel ply" outer surface during composite fabrication also appears to result in a clean bonding surface that would enhance adhesion. Kevlar® peel ply was reported to be as effective as corona discharge treatments for thermoplastic composites.⁽¹¹⁾ Of course, a peel-ply layer will also impart a characteristic texture to the composite surface, which might improve bondability.

A novel approach that was successful for polyethylene and PVC involved a chemical reaction of the outer surface to form a copper sulfide layer on the polymer surface.⁽¹²⁾ A metallic copper layer plated on the electroconductive sulfide coating would then provide a

medium for a strong metal oxide-to-adhesive bond. We are not very hopeful that such a reaction can be found for cured epoxies, but it is an intriguing possibility.

At first, we were puzzled by the relative paucity of research on bonding to thermoset resins, given their large scale use in the aerospace industry. It became clear by the end of our studies that the simple mechanical cleaning treatments currently in use are very effective. Thus, there is no strong motivation to pursue further research.

2.2 Surface Preparation Screening Tests

The first requirement for evaluating the effectiveness of surface treatments for adhesively bonding graphite/epoxy composites was the development of a screening test that would at least reliably indicate qualitative performance, and use a readily prepared specimen. We recognized that we would be dealing with brittle materials, and therefore wanted to identify a test method that would have a low sensitivity to edge and alignment effects. The device we chose for testing was the Pneumatic Adhesive Tensile Test Instrument (PATTI), produced by SEMicro, Rockville, MD.

The PATTI device (Figure 2.1) features a small aluminum test stub (0.5 in. in diameter) that is bonded to the test surface. A metal casing containing a silicone rubber gasket is screwed onto the stub, snugging the gasket against the specimen. Air pressure is then gradually applied in the chamber between the casing and the gasket, forcing the casing up against the stub and thereby applying a tensile force. Three critical features of this test apparatus are 1) the small size of the test specimen, 2) the relative freedom from edge effects due to the round stub on a "semi-infinite" flat surface, and 3) the self-aligning nature of the pneumatic piston that ensures a tensile force perpendicular to the test stub, even if there is a small misalignment. Although this tester is part of an ASTM test method (D4541), there is very little guidance about choosing an appropriate test specimen, since it is intended to be an "in-situ" test. Therefore, we had to determine the correct specimen geometry for our purpose before proceeding with surface preparation testing.

2.2.1 PATTI Test Configuration - Aluminum Substrates

We conducted a number of preliminary tests using the PATTI to determine appropriate test geometries and to validate our test methods. Test samples were constructed

from aluminum substrates and two types of graphite/epoxy composites. Hysol EA 9394 two-part epoxy adhesive (Dexter Aerospace Materials Division, 2850 Willow Pass Road, Pittsburgh, California 94565) was used to bond aluminum stubs whose bonding surface had been prepared with the phosphoric acid anodization (PAA) process. Adhesives were allowed to cure 12 to 18 hr at room temperature, followed by oven conditioning at 50°C for approximately 8 h.

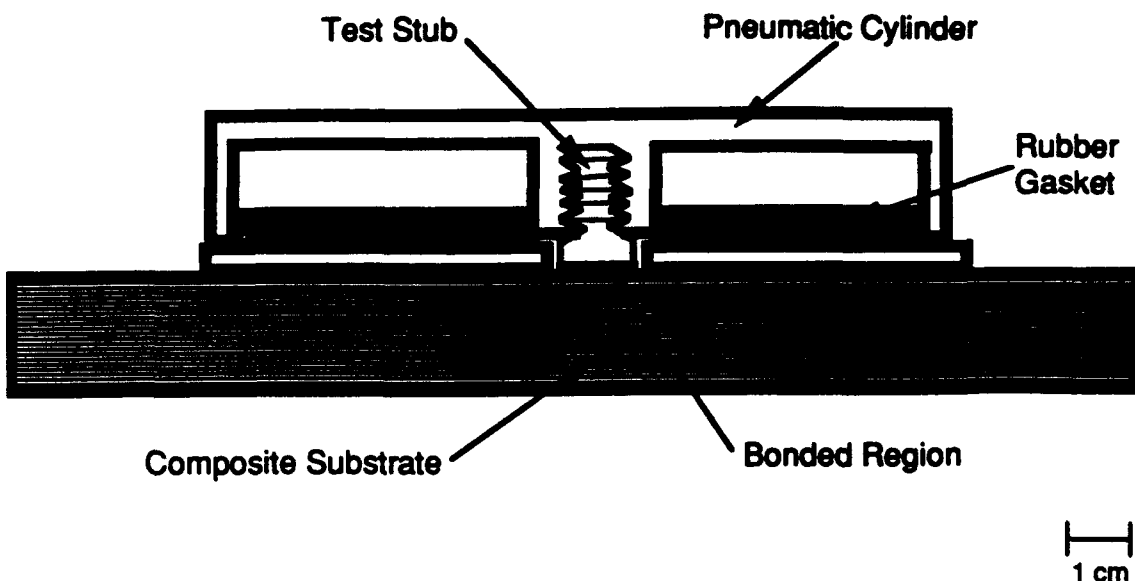


Figure 2.1. Schematic drawing of the PATTI test instrument.

We investigated the effect of substrate and bond-line thickness on the tensile strength measured by this test. Bond-line thickness was controlled with a micrometer gauge fixture that placed the test stubs on the adherends. This ensured that the stubs were bonded with the requisite gap. It proved difficult to bond samples with bond-lines thicker than 30 mil, so only the 15-mil and 30-mil conditions were tested. "Thin" bond-lines (< 10 mil) were prepared by pushing the bond stub against the substrate as tightly as possible.

Table 2.1 lists the average results of this testing (with standard deviation values in parentheses), using three test stubs for each condition. Clearly, the thicker (and stiffer) the substrate, the greater the apparent bond strength. This result is expected, since the thinner substrates are deformed by the test, leading to stress concentration around the edges of the

specimen. However, this essentially rules out the use of thin substrates, and mandates that all testing be performed on equivalent stiffness substrates. There is also a consistent bond-line thickness dependence, with thicker bond lines showing lower strengths, consistent with previous bond-line dependency studies. The "thin" bond line also seems to lead to lower strength bonds, probably because of problems with maintaining good alignment and bond-line consistency when most of the adhesive has been squeezed out. In any case, we standardized on 15 mil bond lines for all testing.

Table 2.1. PATTI Tensile Values for Aluminum Substrates (Hysol 9394 Adhesive)

Substrate	# tests	Bond line	Tensile Strength (psi)
1/16-in. thick	8	"thin"	1420 (± 380)
1/16-in. thick	8	15 mil	2050 (± 310)
1/16-in. thick	6	30 mil	1010 (± 300)
1/8-in. thick	11	15 mil	3980 (± 165)
1/8-in. thick	4	30 mil	2750 (± 750)
3/8-in. thick	4	"thin"	5680 (± 550)
3/8-in. thick	5	15 mil	7092 (± 1130)
1/2-in. thick	3	15 mil	>8450

In other PATTI tests on aluminum substrates, we investigated the use of a special test jig, which was designed for a previous program to allow bonding to thin, flexible substrates. The normal PATTI test consists of placing a piston on the test stub and pulling up on the stub while the base of the piston pushes against the substrate. However, the opening at the base of the piston, about 1 in. in diameter, is sufficiently large to allow thinner substrates to bow up, which concentrates stresses around the edge of the stub. The special test jig reduces this tendency by transmitting the stress from the bottom of the piston to a ring fitted closely around the outside of the stub, thus reducing the bending moment.

We tested stub bonds under three conditions (all with a 15-mil bond line): with no jig, with the test jig, and with a misaligned test jig. Testing three samples in each condition, we found that the stubs with no jig did not fail (> 6000 psi), the stubs in the test jig failed at a value of 3820 (+/- 330) psi, and the stubs in the misaligned jig failed at 2670 (+/- 220) psi. These results indicate that the test jig actually worsened stress concentration effects for our

fairly stiff substrates. The misaligned jig had the worst effect, leading to failures at low stress levels, but even when the load was applied as uniformly as possible, the jig still initiated failures at abnormally low levels. Obviously, the jig did not lead to consistent test results, and did not improve the test values for thin substrates, and therefore was not used during our studies

2.2.2 PATTI Test Configuration – Composite Substrates

Based on the results of the aluminum tests, we recognized the need for a thick composite test specimen to use as the substrate for surface preparation testing. Our standard composite test specimen is a 0.75-in. x 2-in. x 9-in. rectangle of unidirectional graphite composite material machined out of a bridge chord structure. This is a sufficiently stiff beam to give accurate PATTI test results, and has sufficient room to bond three pull stubs to the surface.

Two types of epoxy adhesives were used to bond pull stubs to composite surfaces, Hysol EA 9394 and 3H-F4, an adhesive developed at the Laboratories, and described in Sections 4.1-4.6 of this report. Both are room-temperature-curing, two-part epoxies with good strength and fracture toughness. The type of adhesive used is discussed along with the results of each test series. Two types of prepreg epoxy/graphite fiber composite materials were used to construct test specimens, both from Hercules (Hercules Aerospace Company, Composite Products Group, Box 98, Manus Utah 84044). The unidirectional fiber prepreg used IM-6 fibers in a 3501-6 epoxy resin. Woven prepreg consisted of AS-4 graphite satin weave mats, 20 mil ply, with 3501-6 epoxy resin matrix

We developed methods to utilize the same basic specimen to screen surface modification treatments that utilize a newly cured composite surface. Constructing an equivalent test beam with a fresh composite surface would require many plies of the prepreg materials we used. Instead, we developed a technique to add a single new woven composite layer to a prepared surface of a previously cured beam, considerably reducing the amount of material required for each test. Although the strength of the "bond" across this interface probably is not quite as good as a single-step cured composite, it proved sufficient for all of our testing.

During the course of testing, we noted some problem with consolidating the new woven graphite epoxy layer with the beam specimen. Voids developed on the surface during

the initial heat up during the cure cycle as a result of solvent evaporation. The thermogram shown in Figure 2.2 is the cure hysteresis of the Hercules 3501-6 epoxy matrix. It shows a two-step reaction mechanism in which the initial cure is approximately 113°C and final cure is at onset of ~177°C. Thermal analysis via differential scanning calorimetry (DSC) provided no indication of solvent boiling below the cure temperature. DSC measures heat flow into and out of a test specimen, and thus can detect changes in state such as melting or boiling, and heat energy adsorbed or liberated during a chemical reaction.⁽¹³⁾ Therefore, we ran a thermal gravimetric analysis (TGA) on an uncured composite specimen from 25°C to 300°C at 10°C/min. TGA monitors changes in sample weight as a function in temperature, and thus can determine at what temperature changes, such as vaporization, take place.⁽¹⁴⁾ From the TGA record (Figure 2.3), one can see a 1.7 percent drop in weight over the entire range, which can be attributed to the release of solvent.

Understanding this phenomenon allowed us to modify the preparation of our prepeg material. The modification involved the removal of the solvent by placing the graphite/epoxy single ply under reduced pressure (-30 in Hg) in a vacuum oven set at 250°C. In this step, we could visually observe bubble formation at the surface of the composite,

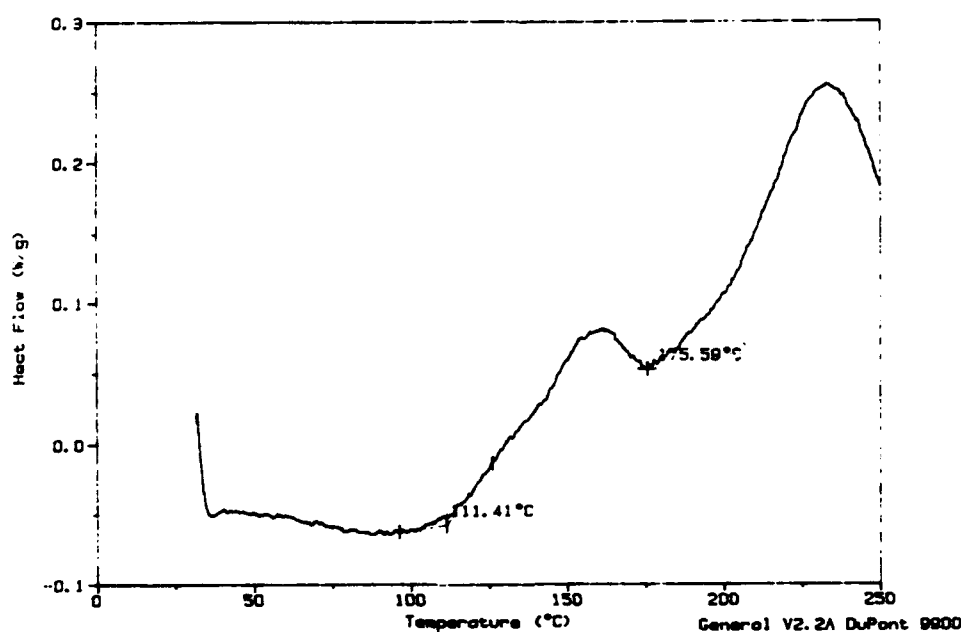


Figure 2.2. DSC trace of Hercules 3501-6 epoxy showing cure hysteresis.

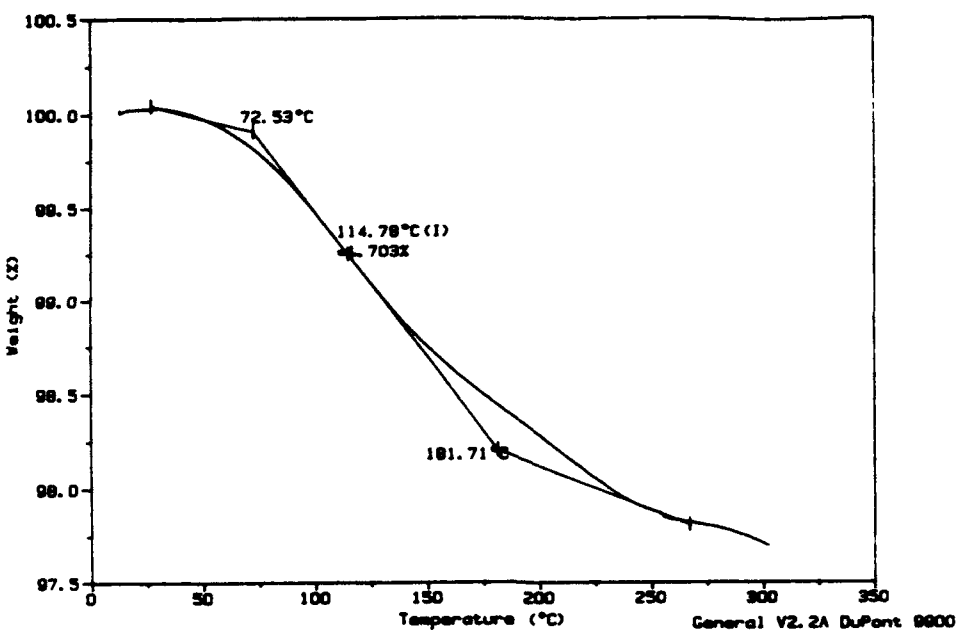


Figure 2.3. TGA record of a piece of composite prepreg showing weight loss.

indicating that evacuation of the solvent was taking place. After 2 hr, the prepreg was removed, layed up on top of a sanded, already cured composite test beam, and transferred to a MPT-14 hydraulic press. The specimen was heated to 350°F at 10°F/min and held at that temperature, under 50 psig pressure, for 2 hr. The temperature was then decreased to ambient at 10°F/min and the pressure removed. The result was a uniform prepreg in which there was an outer matrix layer with a smooth surface completely coating the inner graphite fiber weave.

2.3 Post-Processing Surface Treatments

Surface treatments for adhesive bonding to composites traditionally have been applied to fully cured composite surfaces. This is obviously the most straightforward approach, since no consideration for bonding need be made during construction of the composite material. Less care need be applied during lay-up, and no special tooling would be required. As a result, almost all previous research on composite bonding involves modifying the post-cured composite surface. We based our efforts in this area on the

previous research, that indicated chemical etches, and plasma/corona treatments had beneficial effects under certain conditions.

2.3.1 Mechanically Cleaned Composite Surfaces

A number of mechanical cleaning treatments were examined. Sanding, machining, and grit blasting were tried. Sanding was performed using SiC-grit wet sanding papers with grit sizes ranging from 60 to 120. Papers were hand rubbed on the composite surfaces until a uniform, dull finish was achieved. Machining was done using a band saw with a 16 TPI steel metal cutting blade. Sandblasting surfaces used a glass-bead grit blast machine operating at 50 psi. All surfaces were cleaned after treatment to remove any residue by wiping with toluene, then with tetrahydrofuran, followed by drying in an air oven at 75° C for about 2 hr, prior to bonding. The results of the mechanical cleaning experiments are listed in Table 2.2.

Table 2.2. Bond Strengths to Mechanically Cleaned Composite Surfaces
(PATTI tests using Hysol 9394 adhesive)

Substrate Treatment	# tests	PATTI Strengths (psi)	Locus of Failure
As-cured + solvent cleaned	8	690 (± 290)	Interfacial at surface
As-machined + solvent cleaned	8	1820 (± 700)	Interfacial at surface
60 grit sanded + sol. cleaned	1	5140	Inside composite
80 grit sanded + sol. cleaned	9	4220 (± 1040)	Mostly inside composite
Grit blast + solvent cleaned	6	4800 (± 640)	Inside composite

The low pull-off value in the as-cured case apparently represents the failure of the solvent cleaning to remove all traces of silicone release agent transferred from the curing platens. The as-machined surfaces gave strength values comparable to those reported by other researchers, better than solvent cleaning alone, but much lower than the adhesive could provide on metal surfaces. It is possible that the machining operations left a solvent-resistant residue on the composite. All the roughened surfaces have extremely high bond-strengths. The micrograph shown in Figure 2.4 of a sanded composite surface is typical of those produced by all the mechanical cleaning treatments. These surfaces do not have a particularly good bonding morphology after treatment, since the grooves are shallow and not particularly well suited to forming a strong mechanical interlock with the curing adhesive polymer. Metal surface after grit-blasting are typically much rougher, yet they do not form a

strong mechanical bond with epoxy adhesives. However, the failure mode (inside the outside surface of the composite, pulling out some of the unidirectional fibers) indicates that we have reached the highest possible test strength of these particular composite beams. The bonding interface clearly is stronger than the composite matrix, which is all that is necessary for a good surface treatment. The three mechanical roughening and cleaning treatments therefore give essentially identical measured strengths, since they are actually measuring the strength of the composite matrix..

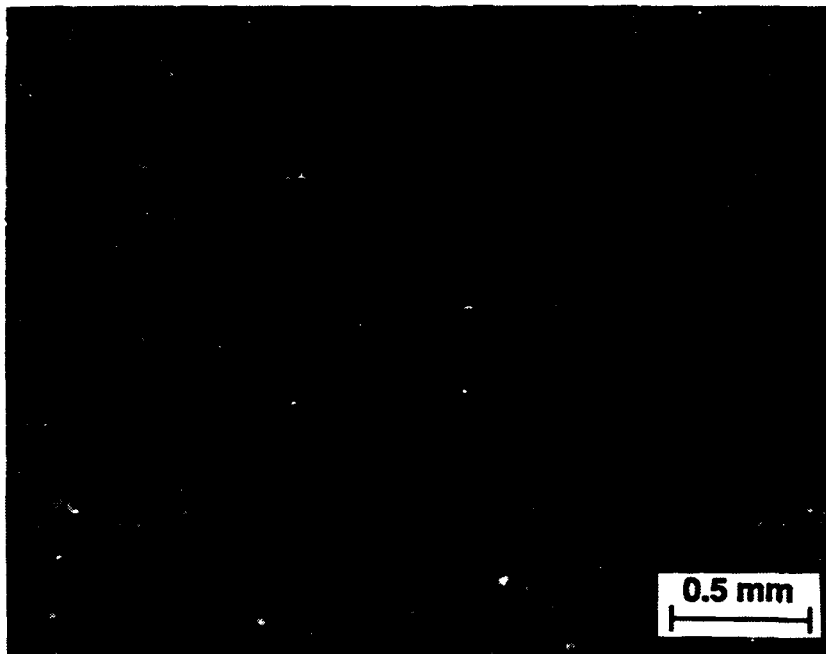


Figure 2.4. Optical macrograph of a sanded composite surface.

We prepared a few specimens using the end of the composite beams as the bonding surface, to see whether pulling along the graphite fibers instead of across them would give us a higher strength before the composite itself failed. As-machined ends produced tensile PATTI strengths of 3690 ± 365 psi, and concentrated H_2SO_4 etched surfaces showed strengths of 4420 ± 440 psi. The first set of stubs failed at the composite/adhesive interface, but the second set failed entirely within the adhesive. The ultimate tensile strength of the etched surface may have been somewhat limited by the small size of the

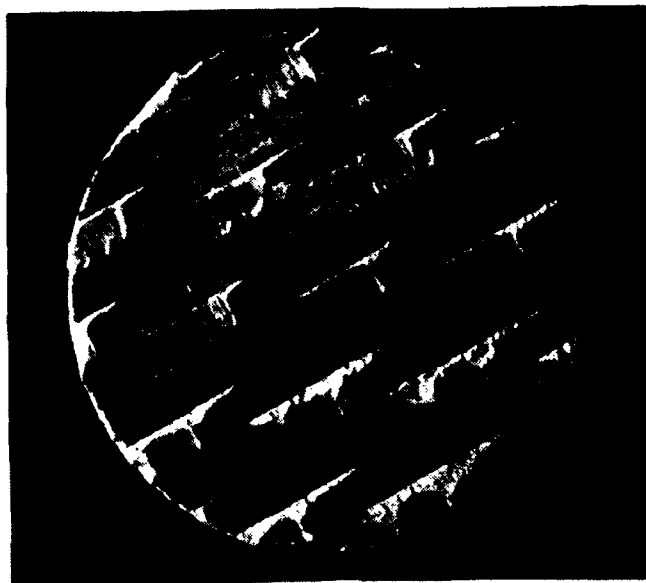
beam cross-section specimen, which made piston alignment difficult. These limited test results do suggest that there is not a significant difference when testing along the fiber reinforcement, or across the fibers. In either case, the strength of the matrix is the limiting factor.

However, the nature of the fiber reinforcement can be a major factor in bond strength, if it compromises the load distribution in the matrix. Stress across or along unidirectional fibers does not lead to large-scale stress concentration. However, our tests involving woven composite fibers did show a significant fiber-orientation effect. An uncured woven-fiber composite prepreg was added to the surface of a precured unidirectional fiber test specimen, as described above. After cure, the outer surface of the woven side was mechanically cleaned and PATTI stubs applied with Hysol 9394 as before. The results of these tests are shown in Table 2.3.

Table 2.3. Mechanical Cleaning and Composite Type Effects on PATTI Tensile Strength (Hysol 9394 Adhesive)

Surface Prep.	Substrate	# of Tests	Tensile Strength (psi)	Failure Mode
80 grit sand	Unidirectional	11	4955 (± 375)	In composite
Sandblasted	Unidirectional	3	5275 (± 320)	In composite
60-grit sand	Woven	2	3450 (± 230)	In composite
Sandblasted	Woven	2	3600 (± 80)	In composite

Clearly, the woven composite surfaces failed at significantly lower tensile strengths than the unidirectional composite surfaces. Although the failure was within the composite material in all cases, the woven composite samples had an intact layer of graphite fiber bundles on the test stub surface, whereas the unidirectional test stubs had few fibers and mostly epoxy (see Figure 2.5). We believe the difference in strength is caused by the tendency of the well-defined fiber layers in the woven composite to concentrate stress at the interface of the fiber bundles, allowing rapid crack growth and lower apparent strength. The random positions of the unidirectional fibers reduce the tendency of cracks to grow together and thus limit the influence of local damage, so that the overall composite has greater "strength."



1 cm

Figure 2.5. PATTI pull stub after testing a woven graphite composite surface.

These results have two major implications for rapid screening tests. The first is that test specimens constructed with woven composite surfaces will necessarily have a lower maximum strength. Whenever the failure is forced into the composite bulk, then no improvement in adhesive or interface can raise strength further. Therefore, all test results must take the nature of the test specimen into account. The second is that the mechanical cleaning treatments are very good. The strengths we report are higher than those of other researchers cited above. We believe that this is not due to better surface preparation, but rather to better test procedures. The self-aligning nature of the PATTI tester, and the stiffness of our baseline composite test specimen allows a very uniform stress distribution that is otherwise very difficult to achieve.

2.3.2 Chemical Etching

A number of chemical etch treatments were investigated for as-cured composite surfaces. Since prior literature mostly discusses acid etches, we tried a number of mineral

acid etch treatments, as well as a few strong basic treatments. The composite samples were the as-machined beams. Room temperature solutions were used in all cases. The PATTI results are given in Table 2.4.

**Table 2.4. Tensile Bond Strengths to Chemically Etched Composite Surfaces
(PATTI Tests using Hysol 9394 Adhesive).**

Chemical treatment	Time	# Tests	Tensile Strength (psi)
Conc. H_2SO_4	15m	3	3980
Conc. H_2SO_4	30m	3	3860
50% H_2SO_4	30m	3	250
50% H_2SO_4	1h	3	150
Conc. HNO_3	45m	3	285
Conc. H_3PO_4	45m	3	1070
KOH in Ethanol	1wk	3	3680
Conc. NH_4OH	45m	3	300

The only promising treatments appear to be the concentrated sulfuric acid etches. The potassium hydroxide etch not only involves a flammable solution, but also is very slow. A 24-hr. treatment was necessary to achieve a visibly altered surface. The sulfuric acid etches left a visibly attacked surface. Individual carbon fibers were protruding from the composite surface. In fact, the fibers were so dense, that they had to be picked off in order to bond the pull stubs down. Figure 2.6 shows a micrograph of a sulfuric-acid-etched surface after most of the carbon fibers were removed. The thin carbon fibers from the unidirectional composite were not well attached to the surface, and therefore interfered with rather than enhanced bond strength.

2.3.3 Plasma/Corona Discharge

The other proven bonding treatment for composites is plasma etch/corona discharge. We tried a number of variations on plasma etch treatments, as well as some corona etches. In general, we found that the resultant sample surfaces were very sensitive to treatment conditions and surface conditions prior to treatment. This sensitivity coupled with the relative difficulty of treatment make these treatments unattractive for general use.

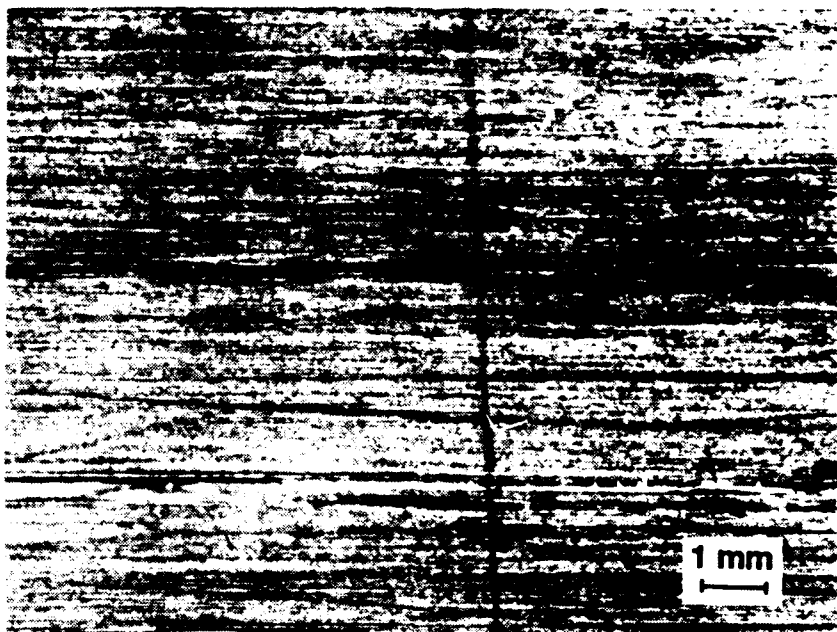


Figure 2.6. Optical micrograph of a unidirectional graphite composite surface after sulfuric acid etching.

2.3.3.1 Plasma-Etched Composite Surfaces

We treated precured, two-ply thick, woven graphite fiber composites in a low pressure (30 to 50 micron) plasma chamber. This composite surface was subsequently bonded to a test beam, PATTI stubs bonded to the treated surface, and tensile tests performed. Thin composite plates were treated rather than entire test specimens because of the small size of the plasma chamber. We did not encounter any problems of plasma-treated composites pulling off the test beam, and feel confident of the test results shown in Table 2.5.

Scanning Electron (SEM) micrographs of graphite/epoxy composite surfaces that were etched in an argon plasma clearly show the surface modifications that result in improved bonding. The as-cured surface is essentially smooth, as shown in Figure 2.7. A low power etch ($\sim 0.1 \text{ W/cm}^2$ at 200 V) leaves a "forest" of small bumps, somewhat like the

oxides on FPL etched aluminum surfaces. At higher power settings (~0.3 W/cm² at 500 V) much larger "tendrils" of epoxy are created, that should provide a much improved bonding interface. However, note that the higher power etch is beginning to expose the graphite fibers. Therefore a significant fraction of the surface will be a very poor bonding substrate. Thus there is a treatment paradox; when enough power is used to texture the surface, too much matrix material is removed and graphite fibers are exposed.

**Table 2.5. PATTI Tensile Strengths Using Argon Plasma Etched Surfaces
(Hysol 9394 Adhesive)**

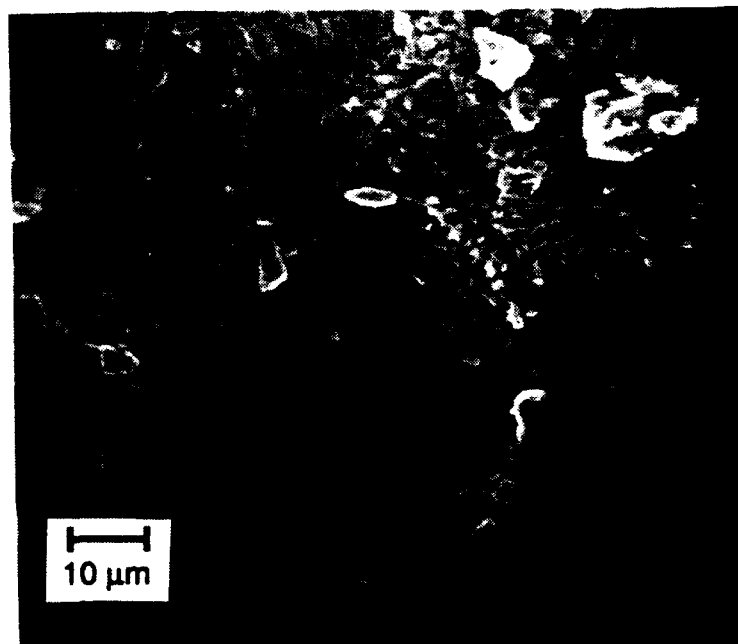
Surface Preparation	Time	# of Tests	Tensile Strength	Failure Mode
Low energy plasma	5m	2	2875 (± 130)	Mixed (at interface and in composite)
High Energy Plasma	5m	3	3350 (± 465)	Mixed
High Energy Plasma	1m	6	1915 (± 970)	Mixed

Reducing the treatment time at high power did prevent the exposure of graphite fibers, but it did not build up the desired surface roughness. The SEM micrograph shown in Figure 2.8 shows a smooth surface. "Shadows" of the graphite fiber can be seen, which indicate that there is very little epoxy on top of the fibers. It appears that this treatment was too short to properly texture the epoxy, and therefore, it did not create a good bonding surface. The PATTI tensile results corroborate this conclusion, since a large deviation was seen in strength values (Table 2.6). This suggests that there was considerable point-to-point variation in plasma etch effectiveness across the specimen surface. It is also possible that the higher energy plasma is causing subsurface damage to the composite.

**Table 2.6. PATTI Strength Values for High Power/Short Time Plasma Etch Surfaces
(Hysol 9394 Adhesive).**

Sample	Strength (psi)	Failure Mode
1	1910	Composite fracture
2	3580	Composite fracture
3	2350	Composite fracture
4	810	Composite fracture
5	1440	Composite fracture
6	1400	Composite fracture

a)



b)

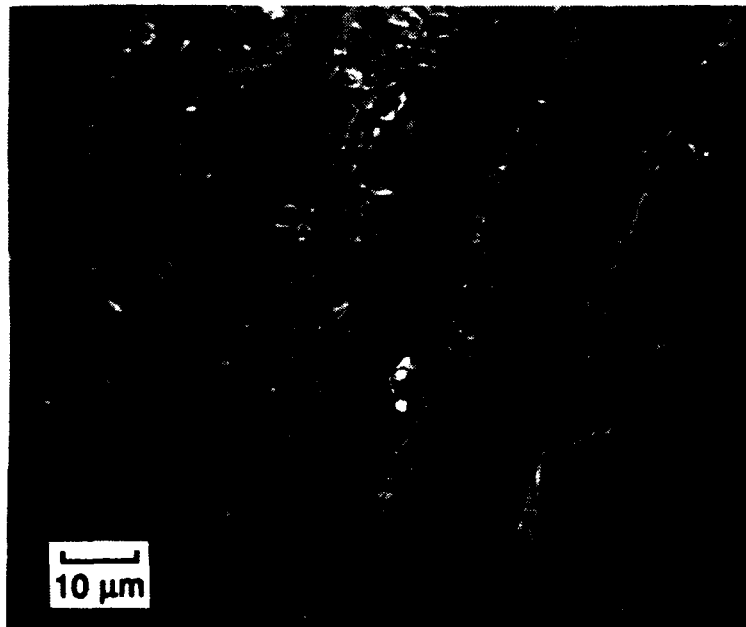


Figure 2.7. Effect of argon plasma etch on composite surfaces. a) surface after "low power" treatment, and b) surface after "high power" treatment.

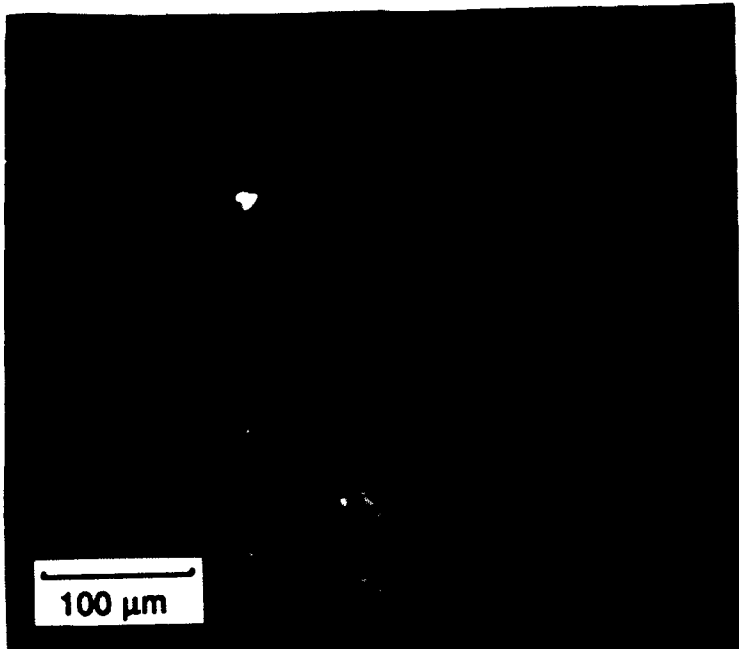


Figure 2.8. SEM micrograph of a composite surface after a "short time, high power" argon plasma treatment.

We made two changes to the plasma treatment that improved the surface morphology. Improved composite processing (described in section 2.2.2 of this report) resulted in smoother, resin-rich surfaces, which are more suitable for plasma processing, since graphite fiber exposure is less likely. Low voltage (200 V) treatments used for longer times still led to textured surfaces, but removed less of the epoxy matrix. Figure 2.9 shows electron micrographs of newer composite surfaces after 200 V argon plasma etching. The surface morphology for the 18-min treatments is much better than any others we have observed. There are no protruding graphite fibers, and the entire epoxy surface has been etched into fine protuberances.

The improved surface treatment did not lead to significantly improved PATTI test results, however. Table 2.7 shows tensile strength as a function of treatment time. In most cases interfacial failure was observed at the adhesive. It is clear that surface morphology is not the proper criterion for judging composite surface treatments.

**Table 2.7. PATTI Tensile test results for 200 V plasma surface treatments
(Hysol 9394 adhesive)**

Treatment Time (m)	# Tests	Tensile Stress (psi)
2	3	965 (± 900)
4	3	1110 (± 725)
8	3	2410 (± 1620)
18	5	2215(± 675)

2.3.3.2 Corona Discharge

Corona discharge is another surface treatment that has shown promise for thermoset composite bonding.⁽¹⁵⁾ It is similar to plasma etching, in that ionized gases are accelerated toward the sample surface by a high voltage electric field. It uses air molecules in the open atmosphere rather than selected gas molecules in a controlled low-pressure atmosphere. The high-pressure gas (one atmosphere) requires considerable higher voltage to cause electrical discharge and plasma formation. The advantage to corona discharge is the relative simplicity of the apparatus, since no vacuum chamber is required. The disadvantages include the use of high voltages at fairly high power levels, and the lack of controls on the discharge (unlike plasma where gas pressure and voltage levels can be readily adjusted). In addition, since electrical breakdown is strongly dependent on distance and surface roughness, it would be very difficult to apply corona discharge to anything but flat shapes, since the discharge would be very localized and nonuniform in the presence of surface asperities. The lower voltage plasma etch treatments are less sensitive to surface roughness, and probably could be adapted to pieces with irregular shapes.

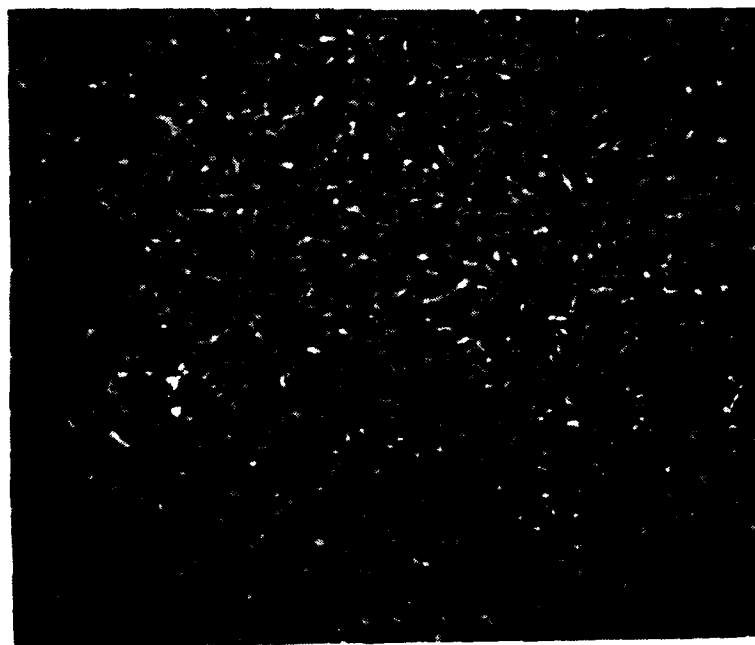
Another problem with corona discharge is the fairly high surface energy that apparently is required to produce a good bonding surface. The Kodokian/Kinloch paper⁽¹⁰⁾ indicate; that 20 J/mm² is needed to produce good bonding, i.e., bonds that fail cohesively. They used an apparatus that translated a table under the discharge electrode. Given the parameters listed in their paper, the 20 J/mm² power level would require 100 passes under the electrode, a time-consuming operation.

We tried using a direct current discharge to condition our PATTI test composite specimen surface. A 20kV DC power supply was used to apply voltage to a wire held over the composite surface to be treated. The wire was manually adjusted to maintain a discharge (purple glow) over the surface, and moved to provide uniform coverage over the bonding area. Visual surface changes occurred after a 5-min treatment over a 4 cm² area, sufficient to bond a PATTI pull stub to the

a)



b)



1 μm

Figure 2.9. Electron micrographs of "smooth" composite surfaces plasma etched at 200 V for a) 8 min and b) 18 min.

treated surface. Electron microscope investigation showed a significantly disrupted surface, with exposed graphite fibers (Figure 2.10). However, the matrix material remaining did not appear to be textured to the same extent that could be seen after plasma treatments. Thus, the bonding morphology does not appear to be as suitable as the best plasma-etched treatments.

PATTI tests performed on corona discharge treated composites yielded inconsistent tensile strengths. Six samples were tested with each adhesive; Hysol 9394 and MML 3H-F4 were used. The Hysol bonded stubs had a average tensile strength of 1635 (+- 615) psi and the 3H-F4 stubs had an average tensile strength of 3665 (+- 690) psi. The Hysol bonded stubs all failed at the metal stub-to-adhesive interface, however. We suspect that the adhesive used for this test was outdated, and no longer meets its original strength levels. The 3H-F4 strengths are quite good, consistent with the mostly cohesive failure of the composite observed. However, given the inherent drawbacks of this technique, there seem to be no overriding reasons to chose this method of surface preparation.

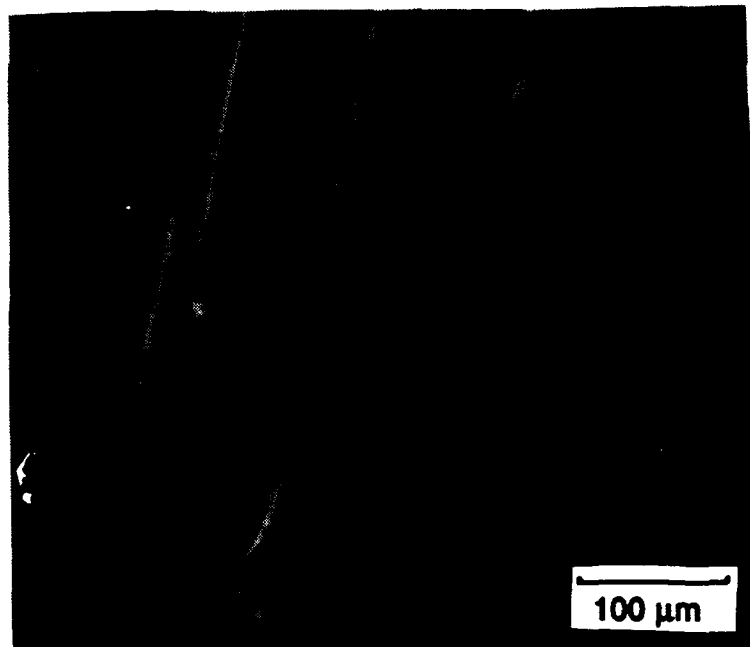


Figure 2.10. SEM of corona-discharge-treated composite surface.

2.3.3.3 NH₃ Plasma Composite Surface Treatments

An experiment was performed to explore the use of ammonia plasma to etch a cured single ply of Hercules AS-4/3501-6 composite weave. Previous research has suggested that ammonia plasma might react and form nitrogen-containing bonds with the cured epoxy surface of the composite.^(16,17) The nitrogen molecules ideally would react with the curing epoxy matrix of an applied adhesive, causing enhanced interfacial bonding and superior shear and peel adhesion to the composite substrate. The plan was to first etch the cured composite with Ar plasma (to produce a microrough surface), then etch with NH₃ plasma to produce nitrogen bonding sites on the surface.

A specimen of Hercules AS4/3501-6 single-ply composite weave was cured, then both sides of the composite were treated with argon plasma at 200 V for 18 min. The treated composite was then carefully packed and shipped to the Center for Adhesive and Sealant Science at Virginia Polytechnic Institute and State University, where it was then treated with ammonia plasma by Joannie Chin, a graduate research assistant. The conditions for treatment were 5 min at 100 W with a NH₃ gas flow rate of 120 cc/min. Both sides of the sample were treated simultaneously. The composite was then shipped back to Martin Marietta Laboratories for testing.

An infrared absorption spectrum was taken of the composite specimen before and after the ammonia plasma etch. The spectra, shown in Figures 2.11 and 2.12, were run on a Nicolet 55XC spectrophotometer. The specular reflectance geometry was used to concentrate on absorption from the surface region.

The surface chemistry of the ammonia-plasma-etched composite is quite different from that of the argon-plasma-etched composite. In Figure 2.12, two distinct absorption peaks at 1606 cm⁻¹ and 1524 cm⁻¹ indicate that nitrogen radicals have been added to the composite surface after ammonia etch. These peaks can be associated with primary and secondary amine substituents caused by reaction of the NH₃ plasma with the carbon-rich matrix surface. They are not seen on the argon-plasma-etched surface. Thus, the FTIR results indicate that the NH₃ plasma treatment has performed the desired chemical modification on these sample surfaces. However, wedge tests performed on this surface demonstrated very poor performance (see Exposure Testing section below for description of test specimen and method). When the wedge was introduced into the end of the test specimen to strain it, a crack propagated at the composite/adhesive interface far along the test specimen, indicating a very weak bond interface. In view of this behavior, no further mechanical testing was undertaken.

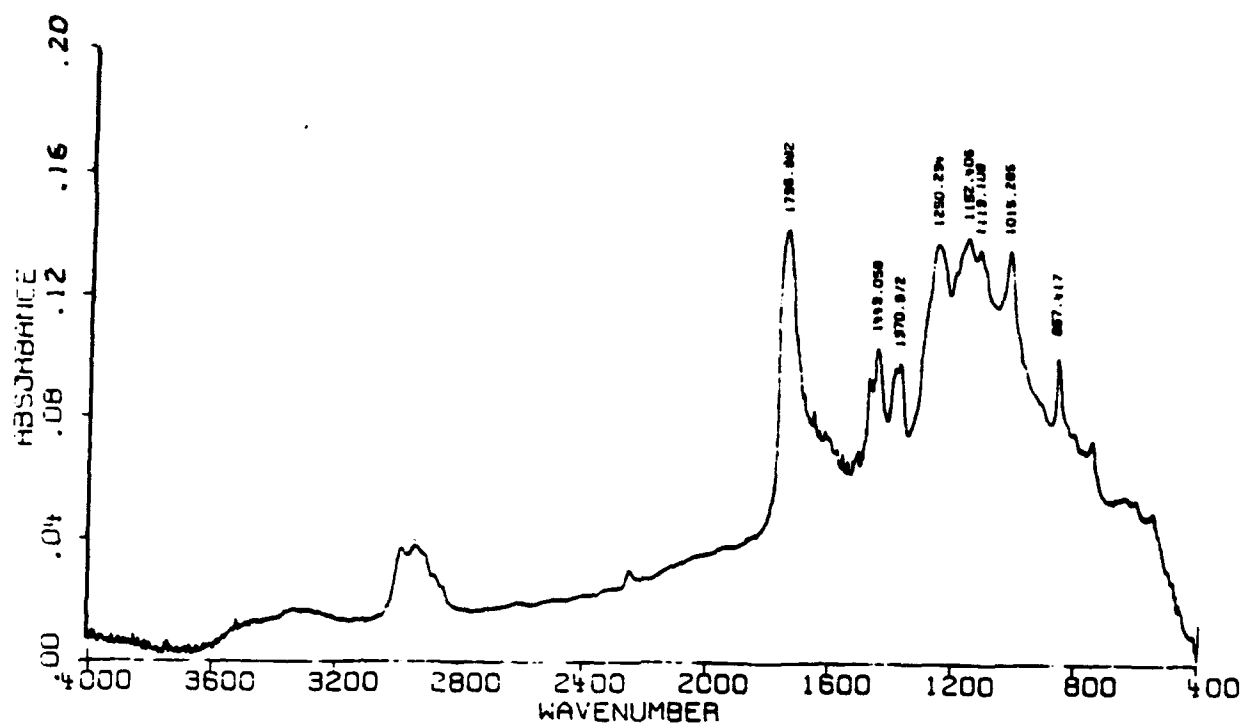


Figure 2.11. Specular reflectance spectrum of an argon-plasma-etched composite.

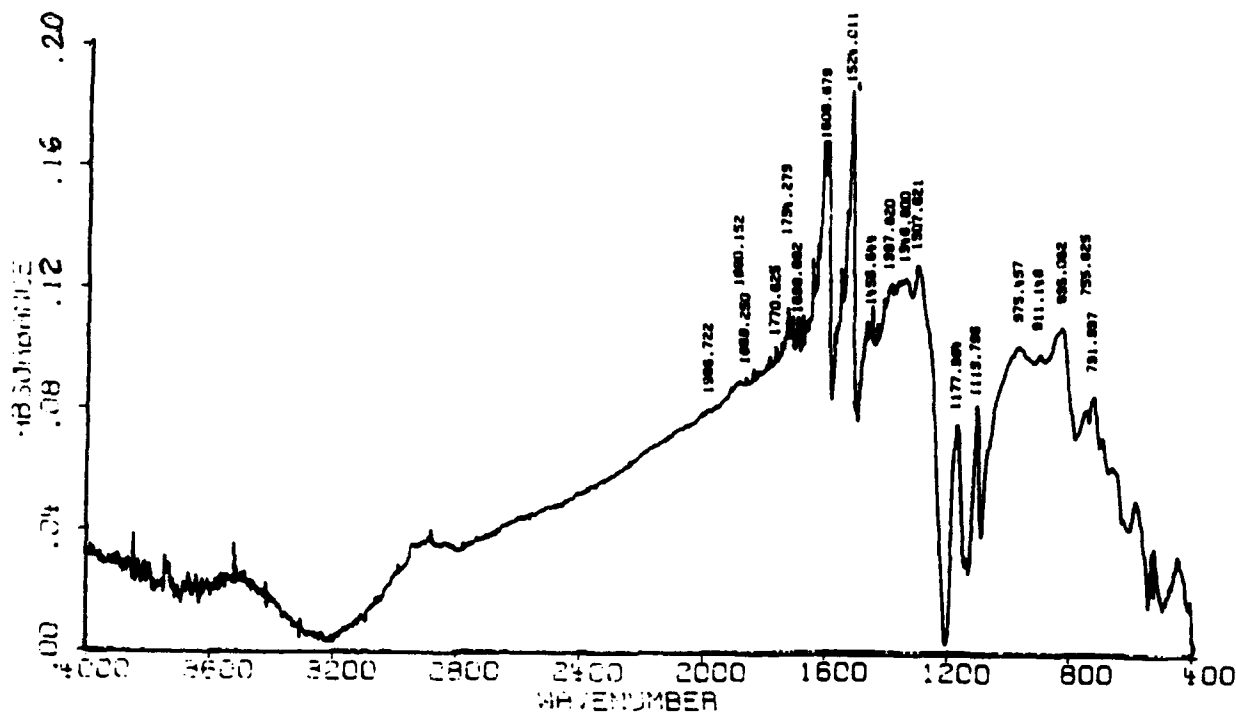


Figure 2.12. Specular reflectance spectrum of an ammonia-plasma-etched composite.

2.3.4 Metal Surface Deposition

We have investigated various means of depositing thin metal layers on composite surfaces. Since pretreatments for bonding metal surfaces are so well developed, it would be fairly easy to make a solid adhesive bond to a metal layer. If the metal were securely anchored to the composite, the resultant bond could be both strong and durable. We prepared the surfaces of the composite specimens for metal coating by the 80-grit sand paper treatment as described above. As shown in Table 2.8, the results were disappointing.

Table 2.8. Tensile Testing of Metalized Composite Surfaces (Hysol 9394 Adhesive)

Surface Coating	# Tests	Tensile Strength (psi)
Electroless nickel	3	2300
Electroless silver	3	2440
Vapor-deposited aluminum	3	1600

Not only are the tensile strengths relatively low, but the failure mode, pull off of the metal layer from the composite, leaves little hope that a strong, durable interface could be formed to the as-cured composite surface.

2.3.5 Chemical Surface Modification

Part of the screening of surface preparations for cured graphite/epoxy composites involved modifying the surface via chemical surface treatments. Initially, we found that exposure to concentrated sulfuric acid or sodium hydroxide did improve the adhesion properties of the composite surface. However, a major drawback of these surface treatments was the damage each induced in the epoxy matrix of the composite. We also found that treating the composite surface with dilute solutions of H₂S0₄ and NaOH reduced adhesion dramatically.

Our approach to promoting better adhesion via chemical surface modification was to chemically or physically attach uncured adhesive backbones to the cured composite surfaces. By using this approach, permanent damage of the cured epoxy matrix of the composite material could be avoided. The two methods that we chose to experiment with were: 1) impregnation of the composite via a swelling agent containing uncured epoxy groups, and 2) electrochemical deposition via anodization of the composite surface.

2.3.5.1 Resin Impregnation of a Swelled Composite

It has long been known that exposure of crosslinked polymeric materials to various solvents (e.g., water, methylene chloride) will cause some degree of swelling. We have previously shown ("Moisture-Resistant, Low-Temperature-Curing Adhesives", Final Report, MML TR-90-26, February 1990) that when a cured adhesive is exposed to water it will swell and deform until an equilibrium is obtained. Adhesive systems will also swell in other solvents such as methylene chloride, usually to a greater extent than in water.

The purpose of the resin impregnation technique was to allow the penetration of an uncured epoxy system into the graphite/epoxy composite weave by swelling the matrix in a dilute solution containing uncured epoxy in methylene chloride solvent. Methylen chloride was chosen as the solvent because of its ability to easily swell cured epoxy systems that are highly crosslinked and its high vapor pressure, which allows it to readily evaporate in ambient environments. The idea of swelling the epoxy matrix, if successful, might create micropores capable of allowing the transport of uncured epoxy (dissolved within the solvent) throughout the epoxy matrix of the composite. Once the solvent had evaporated, the matrix would contract. However, the uncured epoxy left behind would create an interpenetrating network within the matrix, and thus an interphase which could be chemically bonded to another adhesive system. During bonding of the composite surface with another surface, the addition of a slight excess of curing agent would not only cure the adhesive but also the interpenetrating epoxy network thus creating a chemical bond at the composite interface.

A 4.7 weight percent solution was prepared by dissolving 65.8 g of adhesive 3H resin into 1325 g methylene chloride. A composite test specimen was placed in the solution, woven composite side down. The composite was removed from the solution after one-half hour exposure and dried in air overnight. PATTI pull stubs were then bonded to the exposed weave using Hysol EA 9394 adhesive. The PATTI test results are shown in Table 2.9, along with results of a second experiment performed using a 10 weight percent epoxy in methylene chloride solution and a 2-hr exposure.

Although the first treatment seemed to offer a fairly good bond interface, increasing the exposure time and the epoxy concentration produced a poor bond interface. SEM micrographs of the failure surfaces of a sample given the longer treatment show a very clean interfacial break indeed, with a clear sanded surface morphology on the composite side, and a mirror image surface "cast" in the adhesive. It seems most likely that the uncured epoxy

acted as a weak interfacial layer, rather than a strengthening interphase. Even though the shorter time treatment had good tensile strength values, it showed a partial interfacial failure during testing, which casts doubts on this treatment concept.

Table 2.9. PATTI Test Results of the Swelled Composite Experiments.

Treatment	Sample	Strength (psi)	Failure Mode
5% .5h	1	2985	Partial adhesive/composite
5% .5h	2	2492	Partial adhesive/composite
5% .5h	3	<u>2842</u>	Partial adhesive/composite
		2773 (\pm 254)	
10% 2h	1	2250	Interfacial
10% 2h	2	1050	Interfacial
10% 2h	3	1580	Interfacial
10% 2h	4	<u>990</u>	Interfacial
		1470 (\pm 585)	

2.3.5.2 Electrodeposition of a Bond Promoter on the Composite Surface

The purpose of this experiment was to electrodeposit a thin methacrylic acid (MAA) polymer film onto the surface of the graphite epoxy composite. The presence of acid end groups on the outer surface of the MAA polymer film might react with the epoxy and form a chemical bond at the interface which would enhance adhesion, as illustrated in Figure 2.13:

The electrochemical deposition of polymethacrylic acid onto graphite fiber surfaces to promote adhesion with epoxy matrices has been described in previous research.⁽¹⁸⁾ This process reduced delamination in graphite/epoxy prepreg material.

In general, the idea of the experiment was to apply a voltage to a system containing a graphite epoxy anode and stainless steel cathode which were immersed in an aqueous solution of MAA as illustrated in Figure 2.14.

A 500-ml beaker was filled with a 20 percent w/w aqueous solution of MAA. With stirring, concentrated ammonium hydroxide (NH₄OH) was added to adjust pH to 8 to 9. Next, a woven graphite/epoxy rectangular specimen and a stainless steel rectangular

specimen were immersed into the solution and attached to the anode and cathode, respectively. The system was then electrolyzed at 10 V and 0.4 A for 15 min. Over the course of the electrolysis, active bubbling was observed on both the graphite epoxy anode and the stainless steel cathode, as was a coloring of the solution with time. Once the reaction was completed, the graphite/epoxy composite was removed and a dark-colored residue was found to have been deposited on its surface. The specimen was then thoroughly washed with distilled H₂O, and dried in air. Once dried, the specimen was bonded to the prepared graphite epoxy bridge section and cured for 16 hr at room temperature and 7 hr at 70°C. Next, ATT1 stubs were bonded to the electrodeposited surface of the composite and cured as above. PATTI test results are given in Table 2.10.

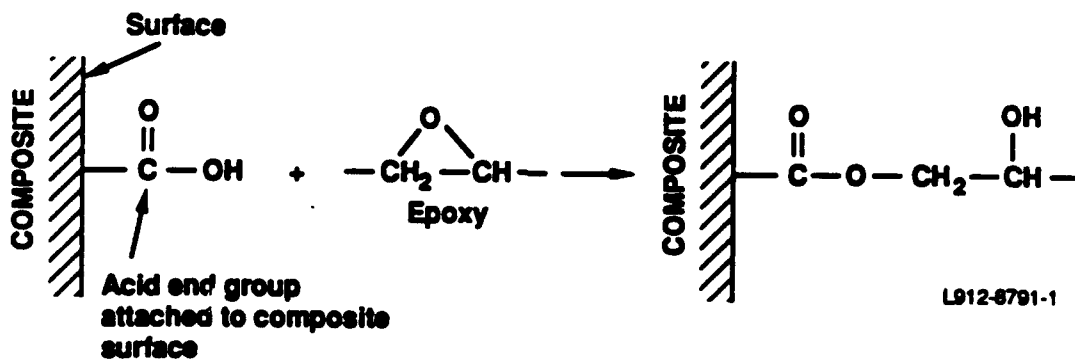


Figure 2.13. Schematic of chemical bond linkage between composite and adhesive.

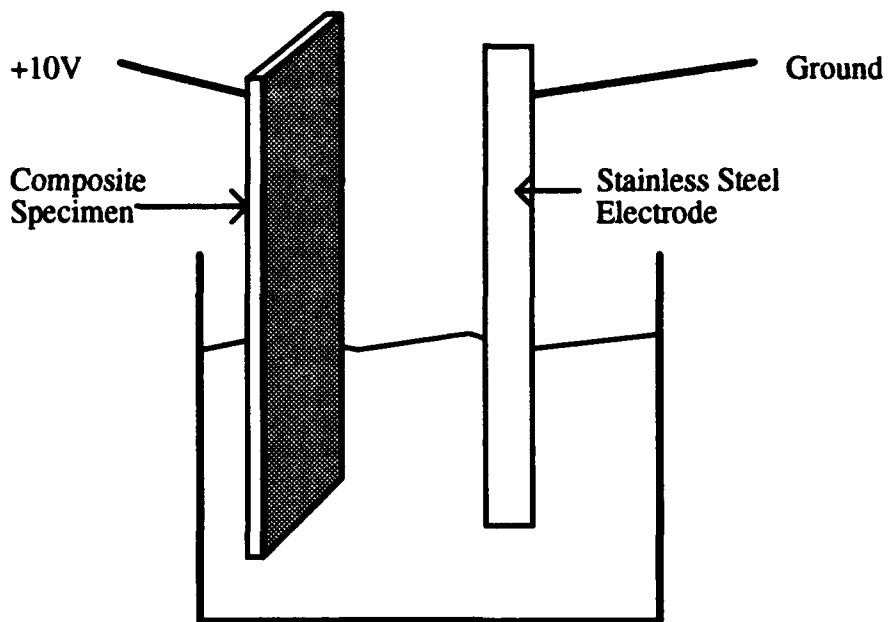


Figure 2.14. Equipment schematic for electrodeposition experiment.

Another test was run using the anodizing treatment in a plain 1M NaCl solution, with no "bond promoter." SEM micrographs demonstrate that anodization erodes the epoxy matrix, exposing graphite fibers. It was hoped that controlled erosion during anodization would lead to enhanced bonding by creating fiber-reinforced surface pores for adhesive to fill. However, the PATTI test results were disappointing (Table 2.9).

Table 2.10. PATTI Test Results from the Electrodeposition Experiment
(Hysol 9394 Adhesive)

Sample	Strength (psi)	Failure Mode
PMMA 1	358	Mostly interfacial
PMMA 2	880	Mostly interfacial
PMMA 3	766	Mostly interfacial
Plain 1	520	Interfacial
Plain 2	195	Interfacial
Plain 3	320	Interfacial

We believe that the anodization is sufficiently violent to disrupt bonding of the outer layer of the composite, leading to failure very near the adhesive interface. In any case, this treatment method was abandoned.

2.4 Surface Conditioning Applied During Composite Curing

We have investigated a number of novel surface treatments designed to be applied during fabrication of the composite.

2.4.1 Peel Ply

Peel-ply outer layers are commonly used in the construction of composite skins to enhance adhesive or paint bonding. A single ply of open weave Teflon®-coated cloth is layed up with the composite prepreg plies, next to a tool surface. After cure, this layer can be readily peeled off, leaving a fresh epoxy matrix surface free of any mold-release contamination. This leaves a surface with smooth-walled furrows where the cloth fibers lay during cure (see Figure 2.15).

Our first composite bonding tests were performed on samples of thin composite skins composed of unidirectional fiber sheets. This material was left over from other projects, and featured a peel-ply surface on one side of the sample and a smooth, as-cured surface on the other. Three surface conditions were tested: smooth surface, peel ply removed long before the test (the surface was exposed for > five years), and peel ply removed just prior to bonding and testing. Six stubs were pulled for each test, with 15-mil bond lines. The results were: smooth surface - 380 (+/- 240) psi; old peel-ply surface-330 (+/- 190) psi; and freshly peeled surface - 410 (+/- 130) psi. The test jig, that proved unsatisfactory during PATTI test development, was used for these measurements since the material was thin and therefore flexed readily. Therefore, the absolute values should not be compared with other test results in this report. However, they paint a clear qualitative picture. It is clear that the morphology of the peel-ply surface was not substantially better than a smooth, clean surface.

We repeated PATTI tests using thin composite skins bonded to bridge chord substrates to provide the necessary stiffness for valid PATTI testing. Using Hysol 9394 (three specimens) average tensile strength was 2505 (+ 310) psi. MML 3H-F4 adhesive (three specimens) showed 2165 (+-120) psi. The failure mode for all specimens was adhesive failure at the composite interface. This result indicates that peel-ply surfaces are clean, but that the surface morphology is

not conducive to strong bonding, since the failure mechanism indicates a poor interface and tensile strengths are consistently below those achievable with sanding.

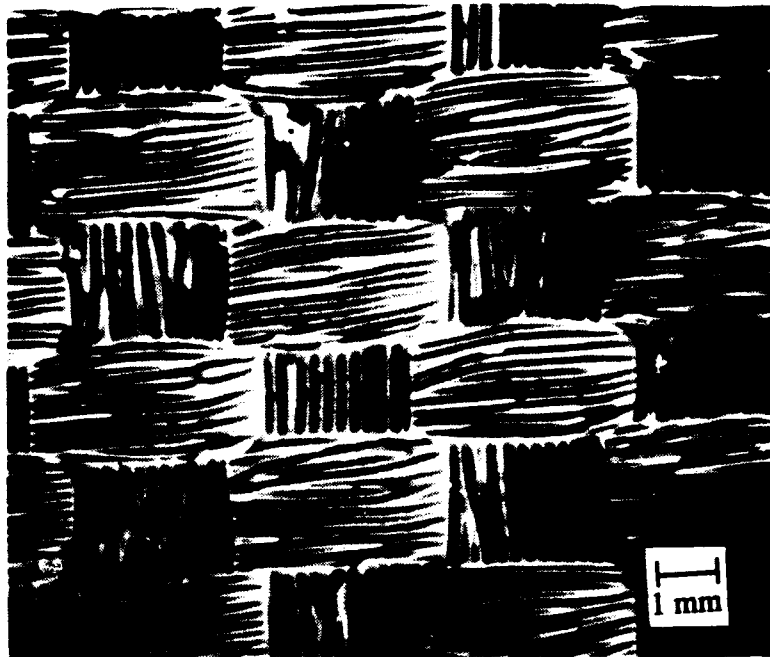


Figure 2.15. Scanning electron micrograph of a composite surface after peel-ply removal.

2.4.2 Surface Particle Embedding

Another series of surface modification tests involved adding another material to the surface that would change the surface morphology, either by its addition, or by its removal after composite curing. Among the materials added were activated carbon, alumina particles, and sodium chloride crystals. In the latter case, we hoped to dissolve the crystals using a water soak to leave a rough surface behind. The micrographs in Figure 2.16 show the composite surface embedded with coarse and fine salt crystals, then soaked. Figure 2.17 shows a surface modified by activated carbon, which presumably might still have fine pores that the adhesive could infiltrate during bonding. Unfortunately, neither of the treatments markedly improved dry bond strengths (see Table 2.11).

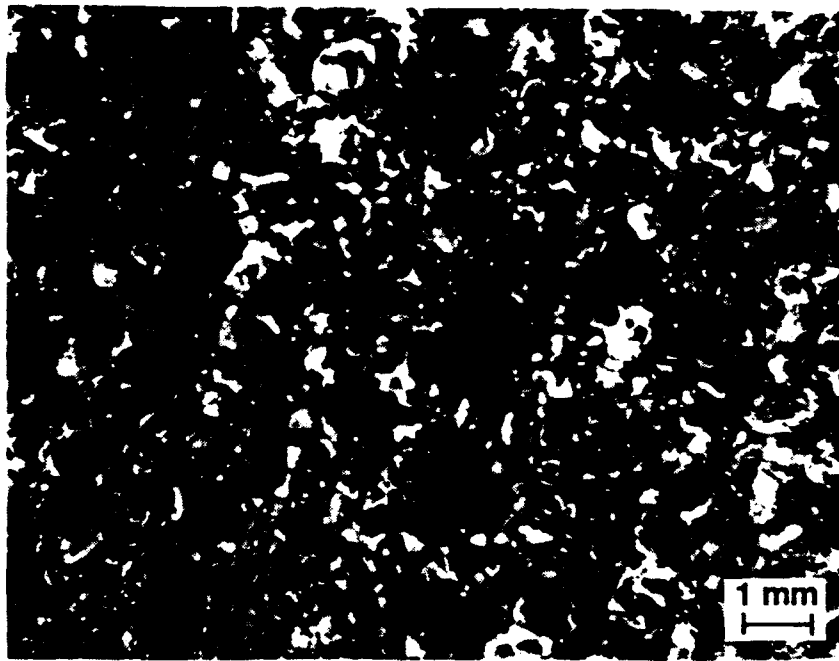


Figure 2.16. Optical macrograph of a composite surface with embedded salt crystals and voids.

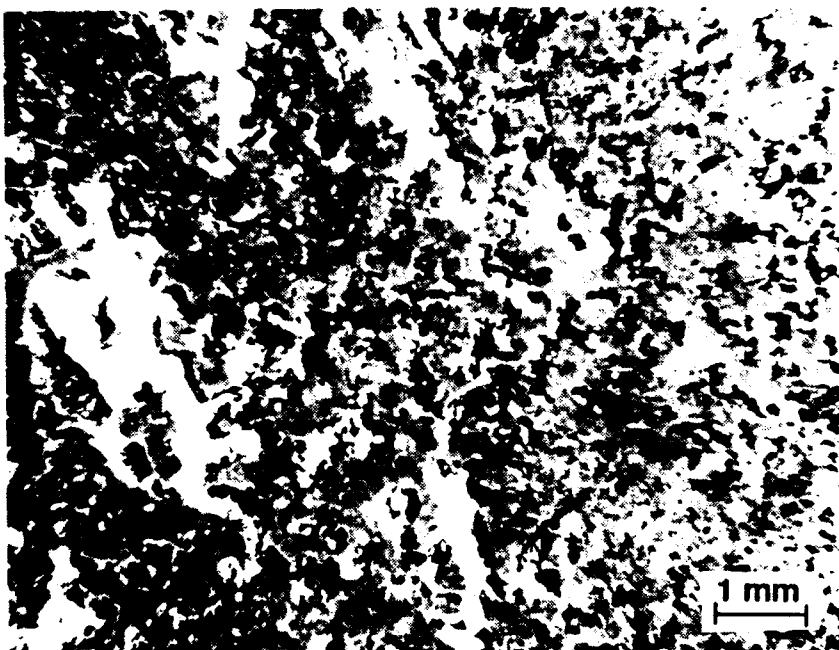


Figure 2.17. Optical macrograph of a composite surface with embedded activated charcoal additions.

**Table 2.11. Tensile Test Results After Surface Morphology Modifications.
(Hysol 9394 Adhesive)**

Treatment	# Tests	Tensile Strength (psi)
Fine NaCl crystals	2	1160 (± 360)
Activated Carbon	4	1340 (± 470)

In the carbon case, the bond fails cohesively in the added carbon layer. This appears to be a fatal flaw. The salt surfaces appear to fail in the composite near the surface. One obvious problem with this technique is that the epoxy matrix material surrounds the crystals during cure, encapsulating them and preventing them from being leached away by the water. Thus, the entrapped particles act as flaws in the composite, encouraging fracture and leading to a weak interface.

2.4.3 Prepared Metal Surface Embedding

One set of test specimens was cast against treated aluminum surfaces, in the hope that a mirror image of the aluminum oxide structure would be formed in the composite surface that could be subsequently etched away, leaving extremely fine pores. Figure 2.18 shows an electron micrograph after a thin aluminum plate was "cast" on the composite surface, then peeled away. The surface flakes indicate that the composite fractured during peeling, leaving some composite material on the aluminum, and therefore not taking the oxide impressions.

Thin aluminum foil was also PAA-treated and "cast" against the composite. Dissolving the bulk of the aluminum away with sodium hydroxide leaves an aluminum oxide surface which should be receptive to an adhesive. Note that this is the same oxide typically used in aircraft bonding, but the oxide morphology is different, since the surface exposed by this process is the one that formerly was in contact with the metal. This "backside" morphology is much less porous than the normal outside surface used for metal bonding. We tried modifying the typical aircraft 10-V treatment to use higher voltages that would encourage a rougher oxide. A 35-V treatment began to develop backside surface features. A SEM photomicrograph shown in Figure 2.19 reveals a nearly smooth surface with a shallow, ridged honeycomb structure that has the same size as the cell walls normally seen on outside PAA surfaces. Increasing the voltage even more led to a rougher "backside" yet, one that by aluminum oxide standards should be a good bond interface (see Figure 2.20). An ultimate voltage of 50 V was used to prepare this specimen, although it proved necessary to increase

the voltage stepwise during anodization, starting around 20 V. The main difficulty encountered was avoiding local dissolution of the foil during anodizing that could occur if the oxide film was not built up gradually.

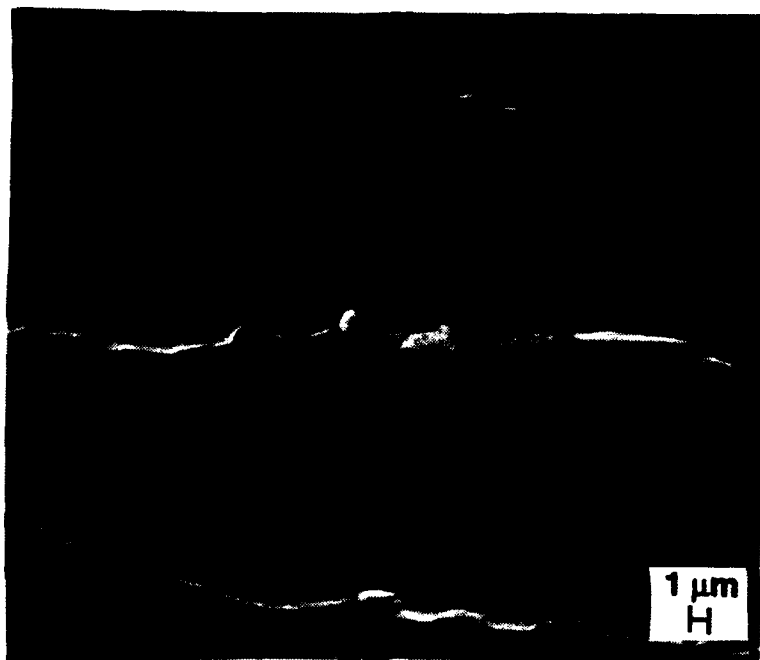


Figure 2.18. SEM micrograph of a composite surface after peeling away a sheet aluminum conditioning plate.

Results of PATTI testing on the aluminum-oxide-surface-textured specimens are shown in Table 2.12. Most of the test stubs were bonded with Hysol 9394 adhesive, except as noted. In general, the strength results are disappointing. Note that woven composite test specimens were used in all cases, since a fresh surface had to be created by the treatment during composite cure. Thus, the best strength values would not exceed 4000 psi.

The results for the high voltage PAA surface require some explanation. The failure mode in all cases was within the composite matrix material very near the bonded surface. Curing the composite with a nonporous metal overlayer caused a thick, matrix-rich region at

the outer surface with very little fiber reinforcement. This region proved a weak link during testing, hence the low tensile strengths. This result does not indicate a failure of the oxide surface, or the design philosophy. It does indicate that there would be significant difficulties in practical implementation, however. Another problem we encountered was creasing and rupturing of the aluminum foil layer, which led to epoxy matrix leaks which coated the metal surface, preventing metal dissolution during etching. This problem would also pose practical difficulties in designing layup patterns and techniques. Thus, although this treatment does show promise at providing a solid bonding interface, considerable development work would be necessary to optimize it for each given part. In view of the excellent performance of simple surface preparation techniques, i.e., sanding, there is little reason to pursue the oxide embedding technique.

Table 2.12. PATTI Tensile Tests of Aluminum Cast Composite Surfaces

Surface Treatment	# Tests	Tensile Strength (psi)
Peeled Al - 20v 1h PAA	3	2100 (\pm 630)
Peeled Al - 10v 30m PAA	6	740 (\pm 80)
Etched Al - untreated	3	2300 (\pm 720)
Etched Al - 10v 30m PAA	3	2500 (\pm 520)
Etched Al 35v 30m PAA	3	3425 (\pm 160)
Etch Al 50v 15m PAA	3	1770 (\pm 615)
Etched Al 50v 15m PAA (3HF4)	3	2590 (\pm 720)

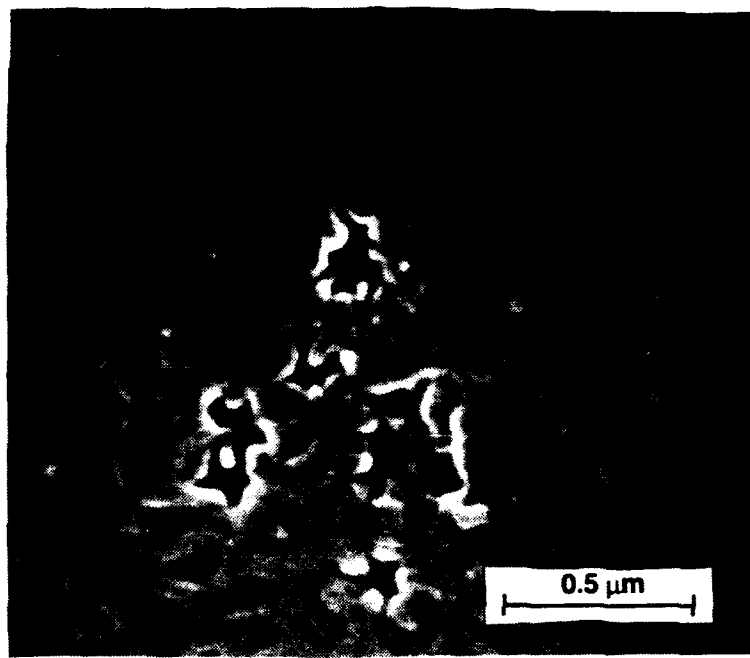


Figure 2.19. SEM photomicrograph of the oxide surface produced by the aluminum oxide embedding treatment on a composite test specimen.

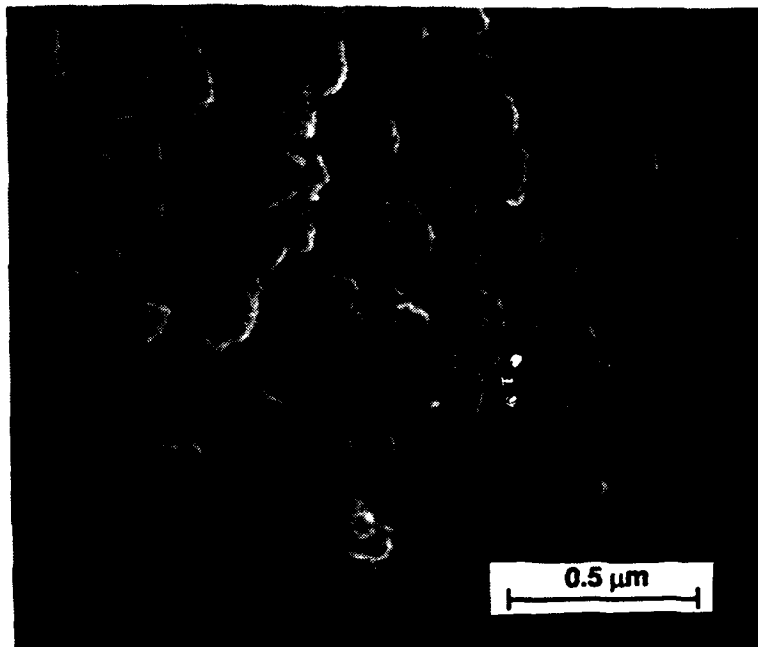


Figure 2.20. SEM micrograph of a 50 V PAA oxide film impregnated composite bonding surface.

2.5 Correlation of PATTI and Lap Shear Tests

Although the PATTI tests yielded good data, we wanted to demonstrate that the tensile values obtained from the test could be correlated with currently accepted test methods. Accordingly we designed and tested a double lap shear test specimen incorporating composite-to-adhesive interfaces.

The design of the specimen is shown in Figure 2.21. Aluminum side laps are PAA-treated and bonded to the composite center lap using Hysol 9394 adhesive. Graphite/epoxy center laps are cured sheets of 12 layers of woven composite, approximately 0.15 in. thick, which are given the desired surface treatment on both sides of the end to be bonded. After 16 hr initial cure at room temperature, the specimen was heated to 70°C in an oven and held for 7 hr, to complete the cure. The test specimen was then stressed in a screw displacement Instron machine at a constant rate of 0.02 in./min. Table 2.13 shows the results.

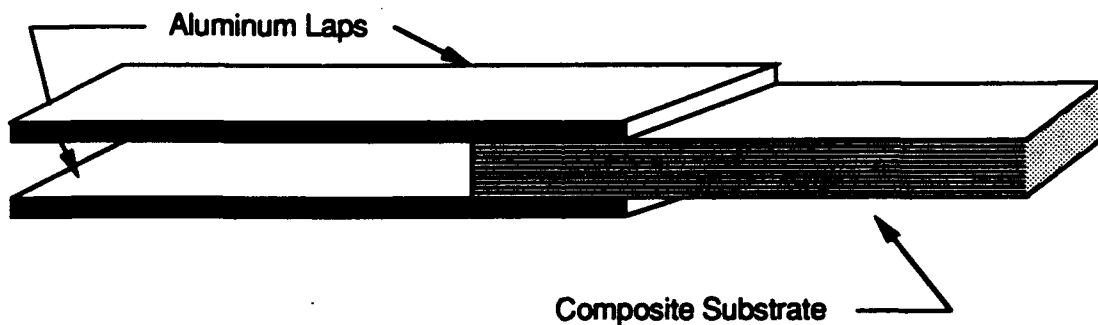


Figure 2.21. Schematic of composite/aluminum double lap-shear specimen.

Although there is a significant amount of scatter, the results of this testing agree quite well with the PATTI results. Composite surfaces are extremely sensitive to peeling stresses induced due to poor sample alignment causing many test values to be lower than expected. But the highest values for a given test correspond to the PATTI numbers for a given surface treatment, i.e., the highest double shear results at 3310 psi compare very closely with the

PATTI result on woven composites of 3450 psi. Once again, the high-strength bonds force the failure into the composite itself. This similarity in measured strengths confirms that the PATTI test gives accurate bond strengths, an important result that meant that surface treatment development did not have to be confirmed with a more difficult test. The results also demonstrate the difficulty of producing reliable test data from very brittle test specimens, like graphite/epoxy composites.

Table 2.13. Hybrid Composite/Aluminum Double Lap-Shear Test Results.

Composite Treatment	Shear Strength (psi)	Failure Mode
60-grit SiC sanding	2260	Mixed composite/interface
	2240	"
	2680	"
	3310	Composite
	1380	Adhesive to composite
Grit blast	630	Adhesive to composite
	2160	Mixed
	3340	Composite
	2420	Mixed
	3100	Composite
Plasma Etch	1700	Adhesive to composite
	2490	Mixed

2.6 Composite Tensile Strength

We performed extensive PATTI tests to establish "data base" properties of composite surfaces bonded using the two target adhesives, Hysol 9394 and MML 3H-F4. The surface treatment tested was hand sanding on unidirectional graphite reinforced epoxy composites. Surfaces of standard test sections machined out of bridge chord composite material were sanded with 80-grit silicon carbide paper and solvent wiped. Three aluminum PATTI test stubs were bonded to each test specimen, using a 15-mil-thick bond line, and allowed to cure at room temperature for 16 hr. A post-cure was then performed in an oven at 70° C for 7 to 16 hr. The tensile bond strengths measured using the PATTI instrument are shown in Table 2.14. The reported values are the averages of 10 test stub pulls for each adhesive.

Table 2.14. PATTI Tensile Test Strengths on Sanded, Unidirectional Graphite Composite Beams.

Adhesive	Tensile Strength (psi)	Standard Deviation (psi)
EA 9394	3785	+392
3H-F4	3930	+140

In all cases, the failure mode was through the composite itself, very near the adhesive interface. Thus, the reported tensile strengths are a lower bound of the joint strength, rather than an absolute value. The effective tensile strength of these joints was limited by the strength of the composite material. It would undoubtedly be higher if a tougher epoxy was used in the composite matrix.

2.7 Durability Testing

2.7.1 Exposed PATTI Tests

We have investigated the use of the PATTI test configuration for bond durability testing by exposing the as-bonded test stub/surface in an elevated temperature and humidity test chamber before testing. Diffusion of moisture along the bond interface and through the epoxy substrate and adhesive tests the stability and durability of the bond.

The test chamber was set for 50°C and >95 percent R.H., the same conditions used for the Wedge Test (ASTM D3672) for adhesive bond durability. Surfaces of woven graphite composite material cured in place and of unidirectional graphite composite beams were sanded using 60-grit SiC paper or were grit-blasted with glass-bead grit. PATTI test stubs. The composite beams with attached pull stubs were placed in a humidity chamber at 49°C and >95 percent R.H. Test beams (with three pull stubs each) representative of each surface treatment were removed at intervals, and tensile strength to remove the stubs measured with the PATTI instrument. The moisture diffusion rate is sufficiently low that the short time out of the exposure chamber before testing would have no effect on the bond strength. Note that the stubs were not under any stress during exposure, and therefore this test does not attack the adhesive or interface as rapidly as the stress-relaxation test for adhesives or the wedge test for bonded surfaces.

Figure 2.22 shows the tensile strength results of the entire test series using Hysol 9394 adhesive. The 120-day sanded specimen shows an unexpectedly high strength, nearly equal to the unexposed baseline, i.e., the 0-day exposure value. In all cases, however, including the long-term exposed sandblasted specimens, the failures occurred within the composite itself, rather than at the bond interface. Thus, the tests demonstrate that the bond interface stands up to exposure quite well. Limited testing with 3H-F4 adhesive and sanded unidirectional composite test specimens yielded the same results. The initial strength (unexposed) was 4070 (+- 20) psi (three specimens). After 120-days exposure in the humidity chamber the tensile strength was 3230 (+- 190) psi (six specimens). Once again the failures occurred within the composite surface.

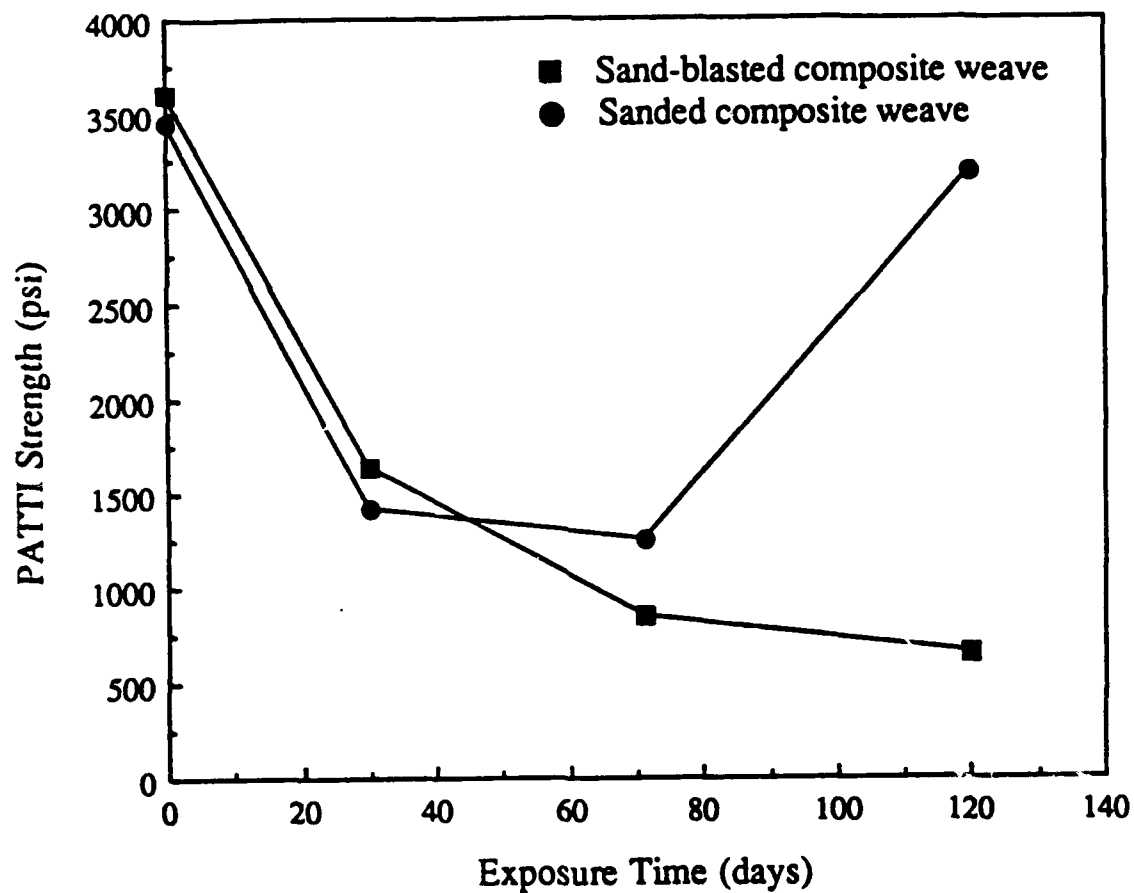


Figure 2.22. Plots of exposed PATTI tensile strength tests, for sanded and sandblasted composite surfaces.

Failure analysis of the pull stubs after the tests indicates that the locus of failure was wholly within the composite's epoxy matrix, rather than in the adhesive or at the interface. Thus, humidity chamber exposure has weakened the matrix material rather than reduced the strength of the adhesive bond. Thus durability problems associated with the composite itself overshadow the potential durability problems of adhesive bonds to the surface. As long as the composite is not protected from moisture exposure, water can migrate through the matrix. Exposed edges are a particular problem, since the network of graphite fibers provides "highways" for rapid water transport.

The predominant failure mechanism obviously is degradation of the composite epoxy matrix due to humidity exposure. This degradation may be controlled by the rate of water ingress to the interior of the composite. The sandblasted surfaces seem to be more damaged, with more visible residue after treatment, which may explain their relatively greater strength loss. A damaged/roughened outer surface could trap moisture and enhance diffusion into the interior of the composite. Removing enough matrix material to expose the graphite fibers would greatly enhance diffusion by exposing the graphite-to-epoxy interfaces that act as "pathways" to the interior. Differences in the degree of removal of the outer epoxy layer due to variations in the severity of the hand-sanding operation may explain some of the variations in strength values for sanded surface specimens. However, for whatever the reason, the high strength of the long-term sanded specimens demonstrates that the bond interface performs well and that moisture intrusion is not a concern from a surface preparation standpoint (although it certainly is when considering the long-term performance of the overall design). The sanded composite surface has proven to be an excellent substrate for adhesive bonding in terms of strength and durability.

2.7.2 Wedge Tests

We made a number of attempts during the program to modify the ASTM D3762 Wedge Test to incorporate composite bond interfaces. This test, which exposes bond interfaces to a combination of stress and an aggressively humid environment, has been a very successful determinant of bond durability using aluminum substrates. Indeed, it is the primary quality control check for proper surface preparation of the aluminum before bonding in many aerospace production shops. It is a relatively quick test that correlates very well with long-term in-service behavior of aluminum-to-aluminum bonds⁽¹⁹⁾, and is a fairly easy test to perform. Thus it would be a very good benchmark test for composite durability.

The test is conducted by constructing a bond between two substrates, and then straining the bond line by driving a wedge into one end of the specimen. A crack propagates along the bond line (or within the adhesive) away from the wedge. The length of the crack to the fourth power is proportional to the retained stress, so crack length is a very sensitive indication of the ability of the adhesive and bond interface to maintain their integrity under stress. The position of the crack tip is marked after a one-hour "conditioning" period, then the specimen (and wedge) is placed in a humidity chamber set to 50°C and >95 percent R.H. The entire specimen is removed from the chamber after a one-hour exposure, the position of the crack tip marked, then returned for continued exposure. The crack tip position is monitored periodically during a one-week exposure.

Our first attempt to duplicate a normal wedge-test specimen involved replacing the aluminum substrates with woven graphite/epoxy composites (see Figure 2.23). A 15-layer 0/90/0/90/.../90/0 lay-up was used to construct 0.15-in. thick plates for substrates. The cure cycle used was a 20 hr hold at 250°F followed by 4 hr at 350°F under 150 psi. The surfaces of two plates were prepared with a surface pretreatment, then bonded together with Hysol EA9394 adhesive, using shims at the corners to achieve a bond-line of roughly 0.020". After room temperature cure for seven hr, the plates were post-cured in a warm-air oven at 70°C for 16 hours. After cutting the bondment into 1-in.-wide strips, a 0.10-in. wedge was driven into the bond line at a narrow edge, and a crack forced along the bond line between the composite plates.

20-layer woven graphite composite substrates

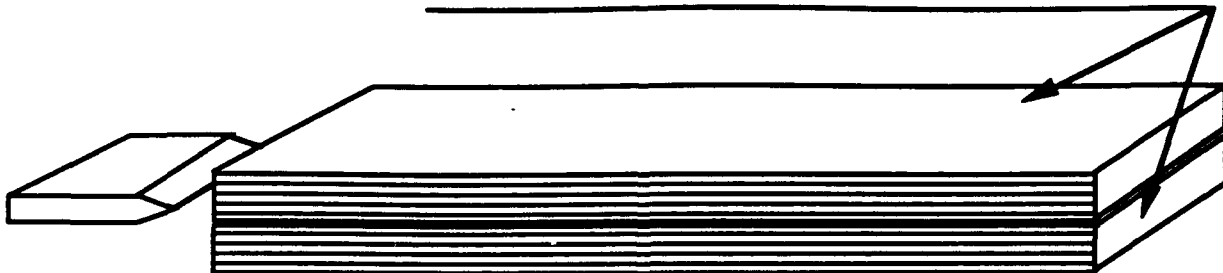


Figure 2.23. Schematic of the all-composite wedge-test specimen.

It was immediately apparent that the test specimen was not performing in the intended fashion. Despite efforts to ensure that the crack started within the adhesive, the advancing crack due to the insertion of the wedge inevitably jumped into the composite material itself, splitting the first ply of graphite away from the rest of the material, rather than proceeding through the adhesive, or along the bond interface. Another clear indication of the weakness of this internal interface was the length of the initial crack, roughly 2.5 in. long. Typical crack lengths using aluminum substrates are 1.5 in. Since the stress at the crack tip is a fourth-order function of crack length, this increase in initial length represents a considerable reduction in stress across the bond interface.

We then constructed wedge-test specimens using substrates cut from unidirectional graphite composite specimens that had higher tensile pull-apart strengths in PATTI tensile testing, hoping that this increased strength would reduce the tendency for the crack to jump into the substrate. The specimen surfaces were sanded and grit blasted as before, and bonded in the same fashion. However these specimens also failed in the composite near the bond interface during insertion of the wedge. Despite the lack of a distinct interlayer interface, the composite still proved to be the weak link in this testing.

Accordingly we tried another test specimen design, Fig 2.24. In this design we used a single ply of woven graphite epoxy as the test surface, hoping that the composite would prove stronger with a relatively continuous fiber reinforcement. In this case, surface of a 0.125-in-thick aluminum substrate that had been prepared with a phosphoric acid anodized surface. After composite cure, the surfaces of two specimens were sanded/blasted, and then bonded together to make a wedge-test sandwich specimen.

Figure 2.25 shows the all-composite wedge test specimens after testing, and the hybrid aluminum/composite specimen as-tested, with a wedge still inserted. The failure surfaces of the composite specimens clearly show the characteristic graphite-fiber-reinforcement patterns on both sides of the test specimens, indicating that the crack progressed through the composite, rather than at the bond interface, or through the adhesive, as would be expected of aluminum wedge-test specimens. The crack path in the hybrid specimen also clearly proceeds between the aluminum substrate and the composite overlayer, again avoiding the desired interface.

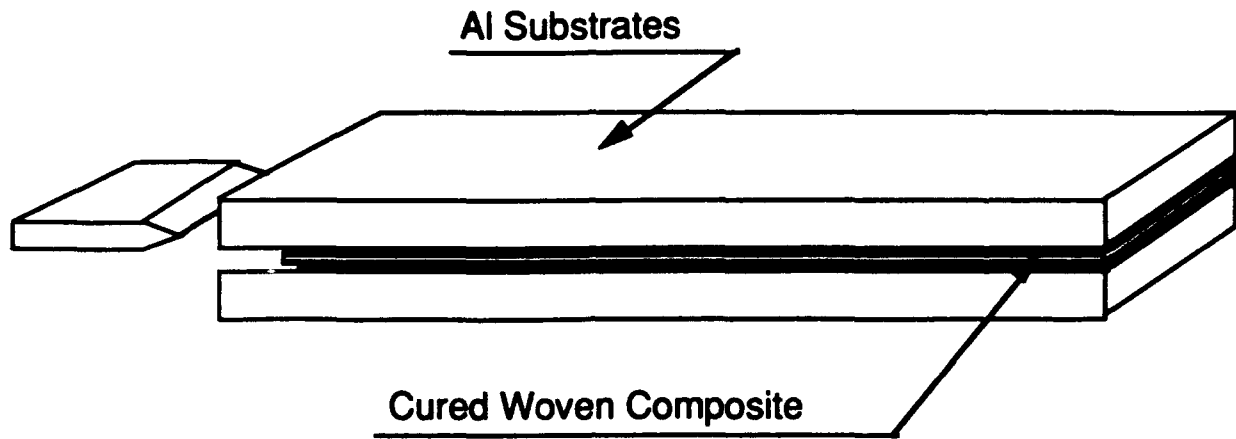


Figure 2.24. Schematic of Aluminum/composite hybrid wedge-test specimen.

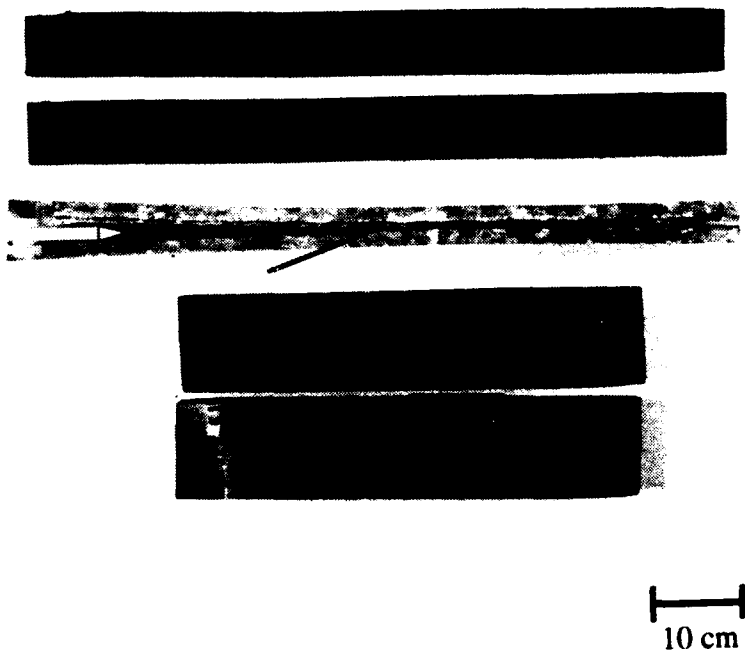


Figure 2.25. Photograph of wedge-test specimens after testing. Note the extensive crack opening on the specimen in the middle (arrow).

Plots of crack growth in the all composite wedge-test specimens are shown in Figure 2.26. Four test conditions are plotted together, woven graphite composites with 60-grit sanded surfaces, woven composites with sandblasted surfaces, unidirectional composites with 60-grit sanded surfaces, and unidirectional composites with sandblasted surfaces. Three specimens were tested for each combination, and the average crack length plotted. All four data sets are similar. None of the cracks grew after the initial environmental chamber exposure. The slight crack growth at the first measurement interval was probably due to thermal expansion of the wedge, leading to a higher stress at the crack tip, rather than a humidity-induced weakening of either the composite matrix or the adhesive bond. The other important point about these data is the large initial crack growth in all the specimens, due to the low peel strength of the composites. The initial crack grows about 1.5 in. long in the typical aluminum-to-aluminum wedge test specimen. The long crack in the composite specimens means that there is very little effective stress at the crack tip to test the bond. Nevertheless, experience with aluminum-substrate wedge-test specimens has shown that poorly prepared surfaces will suffer crack growth lengths that exceed those experienced by the composite wedge-test specimens.

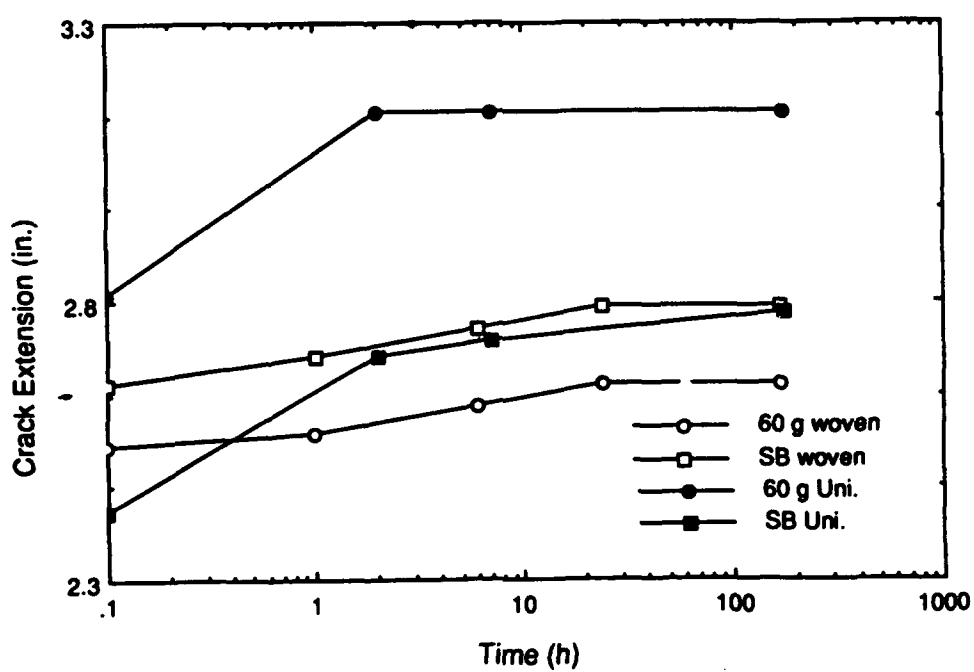


Figure 2.26. Wedge-test results for the all-composite wedge-test specimens.

A second hybrid wedge-test specimen design was tried, which featured a single bond-to-composite surface interface that more closely mimicked the all-aluminum wedge-test specimen, as shown in Figure 2.27. In this case, single plies of woven composite preps were cured in place on PAA treated aluminum panels. The composite surfaces were then sanded, and bonded together to make the sandwich specimen. Once again, the initial crack length is too long to test the bond interface as severely as we wished. In this case, the failure path proceeded between the composite and the aluminum surface.

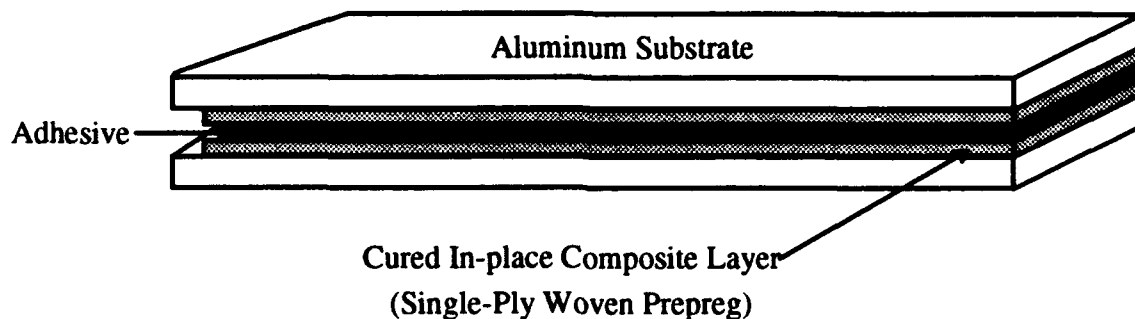


Figure 2.27. Schematic drawing of the second hybrid aluminum/composite wedge-test specimen.

After developing improved processing conditions for the woven prepreg material, as described in Section 2.2.2, we again tried the wedge-test configuration shown in Figure 2.24. Once again the crack proceeded through the interior of the composite, but it stopped at a much shorter distance. The composite cross-ply tensile strength was much higher, and the crack length in the wedge test now nearly matched that of standard aluminum substrate wedge tests. Thus, the stress conditions in the hybrid composite-aluminum test specimen were essentially the same as the standard test, and therefore test results would correctly reflect the durability properties of the bonding surfaces.

The plots of the wedge specimen testing for these specimen are presented in Figure 2.28. These show the crack extension versus time for bonded Al-composite-Al sandwich wedge tests in which the composite surfaces were prepared by sanding, and by aluminum oxide impregnation (35 V-15 m). Also shown for comparison is the plot of the wedge test obtained for bonded PAA aluminum wedge specimens. Each test result was based on an average of at least four specimens.

All of the surface treatments that performed well in wedge testing, sanding, grit-blasting, and oxide impregnation, showed no visible sign of humidity-induced bond degradation. Optical macrographs of the wedge-test surfaces after the test show that the crack growth before, during, and after exposure in the humidity chamber all occurred within the composite rather than at the bond interface. There was no sign of a change in the nature of the crack, i.e., no visual clue where the crack stopped before or after humidity chamber exposure.

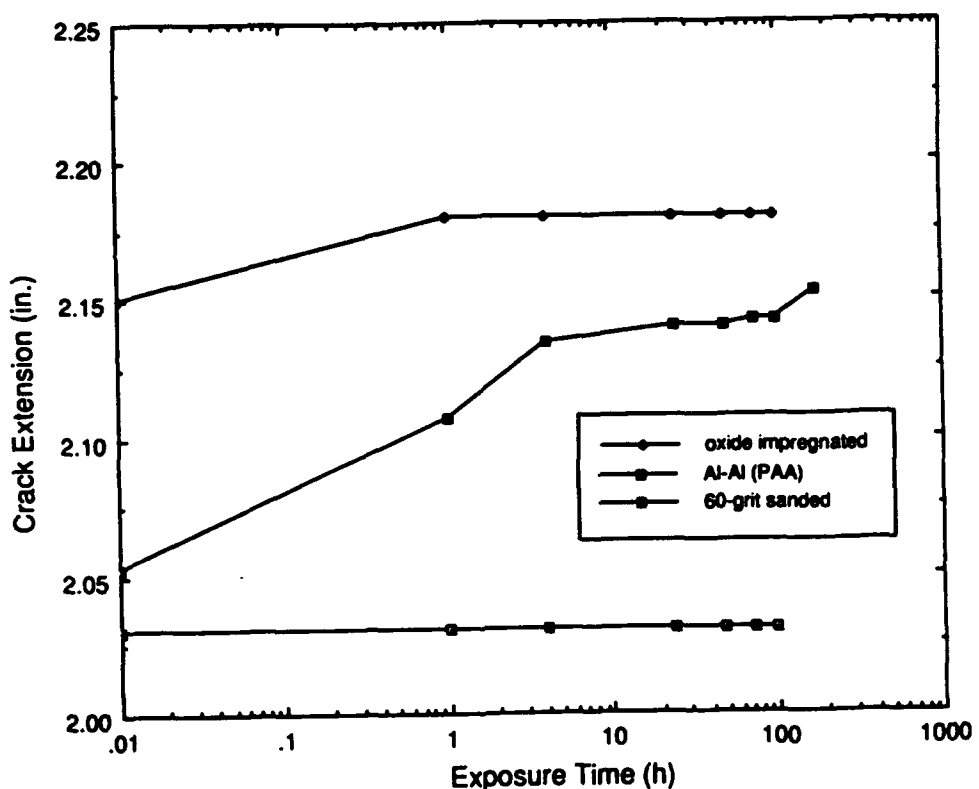


Figure 2.28. Results of aluminum/composite-sandwich wedge-tests, compared with the ASTM standard phosphoric acid anodized all-aluminum specimen.

The crack growth behavior of the Al-composite-Al sanded, sandblasted, and oxide-impregnated specimens mimic the behavior of the all-aluminum wedge-test result. Most of the crack extension occurred initially when the wedges were driven into the specimens and very little was observed thereafter. In no case is there significant humidity-induced crack growth. The crack growth occurs at the composite-to-adhesive interface, which is the desired locus of failure for this specimen. This indicates that the Al-composite-Al sandwich configuration is a good one for testing composite/metal bonds, and that mechanical cleaning and oxide impregnation surface treatments have good bond durabilities.

Results of wedge tests using plasma-treated composite surfaces were inconsistent. There was more scatter in the initial crack lengths among the five specimens used for each test, along with greater crack growths during humidity chamber exposure. Figure 2.29 shows the average data for a 200-V and a 500-V plasma-treated-surface test series. Thus, the wedge-test results are in accord with PATTI results; plasma treatments do not appear to yield uniformly treated surfaces.

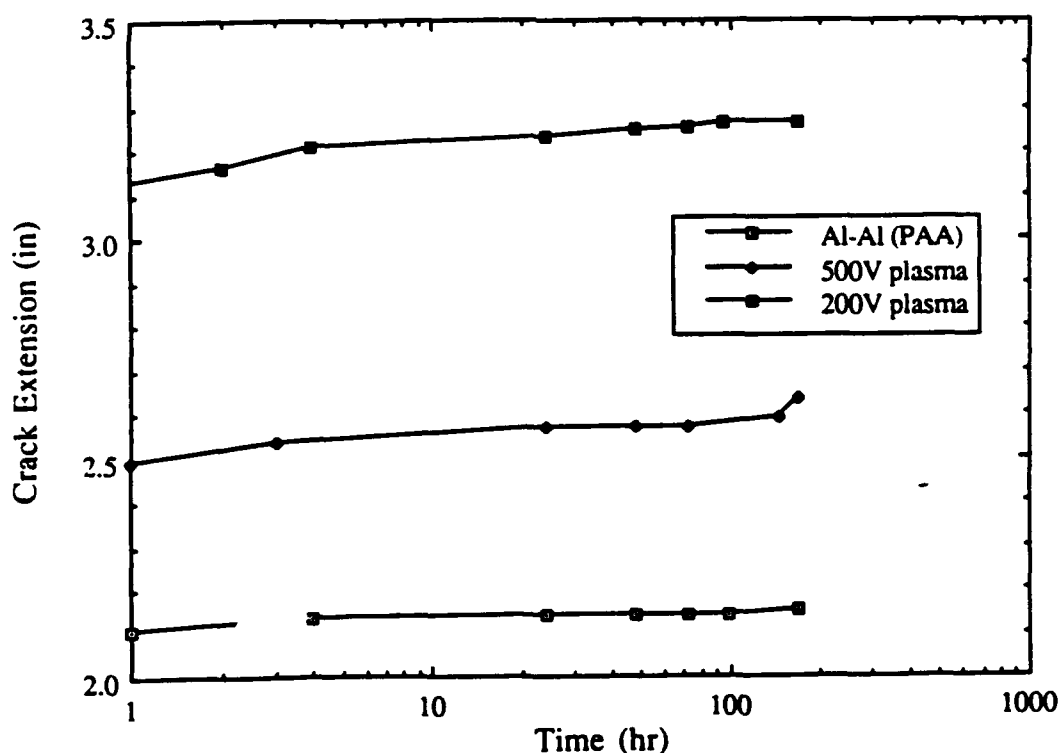


Figure 2.29. Wedge-test results of plasma-etched composite specimens.

2.8 Fracture Testing

We conducted fracture tests using the basic test scheme developed during our previous contract (15), utilizing small aluminum compact-tension specimen halves bonded together along the crack propagation line. We added a composite interlayer, as with the successful wedge-test specimens, in order to incorporate a (or in this case two identical) composite interface. Unload compliance testing allowed the collection of a complete data series to be completed with each specimen, and plastic/elastic analysis of the load line allowed a number of fracture parameters to be extracted from the data.

Fracture analysis was performed on bonded 1/2 T-plan compact tension (CT) aluminum specimens containing either a precured single-ply 0.02-in.-thick woven cross-grain composite interlayer or a 0.04-in.-thick end-grain composite interlayer. Each of the composite surfaces were sanded prior to bonding. The aluminum CT specimen surfaces were prepared by degreasing for 20 min at 65°C in a Turco bath, FPL etch at 65°C for 15 min, then anodizing at 10 V for 15 min in 10 percent aqueous H₃PO₄.

The specimens were bonded in jigs to control the bond line thickness. Hysol's 9394 adhesive was applied to both metal adherend surfaces, and to both sides of the composite surface then the composite was sandwiched between the two aluminum half CT specimens, as shown in Figure 2.30. The specimens were then cured at ambient temperature for 16 hr and postcured for 7 hr at 70°C.

Fracture testing was performed on an Instron model 1125 mechanical tester equipped with a clip-on displacement gauge. The test machine was interfaced to a personal computer to collect data and calculate fracture parameters. Although the test was the standard unload compliance test used for J-integral analysis, we used the separation of energies method to obtain values for elastic and plastic energies. For more details of this test, please refer to our earlier publication on adhesive fracture testing.(20)

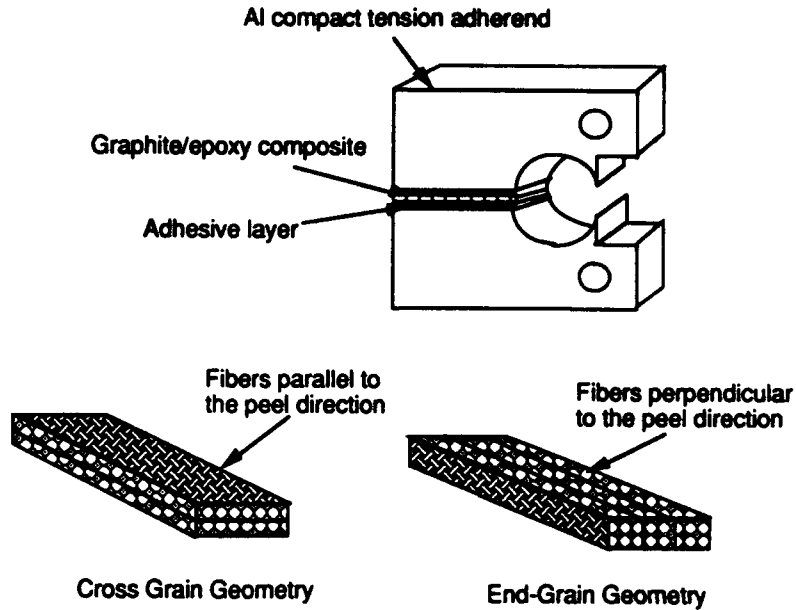


Figure 2.30. Schematics of the two types of compact tension test specimens used for fracture testing.

Table 2.15 shows the fracture parameters obtained from the unload-compliance testing we performed on the Al-composite-Al cross-grain and end-grain sandwich compact tension specimens. The peak load, the elastic energy release rate (G), and the plastic energy dissipation rate (I) are reported for all three specimens for each composite geometry.

The fracture parameters for the end-grain composite sandwich specimens were significantly higher than those for the cross-grain specimens. Peak loads were twice as high, on average. G and I values for the end grain were three and four times greater, respectively, than the corresponding cross-grain sandwich specimens.

Table 2.15. Fracture Data from Composite Sandwich CT Specimens

	Specimen	Peak Load (lb)	G (in.-lb/in. ²)	I
Cross-grain composite	1	62	0.37	0
	2	70	0.63	0
	3	47	0.69	0.40
	avg	60	0.56	0.13
End-grain composite	1	135	1.1	0
	2	95	2.2	1.7
	3	140	1.8	0
	avg	123.3	1.7	0.57

The results indicate that the geometry of the fiber can greatly affect peel strength of the composite as a whole. In the case of the cross-grain composite specimen, the fibers are aligned parallel to the surface of the aluminum adherends. Therefore, the fracture occurs within the composite during testing because the peel stresses exerted on the specimen exceed the strength of the matrix and delamination is observed. The end-grain composite, however, allows for higher peak loads since the fibers are aligned perpendicular to the peel direction. So even though the matrix is weak, the anisotropic behavior of the composite fiber allows the specimen to sustain higher loads before fracture. Thus, the elastic and plastic fracture parameters will be greater. This demonstrates the advantage of three-dimensional composite weaves for bonding to metals.

Failure analysis of the test specimen supports this conclusion. The fracture path of the cross- (or transverse-) ply laminates is strictly through the epoxy matrix between graphite fibers. However, even the end-grain specimen exhibits a considerable amount of cohesive, through-matrix failure. Figure 2.31 shows opposing faces of the cross-grain laminate compact-tension test specimen after test. It is clear that failure proceeded inside the composite in regions where the graphite fibers were arranged parallel to the bond interface, i.e., they were still attached to the adhesive. Those regions of the 2-D weave where fibers were perpendicular to the adhesive show fracture through the adhesive.

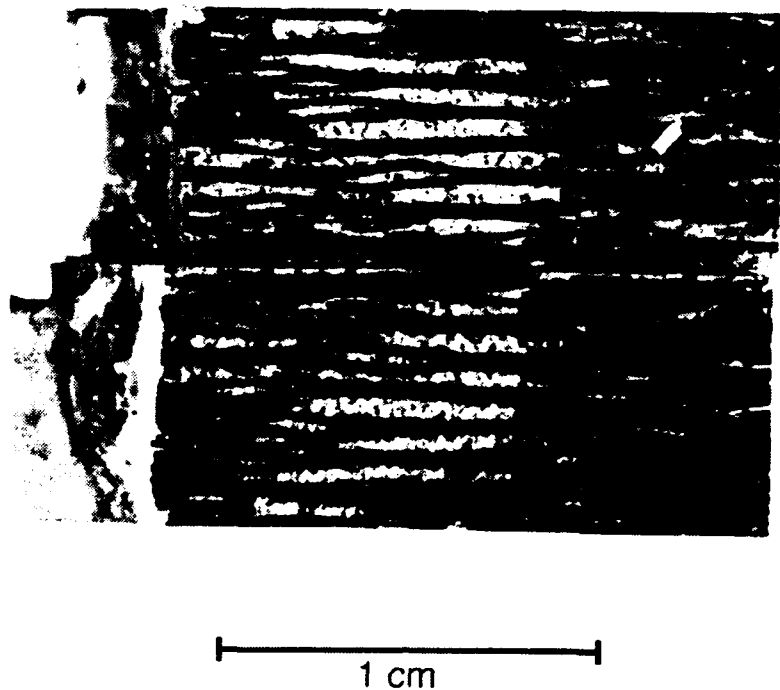


Figure 2.31. Optical macrograph of a cross-grain compact tensions specimen after test. The crack front passed through the graphite fiber bundles in the epoxy matrix over more than one-half the total area.

There are two points to note about this failure. 1) The fracture properties are still largely driven by the weak interface between brittle epoxy and graphite fibers, rather than by anything related to adhesive bonding. The area covered by graphite fibers on the adhesive is greater than 50 percent of the total. Thus, the effective area of the weak phase and thus the effective area of the specimen is much smaller than its physical area. 2) There is no region where the bond interface was a controlling factor. The entire fracture surface is either cohesive failure of the composite, or cohesive failure of the adhesive. The bond preparation had no effect on the fracture.

Thus, our testing has shown that the primary determinant of a bonded composite's properties is determined by the cross-ply properties of the composite itself. The high-strength, high-stiffness epoxy matrix materials favored by aerospace engineers for skin applications may be a poor choice for structural materials that will have significant cross-ply loading, and that will be bonded over smaller areas, rather than across the entire composite

surface. A higher toughness matrix should enhance bonding properties, such as tensile strength, durability and fracture toughness, as well as protect the structure from damage during off-design-axis loading. A tougher epoxy formulation, like adhesive 3H as a composite matrix material, would allow more reliable and higher performance adhesive joining of composite to metals.

2.9 Lessons Learned

This phase of the program has many significant results, and supports many significant conclusions. A paper outlining the program and its results was presented at the 6th International Symposium on Structural Adhesive Bonding, Morristown, NJ, May 1992, and published in its proceedings by the American Defense Preparedness Association.

The primary conclusion is that sanding/grit blasting followed by solvent surface cleaning is an entirely satisfactory way to prepare graphite/epoxy composite surfaces for adhesive bonding. In all cases, woven and unidirectional graphite fiber, humidity exposure lap shear and fracture testing, high strength, durable bonds were formed that fractured inside the composite when tested to failure. Other participants at the symposium related similar experiences with the strength of composite bonds. We appear to be the first that have published data, and are certainly the first to investigate durability and fracture of such bonds.

The second major conclusion is the severe limitation on bonding imposed by the nature of the graphite/epoxy substrate. All of our better bonding treatments caused failures within the composite matrix. We observed significant fiber-orientation effects in testing. These results demonstrate the difficulty of designing structural composites that must be adhesively bonded. Cross-ply loading poses severe problems with brittle matrix materials, a situation that is very difficult to avoid in bonded structures. It seems clear that tougher matrix materials will be needed before structural applications for composites, such as bridging, will be successful.

We have achieved higher tensile/shear strength values for composites than those reported by other investigators. We believe that this is a demonstration of the importance of the role of the brittle matrix. Our PATTI test specimen appears to be much better suited to testing this material than specimens used by others. The double-lap-shear results confirm the absolute numbers obtained with the PATTI tester, but they also demonstrate the difficulty of

obtaining repeatable measurements with conventional tests that were developed using ductile substrates. Thus, we feel that development of this test method is a significant achievement in the field.

A second significant development is the demonstration of a viable wedge-test specimen. Bond durability testing simply had not been performed on composite surface prior to our research. Our demonstration that the bond interface is not a weak link was not an obvious presumption before the tests, and lends considerable support to the use of adhesive bonding with composites.

Our fracture tests demonstrated that fracture parameter measurements are possible with composite materials, using a relatively simple test specimen. Although the measured values are very low, the test method can be used to look for ways to improve their performance.

3.0 JOINT ARCHITECTURE AND PREDICTIVE MODELING

The efforts devoted to design and modeling were divided into four phases. Finite element computer modeling was the primary tool in all phases, and Dr. Abhijit Dasgupta was the principal investigator. Dr. Marion Mecklenburg was a design consultant.

The first phase was devoted to confirming the results of computer modeling for adhesive joints, and developing an appropriate failure criteria that would be the basis for all other work. A model was constructed to apply to preexisting mechanical testing data for a quad-lap shear joint specimen, and the computer model used in an elastic-plastic analysis to determine the load-bearing capacity of the joint. Comparison of the model results with experimental data indicated that von Mises' equivalent stress was the best criterion to use.

The second phase involved investigating a variety of schemes to reduce the stress concentration effects typically seen in bonded shear specimens. An aluminum tube-aluminum end fitting lap joint geometry was chosen, to simulate the lower hinge fitting bond in the "Light Vehicle/Foot Bridge" design. A scheme for tapering the adherend tubes was shown to be most effective in reducing stress concentrations.

The third phase featured extensive parametric studies of the tubular joint to develop design guidelines. It was found that a taper was not necessary when shorter bond overlap lengths were used. A full set of design curves was developed based on the finite element models for each of three substrate configurations: aluminum tube to aluminum end fitting, composite tube to aluminum end fitting, and composite tube to composite end fitting. Contour plots of the modeling results let a designer determine the load-carrying capacity of the joint, decide whether or not to apply taper, and determine the magnitude of stress concentration in the joint for the three adherend combinations.

In the final phase, the computer models were applied to the prospective adhesively bonded center span design for the LV/FB, to guide the development of the demonstration article.

3.1 Three-Dimensional Finite-Element Analysis of Quad-Lap Adhesive Joint

The first necessary element in developing a finite element model of adhesive joints and using computer models to optimize joint design is validation of the model assumptions. In particular, we needed to determine the correct failure criteria, since the many different theoretical failure criteria could lead to different conclusions. Thus we began by choosing a test geometry for which good experimental data was available, and performing finite element analysis to match the computer prediction with the real results. We chose a steel substrate quad-lap joint used in a study sponsored by the Federal Highway Administration to test structural adhesives.⁽²¹⁾ We applied finite-element modeling techniques to understand the stress distributions for this specimen geometry. The agreement between the finite-element results and experimental results was used to pick the appropriate failure criteria, and demonstrate the validity of the finite-element method as a feasible tool for adhesive joint analysis in the Light Vehicle/Footbridge (LV/FB) development program.

3.1.1 Analysis

PATRAN is a finite-element analysis software program from PDA Engineering, which is principally used for mesh generation (preprocessing) and results evaluation (postprocessing). The actual finite-element analysis (stress calculation, etc.) is done by interfacing PATRAN with the analysis software ANSYS. The finite-element model created in PATRAN (preprocessing) is first translated into the format of the analysis program. After the analysis is performed, the results are translated back into PATRAN-compatible files for postprocessing (e.g., contour or fringe plotting of stresses, deformed geometry plotting).

3.1.2 Model

Figure 3.1 shows the dimensions of the actual quad-lap specimen. Since there is a four-fold symmetry, the finite-element model addresses only one-eighth of the actual specimen. Figure 3.2 is the enlargement of the right-hand portion of the model (front view). The distribution of the finite-element meshes is finer near the locations where higher stress states are expected: near the interface of the adhesive and the adherend, and on the adherend to the left and right of the adhesive joint. The adhesive is divided into three horizontal mesh layers (top, middle, and bottom). The model consists of 1844 nodes and 1424 three-dimensional solid, linear hexahedron (HEX/8) elements, where each HEX/8 element consists

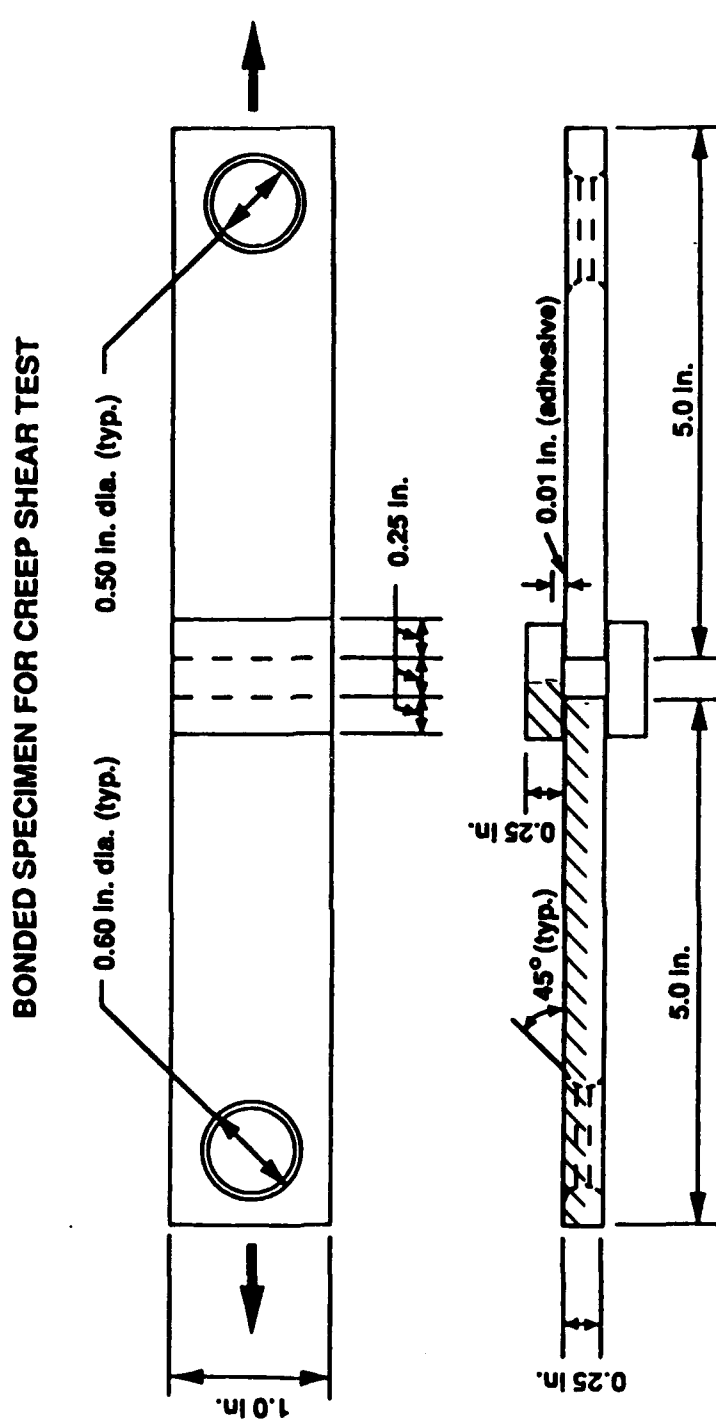


Figure 3.1. Quad-lap specimen geometry, steel specimen. The shaded region indicates the one quarter section used in the finite element model..

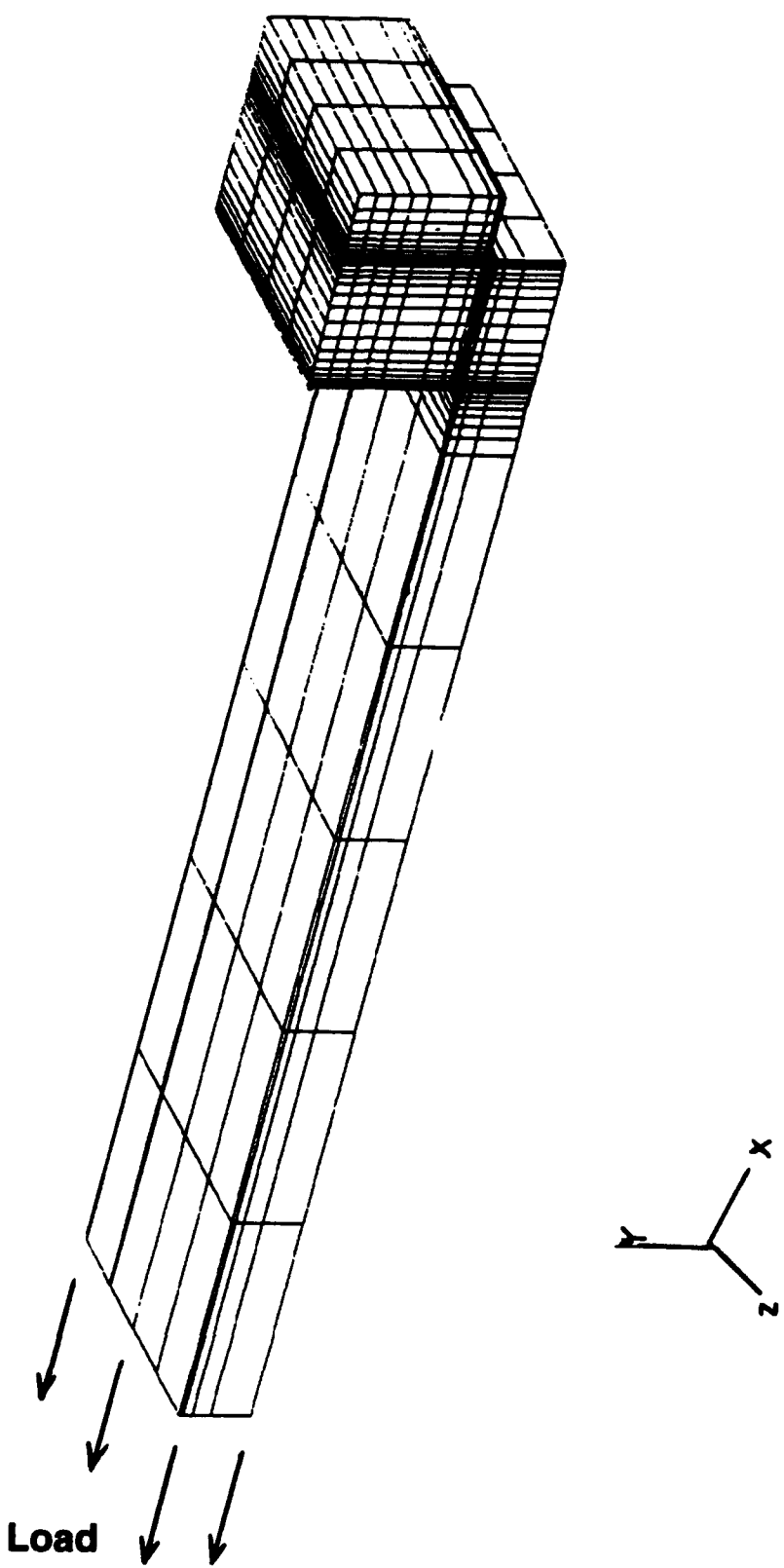


Figure 3.2. Finite element model of one quarter of the quad-lap specimen.

of 8 nodes and 24 degrees of freedom (3 per node). We analyzed the stress in two specimens with adherends of aluminum and steel, respectively. Elastic isotropic properties for the adherends and adhesive are given in Table 1.

Table 3.1. Properties of Adherends and Adhesive

MATERIAL	ELASTIC MODULUS (E) (psi)	POISSON'S RATIO (v)
Aluminum	10.15×10^6	0.345
Steel	29.00×10^6	0.270
FM-300 Epoxy Adhesive @50°C, 50% RH	1.460×10^6	0.450

3.1.3 Boundary Conditions

Displacement geometry constraints were applied to all planes of symmetry, including the face in the global positive Z-direction, the bottom face (negative Y-direction), and the cutting cross-section face located just above the adhesive portion in the positive X-direction. A pressure of 4 psi in the negative X-direction was simulated on all elements on the left-hand negative X face of the adherend in the model, and stresses calculated for the adhesive layer.

3.2.1 Results-Aluminum Specimen

Stress distributions in the middle layer of the quad-lap adhesive for an aluminum specimen were plotted. The ranges are given below:

Sigma xx: 1.32 to -0.655 (psi)
 Sigma yy: 1.96 to -1.82 (psi)
 Sigma zz: 1.02 to -0.757 (psi)
 Sigma xy: 2.22 to 1.47 (psi)
 Sigma yz: 0.262 to -1.54 (psi)
 Sigma xz: 0.0162 to -0.00714 (psi)
 Von Mises' equivalent stress
 (Sigma E): 3.87 to 2.65 (psi)

As can be seen, the most prominent stresses within the quad-lap adhesive are the shear stress (σ_{xy}) and the peel (bending) stress (σ_{yy}). σ_{xx} and σ_{zz} , the stress components in the X- and Z-directions, are also quite large compared with the equivalent stress (σ_E): σ_{xx} is about 34 percent of maximum σ_E , and σ_{zz} is about 26 percent. σ_{yz} and σ_{xz} can be ignored because of their small values compared with the equivalent stress (less than 7 percent). Therefore, σ_{xx} , σ_{yy} , σ_{xy} , and σ_{zz} are the stresses important for stress-based failure criteria.

The shear stress acting along the free edge of the middle adhesive layer is larger than that at the constrained edge, which clearly demonstrates a boundary layer effect. However, the bending stress (σ_{yy}) at the free edge is smaller than that at the constrained edge. From a plot of σ_E (Figure 3.3), it is clear that the equivalent stress acting on the free edge is larger than that on the constrained edge of the finite-element model. The relative maximum equivalent stresses are located at the inner edge of the lap, but the stress concentrations are relatively small and the equivalent stresses on the central portion of the adhesive are nearly uniform. The difference in equivalent stress between the constrained edge and free edge is larger at the right-hand portion of adhesive, primarily because of the larger shear stress acting on the constrained edge of the aluminum specimen.

3.2.2 Results-Steel Specimen

The ranges of stress distributions acting on the middle layer of the quad-lap adhesive for a steel specimen are listed below:

σ_{xx} :	0.562 to -0.389 (psi)
σ_{yy} :	1.24 to -1.14 (psi)
σ_{zz} :	0.431 to -0.455 (psi)
σ_{xy} :	2.13 to 1.54 (psi)
σ_{yz} :	0.101 to -0.043 (psi)
σ_{xz} :	0.0119 to -0.0839 (psi)
Von Mises' equivalent stress	
(σ_E):	3.64 to 2.95 (psi)

Shear stress is the dominant stress among all the components. σ_{xx} , σ_{yy} , and σ_{zz} are reasonably large compared with the equivalent stress (15 percent, 34 percent, and 11 percent of σ_E , respectively), while σ_{yz} and σ_{xz} are significantly smaller (less than

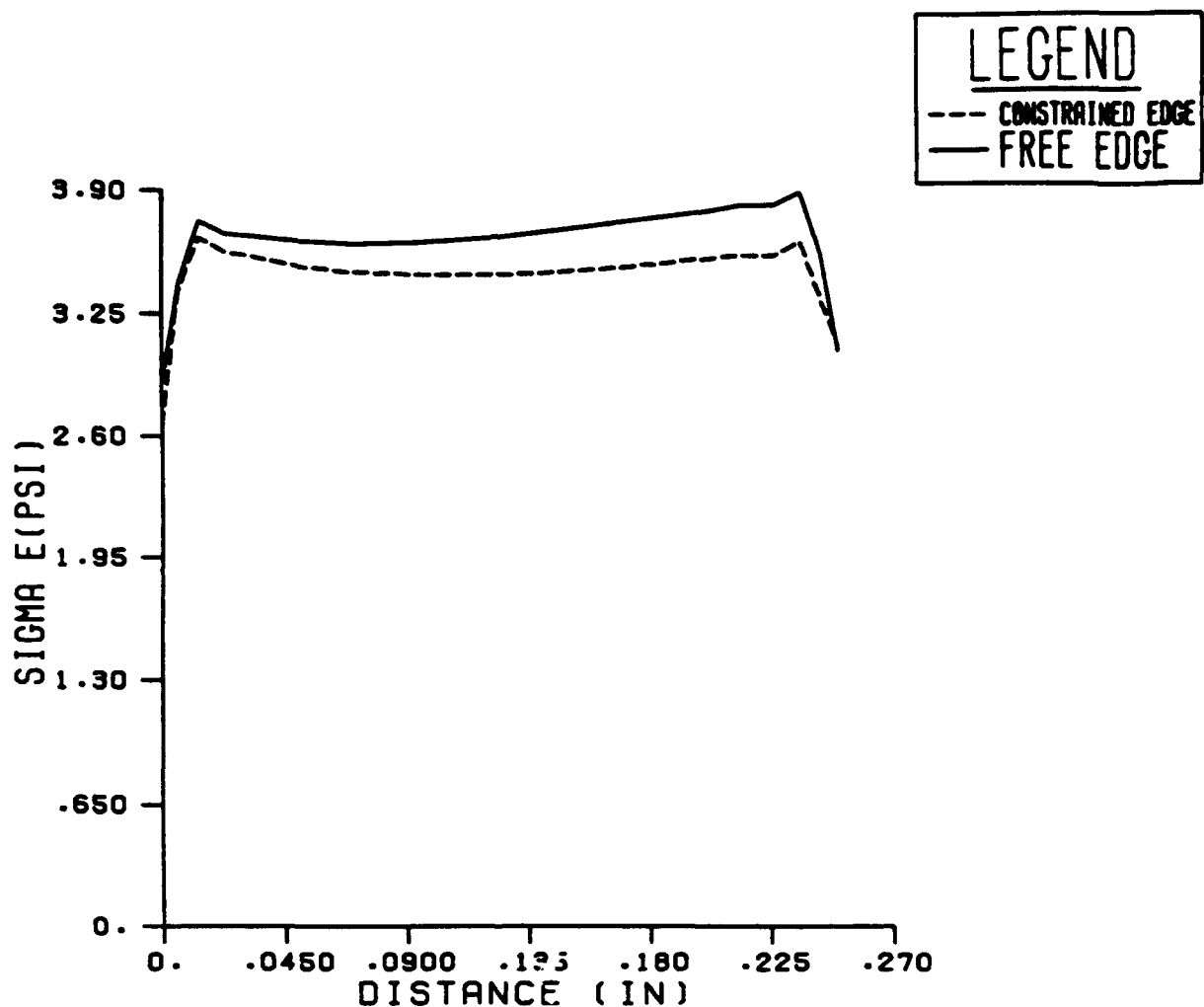


Figure 3.3. Equivalent stress acting on the middle adhesive layer for an aluminum quad-lap specimen.

10 percent). Both bending stress and equivalent stress acting along the free edge of the middle adhesive layer are larger than those along the constrained edge. Conversely, shear stress acting on the constrained edge is larger than that on the free edge. Equivalent stresses acting at 0.0234 in. and 0.243 in. from the left-hand side of the adhesive are relatively higher than at other locations in the X-direction of both edges (Figure 3.4). The equivalent stress is quite uniformly distributed along the central portion of the middle layer of the adhesive.

The results show that the finite-element analysis approach is a convenient tool for analyzing the stress concentration in a bonded joint. Equivalent stress in the aluminum specimen was marginally larger and less uniform than the steel specimen, primarily due to the larger peel stress (σ_{yy}) and normal stress (σ_{xx}) acting on the adhesive. Shear stress (σ_{xy}) is the dominant stress in both specimens.

3.2 Elastic-Plastic Analysis of Quad-Lap Specimen

Elastic-plastic deformation of the quad-lap steel specimen was analyzed to see how much difference including plastic deformation effects would make on the calculated outcome. The ANSYS program uses an incremental Newton-Raphson approach for satisfying equilibrium equations in the nonlinear range. Sixty-one load steps were needed to reach the maximum failure stress of 820 psi. The yield strength of the adhesive (FM-300) was extrapolated from the Von Mises' equivalent stress versus strain plot, and was determined to be 326 psi (at equilibrium humidity and stress conditions for the actual test). The increment of load step was based on the criterion that change in strain not to exceed the magnitude of elastic strain. Each load step for plastic deformation required 30 to 36 iterations to reach plastic convergence. Stress distributions in the three adhesive layers (top, middle, and bottom) were obtained and plotted. Distributions of Von Mises' equivalent stress, bending stress, and shear stress acting on Gauss (integration) points of the finite elements for each adhesive layer are shown in figs. 3.5-3.7.

Figure 3.8 shows the stresses during the last load step of plastic deformation in the middle adhesive layer, with stress ranges as follows: σ_{xy} : 636 to 869 psi, σ_{yy} 636 to 869 psi, and Von Mises' equivalent stress (σ_E) 1110 to 1510 psi. The stresses are distributed uniformly through the central portion of the adhesive. Bending stress is approximately zero because the effect of the adherend is not felt in this layer, and the end

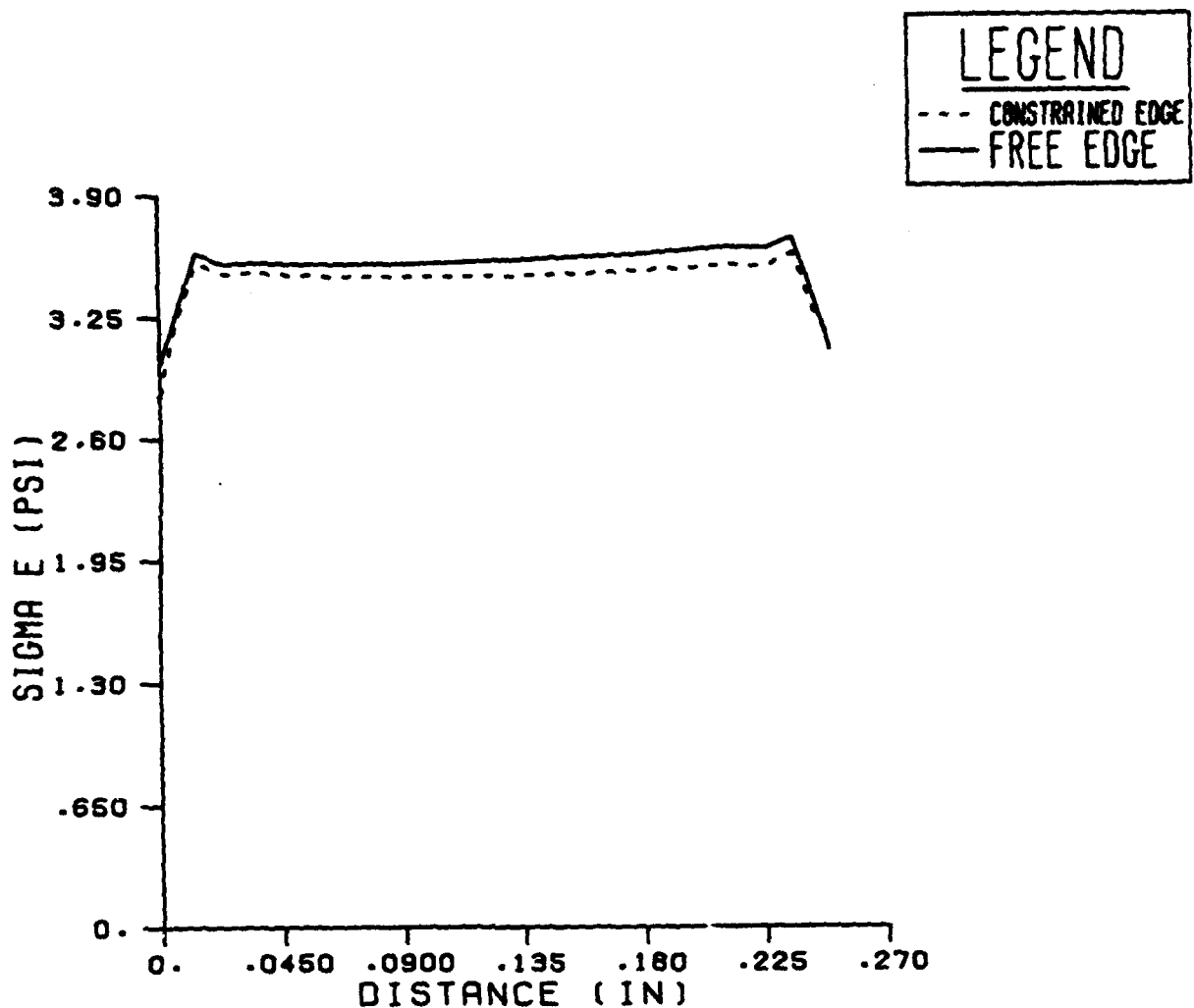


Figure 3.4. Equivalent stress in the middle adhesive layer for a steel quad-lap specimen.

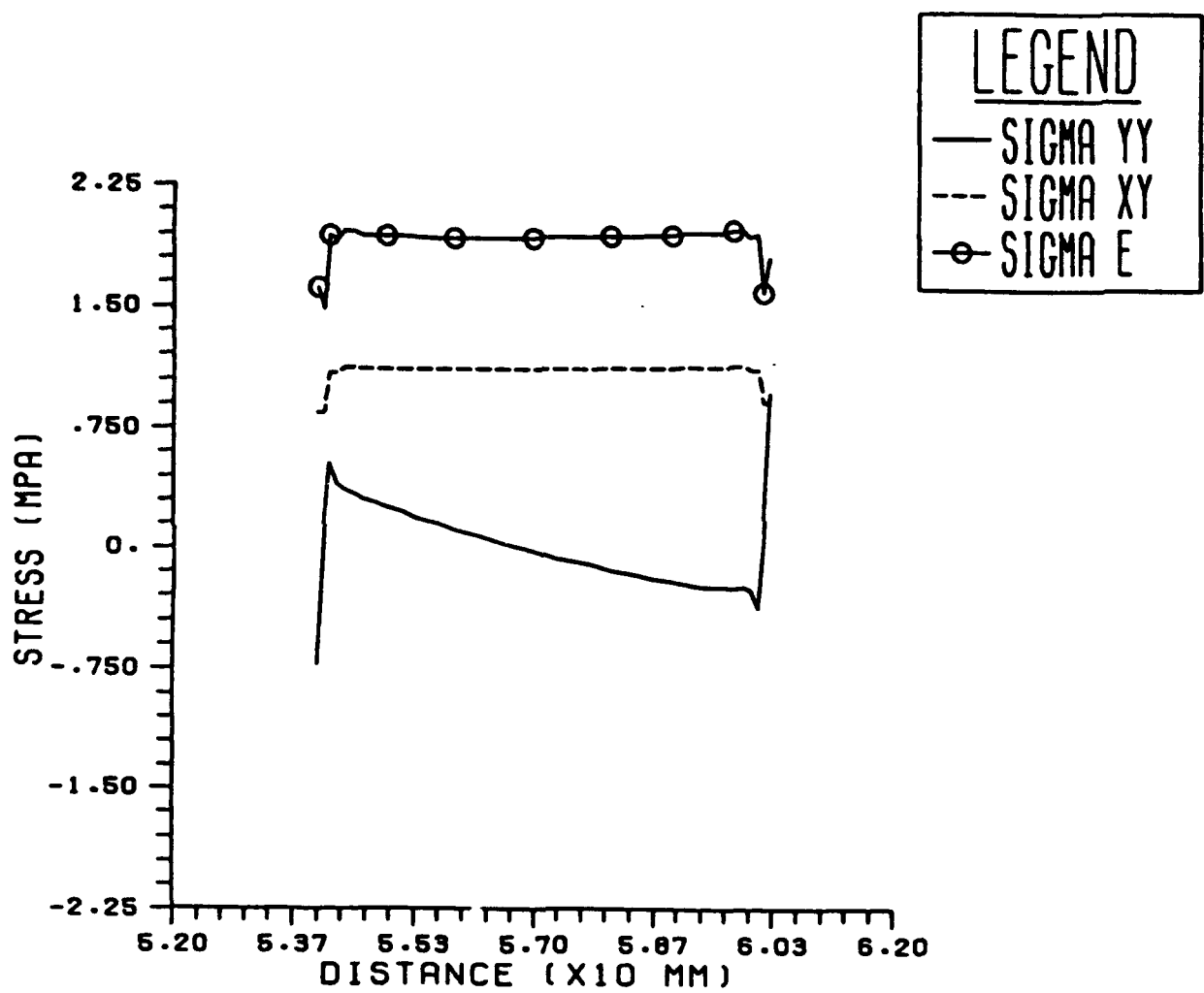


Figure 3.5. Elastic-plastic analysis equivalent stress in top layer of a steel quad-lap specimen.

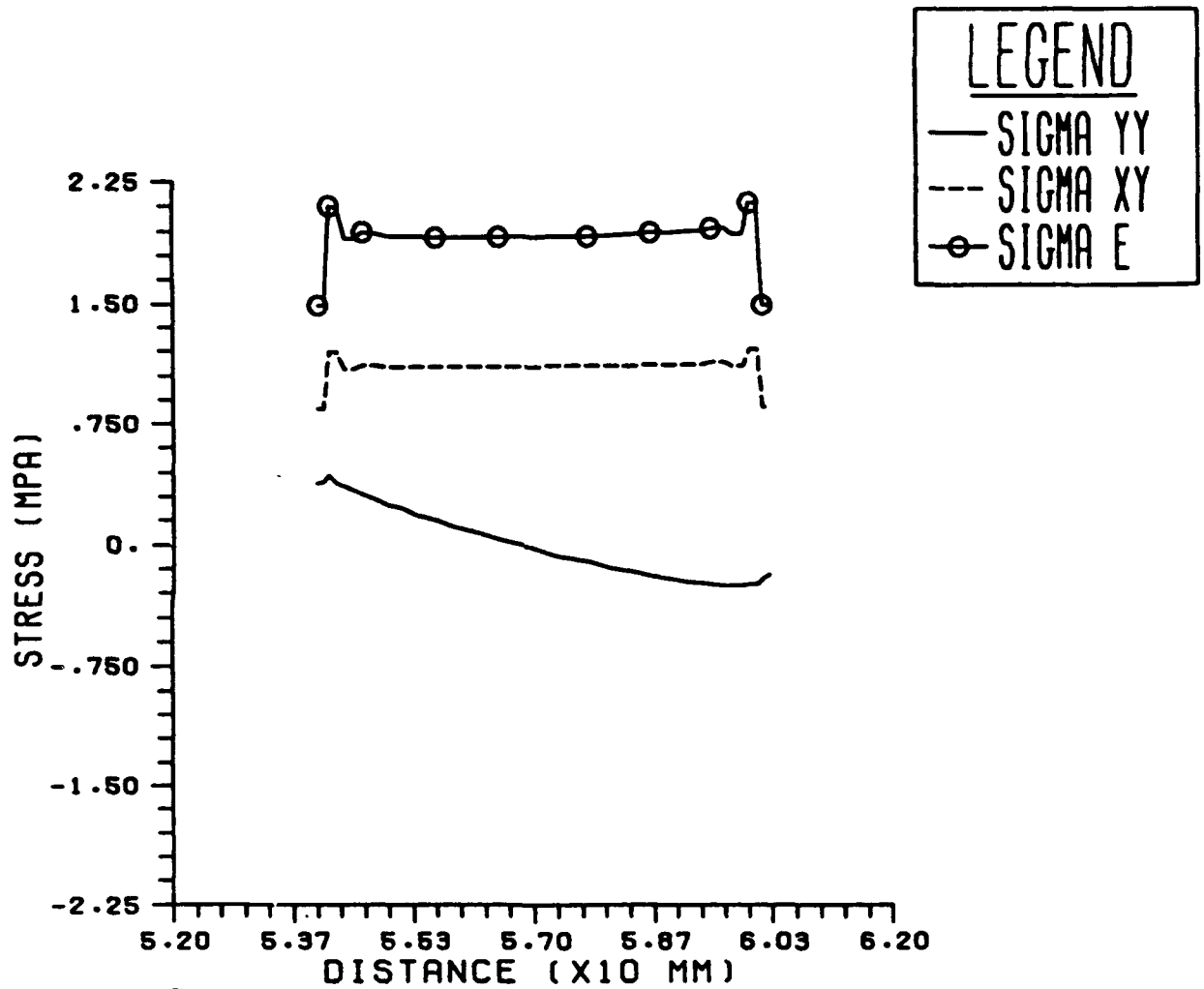


Figure 3.6. Elastic-plastic analysis equivalent stress in the middle adhesive layer of a steel quad-lap specimen.

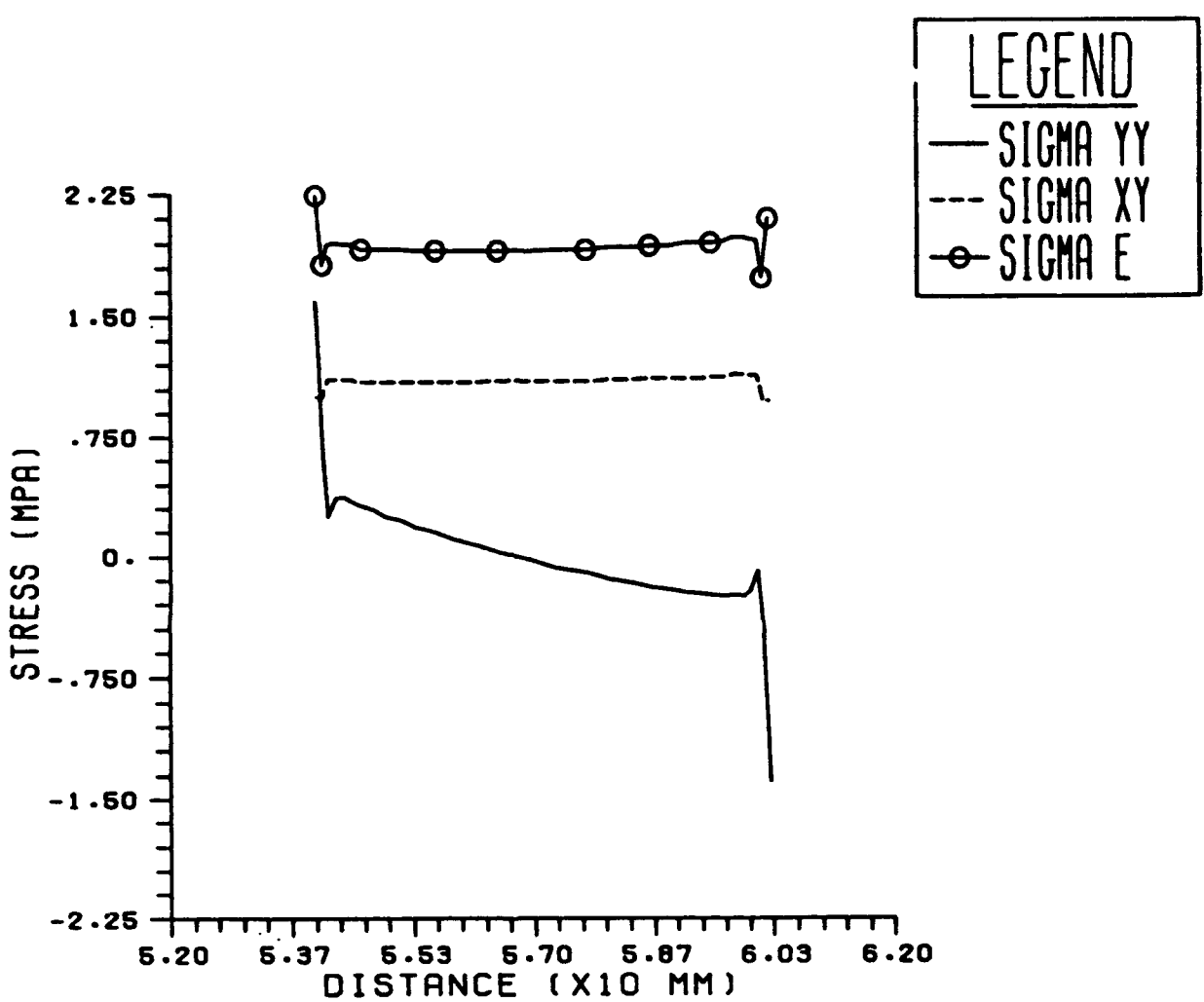


Figure 3.7. Elastic-plastic analysis of the bottom adhesive layer in a steel quad-lap specimen.

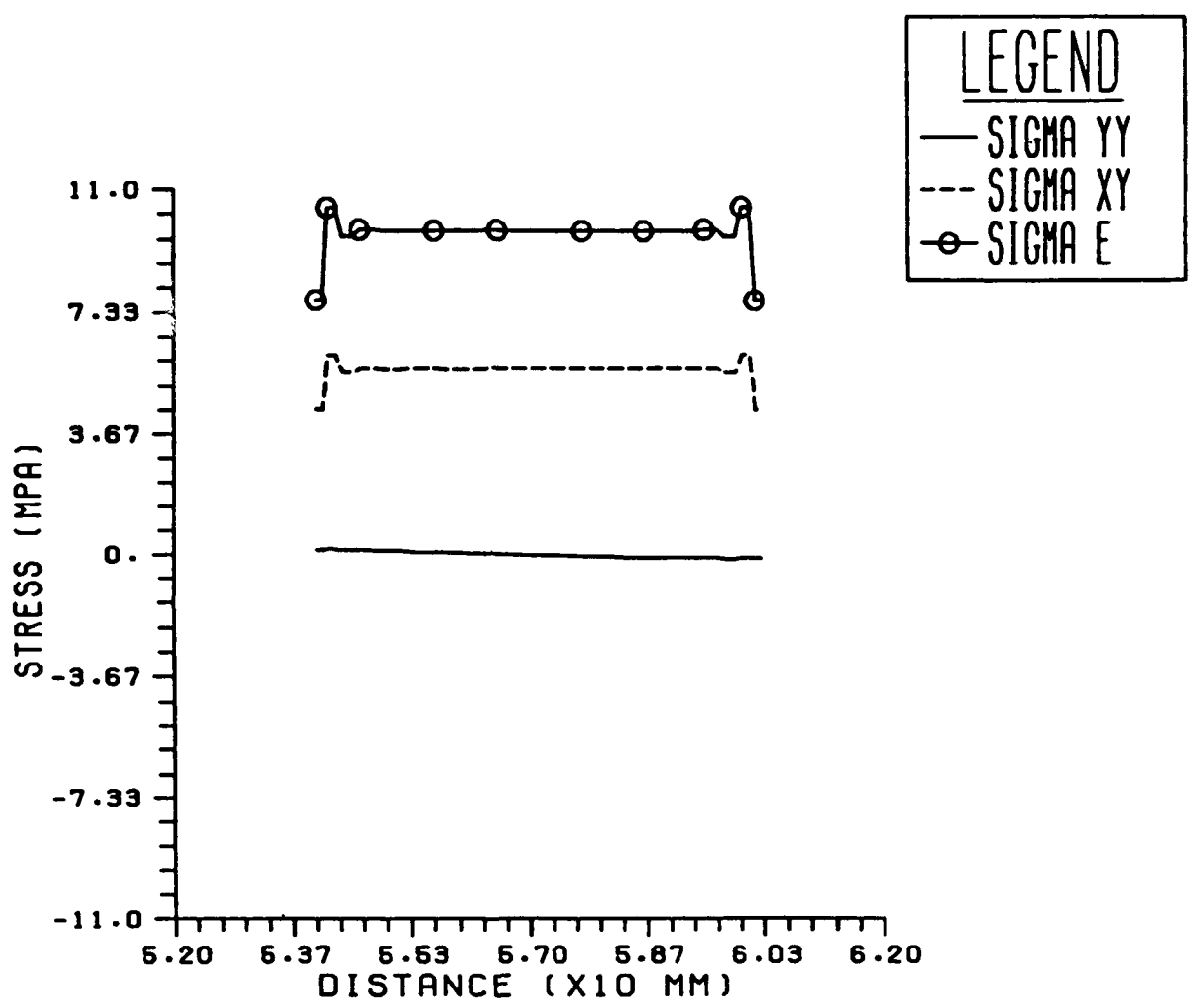


Figure 3.8. Middle adhesive layer stress at joint failure for the steel quad-lap specimen.

point bending stress variation is eliminated. The stress components acting on the middle portion of the adhesive become uniformly distributed when the specimen undergoes elastic-plastic deformation. Shear stress (σ_{xy}) in the specimen is the dominant stress.

3.3 Failure Criteria

The nonlinear analysis in this study was utilized to aid in the selection of an empirical failure model for the adhesive. The importance of selecting an appropriate failure criterion from the fact that the appropriate stress parameter to be monitored in all parametric and optimization studies depends, in part, on the components that are responsible for failure. For example, the maximum shear stress must be monitored for materials which are empirically known to follow a Tresca's failure criterion. On the other hand, the octahedral shear stress (or alternatively, the equivalent stress) must be monitored for all materials which are observed to follow a Von-Mises' distortional energy criterion for failure.

The selection of an appropriate failure law for adhesives is difficult because experimental evidence from laboratory tests have repeatedly illustrated that adhesives in lap or butt joint configurations do not follow any of the existing, conventional small-deformation failure theories for isotropic, homogeneous, bulk materials. For instance, experimental evidence suggests that the average or nominal shear strength of polymeric adhesives in lap-shear tests is numerically similar to the average or nominal tensile failure strength obtained from uniaxial butt-joined specimens, or from homogeneous flat-coupon adhesive specimens. Thus at failure,

$$\tau_{nom} \equiv \sigma_{nom} \quad (1)$$

Clearly, new empirical failure theories are required to account for adhesive joint failure, and further investigations are warranted to explore appropriate failure theories. Experimental evidence obtained from related studies are utilized in conjunction with nonlinear finite element studies in this program, to postulate a new empirical failure criterion which can be utilized to guide optimization and parametric studies.

In order to establish a convenient failure criterion, we consider first, the maximum value of the stresses generated in the specimen, as a function of the applied load. The nonlinear finite element analysis is utilized for this purpose. The nonlinear constitutive law

for the adhesive is idealized as a bilinear stress-strain curve as illustrated in Figure 3.9. The different stress components monitored as a function of the applied load are:

- (i) maximum principal stress
- (ii) maximum hydrostatic stress
- (iii) maximum shear stress
- (iv) maximum Von Mises' (or equivalent) stress
- (v) maximum octahedral shear stress

Of these, the first two stress components represent a material's vulnerability to extensional (or normal) stresses and are the common failure-drivers in brittle materials. The last three stress components are all measures of multiaxial shear stress fields and are commonly believed to be the failure-drivers in ductile materials. In particular, the last two stress measures are functionally the same and only differ by a constant multiplicative factor.

Commonly utilized conventional failure criteria are usually formulated in terms of these stress components by specifying failure threshold values for the critical stress component, based on data from a uniaxial tensile or pure shear test-to-failure in a controlled laboratory specimen. For instance, the Von Mises' failure criterion for isotropic materials states that the material will fail when the distortional energy in the material reaches the same value as that in a uniaxial specimen at failure. Since the equivalent (or Von Mises') stress and the octahedral stress components are both measures of the distortional energy in isotropic materials, these stresses are used to define the failure threshold or strength in this case. On the other hand, Tresca's failure criterion states that an isotropic material fails when the maximum shear stress reaches the same value as the shear stress at failure in a pure shear test. It is important to emphasize here that the maximum shear stress must be computed in principal stress coordinates at each point, based on multiaxial stress information. As a final example, failure of a brittle isotropic material can be expressed in terms of the critical stress intensity factor at the tip of microscopic flaws in the material. The critical stress intensity factor, in turn, is dependent on the maximum normal stress at the flaw tip and on the flaw size. Thus if an average flaw size is known and if the flaws are assumed to be uniformly distributed in the material (in a statistical sense), then the fracture strength of the material can be expressed in terms of the maximum principal stress in the material.

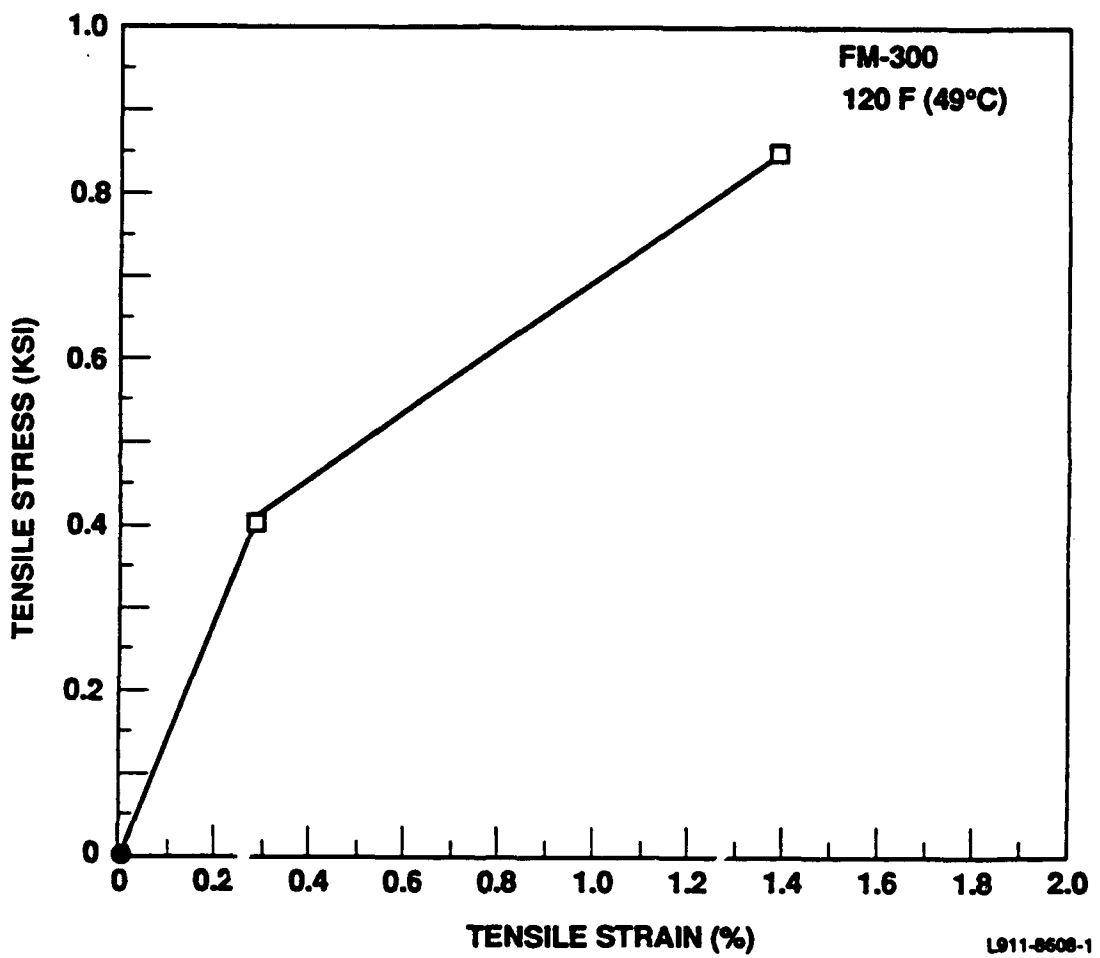


Figure 3.9. Idealized bilinear constitutive model of adhesive for finite element analyses.

The finite element results for five different conventional failure criteria are shown in figure 3.10. The failure strength is computed in terms of the five different stress parameters listed above, based on the uniaxial strength shown in figure 3.9. The data is presented as the applied load level at anticipated failure. This allows comparison with other time-dependent creep failure data in figure 3.10. Recalling that the idealized constitutive model and uniaxial failure data chosen in this study represent relatively rapid, elastic-plastic, nonlinear loading; it is expected that the finite element predictions of failure should be comparable to short-term failure data from the creep failure experiments. Hence, the finite element predictions are shown on the vertical axis for elapsed time equal to zero hours. Clearly none of the failure criteria agree well with the experimental trends. The discrepancy described above highlights the need for examining non-conventional failure criteria. Detailed comprehension and modeling of the actual physics of failure is a complex task and is well beyond the scope, intention and purpose of this program. Thus, this effort was limited to seeking a semi-empirical model which can numerically correlate with the experimental data without having to model the failure processes. Guided by the experimental observation mentioned in equation (1), five different non-conventional failure criteria were explored. In accordance with equation (1), failure is defined when the applied load causes any one of the five stress components defined above to reach the uniaxial tensile failure strength. While this definition is arbitrary in nature and without any explicit physical basis, it can nevertheless provide an efficient numerical optimization criterion if any of these non conventional criteria agree with the experimentally observed failure data.

The failure predictions due to the non conventional failure criteria are shown in figure 3.11. Clearly the criterion that comes closest to agreeing nominally with the experimental data is the octahedral shear stress criterion which can be stated as:

$$\sigma_{oct} \equiv \sigma_{nom} \quad (2)$$

Noting that the Octahedral shear stress is related to the Von Mises' stress, equation (2) can also be rewritten as:

$$\sigma_{v.m.} \equiv \sqrt{\frac{3}{2}} \sigma_{nom} \quad (3)$$

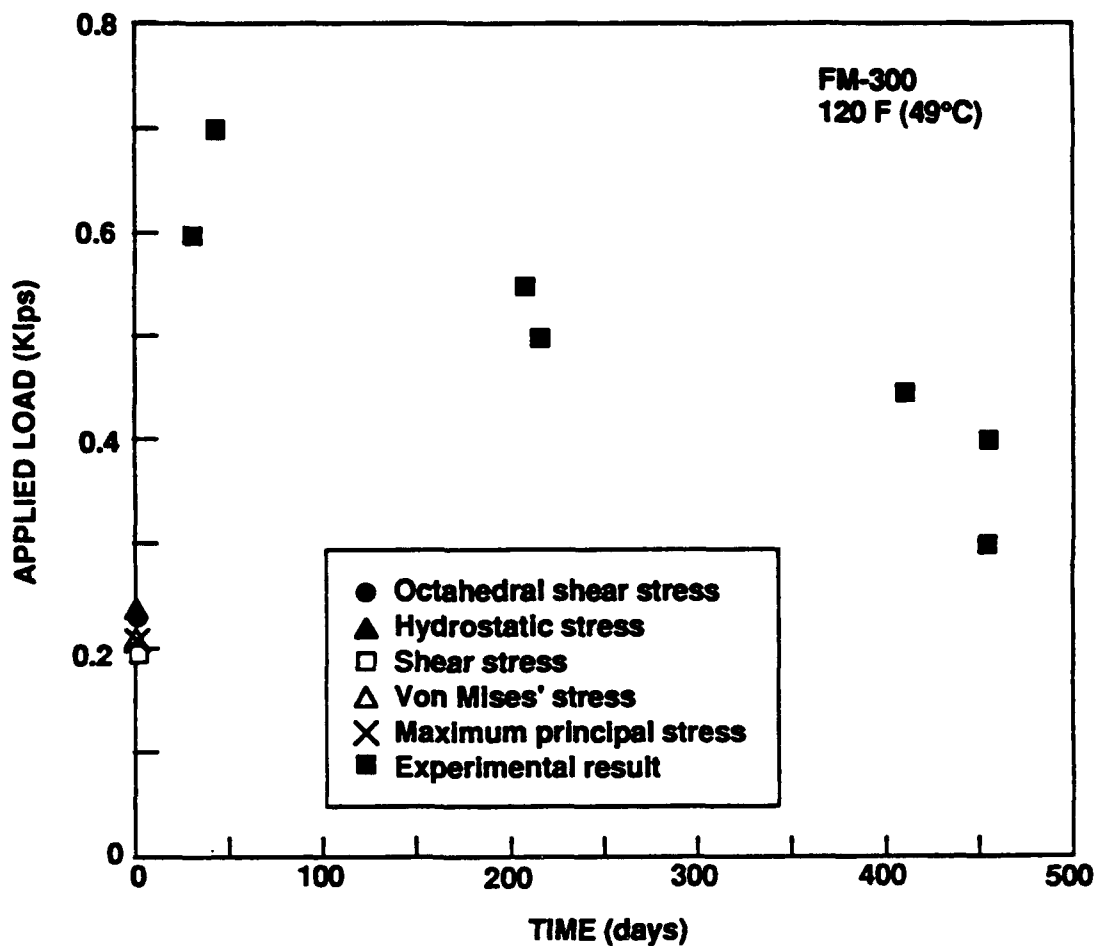


Figure 3.10. Comparison between finite element model prediction and experimental results for failure load of the quad-lap specimen.

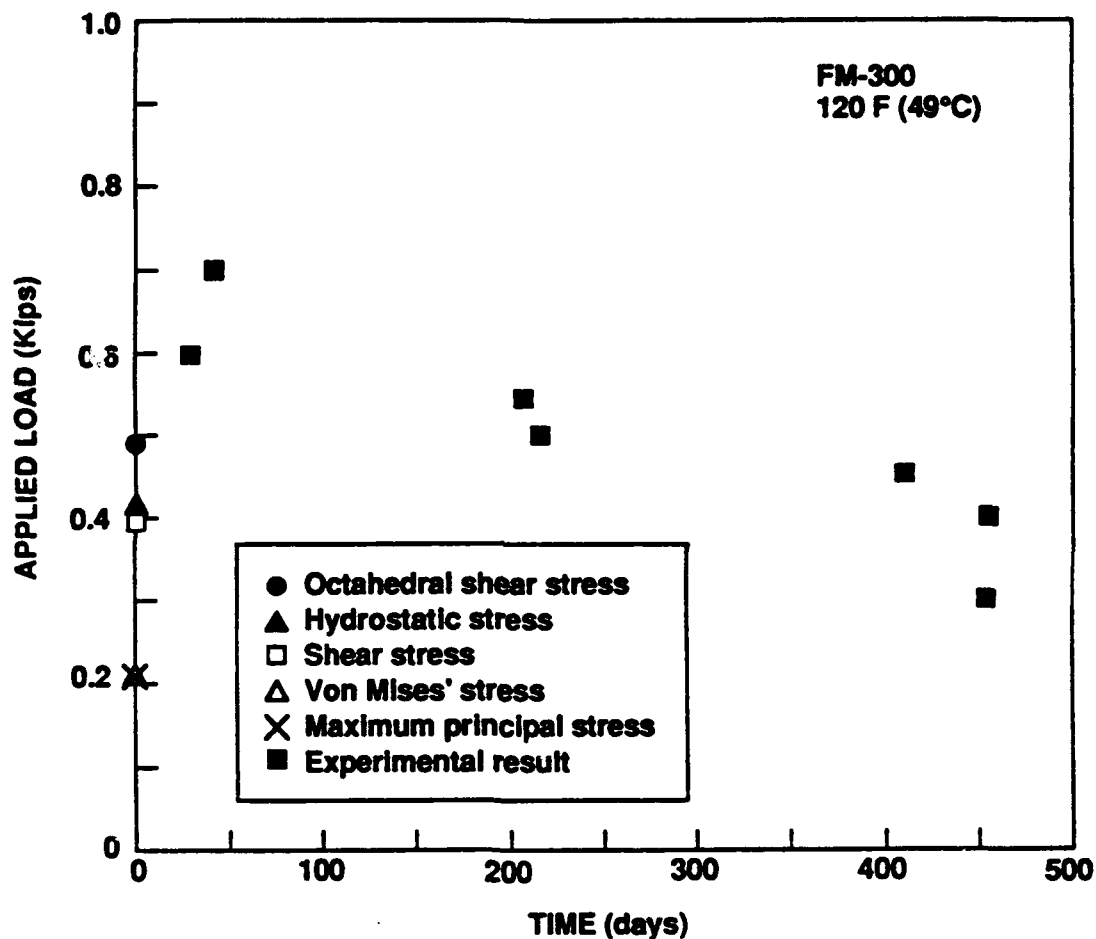


Figure 3.11. Comparison between finite element predictions and experimental results using nonconventional failure criteria.

Thus, the nonlinear finite element analysis when used in conjunction with the idealized stress-strain behavior of the adhesive and the experimental failure data, can prove useful in postulating a semi-empirical multiaxial failure model for the polymeric adhesive material used in the bonded joint. As discussed above, the utility of this failure model lies in the fact that it served as a pointer to the critical component of stress to be monitored and minimized in the parameteric and optimization studies.

3.4 Parametric Studies of Tubular Joint Design - Reducing Edge Effects

Four two-dimensional finite element models of axisymmetric tubular bonded aluminum joints were developed for parametric studies. Two types of tapered lap joints, an untapered lap joint with an external stiffening ring, and a chamfered joint were considered.

3.4.1 Finite Element Models

A type I tapered joint represents gradual thinning of the leading edge of the inner and outer tubes. The taper is always carried over the entire length of the bonded region. The type I tapered joint was studied in five configurations, with increasingly thin leading edges. The first, third and fifth steps are shown in Figs. 3.12, 3.13, and 3.14, respectively. The finite elements have been designed to be finer in areas of higher stress, and coarser in low stress regions. Quad/4 axisymmetric elements are used in most cases, but tri/3 elements were used at the two tips of the extreme tapers in step 5. Tri/3 is a two-dimensional triangular element with three nodes and six degrees of freedom. The global x and y axes shown in the figure represent the radial and axial directions of the axisymmetric structure, respectively. The inner and outer geometries are varied simultaneously for each step.

Type II taper starts with a knife edge at the leading edge of the inner and outer tube ends, but varies the distance of the taper from nothing, step 1, to the entire length of the bonded region, step 5. Step 3 (Figure 3.15) represents a taper that begins with zero thickness at the leading edge, and is full material thickness midway along the joint.

The lap joint with external ring was also studied in five configuration, in this case with increasingly shorter outer stiffening rings (Figs. 3.16, 3.17). The outer ring was as

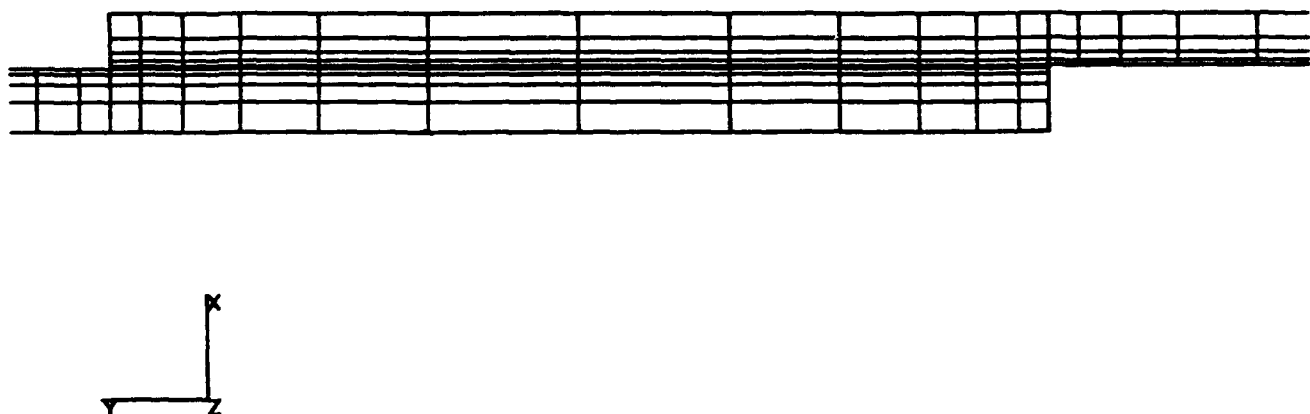


Figure 3.12. Finite element model of tubular lap joint (Step 1).

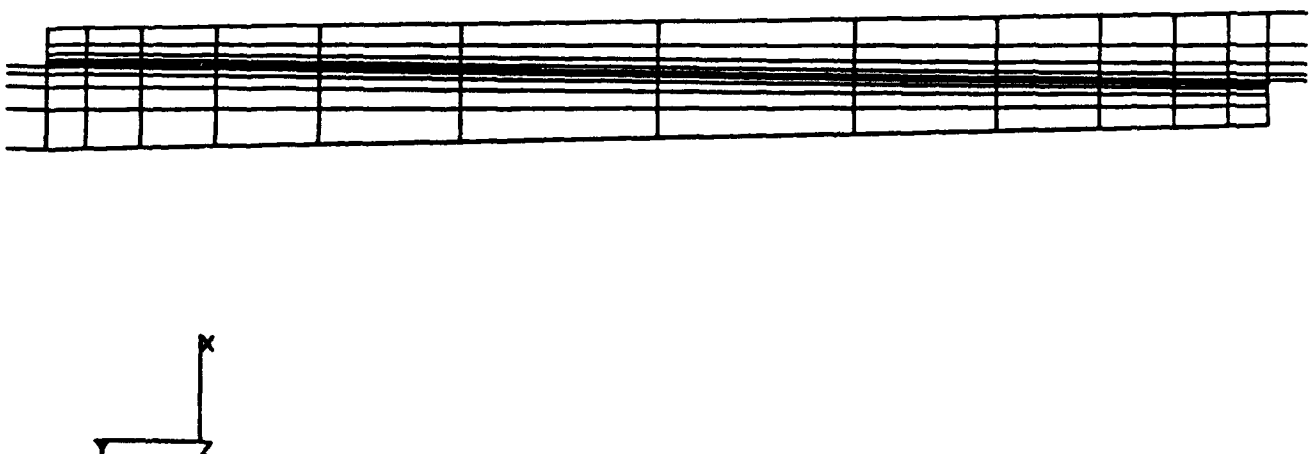


Figure 3.13. FEM model of a Type I taper tubular lap joint (Step 3).

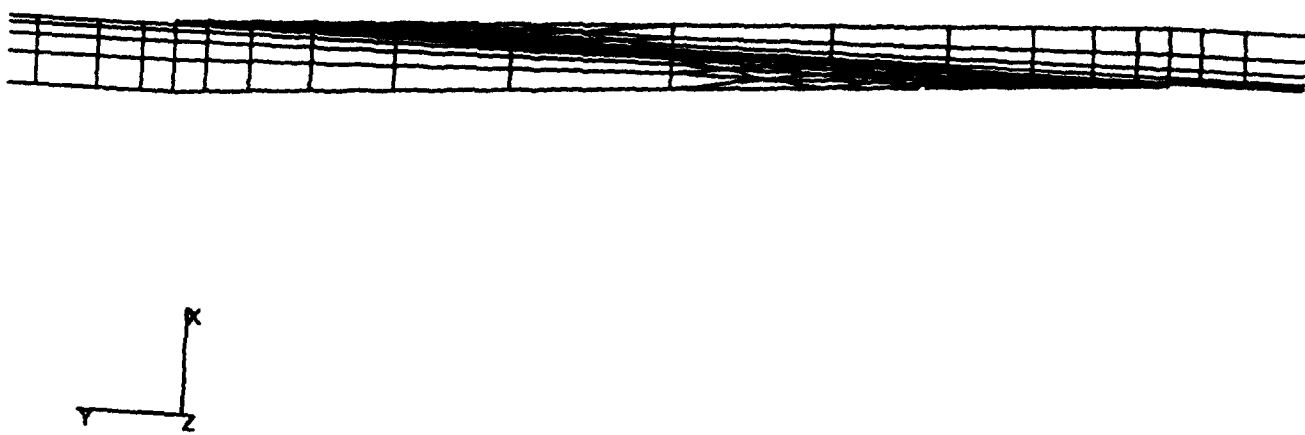


Figure 3.14. FEM model of a Type I tubular lap joint (Step 5).

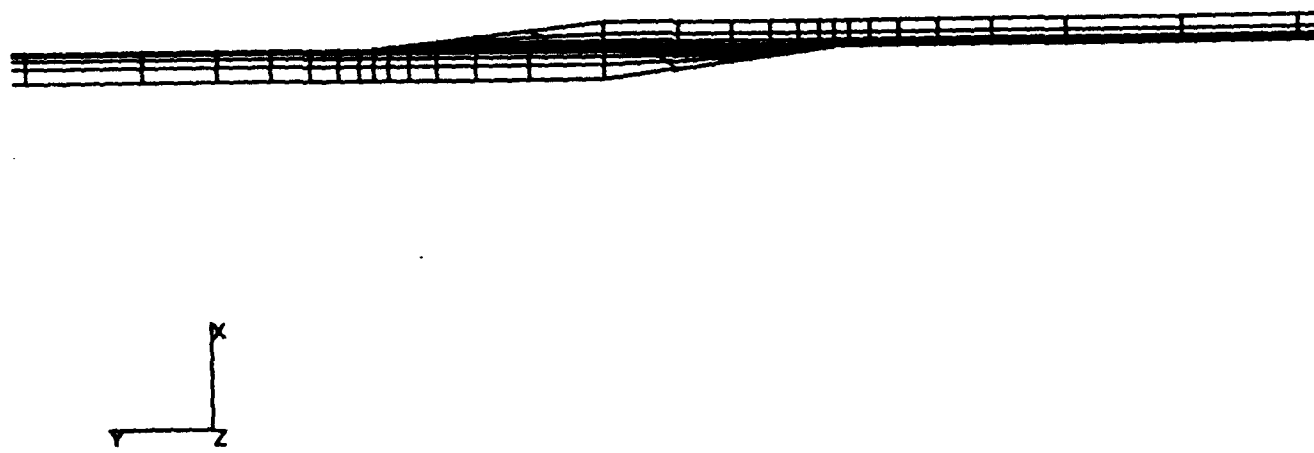


Figure 3.15. FEM of a Type II tubular lap joint (Step 3).

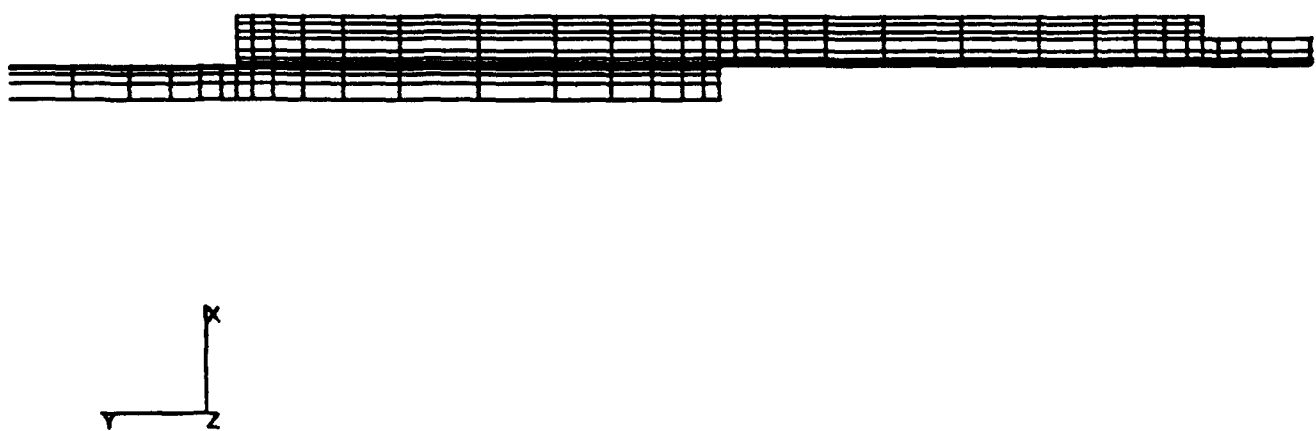


Figure 3.16. FEM of an exterior ring tubular lap joint (Step 1).

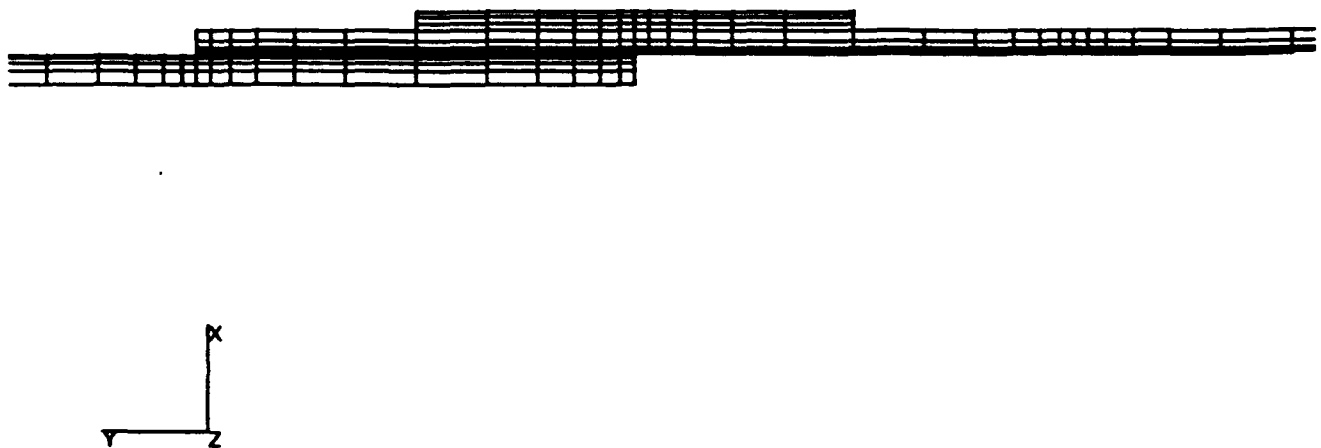


Figure 3.17. FEM of an exterior ring tubular lap joint (Step 5).

thick as the tube, and always centered over the inner end of the adhesive joint. Quad/4 elements were used for the finite element mesh.

The chamfered joint has a chamfer, or relief of the inside edge of the tube ends of both inner and outer tube. The overlap between the inner and outer tube was varied in 5 steps, from no chamfer (step 1), to chamfers occupying 1/3 of the bond line length at each end (step 5, Figure 3.18).

Displacement geometry constraint was applied to the left-most edge of the inner adherend. A distributed load of 11.7 psi was applied to the right-most edge of the outer adherend, to simulate a 1 lb load on the joint in all cases.

3.4.2 Parametric Study Results

The principal results of the type I taper analysis are shown in Figure 3.19. The distribution of the Von Mises' equivalent stress acting along the middle adhesive layer is plotted as a function of distance along the bond line. High sigma e concentrations are found at both sides of the joint for most of the configurations (step 1 through 4). There is relatively low stress acting in the center of the joint, and therefore a significant stress concentration factor ($\sigma_{\text{max}}/\sigma_{\text{min}}$) for these configurations. It is difficult to calculate the load bearing capability of a joint with high SCF, since the effective area of the joint is much smaller than the physical area. In addition, when such joints are highly strained rapid overload failures are much more likely. Note, however, that with a full taper (step 5), the stress concentration is quite low, and the center of the joint is now carrying a significant load. This joint can be easily modeled, since its load bearing capacity is very nearly $\sigma_E * \text{joint area}$.

Results from the type II taper studies, shown in Figure 3.20 , are very similar. The stress concentration at the edges of the joint decreases as the length of the taper increases. In this case, however, there is a significant reduction in SCF by step 3, or taper halfway along the joint. This shows that it is much more important that the leading edge of the joint be reduced in thickness, so that there is less adherend material to transmit stress to the adhesive at the edge, than it is to have a uniform taper. The type II taper would be easier to achieve for long overlap lengths, since it need not be carried the entire distance, and would therefore be more easily machined.

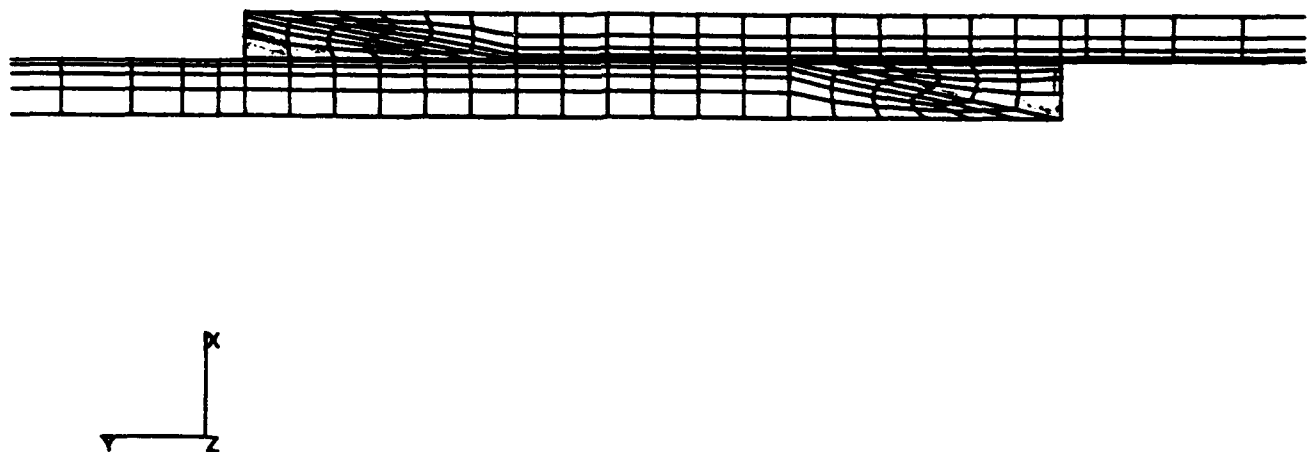


Figure 3.18. FEM of a chamfered tubular lap joint (Step 5).

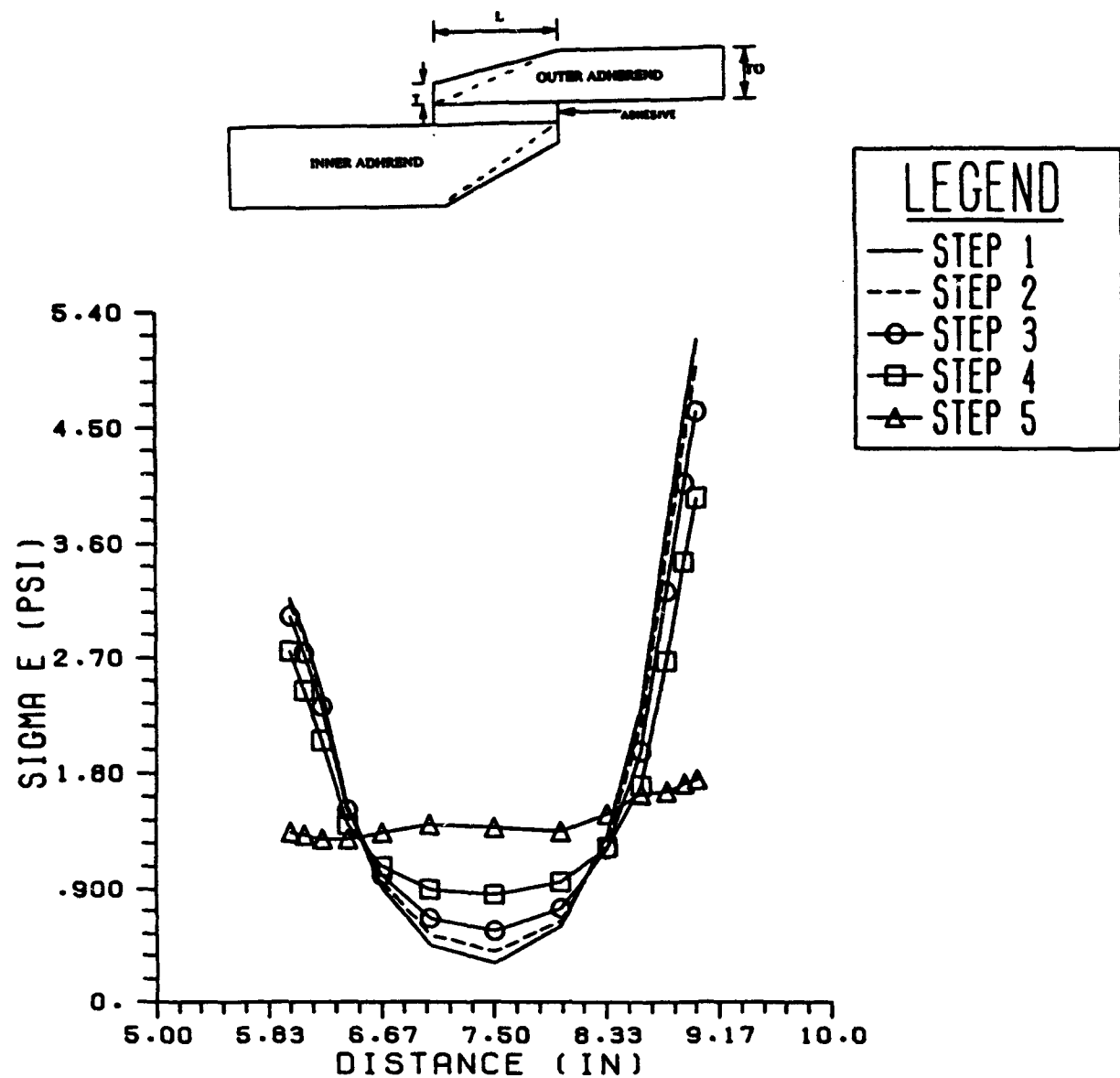


Figure 3.19. Equivalent stress along the middle adhesive layer for Type I taper lap joints.

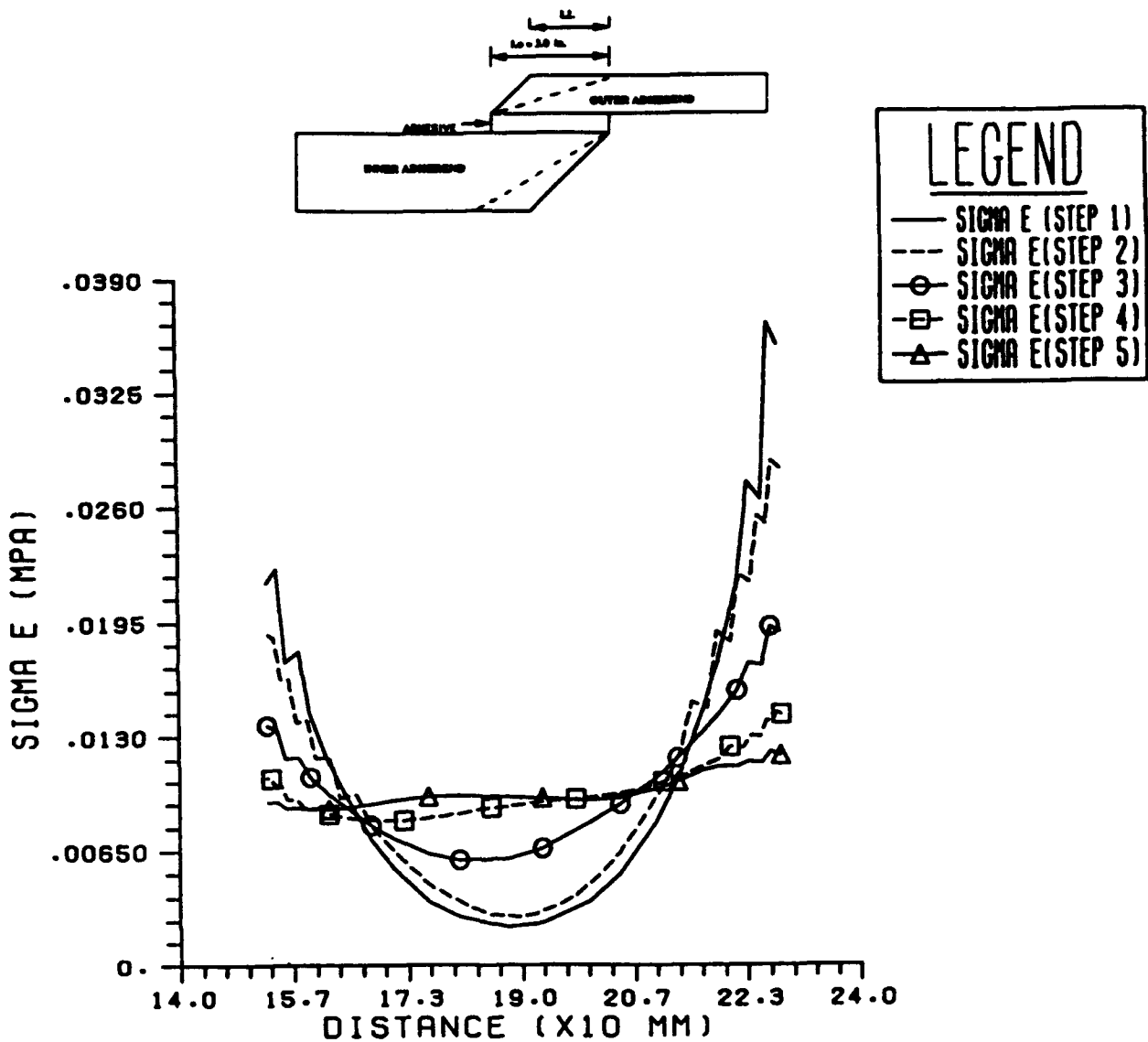


Figure 3.20. Equivalent stress as a function of distance along a Type II lap joint.

Figure 3.21 shows the results for a lap joint with external ring. It was thought that the stiffening ring would reduce torsional stresses on the joint, leading to some improvement in stress distribution. It is clear that it does not improve stress concentration, and therefore the ring has no practical value.

Chamfered joint stress distributions are shown in Figure 3.22. Here as the length of the chamfer is increased, and thus the overlap length is shortened, the SCF is reduced, not because the edge peak stresses are reduced, but because the center of the joint begins to take more of the stress as the joint area is reduced. Again, the stresses in the center of the adhesive are the highest in the joint.

3.4.3 Mesh Refinement

The results discussed above were based on a 250 element finite element model. This was chosen as a reasonable compromise between complexity (and therefore increased computer time) and accuracy. In order to verify that this choice was valid, a study using a range of mesh sizes was undertaken. By varying the mesh size, and calculating the strain energy and von Mises' equivalent stress for each model joint, a quick validity check could be performed. As the mesh size was reduced, i.e., the number of elements increased, the computer prediction should become more accurate. The strain energy and stress values vary with the number of elements, approaching a plateau as a sufficient number is reached. As can be seen from the Figure 3.23, the 250 element model used in the previous studies was well into the plateau region, and therefore is confirmed as a reasonable choice. All of the parametric studies below used the 250 element model.

3.5 Parametric Studies of Tubular Lap Joints - Joint Length and Overall Geometry

The first part of this study involved determining the equivalent stress as a function of joint overlap length for an Al-to-Al bonded tubular joint. In Figure 3.24 the stress is plotted as a function of normalized distance from the center of the joint for a variety of different joint lengths. As joint overlap decreases, the average stress increases (more stress per unit area as the area decreases). This information can be compressed and presented more simply by considering either factors of safety or stress concentration factors. The factor of safety

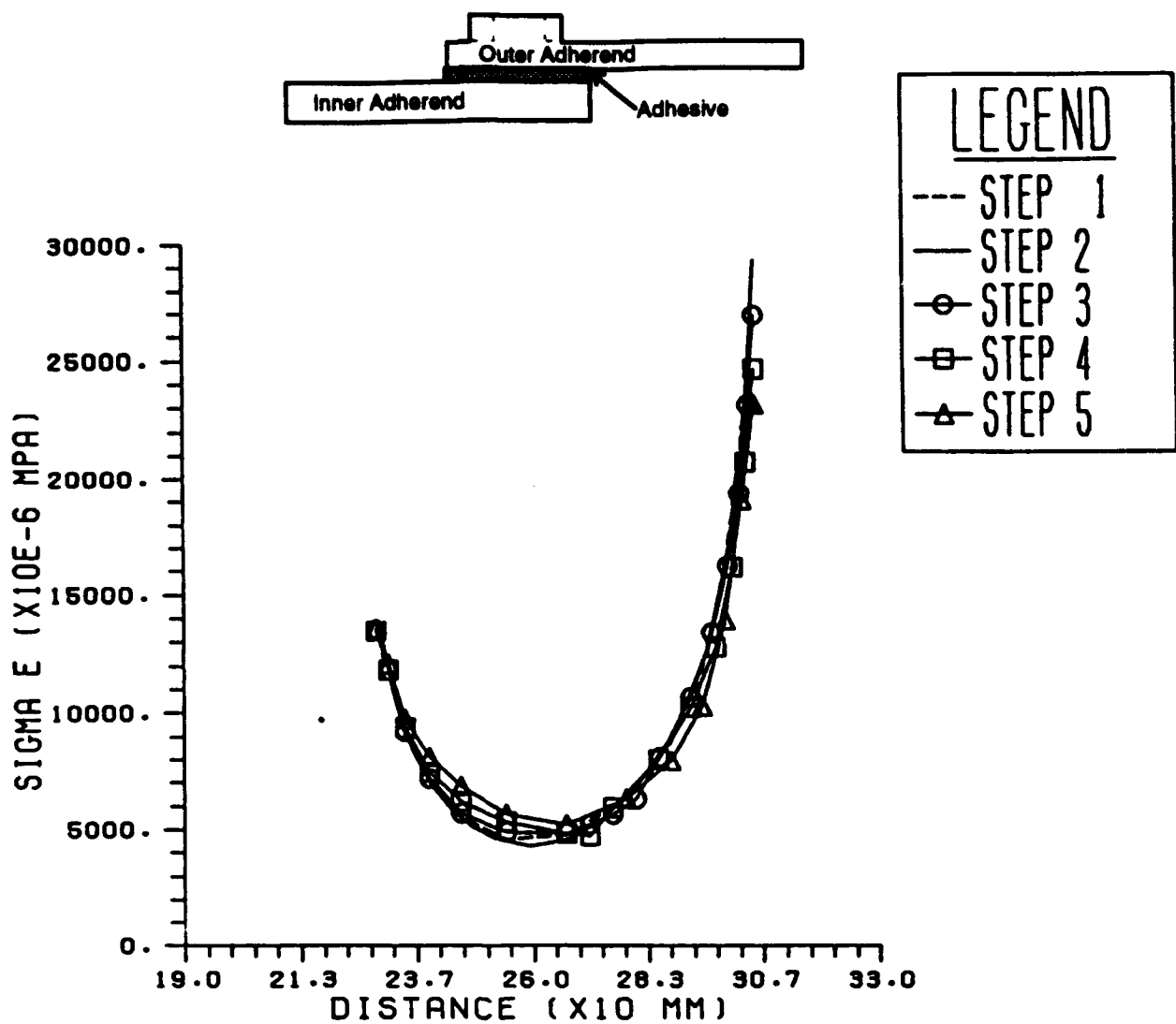


Figure 3.21. Equivalent stress as a function of distance along an exterior ring stabilized lap joint.

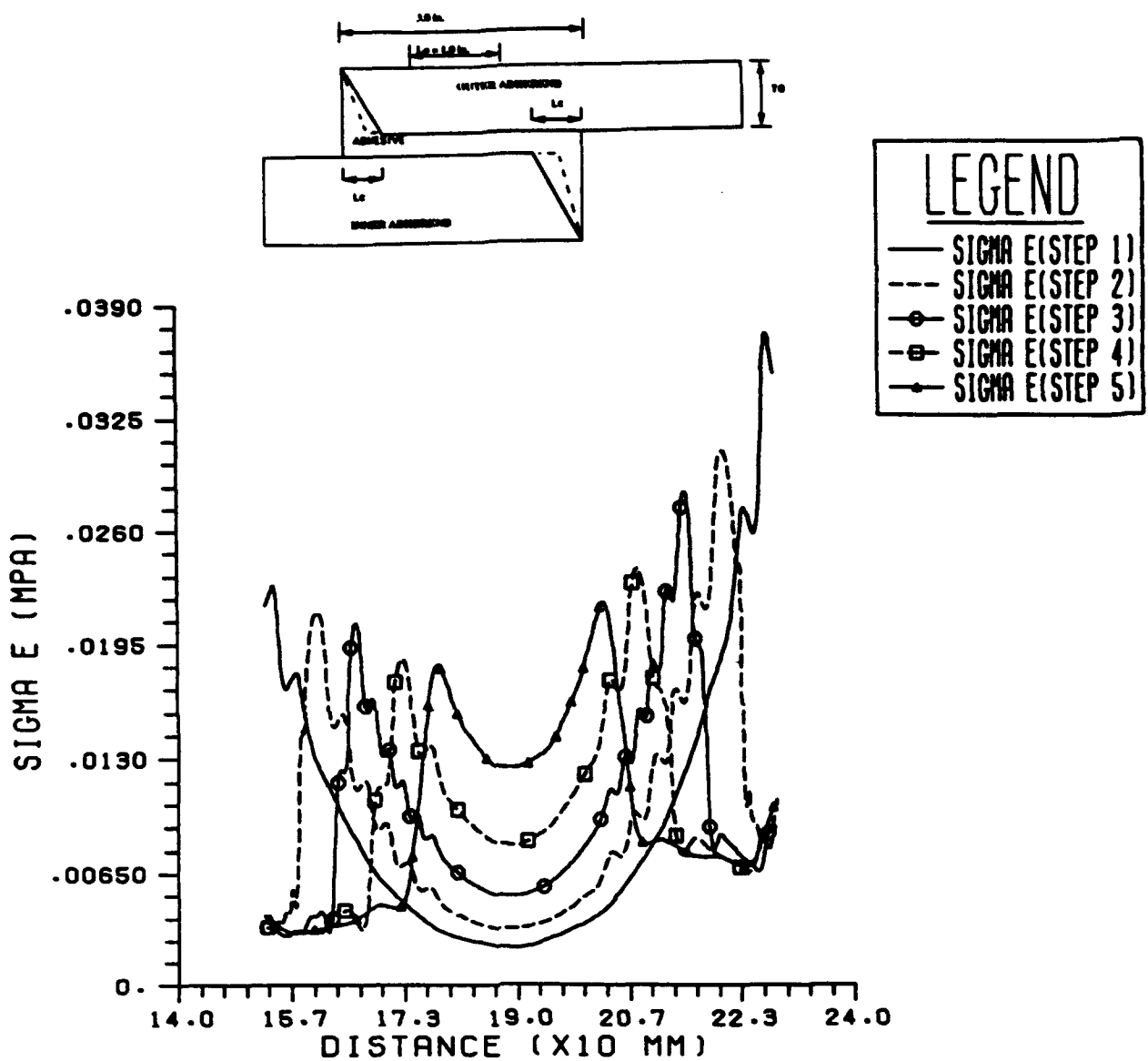


Figure 3.22. Equivalent stress as a function of distance for a chamfered lap joint.

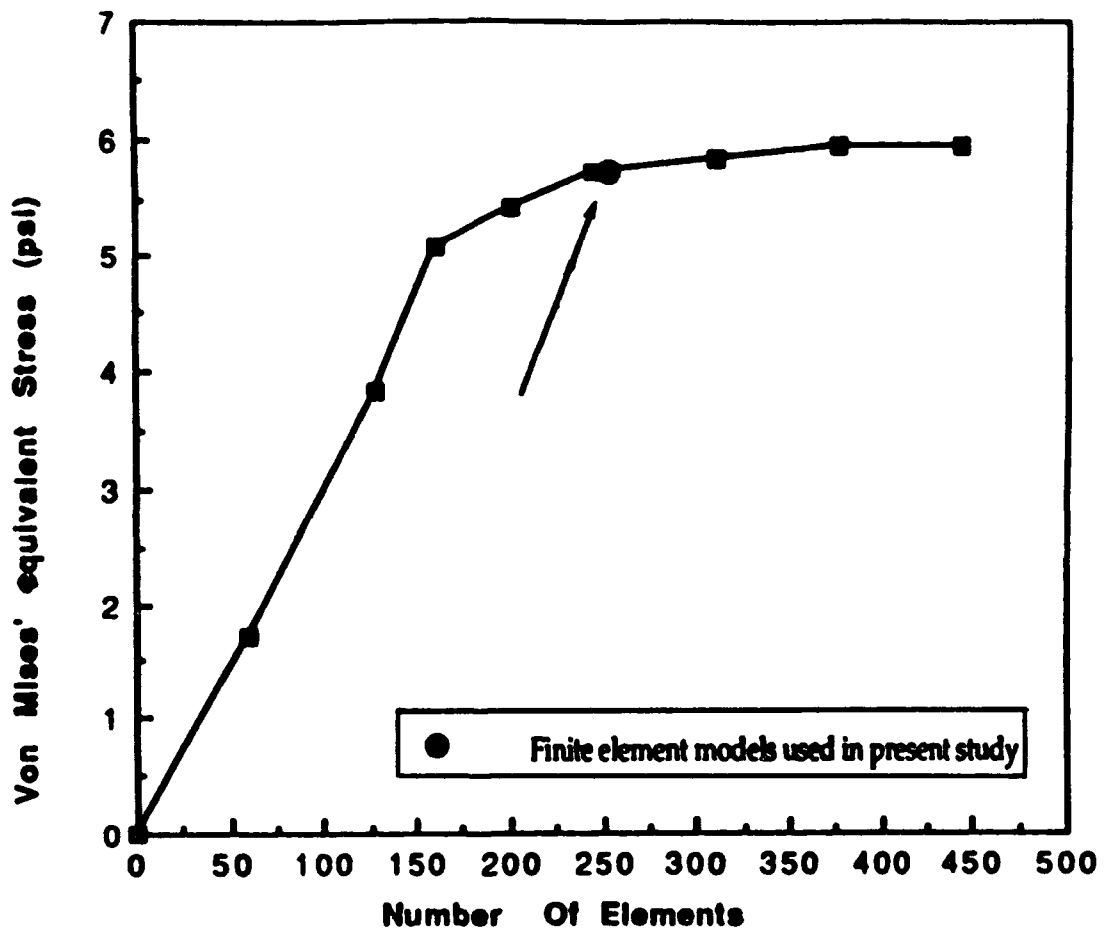


Figure 3.23. Maximum von Mises' equivalent stress in the adhesive as a function of the number of elements used in the finite element model.

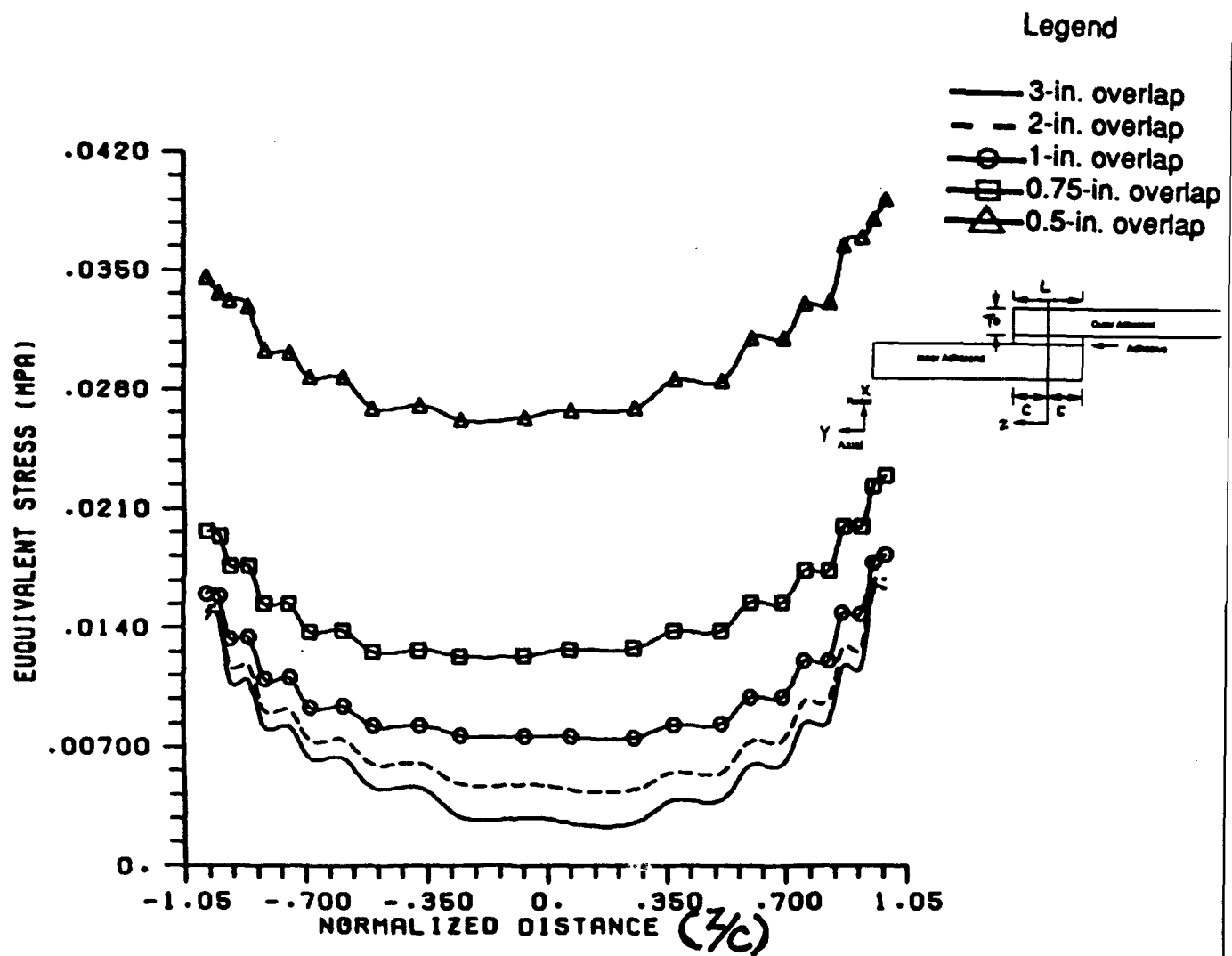


Figure 3.24. Equivalent stress as a function of position for tubular joints with differing bond lengths.

viewpoint is expressed by plotting the ratio of yield stress to maximum stress in the joint. When the two numbers are the same, i.e., the ratio = 1, then the joint is at the edge of failure.

Figure 3.25 shows the factor of safety plots for stress ratio in both the adhesive (solid line) and adherend (dotted line) as a function of overlap length. As the joint overlap increases, the maximum stress is reduced for both members, and thus the factor of safety increases. The adhesive is obviously the more crucial component, since it has a much lower factor of safety. Note that the factor of safety margin reaches a plateau for longer overlaps ($L/T_0 > 12$), since the stress concentration at the ends of the joints is still relatively high while most of the joint has low stresses and contributes very little to strength.

An alternative viewpoint uses stress concentration factors. These are ratios of the maximum equivalent stress to the minimum equivalent stress in either the adhesive or the adherend. The ideal joint will have no stress concentrations, so the ratio will be one. If this were the case, the entire joint area would equally bear the load, and the capacity of the joint could easily be calculated from the adhesive's properties and the area of the bond.

Figure 3.26 shows stress concentration factor plots as a function of joint overlap length to adherend thickness ratios for both adhesive and adherend. In this case they increase in the adherend when the overlap length is short, but decrease in the adhesive. The point where the two curves cross, i.e., the mutual lowest point, could be considered the joint with optimum load bearing properties, since the maximum area in the joint is involved in carrying the load. The stress concentration factor at this point can be used as a factor, related to the effectiveness of the joint, to adjust the load limit calculation. The carrying capacity of the joint can then be easily calculated by multiplying the area by the shear strength of a unit area bonded joint, and dividing by the stress concentration factor for this overlap length.

Adding a taper to the joint as an independent variable adds considerable complexity to the analysis. The study examining degree of taper described above featured joints with a fixed 3 in. overlap length. Figure 3.27 shows the stress concentration factor in the adhesive as a function of degree of taper (expressed as a ratio between remaining thickness/total thickness or taper length/total length) for the two taper types. In Taper I joints stress concentration factors increase linearly as the thickness of the thin section increases, which means that only the "knife-edge" is truly effective in reducing peak stresses in the joint. The Taper II plot shows that the taper need not extend over the entire joint length. A taper only half as long as the total joint is just as effective as the full taper.

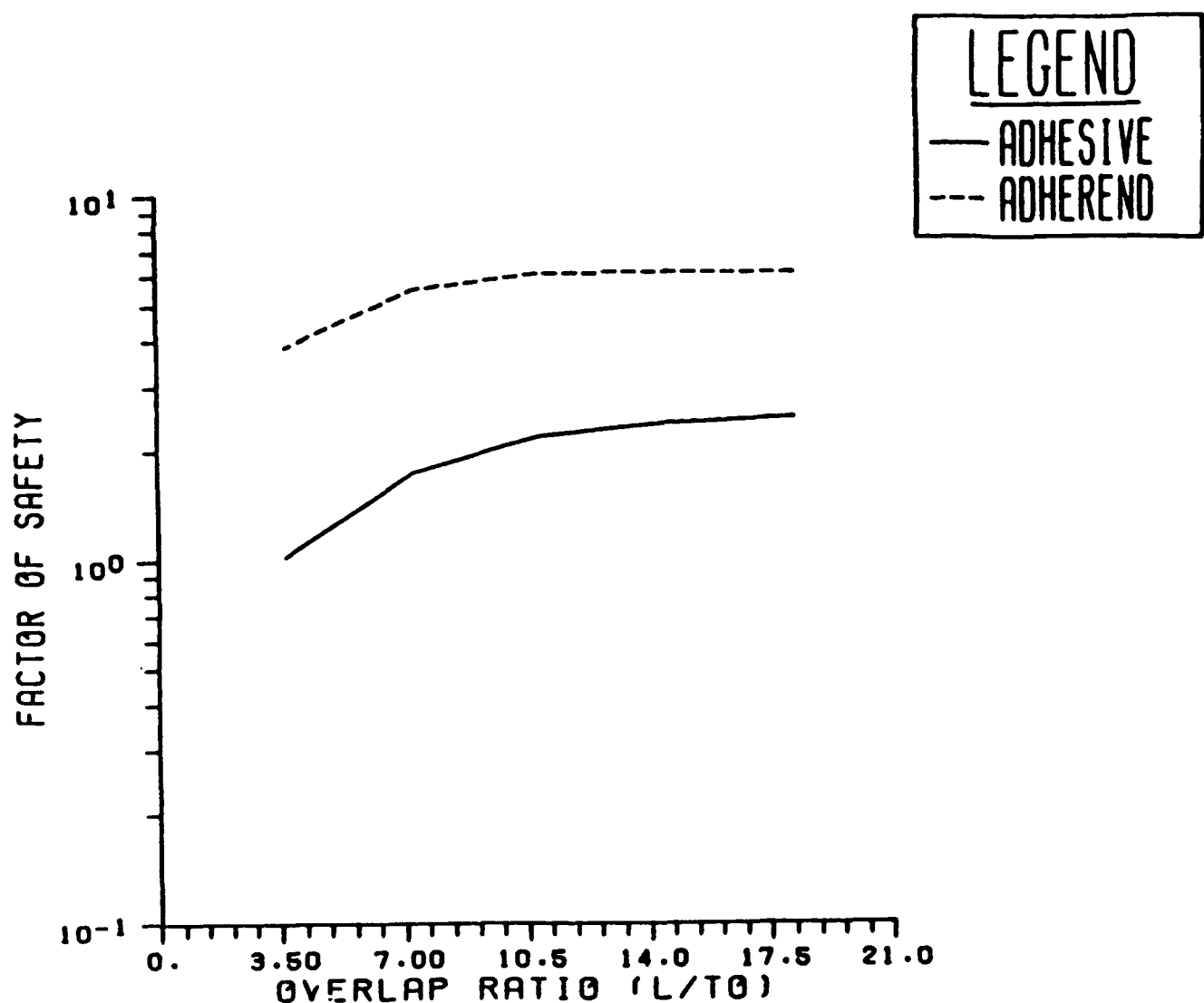


Figure 3.25. Factors of safety for an untapered tubular lap joint as a function of overlap length-to-wall thickness ratio for aluminum substrates.

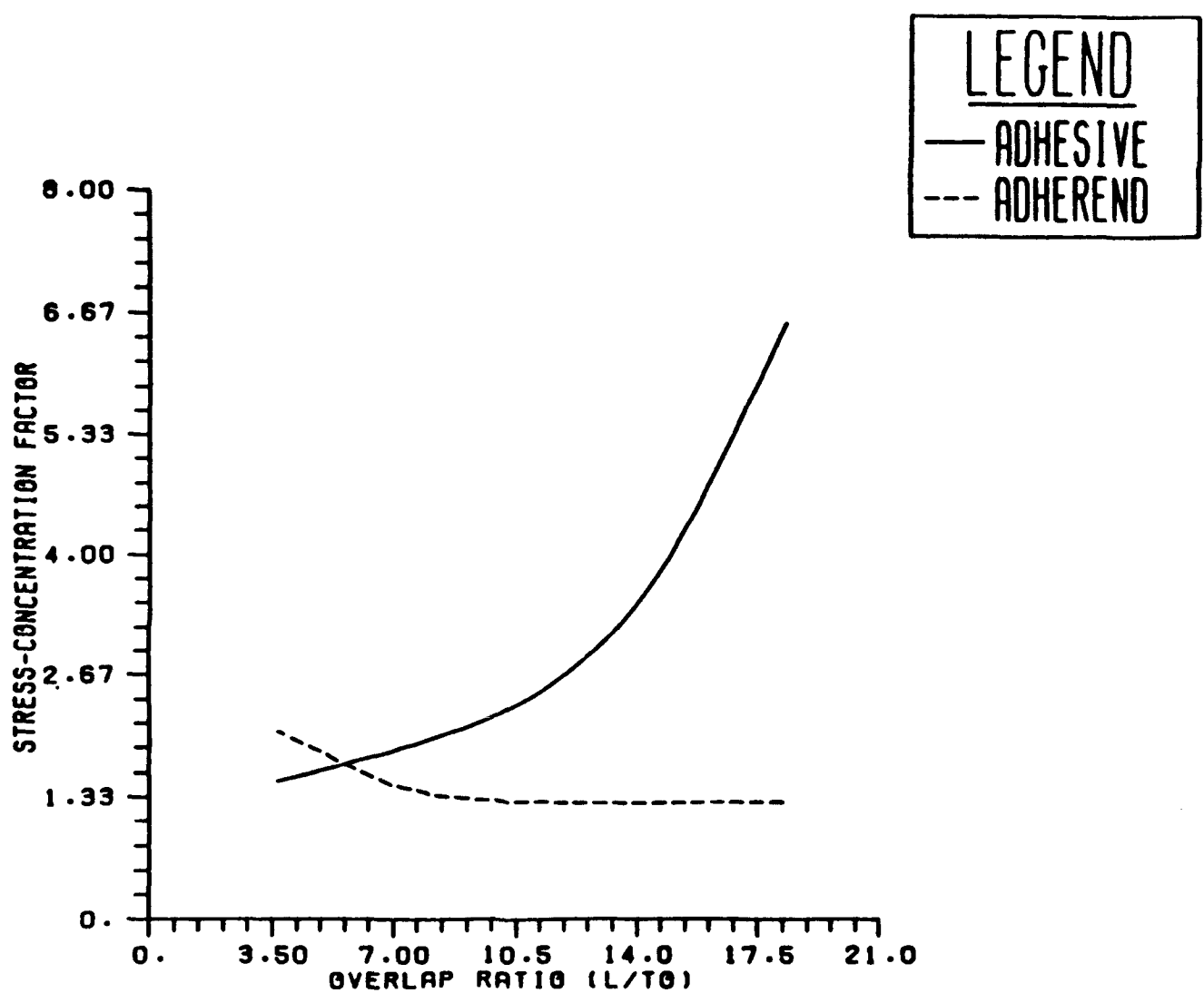


Figure 3.26. Stress concentration factor plots as a function of overlap ratio for an untapered aluminum tubular lap joint.

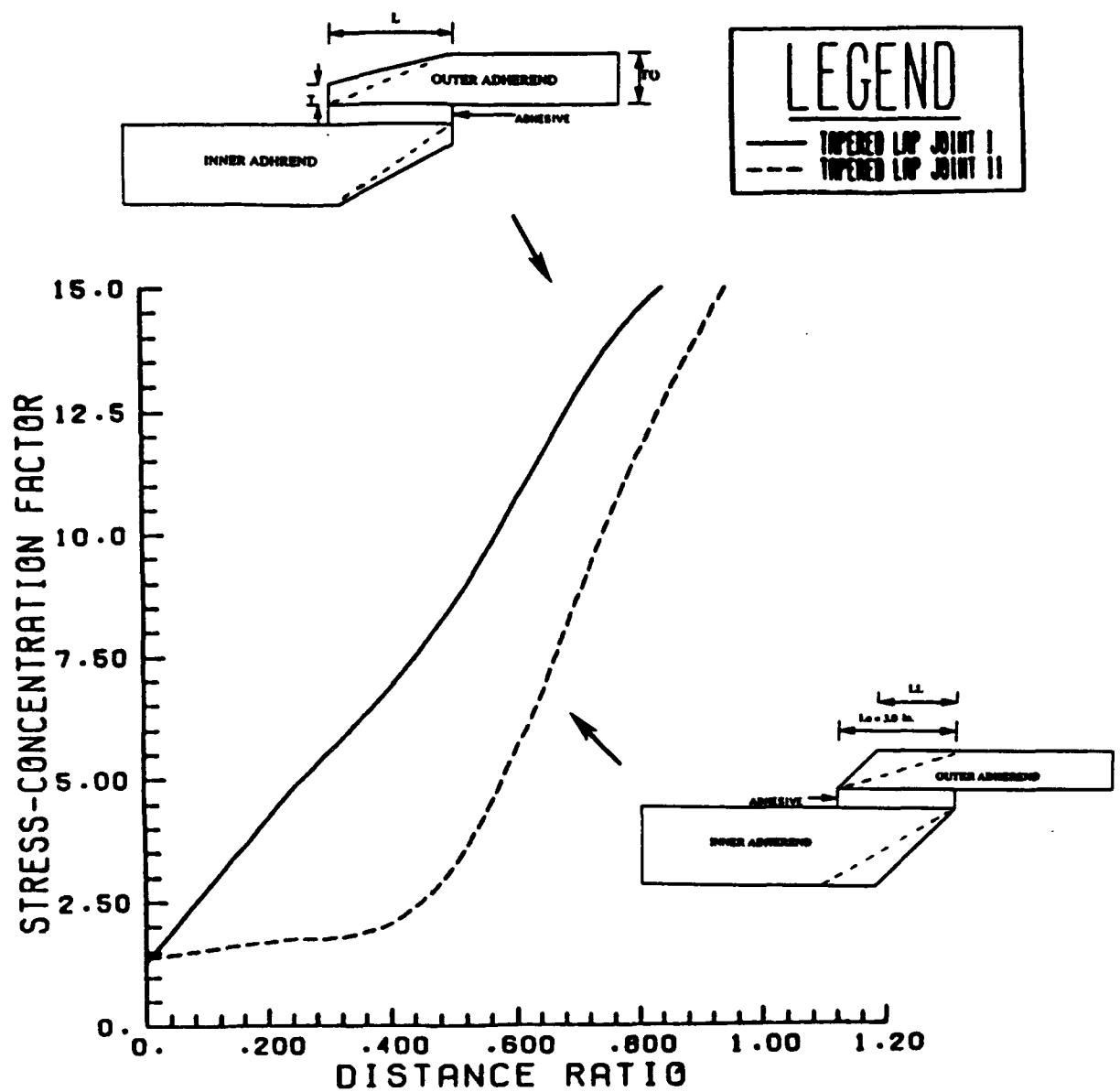


Figure 3.27. Stress concentration factor plots for the adhesive layer as a function of overlap ratio for Type I (solid line) and Type II (dotted line) taper joints.

This picture can change as the bond length is decreased. In Figure 3.28 the stress concentration factors for both adherend and adhesive are shown for a 3 in. overlap joint using Taper I. Again the optimum taper requires that the thickness of the adherend be fully removed at the end, i.e., brought to a knife-edge. However, when the overlap length is reduced, the effect of taper changes. Figure 3.29 shows the stress concentration plots for a Taper I joint with a 0.75-in. bond length. Now the taper has a relatively small effect on adhesive stress concentration, and the opposite trend in the adherend. For the shorter bond length the best taper appears to be an intermediate one. For the 0.5-in bond length Taper I joint, Figure 3.30, the stress concentration factor for the adherend is always higher than that of the adhesive, but is least in the adhesive for a straight (untapered) joint. In this case no taper is the optimum.

Figure 3.31 shows a plot which relates optimum degrees of Taper I to bond length ratios, condensing all the relevant design data into a single plot. There is an abrupt transition from the full taper to no taper as the bond length is reduced to less than 6 times the tube thickness.

3.5.1 Computer Optimization and Confirmation of Parametric Studies

In order to further examine the parametric studies, a new finite element model was formulated that would allow the computer code to iteratively seek the optimum stress-concentration reduction and most accurate mesh. This model included two degrees of freedom for computer optimization; the degree of Taper I, and the amount of chamfer. The schematic of the joint design is shown in Figure 3.32. A fixed L/T ratio was used for each run and the computer was allowed to pick its own gridding. Iterative runs were made with the program varying the degree of taper and chamfer in the search for the minimum combined stress concentration factor.

The optimum design for $L/T = 4$, i.e., 1-in. overlap using 1/4-in.-thick tube, is shown in Figure 3.33. Note that a slight taper and chamfer are used for this relatively short bond length joint. Figure 3.34 shows the computer-generated result for $L/T = 24$, i.e., a long bond length. The computer has chosen a full taper. Note that the chosen mesh is very different from the rectangular mesh used for the earlier FEM studies (Figure 3.15).

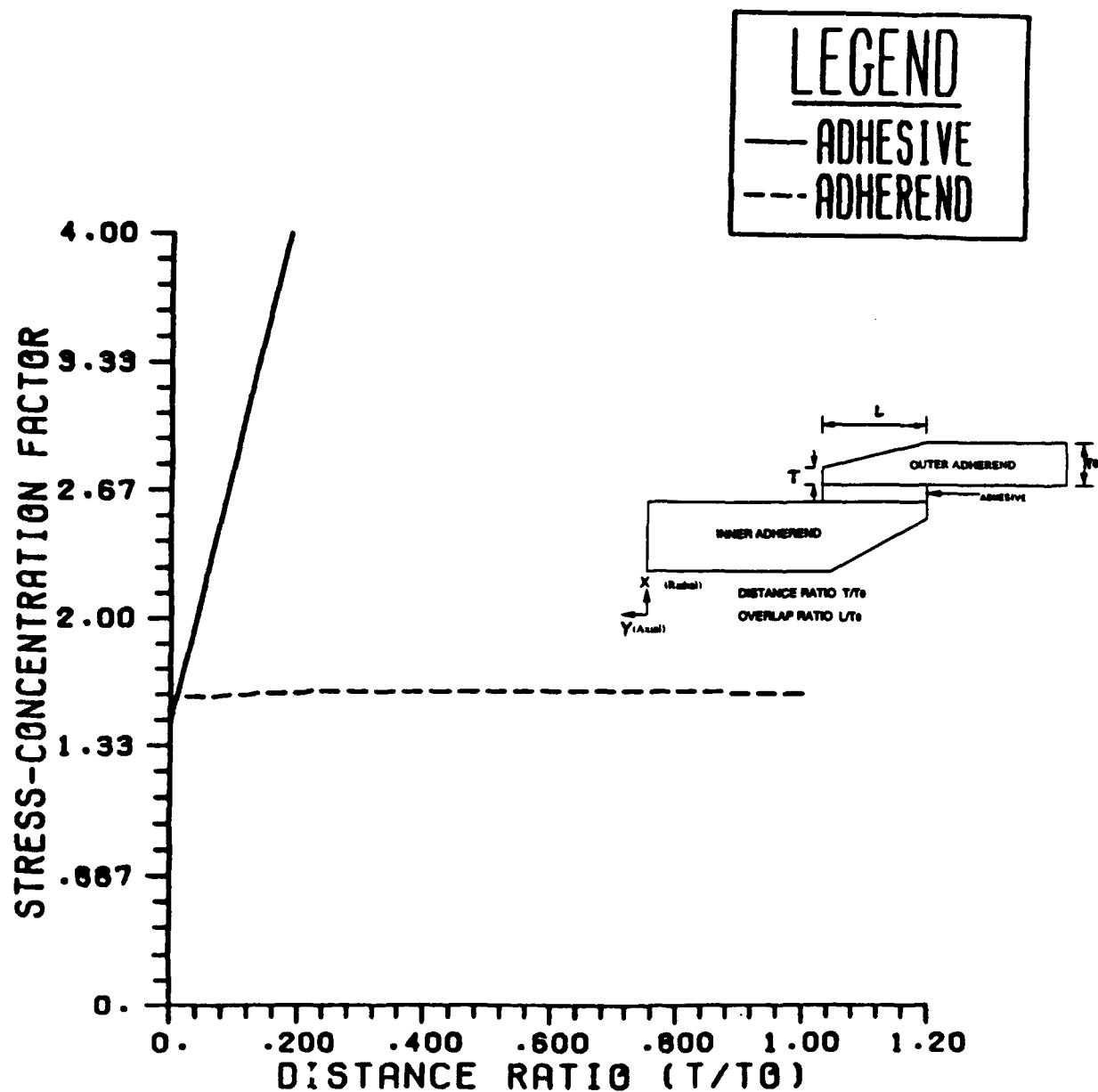


Figure 3.28. Stress concentration factors in a Type I tapered aluminum lap joint with a 3-in. overlap as a function of degree of taper.

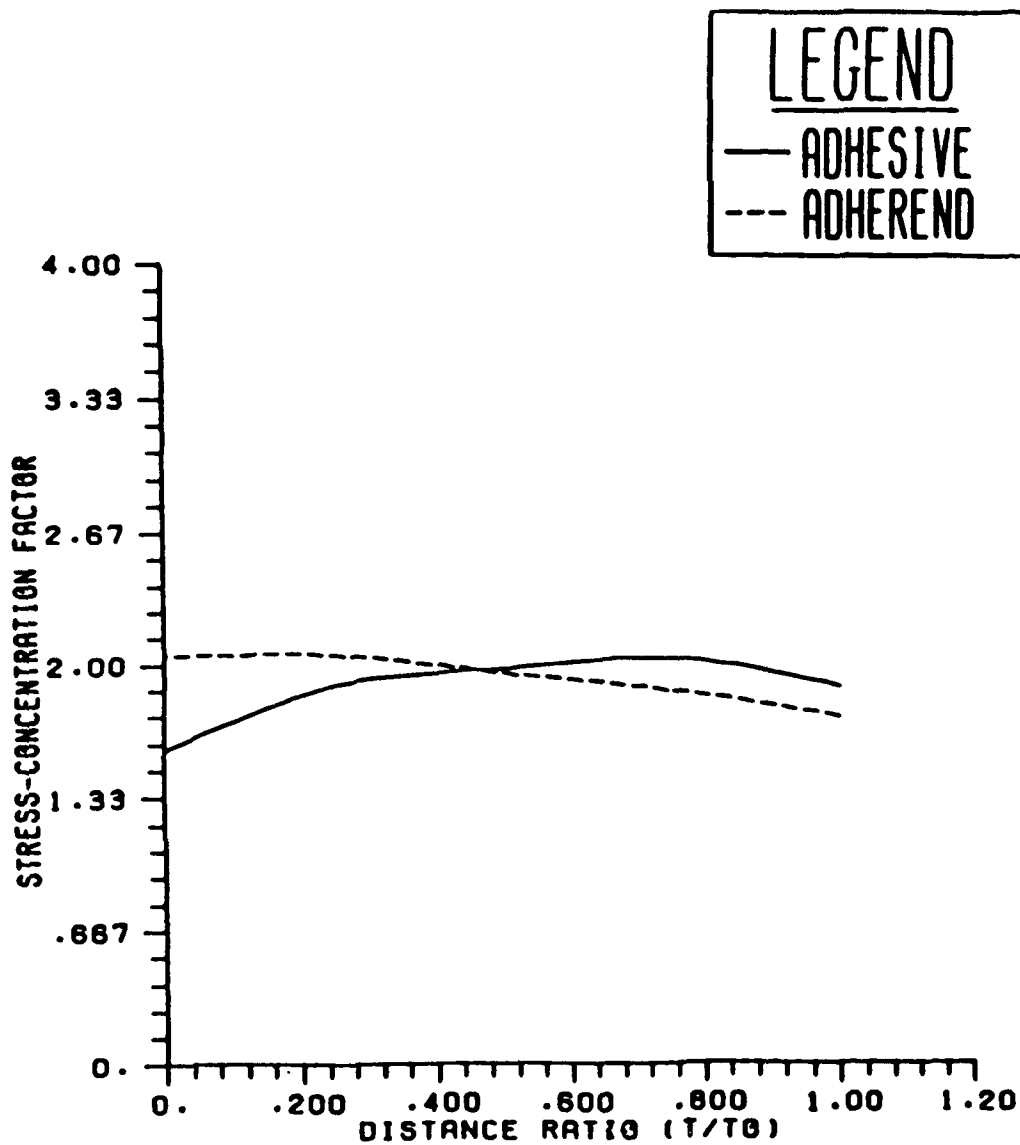


Figure 3.29. Stress concentration factor plot for a Type I taper aluminum lap joint with a 0.75-in. overlap, as a function of degree of taper.

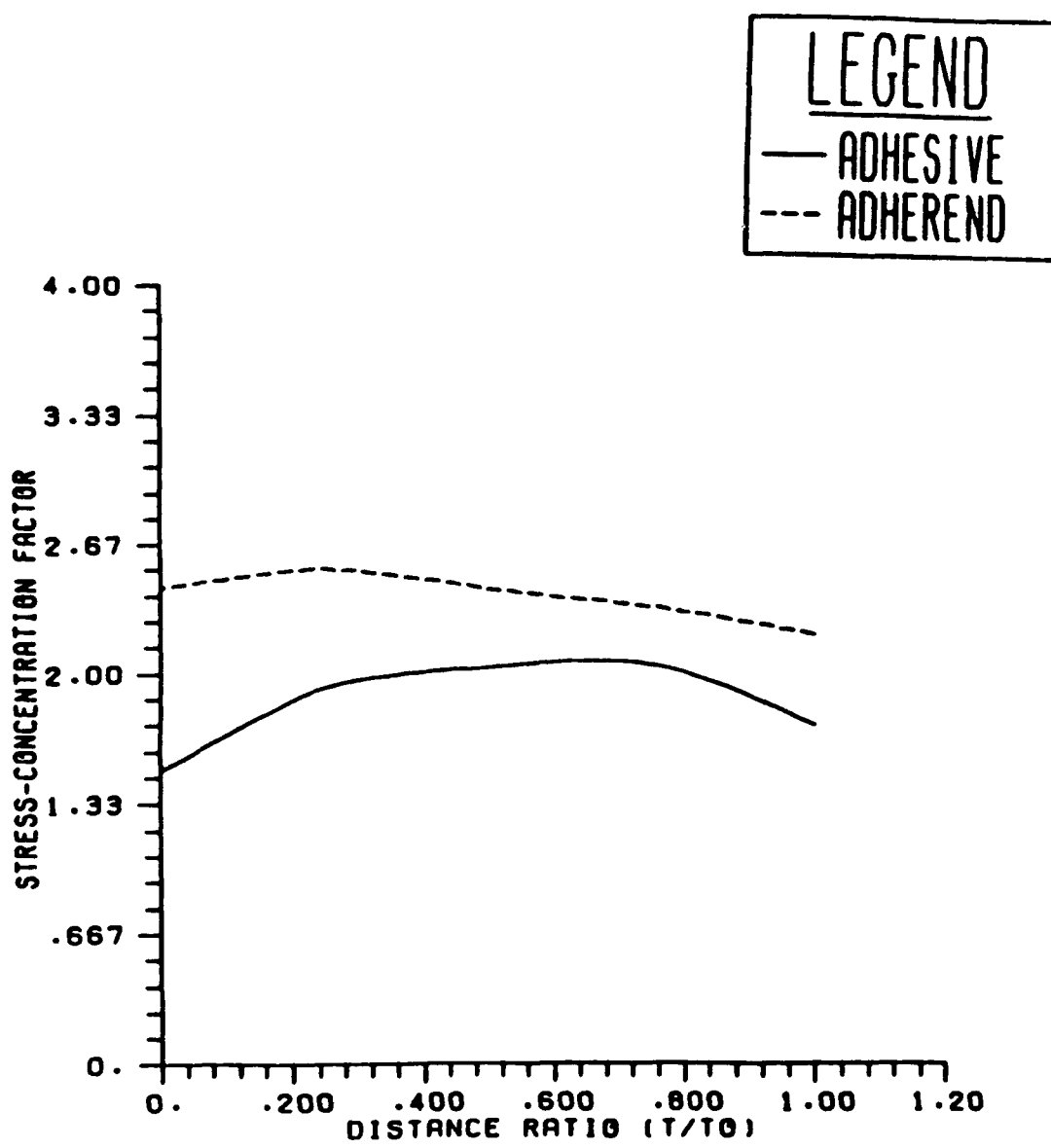


Figure 3.30. Stress concentration factor plot for an untapered tubular aluminum lap joint with a 0.5-in. overlap.

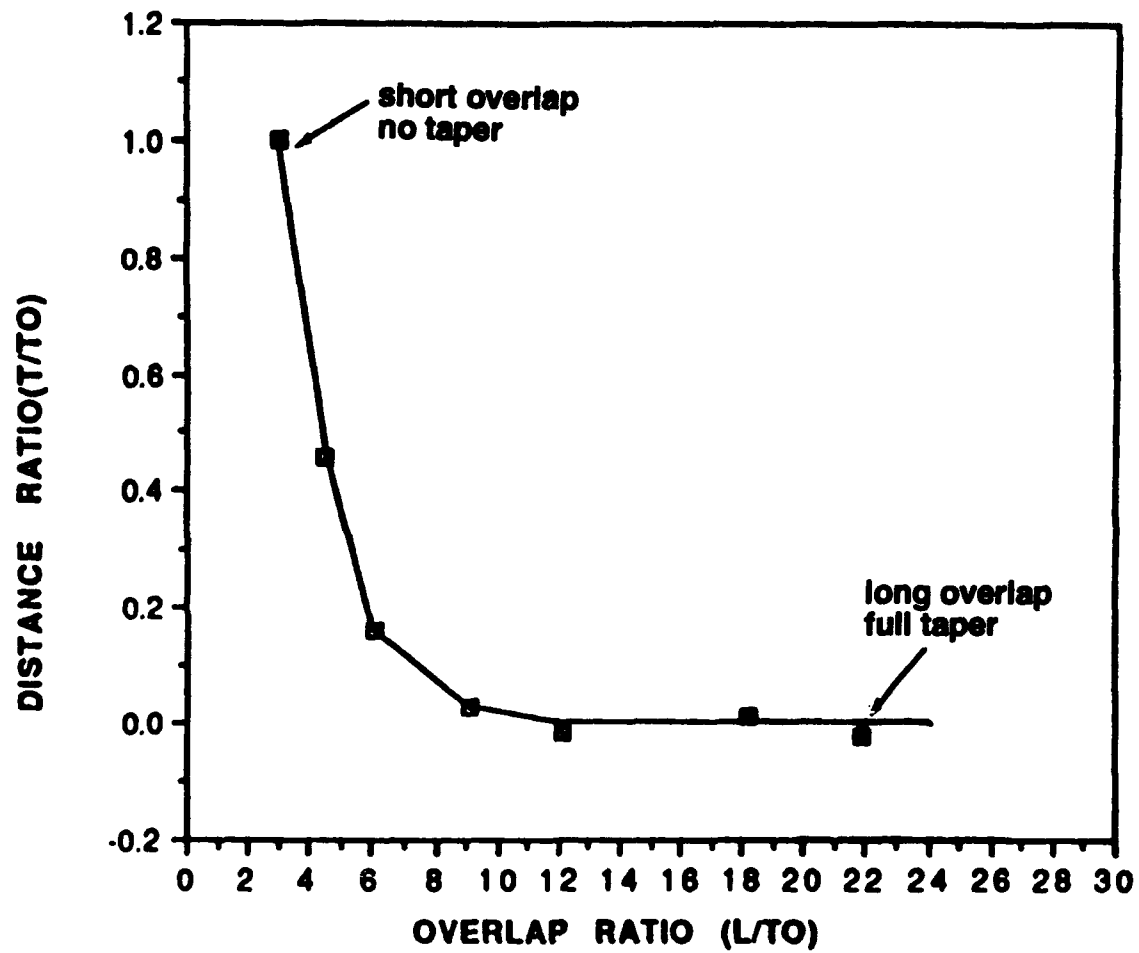
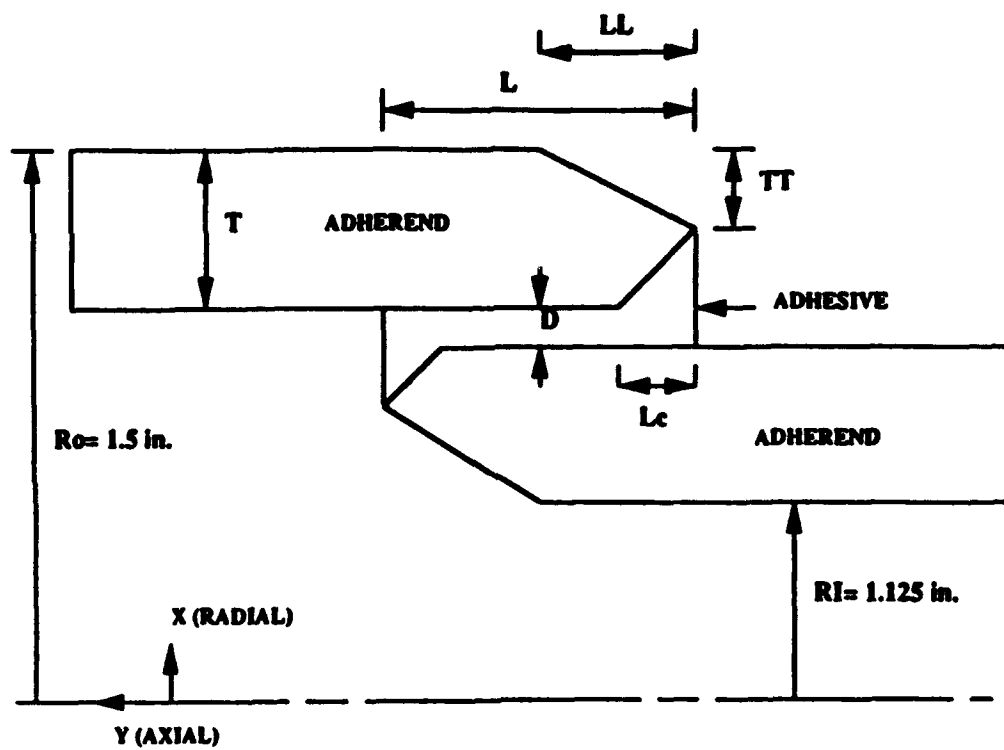


Figure 3.31. Optimum thickness of leading edge of taper-to-tube-thickness ratio as a function of the joint overlap length-to-tube-thickness ratio.



LEGENDS:

- T:** ADHEREND WALL THICKNESS
- TT:** AMOUNT OF TAPER (X-DIRECTION)
- LL:** AMOUNT OF TAPER (Y-DIRECTION)
- L:** OVERLAP LENGTH
- LC:** AMOUNT OF CHAMFER
- D:** BONDLINE THICKNESS

Figure 3.32. Schematic diagram of the joint cross section used for the computer optimization study.

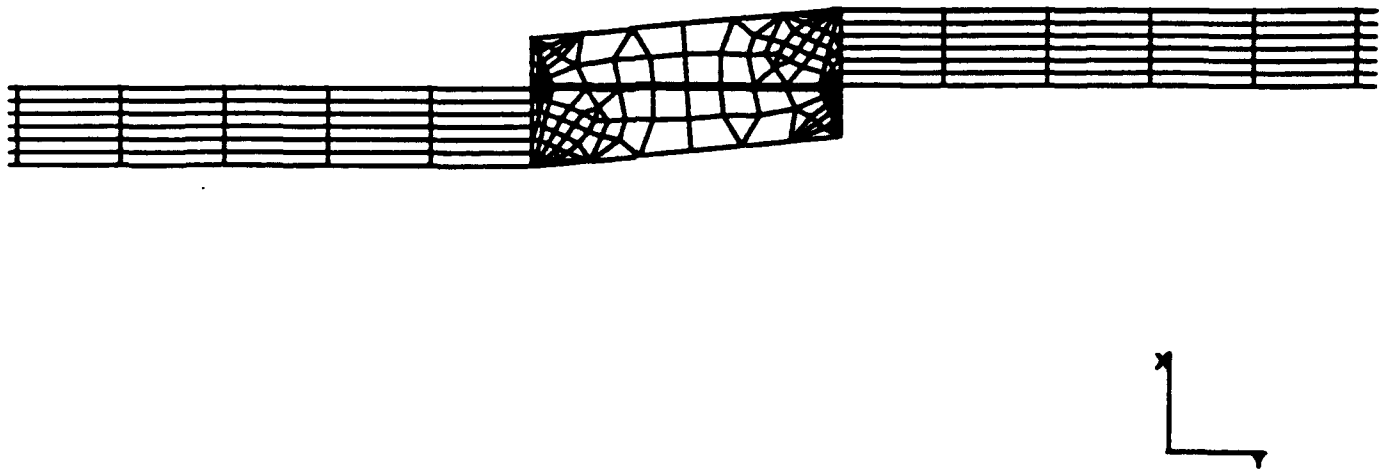


Figure 3.33. Computer optimized joint design for an aluminum tubular lap joint with overlap ratio (L/T_0) = 4.1.

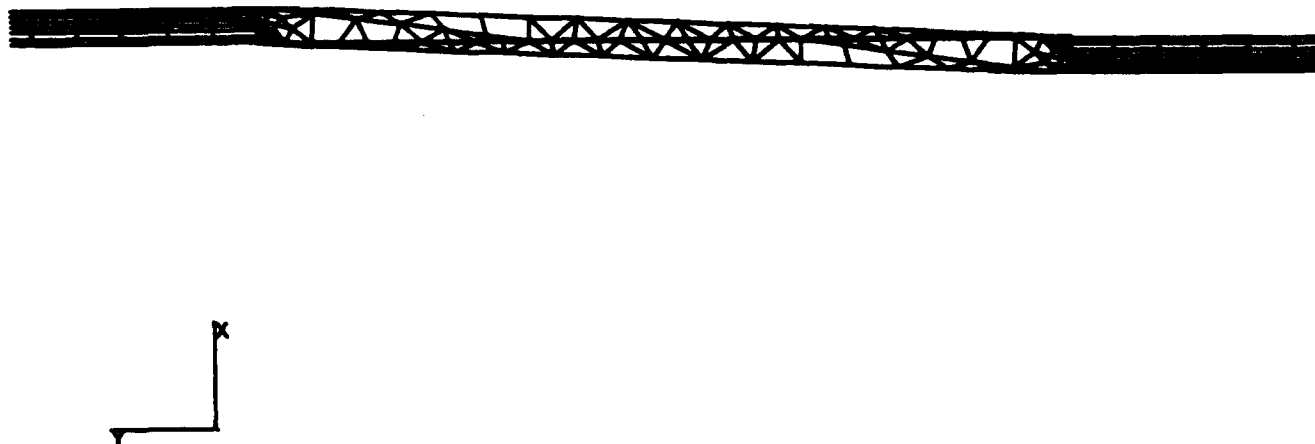


Figure 3.34. Computer optimized design for an aluminum tubular lap joint with overlap ratio (L/T_0) = 24.

Figure 3.35 shows the computer-generated degrees of taper for these two bond lengths superimposed on the parametric-study-generated curve. Despite the very different computer models used to generate the two data sets there is almost perfect agreement, which increases our confidence that the models are generating correct results.

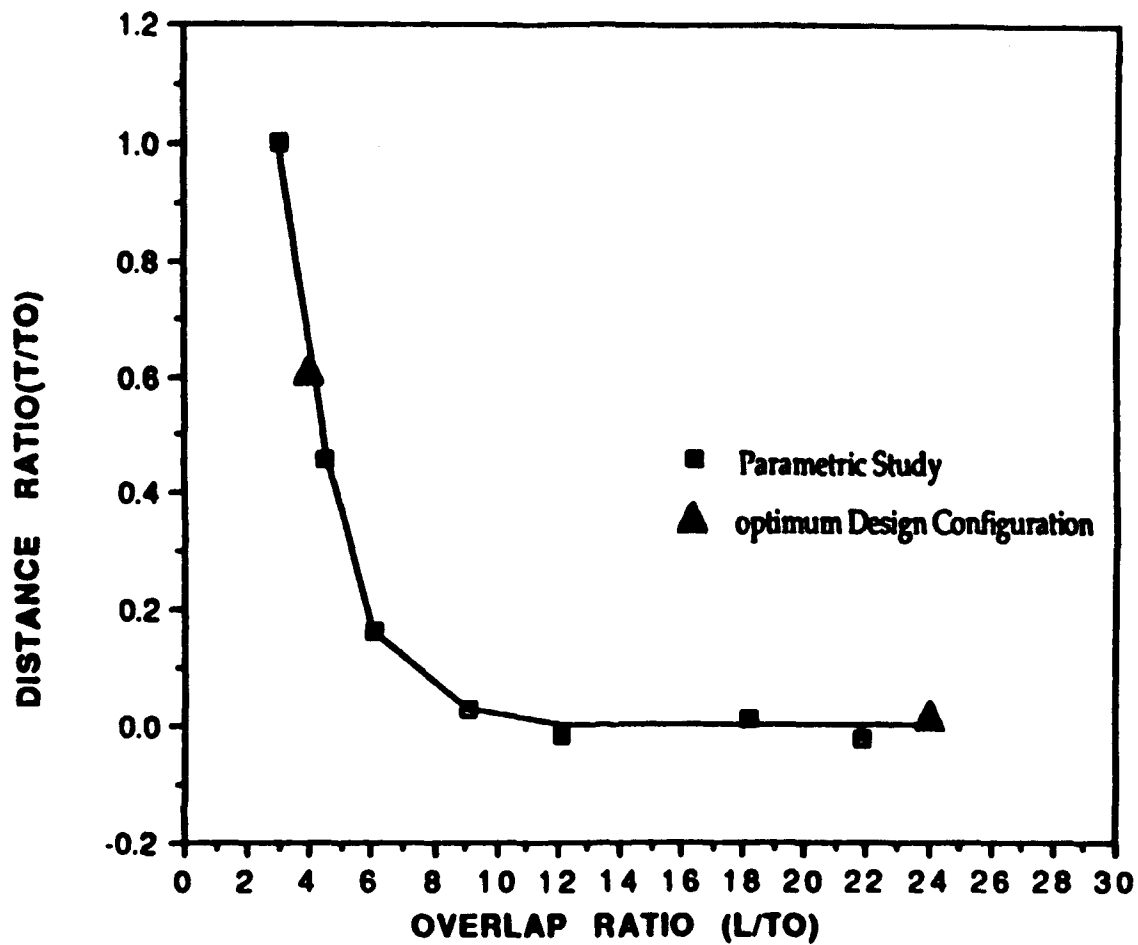


Figure 3.35. Distance-ratio-to-overlap-ratio optima for the computer-based designs compared to the parametric study results.

3.5.2 Mechanical Tensile Validation Test

Double-lap-shear specimens were designed and constructed to test FEM predictions that taper would improve ultimate joint strengths. Sets of three specimens each were constructed of 0.25-in. thick 6061-T6 aluminum with three styles of side lap pieces (see Figure 3.36), to simulate three taper conditions studied for the tubular joint. Using three types of specimens, we represented the case of no taper (0° ends, a), half taper (22.5° ends, b), and full taper (45° ends, c). The joint overlap length in all three cases was 0.25-in.

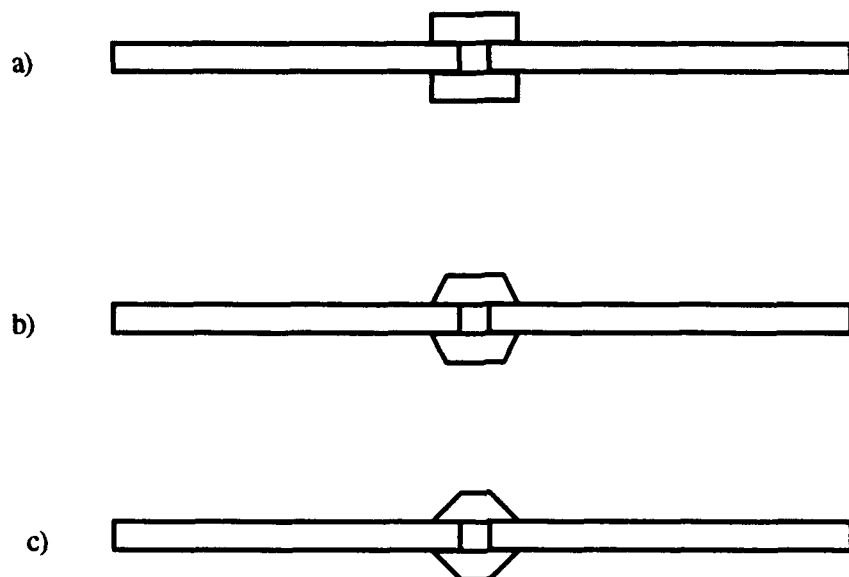


Figure 3.36. Double lap specimen configuration for taper testing.

The specimens were prepared using the PAA treatment, and bonded with Hysol EA 9394 adhesive in a simple alignment jig. After a room temperature cure of at least 24 hours, the samples were post cured in an oven at 70°C for 7 hours. Tensile testing was performed in an Instron screw-displacement load frame, using a strain rate of $0.02''/\text{min}$. The test results are shown in Table 3.2.

Table 3.2. Double-Lap-Shear Validation Test Results -Tensile Strength (psi)

	0° Ends	22.5° Ends	45° Ends
#1	3640	5540	4860
#2	4460	5590	5130
#3	5110	5960	5730

The variability in measured strengths indicates a problem with the test method. We believe that misalignment of the specimens during bonding was the main problem, and that a better jig would be needed to obtain more consistent results. As a result, the measured strengths can only be taken as a lower limit for the true shear strength of the bonds. However, these results still suggest a number of useful conclusions:

- The highest tensile strengths in this test are very similar to those measured using a traditional, thin adherend double lap shear test specimen, which indicates that the results are reasonably valid.
- The highest measured strengths for the three types of specimen do not differ that greatly. At first, we expected a greater difference between them, but given the recent results of the overlap length study described above, we now realize that for such a short bond overlap ($L/T_0 = 1$ in this case), taper should have almost no effect on bond strength, since it does not affect the stress concentration factor. Thus the results of this test thus agree with the computer model.
- The 0° end specimens show the greatest degree of data scatter. This makes sense given the non-uniform loading of misaligned specimens. Although taper should not make a significant difference in ultimate strength for a uniform shear stress, even small increases in stress concentration will be detrimental when the specimen is loaded in such a way to increase the tendency to concentrate stress.

Although this test did not produce the intended results, it was valuable in increasing our understanding of the factors that are important to joint design.

3.6 Design Guidelines

The ultimate goal of the parametric study of the tubular lap joint was to produce a set of design guidelines that could be used in "cookbook" fashion to predict the load carrying capability of a particular joint, and assist the design engineer in producing an optimum joint design. The parametric studies showed that one of the most important factors in tubular joints was the joint overlap length. They also demonstrated that type II taper could be beneficial for long joint overlaps, but a designer would need to know when to apply this

technique. Generalized guidelines for determining this threshold overlap length for a variety of geometric and material configurations were developed, based on the finite element parameteric studies. Three types of material configurations were considered; Al-to-Al joints, graphite epoxy composite-to-composite joints, and aluminum to graphite epoxy composite joints. The design plots are contour plots that further condense the stress concentration factor information..

In every case, the SCF in the adhesive and in the adherend corresponding to the optimum overall length is presented as is the corresponding maximum load-carrying capacity of the joint (based on elastic overstress of the adhesive). In summary, these guidelines can be utilized to select an optimum bonded-joint design for satisfactory performance under axial loads.

The geometry for the tubular lap joint is presented schematically in Figure 3.37. The "outer adherend" represents the tubular longitudinal stress member, and the "inner adherend" the end fitting for the hinge joint in the prototype LV/FB design. As documented in the previous section, the SCF in the joint (in the adhesive as well as in the adherend) can be reduced by introducing a taper in the adherends, as shown in Figure 3.38. A uniform stress distribution (low SCF) is considered desirable because it (i) minimizes chances of premature failure initiating at local stress concentration sites, (ii) maximizes joint utilization, and (iii) allows the use of simple closed-form design equations to compute the nominal shear stress in the joint.

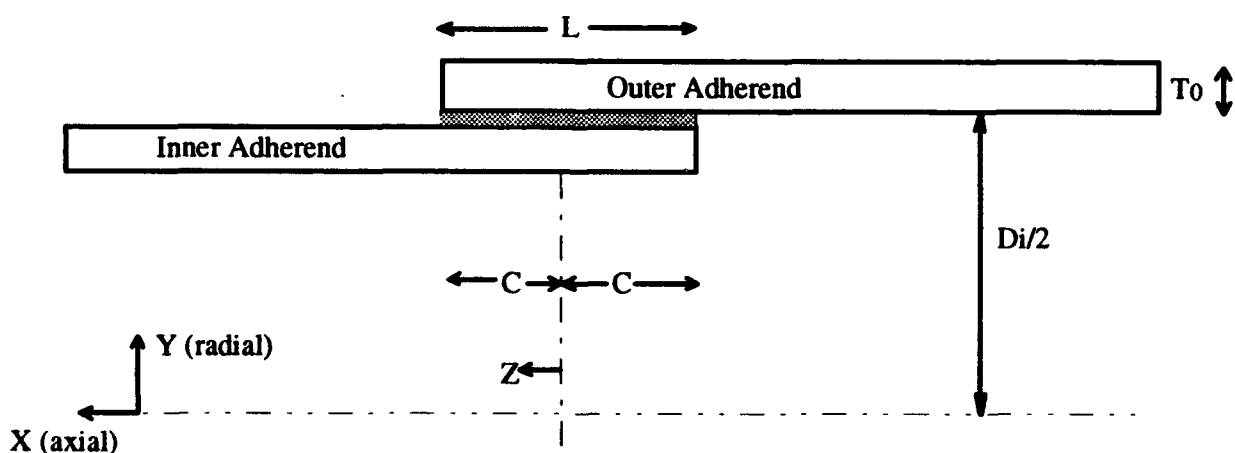


Figure 3.37. Tubular lap joint geometry and critical dimensions.

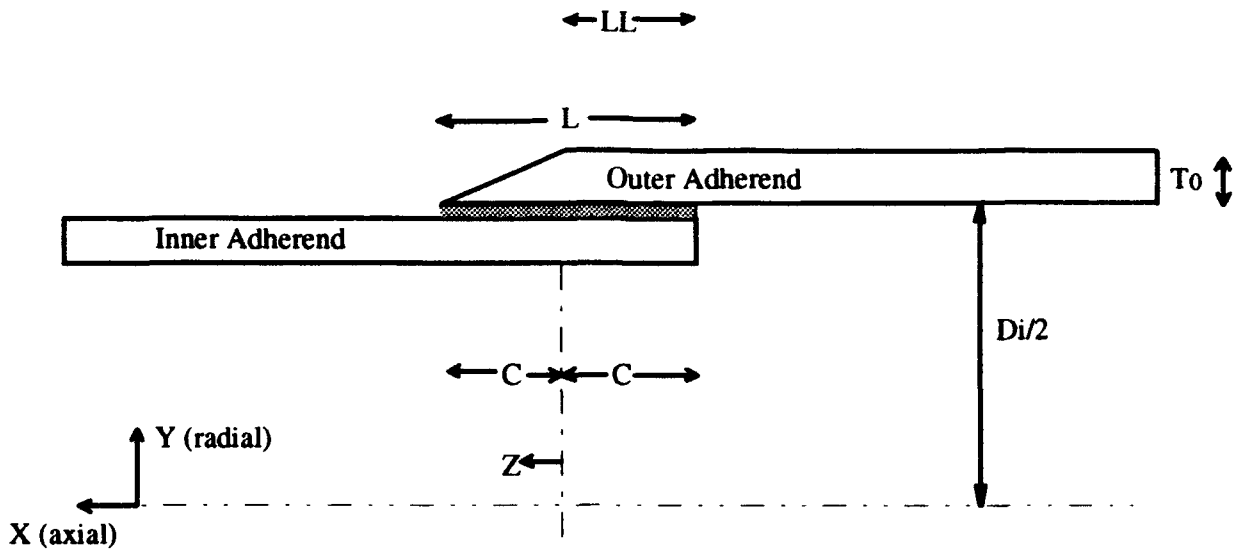


Figure 3.38. Type II tapered lap joint geometry and critical dimensions.

As discussed in the previous section, the effectiveness of the taper in reducing the SCF was found to decrease with decreasing joint length. Previous phases of this study have shown the existence of a threshold or optimum overlap length, below which tapers are useless in further reducing the overlap length. This critical overlap length, L^* , was found to occur when the SCF in the adherend was the same as the SCF in the adhesive for the untapered joint.

The task then is to determine the threshold L^* for different geometric and material configurations of adherends. Specifically, we are interested in L^* as a function of nominal thickness, T_0 , and inner diameter, D_i , of the tube for three adherend material configurations:

- (i) aluminum
- (ii) graphite epoxy composites
- (iii) hybrids with one tube made of aluminum and the other made of graphite-epoxy composite.

Joints with $L > L^*$ should be tapered as per Figure 3.38, with the taper extending at least half-way along the joint. This will result in a nominally uniform shear stress distribution under axial loads, thereby allowing stress computations from simple equilibrium considerations.

If $L < L^*$, a taper is no longer recommended. This saves an additional manufacturing step, but makes the stress distribution non uniform, thereby necessitating numerical stress evaluation. This evaluation has been accomplished during this study for a wide range of D_i and T_0 values using finite element methods. The data are presented in terms of three contour plots for each material system. The first contour presents the optimum load-carrying capacity P^* based on elastic overstress failure of the adhesive. For convenience P^* has been normalized by the adhesive strength. Thus, the value presented is per unit strength of the adhesive. The load value must be multiplied by the strength of the adhesive (in psi) in order to obtain the actual load carrying capacity (in lbs.). The second contour plot presents the corresponding optimum L^* (normalized with respect to T_0 of the adherend tube), and the final plot for each material system presents the stress concentration factor SCF^* in the joint.

The designer typically is provided with the nominal diameters of the adherend tubes and the load in the joint, which are system-level considerations. Thus, the design must be performed for a given load-carrying capacity. The designer usually utilizes this information and picks the corresponding thickness value T_0 from the P^* plot such that the minimum load-carrying capacity requirement is satisfied. Note that the plot is normalized for adhesive tensile strength, and may be used with any adhesive that has a modulus typical of a structural epoxy, if the tensile strength of the adhesive is known. The load bearing capacity of the joint is determined by multiplying the tensile stress by the value of the contour line which intersects the values of D_i and T_0 , see below. The chosen T_0 value and the given D_i values are then used to determine the corresponding optimum overlap length from the L^* contour plot. This is the threshold length to be used in order to avoid having to taper the adherends. Finally, the corresponding SCF^* value in the adhesive can be obtained from the third contour plot. This SCF^* value serves two purposes. First, it serves as a kind of a figure of merit since a low SCF implies a good design because it indicates better utilization of the joint. Second, it also yields the maximum stress value in the adherend tube since the far-field nominal axial stress in the adherend tube is already known from the load-carrying information. Hence, reliability and durability estimates can be performed for the adherend tube as well.

3.6.1 Aluminum-to-aluminum Adherend Adhesive Joints

The material properties used in this analysis are given in Table II. P^* , L^* and SCF* values have been computed for a total of 25 combinations of D_i and T_0 values and are presented in Figs. 3.39-41.

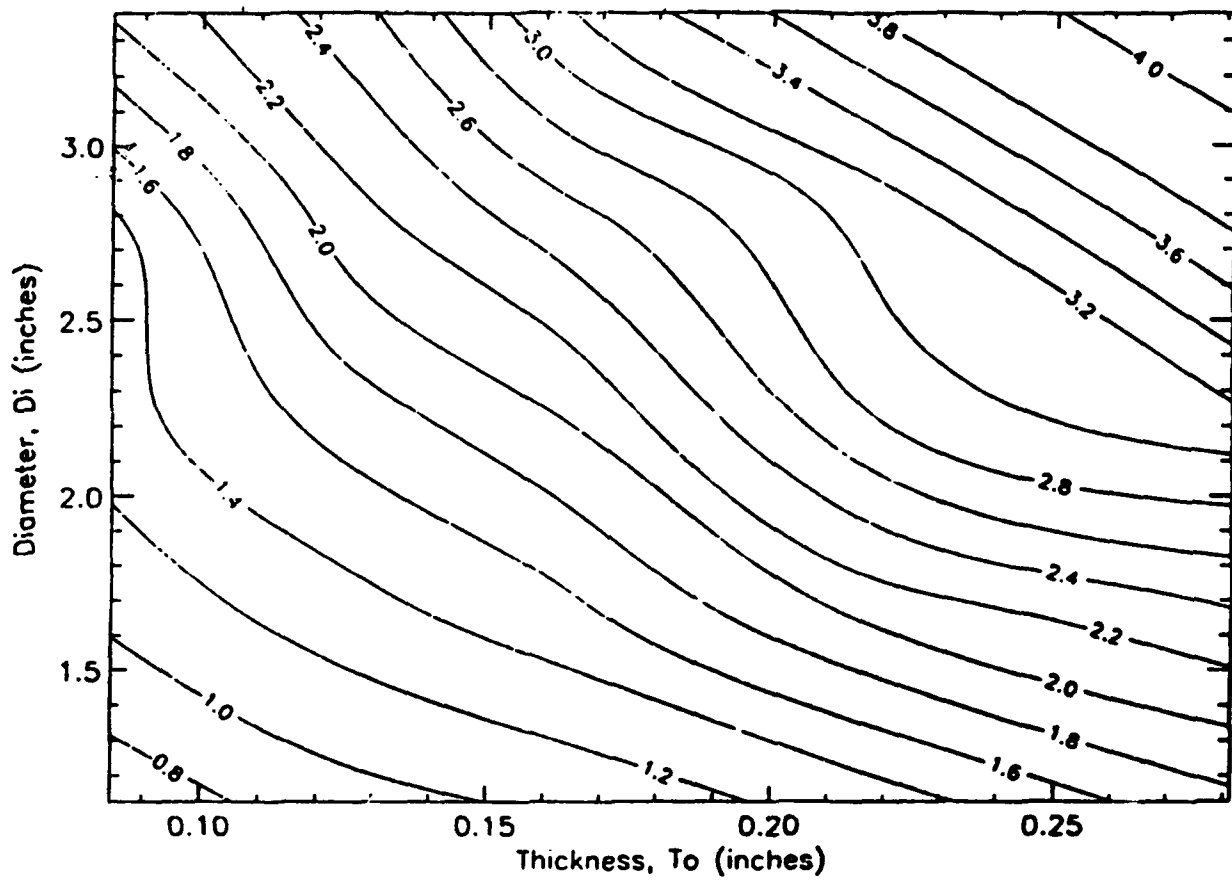


Figure 3.39. Optimal applied load plot (normalized for adhesive tensile strength) for aluminum-to-aluminum adherends.

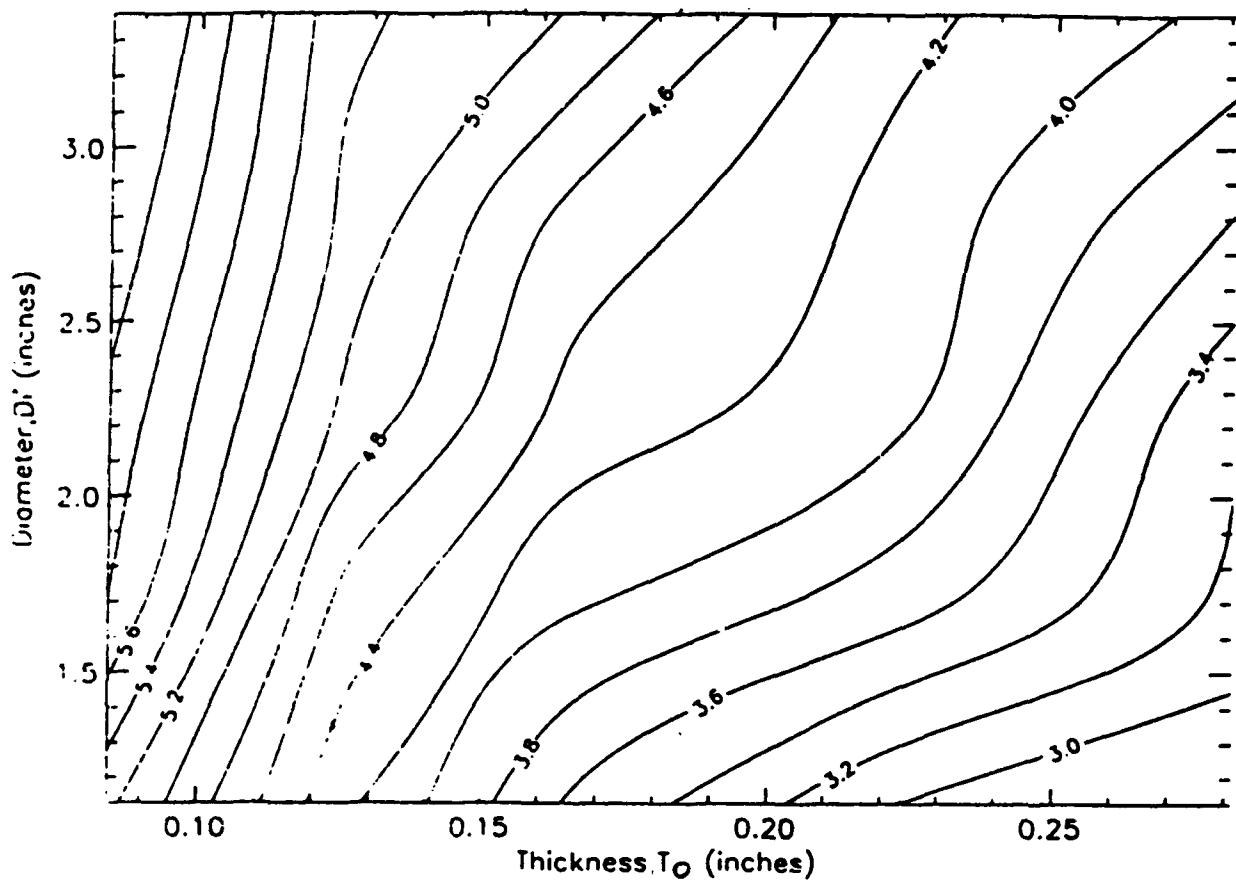


Figure 3.40. Threshold overlap ratio for aluminum-to-aluminum adherends.

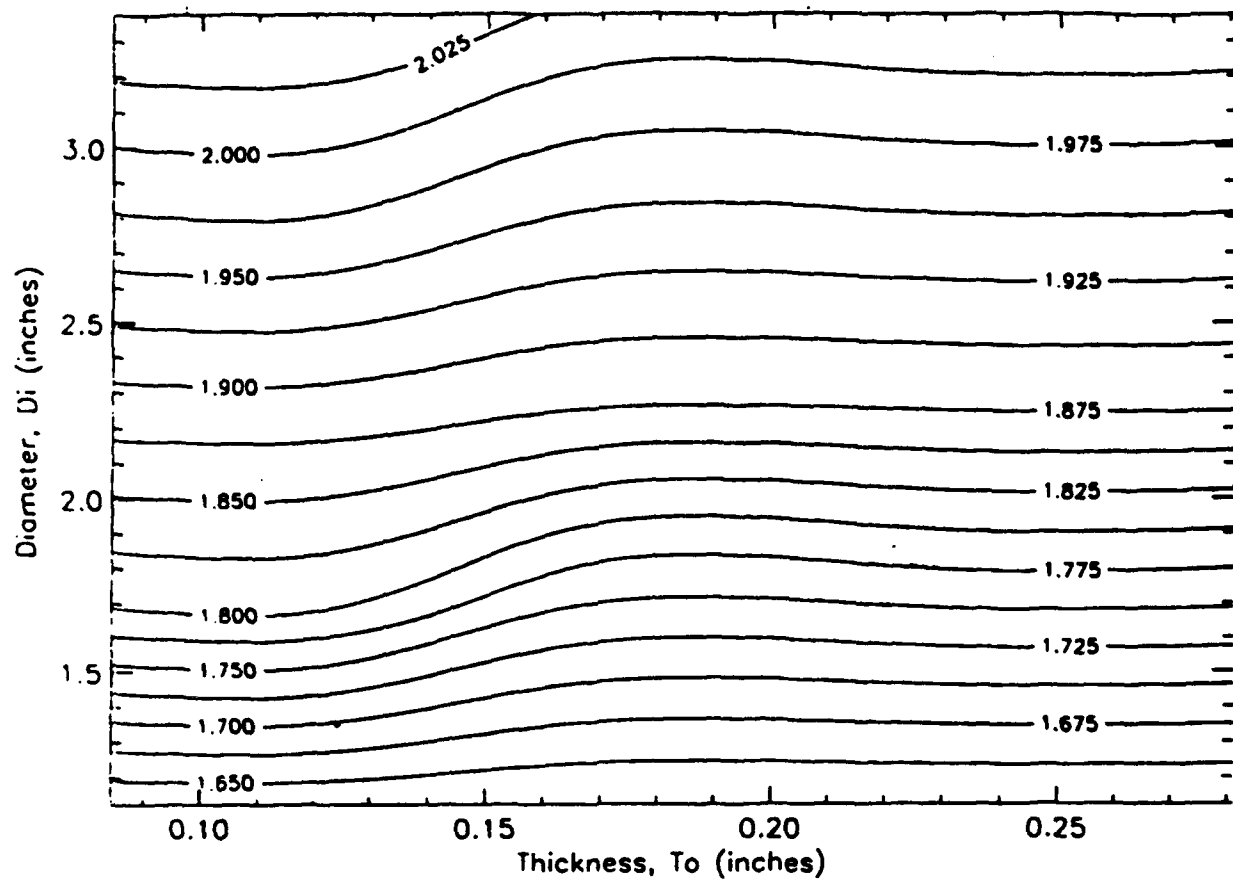


Figure 3.41. Stress concentration factors for aluminum-to-aluminum adherends.

Table 3.3. Material Properties of Adherends and Adhesive

Material	Elastic Modulus (E) psi	Poisson's Ratio (v)	Yield Strength ksi
Aluminum	10.15×10^6	0.345	35
Steel	30.00×10^6	0.270	150
FM-300 @ 49 °C, 90% RH	1.46×10^6 Tangential Modulus 8.08×10^3	0.350 Plastic Range 0.450	0.83

3.6.2 Graphite/Epoxy Composite-to-Composite Joints

Tubes with a lamination sequence specified by BRDEC were chosen as adherends in this study. The sequence and the effective properties, computed from classical lamination theory, are given in Table III. The P*, L* and SCF* values, computed for 25 combinations of D_i and T₀ values are presented in Figs. 3.42-44.

Table 3.4. Stacking Sequence and Material Properties of Graphite/epoxy Composites Used for Joint Modeling

Volume fractions: graphite 60 percent, epoxy 40 percent
 12-layer stacking sequence: [90/+8/-8/+8/-8/90/90/-8/+8/-8/+8/90]

Layer Properties: Elastic Modulus (mpsi) E ₁₁ =19.69 E ₂₂ =1.124 E ₃₃ =1.124	Shear Modulus (kpsi) G ₁₂ =489.45 G ₂₃ =402.60 G ₁₃ =489.45	Poisson's Ratio v ₁₂ =0.02552 v ₂₃ =0.03966 v ₁₃ =0.02552
Laminate Properties Elastic Modulus (kpsi) E ₁₁ =13.04 E ₂₂ =7.328 E ₃₃ =1.294	Shear Modulus (kpsi) G ₁₂ =721.97 G ₂₃ =432.68 G ₁₃ =459.37	Poisson's Ratio v ₁₂ =0.07075 v ₂₃ =0.03717 v ₁₃ =0.03431

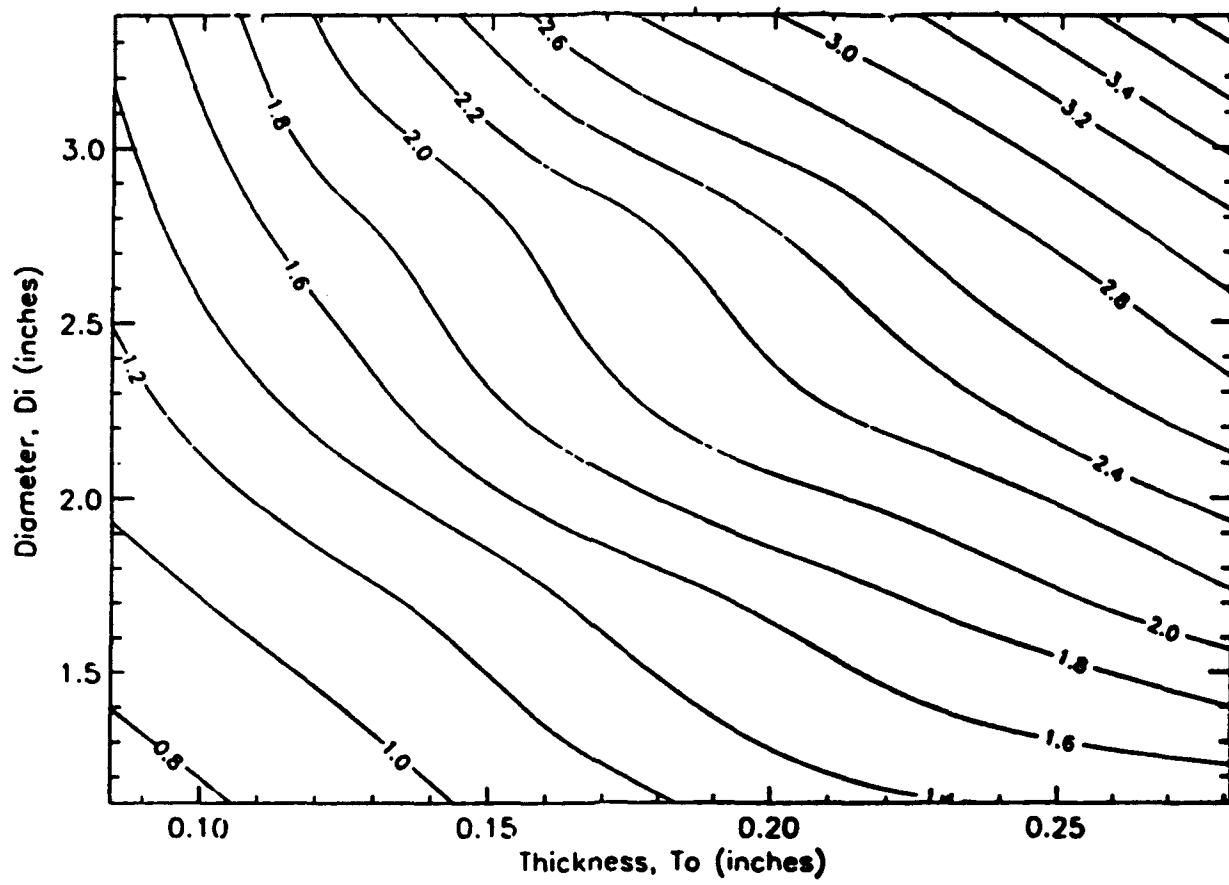


Figure 3.42. Optimal applied load plot for composite-to-composite adherends.

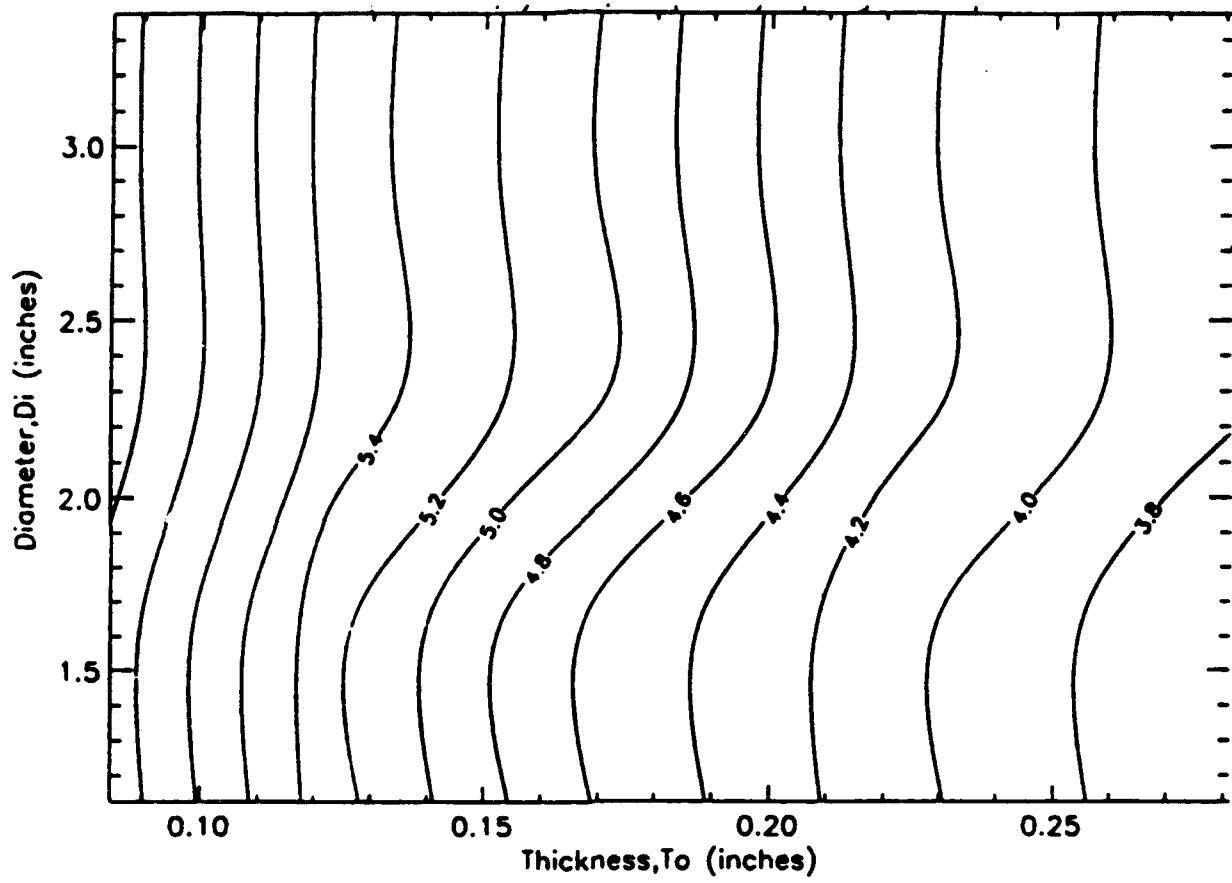


Figure 3.43. Threshold overlap ratio for composite-to-composite adherends.

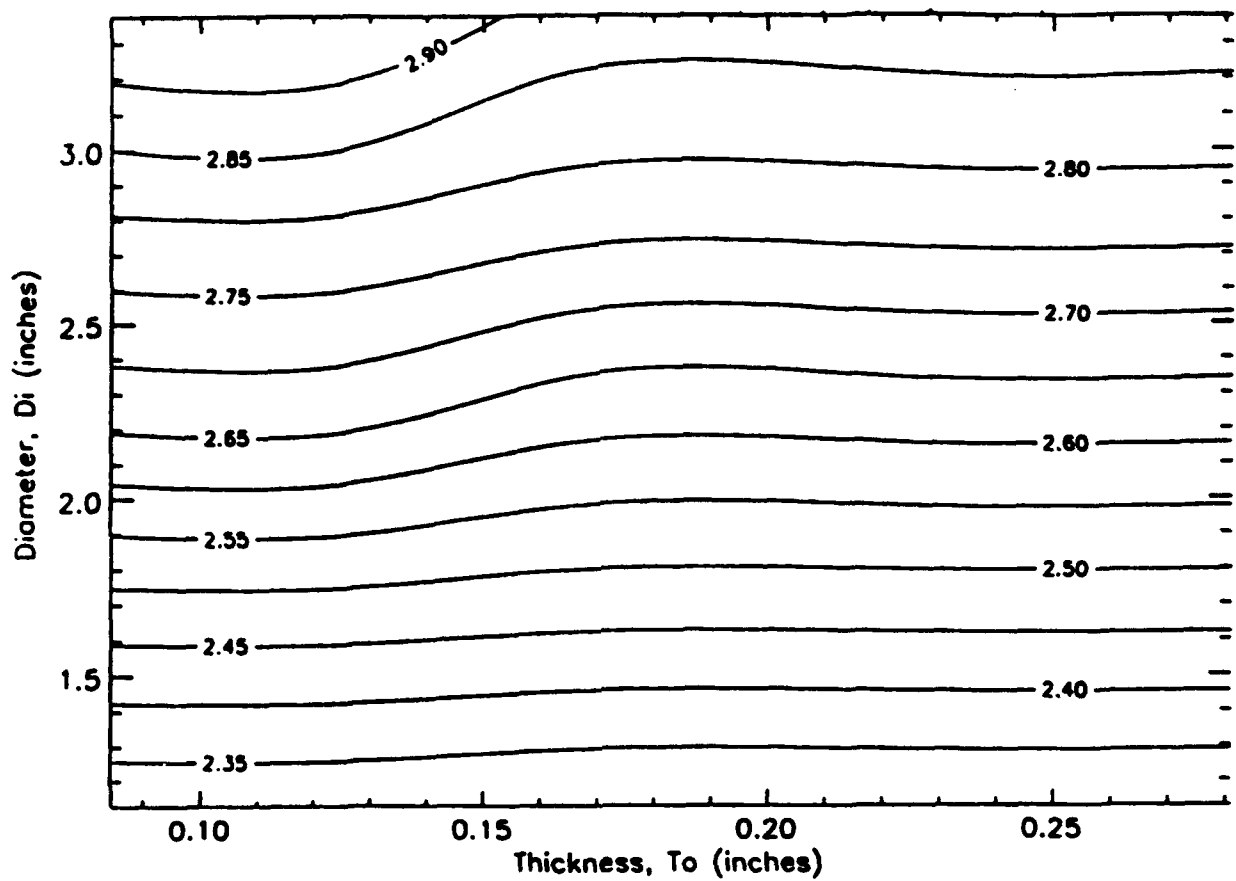


Figure 3.44. Stress concentration factors for composite-to-composite adherends.

3.6.3 Aluminum and Graphite-Epoxy Tubular Adherend Adhesive Joints

For a hybrid adhesive joint where one adherend tube is made of Aluminum and the other is made of a graphite-epoxy filament-wound composite, the material properties are the same as those listed in Tables II & III. The P^* , L^* and SCF^* values, computed for 18 combinations of D_i and T_0 values, are presented in the form of contour plots in Figs. 3.45-47.

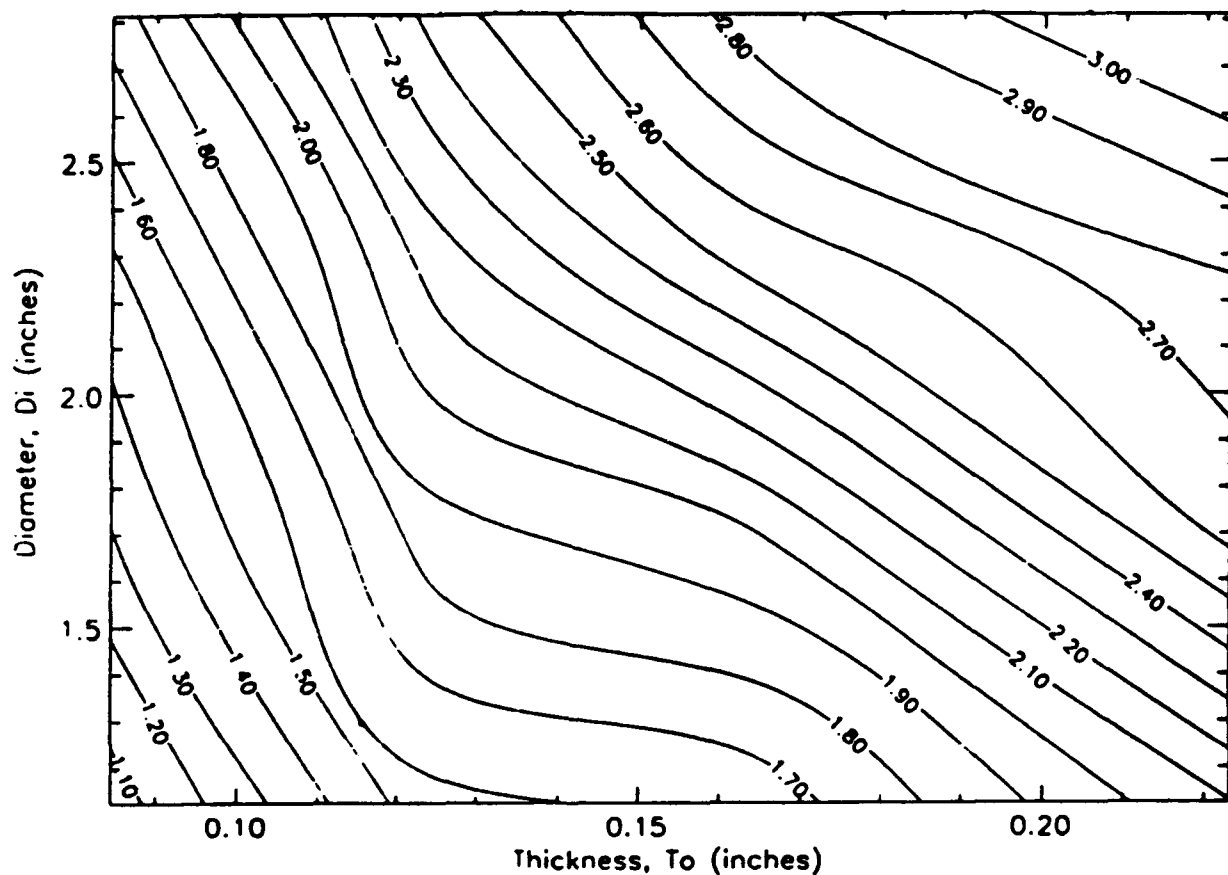


Figure 3.45. Optimal applied load plot for aluminum-to-composite adherends.

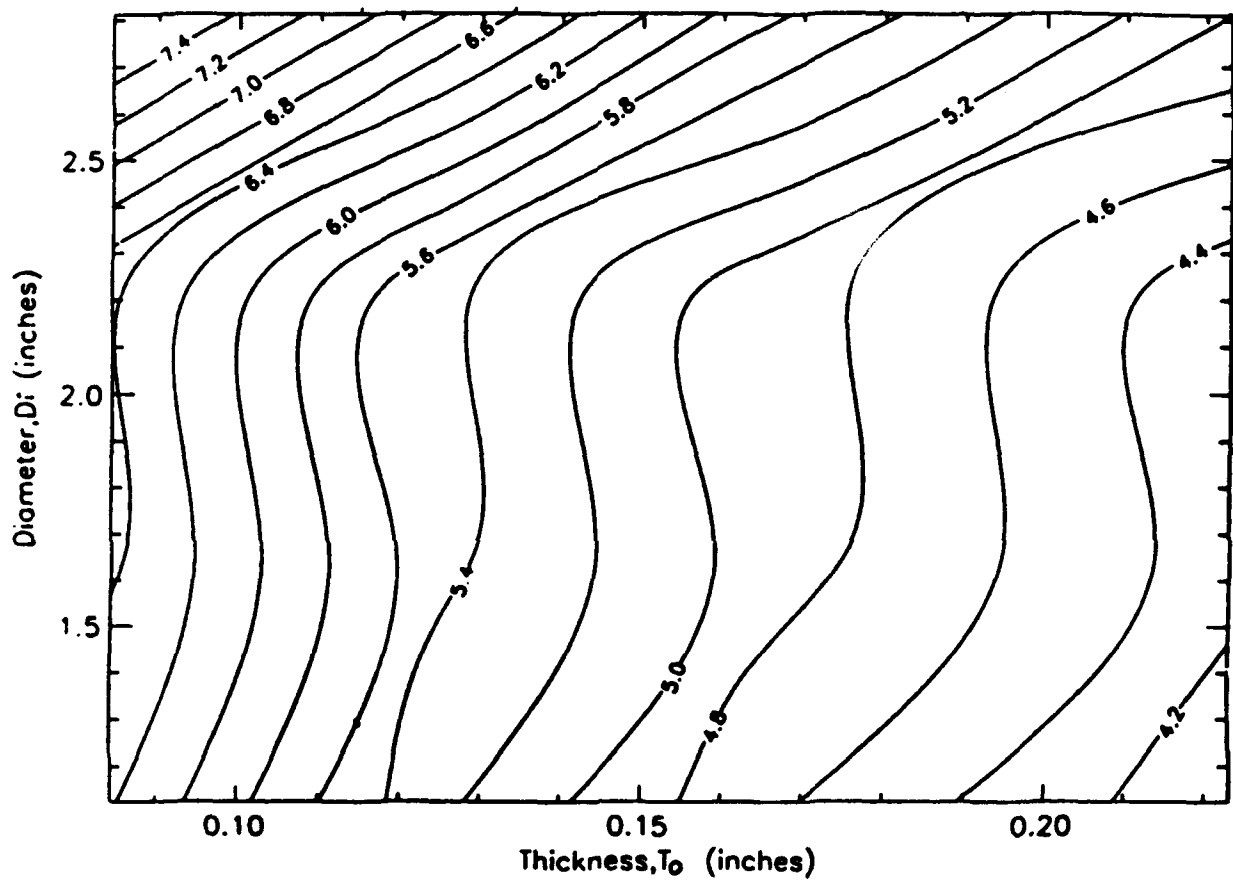


Figure 3.46. Threshold overlap ratio for aluminum-to-composite adherends.

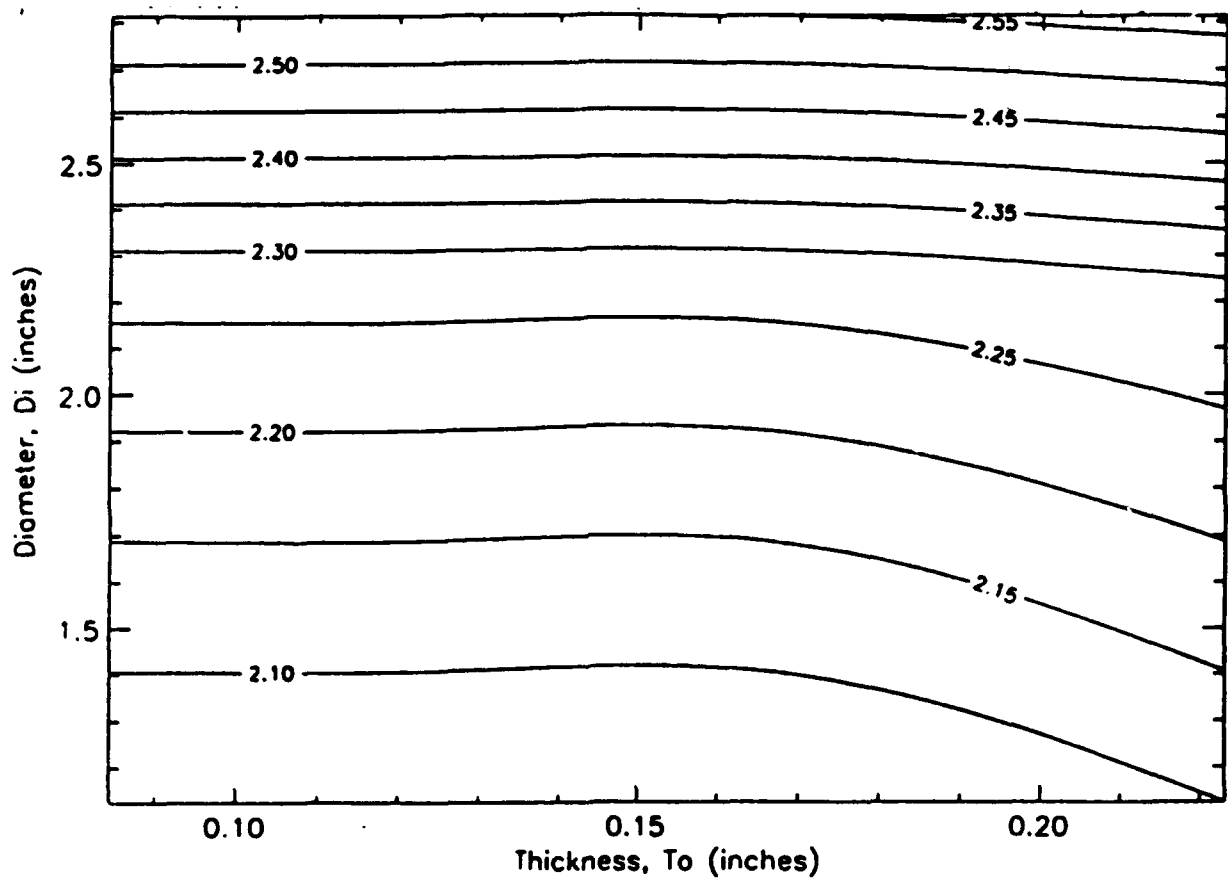
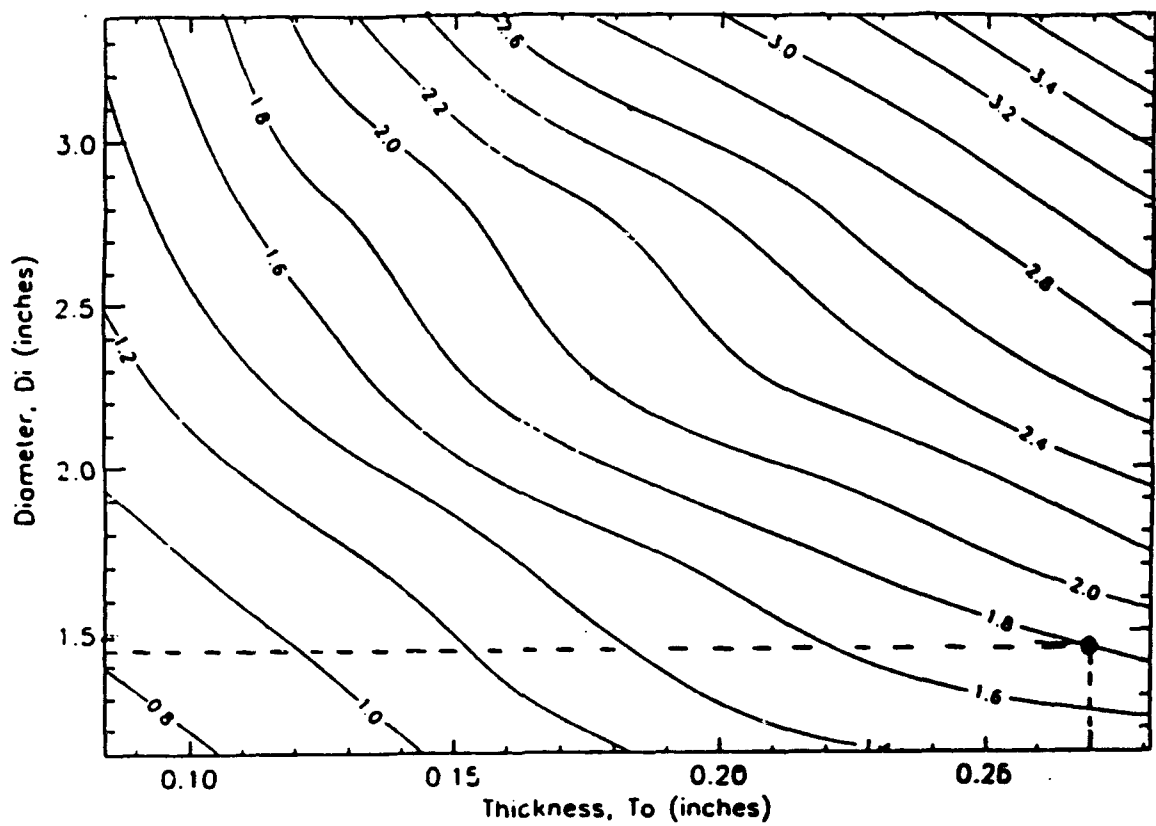


Figure 3.47. Stress concentration factors for aluminum-to-composite adherends.

3.6.4 Use of the Design Guideline Plots: a Design Example

In the design of tubular lap joints we assume that the designer will have determined both the range of nominal tube diameters and the load the joint is expected to bear from system-level considerations. The designer would then pick the appropriate design plots based on the materials he intends to use for the joint. For this example we will assume the following critical parameters (which are based on our previous modeling of the interior bay of the light vehicle foot-bridge): adherends, graphite/epoxy filament-wound composites; adhesive ultimate tensile strength, 8,300 psi (3H-F4); axial load, 15,000 lb. To use the design plots the load must first be normalized by the tensile strength of the adhesive to be used to bond the joint. In this case $P_n = 15,000/8300 = 1.80$. The designer can then draw a horizontal line from the tube diameter (D_i , chosen to be 1.48 in. for this example) to the normalized load contour plot, Figure 3.48. Dropping a vertical line from the load contour plot to the axis, the designer determines the ideal tube thickness (T_0); in this case 0.27 in. Since the load is normalized by the tensile strength of the adhesive in Figure 3.47, it can be used for any desired adhesive with a modulus that resembles a typical epoxy, i.e., 500,000 psi.

With the tube parameters now determined, the designer would consult the threshold overlap ratio contour plot (Figure 3.49) to determine the correct bond overlap length. The value of the contour field is read at the intersection of the diameter and thickness axes, in this case 3.7, which yields the normalized threshold overlap length. This length is the longest bond overlap with a reasonably flat stress concentration profile that can be achieved without tapering the tubes. This is the best choice from an ease of construction standpoint. This value is normalized by the thickness of the outer adherend tube, so the actual overlap length would be $L = L/T_0 * T_0 = 3.70 * 0.27 = 1.0$ in.



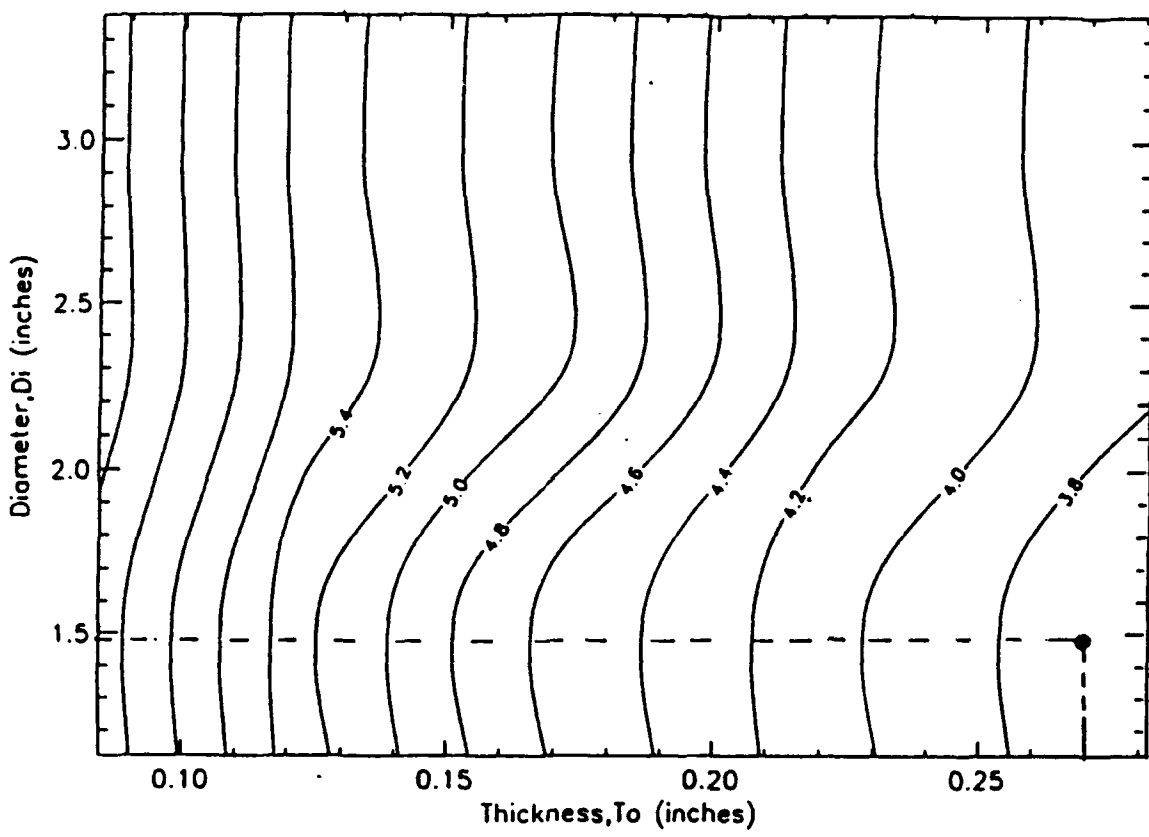


Figure 3.49. Threshold overlap length design plot, composite-to-composite tubular lap joints.

The third plot (Figure 3.50) is used to determine the stress concentration factor (SCF). Again the intersection of the inside tube diameter and the thickness axes gives the correct values, in this case 2.40. The SCF value serves two purposes. First, it serves as a figure of merit since a low SCF value implies a good design with better utilization of the joint in terms of load per unit weight of the adherend material. Second, the SCF value in the plot is the same for the adhesive and the adherend. Thus, it also yields the maximum working stress in the adherend, since the far-field nominal axial stress in the adherend tube is already known from the load information.

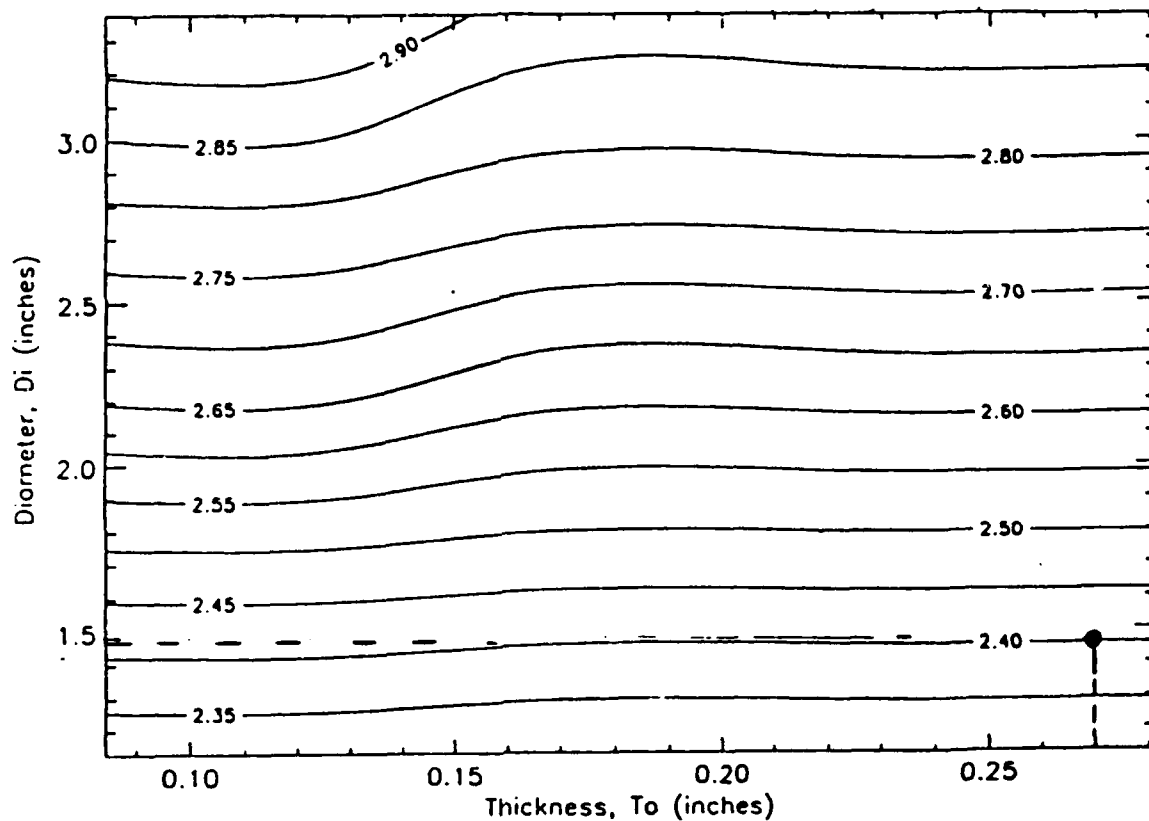


Figure 3.50. Stress concentration factor plot, composite-to-composite tubular lap joints.

If a longer overlap is required to meet the loading requirements, then a tapered lap joint should be used to minimize the CCF. If a type II taper is used with a taper length (L_t) at least one half of the overlap length (L) the shear stress distribution will be nominally uniform under axial loading, i.e., $SCF = 1$. Then the load carried by the joint can readily be calculated by multiplying the allowable tensile stress in the adhesive by the bonded area, i.e.,

$$P = \tau_{av} * (\pi D_i L).$$

3.7 LV/FB Design Assistance

Computer modeling was performed on prospective designs for a demonstration article for the Light Vehicle/Foot Bridge (LV/FB) structure, in order to guide design choices. A preliminary design of the bridge span structure, utilizing adhesive bonding technology, was investigated to understand the stress distributions in the bridge span and in the adhesively bonded joints subjected to wheel loads.

The initial modeling effort featured a box design with four 0.125 in thick box extrusions at the corners, and 0.063 in thick sheet aluminum on the four sides. Properties of 6061-T6 Al were used in the model.

3.7.1 Global Stress Analysis of Bridge Span

The stresses in the bridge span were first analyzed by using the classical strength of materials theory. Figure 3.51 depicts the simplified bridge span; and a cross-sectional area is shown in Figure 3.52. The calculated maximum bending stress was 9823 psi, and the torsional shear stress due to misalignment loads in the structure was estimated to be 2079 psi. The corresponding von Mises' stress for the combined bending and torsion was approximately 10 kips, which gives a factor of safety of 3.5 on yield strength of the aluminum material.

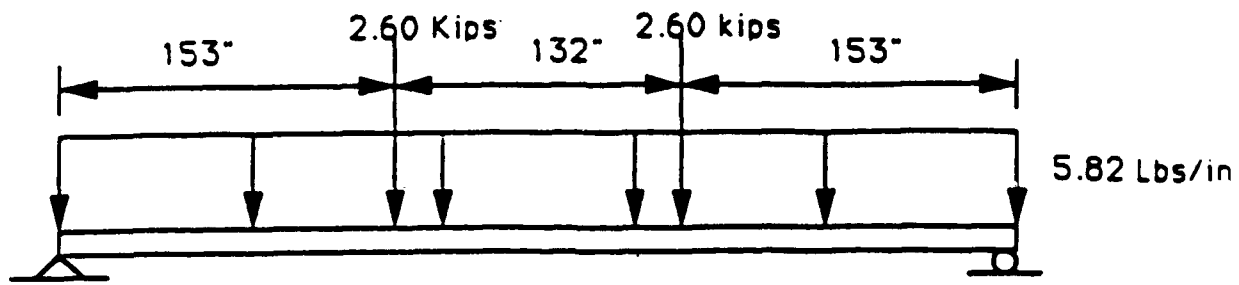


Figure 3.51. Simplified bridge span loading.

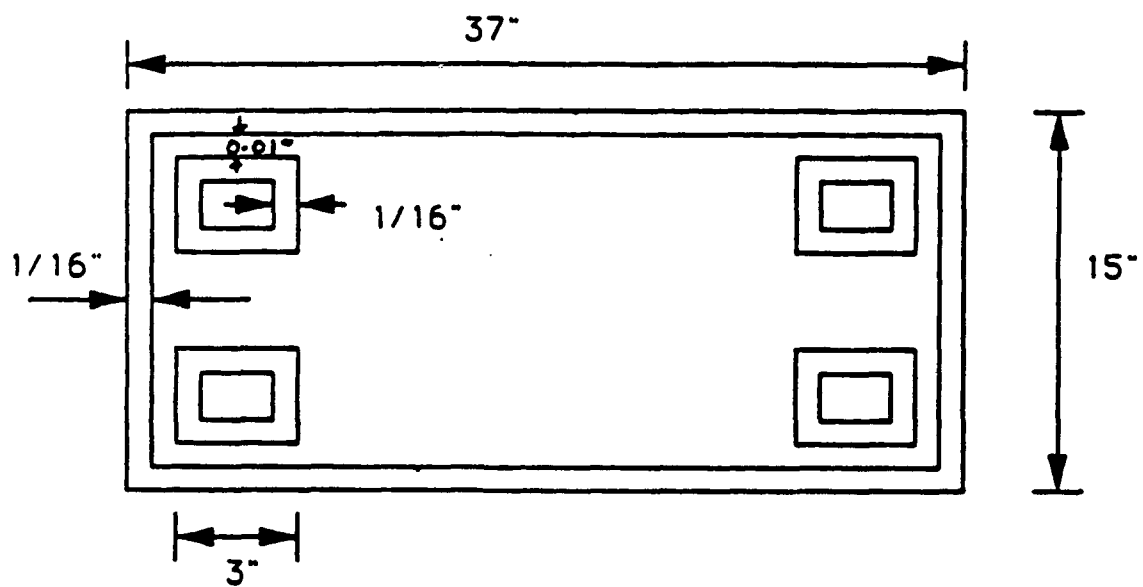


Figure 3.52. Cross-section of the simplified bridge span.

Since the results obtained from this section were based on basic strength of materials theory, they did not provide sufficient information on the local stress distributions in the bridge span in the vicinity of the applied loads. A finite element analysis was therefore performed.

3.7.2 Finite Element Analysis

A combined global-local analysis approach was used in this study to circumvent the limitations of computational resources. A relatively coarse global finite element model was first subjected to the wheel load and appropriate boundary conditions. The results of this global analysis were then used as the load condition in a subsequent detailed local analysis to obtain the local stresses in the vicinity of the wheel load.

3.7.2.1 Three-Dimensional Global Finite Element Analysis of Bridge Span

In considering the geometry of the bridge span and the limited memory storage space allowed by the finite element analysis software code (ANSYS) some simplification of the bridge span structure was necessary. Based on the symmetry of the bridge span geometry and its loadings, only one-quarter of the bridge span needed to be analyzed. Figure 3.53 represents the finite element mesh of one-quarter of the bridge span. For the reasons of the software code capabilities and analysis time expenditure, the mesh consisted of two types of linear finite elements: plate elements and three-dimensional solid elements. The plate linear finite element had 4 nodes and each node had three translational and rotational degrees of freedom. The three-dimensional solid linear finite element had 8 nodes and each node had three translational degrees of freedom. Kinematic constraints were applied to all the symmetry planes (yz-plane and xy-plane), and a generalized constraint (or coupled constraint) was applied to the left-most end of the bridge span. A distributed pressure load was applied to the bridge

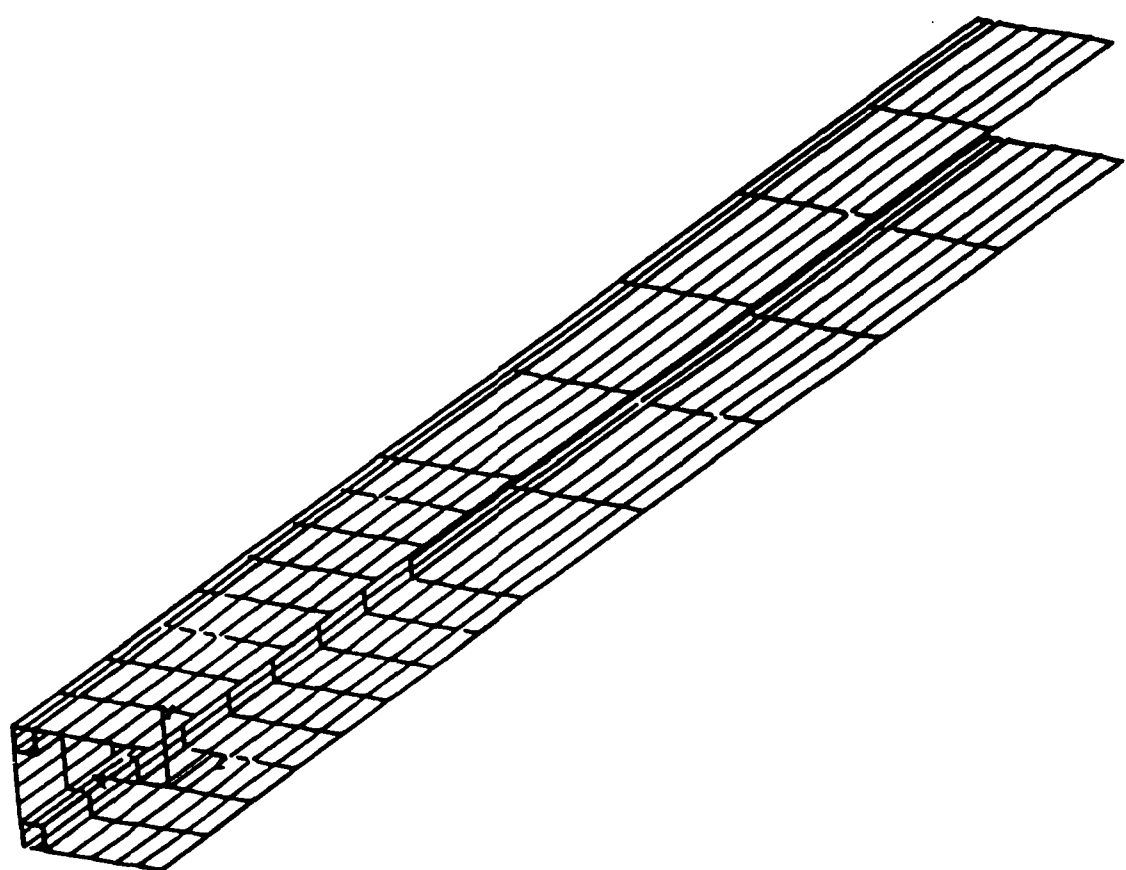


Figure 3.53. Three-dimensional finite element mesh of one-quarter of the bridge span.

structure, as shown in Figure 3.54, to simulate the wheel load. For convenience, a normalized wheel load of 10 pounds was applied in this study. Thus, all results must be scaled up by a factor of 260, to simulate the wheel load of 2.6 kips.

3.7.2.2 Three-Dimensional Local Finite Element Analysis of the Central Portion of Bridge Span

Upon completion of the global finite element analysis of the bridge span as described in Section 3.7.1.1, a more refined analysis was conducted to examine the detailed stress distributions in the portion of the bridge span where the wheel load is applied. The central bridge span was modeled with a more refined three-dimensional mesh of solid 8-node elements. The mesh refinement was required to provide more accurate information about stress distributions in the bridge span and its adhesively bonded interfaces. The boundary conditions applied to this local model were the displacements obtained from the global analysis in section 3.7.1.1. One-quarter of the central portion of the bridge span and its associated boundary conditions are shown in Figure 3.55.

For convenience of discussing the stress distributions in the subsequent paragraphs, the middle cross-section of the original bridge span is designated as $Z=0$, and the cross-section where the plate elements transition to solid elements is designated as $Z=L$. The bonded joints are further classified as 'top' and 'bottom' joints, as shown in Figure 3.56. Thus, stress results are presented for 'top' joint and 'bottom' joint both at $Z=0$ and at $Z=L$.

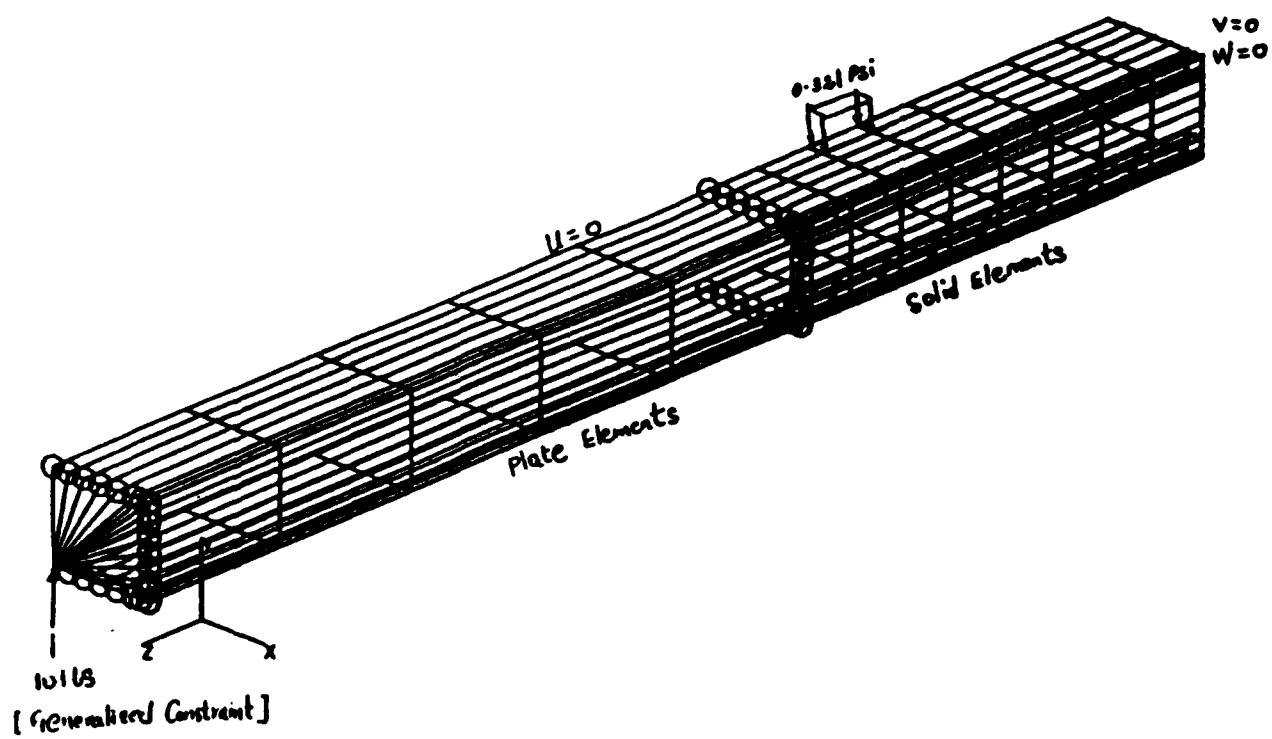


Figure 3.54. Boundary conditions and applied load for one-quarter of the bridge span.

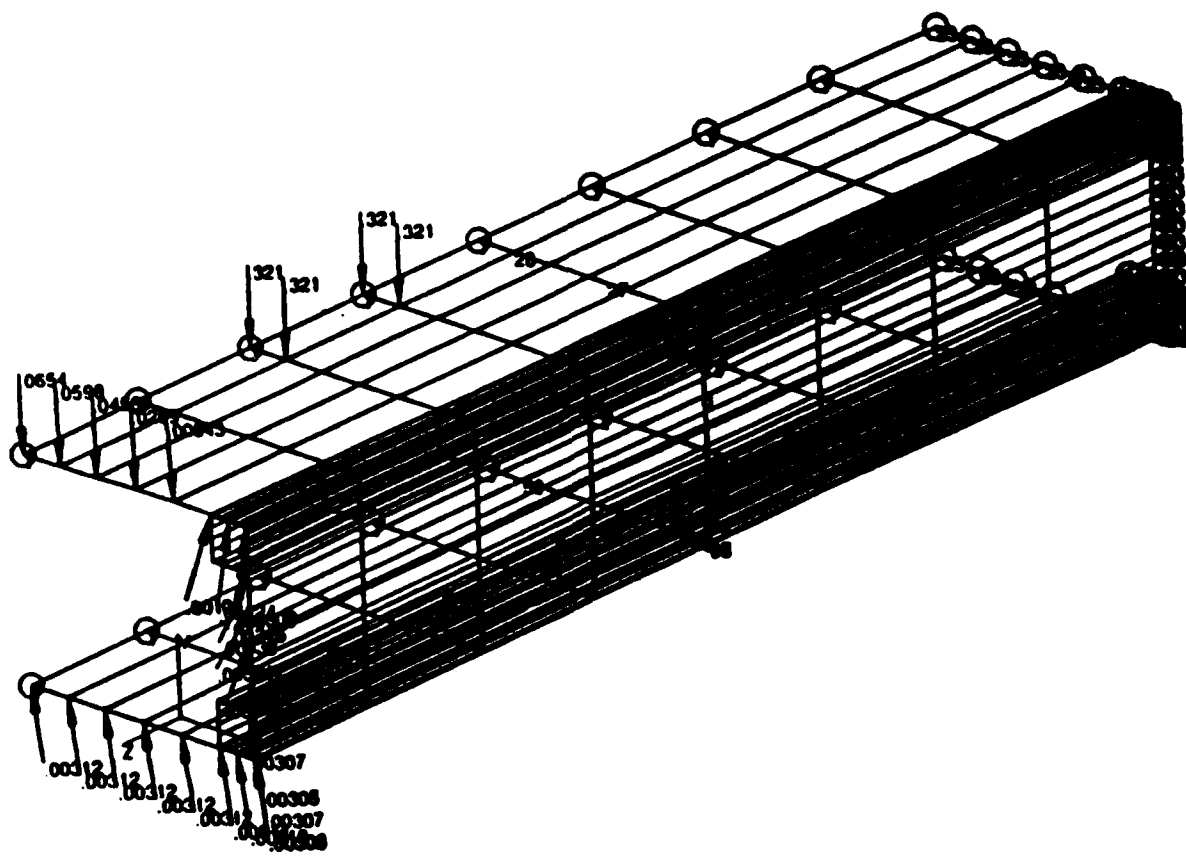


Figure 3.55. Boundary conditions and applied displacements for one-quarter of the bridge span.

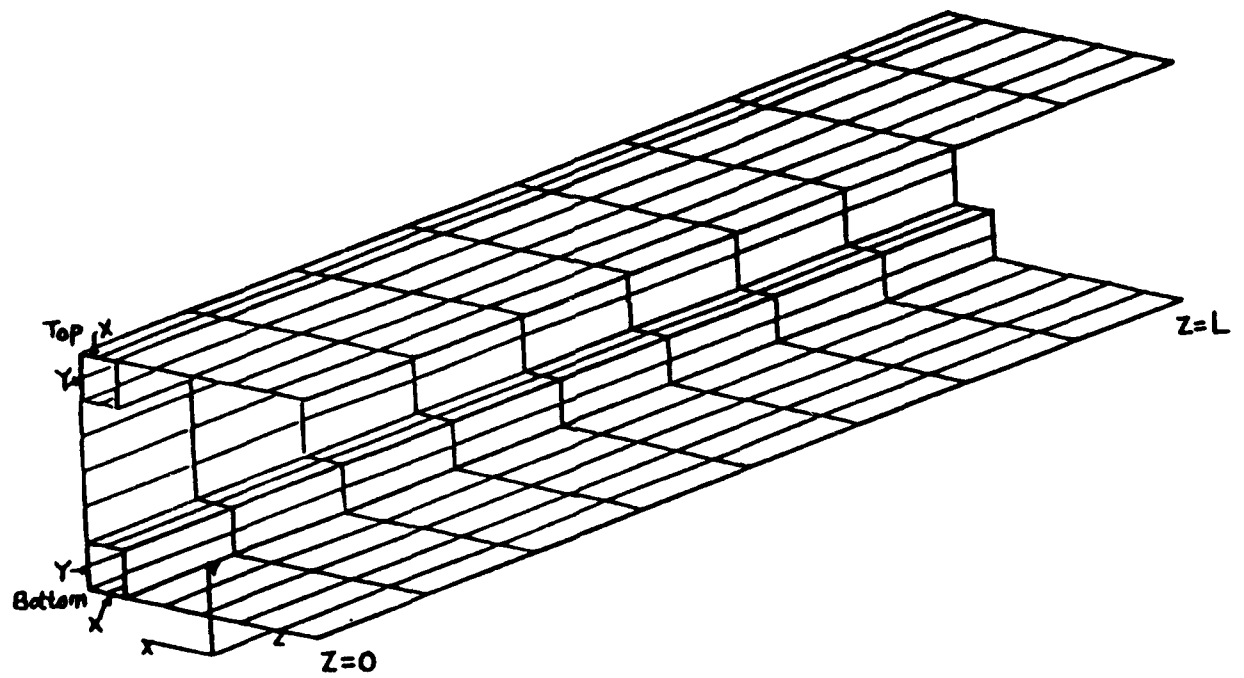


Figure 3.56. Explanation of the locations for "Top" and "Bottom" joints in the central bridge span.

The von Mises' stress was chosen as a design failure criterion. The von Mises' stress in the middle of the adhesive layer was obtained and plotted. From the stress plots, it is evident that the maximum von Mises' stress was acting at the 'top' joint at cross-section $Z=L$. The von Mises' stress acting at $Z=0$ was always smaller than at $Z=L$. Also, The von Mises stresses acting at the 'top' portion of the adhesive layer was larger than those at the 'bottom' portion. Since the $Z=L$ edge was also the edge where the displacement constraints were applied, the magnitude of stresses obtained from this edge could have been erroneous due to the boundary constraint effect. Therefore, the stresses acting should be examined in regions located further away from the $Z=L$, for more accurate information.

The magnitude of the stresses in the bridge span were found to be unacceptably high. For example, at the outer edge of the top joint under the wheel load the shear stress was over 10,000 psi at the edge of the joint. The same maximum stress in the bottom joint was only 1500 psi.

Top plate buckling was suspected as the primary culprit in causing this high loading. Since a composite deck plate was planned for the demonstration article, computer modeling was repeated with this modification. This stiffer bridge deck reduces the deformation of the bridge span, and the average stress levels are lower. Shear stress in the side panels was also considered, to insure that the final design will not suffer from shear buckling.

3.7.3 Composite Deck Finite Element Analysis

Three cases were considered. The only difference between them was the design of the side plates. In case I the side plate was bent in a U-shape, and the bonded region ran between the edges of the U and the extrusions. Case II considered a flat side plate bonded to the sides of the upper and lower extrusion. Case III added an inner, bracing side wall to the flat configuration of Case II. Figure 3.57 shows cross-section layouts of the three configurations.

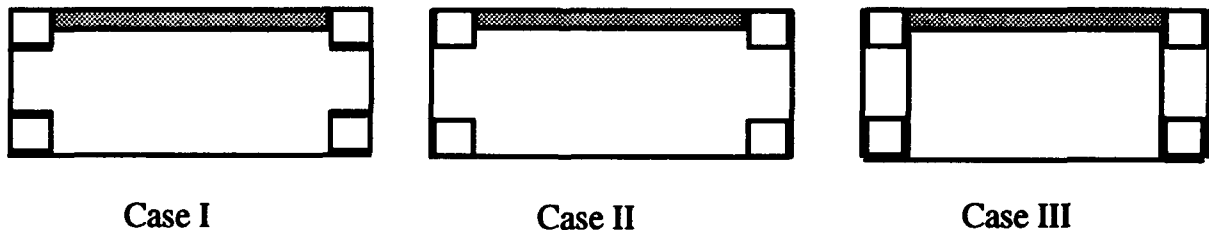


Figure 3.57. Configurations of components used for composite deck plate models.

3.7.3.1 Results of Case I

The shear stress, τ_{yz} , in the side panel is shown in Figure 3.58. Maximum shear stress in the side panels occurs in the region near $Z=L$ and its magnitude is 12.5 psi with 10 pounds load, which corresponds to 1.625 ksi with 2.6 kips of total load. The corresponding critical shear stress for shear buckling is 2.4 ksi [1]. The Von Mises' stress acting in the "top" adhesive layer is largest, and the stress acting in "bottom" layer is smallest. The maximum stress in the top adhesive layer (Figure 3.59) is 2.02 psi with 10 pounds load, which corresponds to 262 psi with 2.6 kips load.

3.7.3.2 Results of Case II

The shear stress, τ_{yz} , in the side panel is shown in Figure 3.60. Maximum shear stress in the side panels occurs in the region near $Z=L$ and its magnitude is 14.7 psi with 10 pounds load, which corresponds to 1.911 ksi with 2.6 kips of total load. The corresponding critical shear stress for shear buckling is 2.4 ksi. The Von Mises' stress in each adhesive layer is similar to Case 1. The Von Mises' stress acting in the "top" adhesive layer is largest, and the stress acting in "bottom" layer is smallest. The maximum stress in the top adhesive layer (Figure 3.61) is 3.67 psi with 10 pounds load, which corresponds to 477 psi with 2.6 kips load.

3.7.3.3 Results of Case III

The shear stress in the outer side panel is shown in Figure 3.62. The maximum shear stress is 6.7 psi with a 10 pound load, corresponding to 870 psi. However, the load on the inner panel is much higher (Figure 3.36), with a distinct maximum at the wheel load position. Edge effects confuse the determination of a stress maximum, but it appears to correspond to at least 2.68 ksi with full 2.6 kips load. The stress load in the outer top adhesive joint is also reduced, to 420 psi. The highest adhesive load is in the inner top joint, and corresponds to 1120 psi at full load.

3.7.3.3 Discussion

With 2.6 kips load, the maximum shear stresses in the outer side panel are 1.652 ksi, 1.911 ksi, and 870 psi for Case I, Case II, and Case III respectively and the maximum Von Mises' stresses in the adhesive layers are 262 psi, 477 psi, and 420 psi , respectively, for the

same load. The maximum shear stress and Von Mises' stress in Case I are lower than those in Case II. It is evident that the cross-section design of Case I is better for both buckling and adhesive shear stress than that of Case II. However, the analysis neglects the effect of bending on the side plate material, and the concentration of bending and load stresses at the bend. Since the loads in the adhesive joints and the side panels are acceptably low in either case, the flat panel Case II design was chosen for the demonstration article. This design was easier to manufacture, and avoided potential fatigue problems at the bend.

The internal stiffener used in the Case III design does reduce the buckling load on the outer skin, but at a high cost. The buckling load on the inner skin, 2.68 ksi, exceeds the critical shear stress for the material, and the maximum shear stress in the inner top adhesive joint, 1120 psi, is higher than any other location. This analysis thus does not support the use of internal stiffening plates. Unfortunately, it was completed after construction of the demonstration article, which did include internal stiffeners. The stiffeners used in the demonstration article did not exactly match the continuous flat plates modeled in Case III. The design analysis does indicate that the bridge section should perform well without stiffeners, should these fail during testing.

The other primary conclusion of this analysis was that the stiffer deck plate significantly reduced the overall stress levels. This is because the increase in the stiffness of the composite deck reduces the amount of local deformation of the bridge deck due to the wheel load. In all cases considered, the maximum shear stress in the side panels are lower than the corresponding critical shear stress for shear buckling.

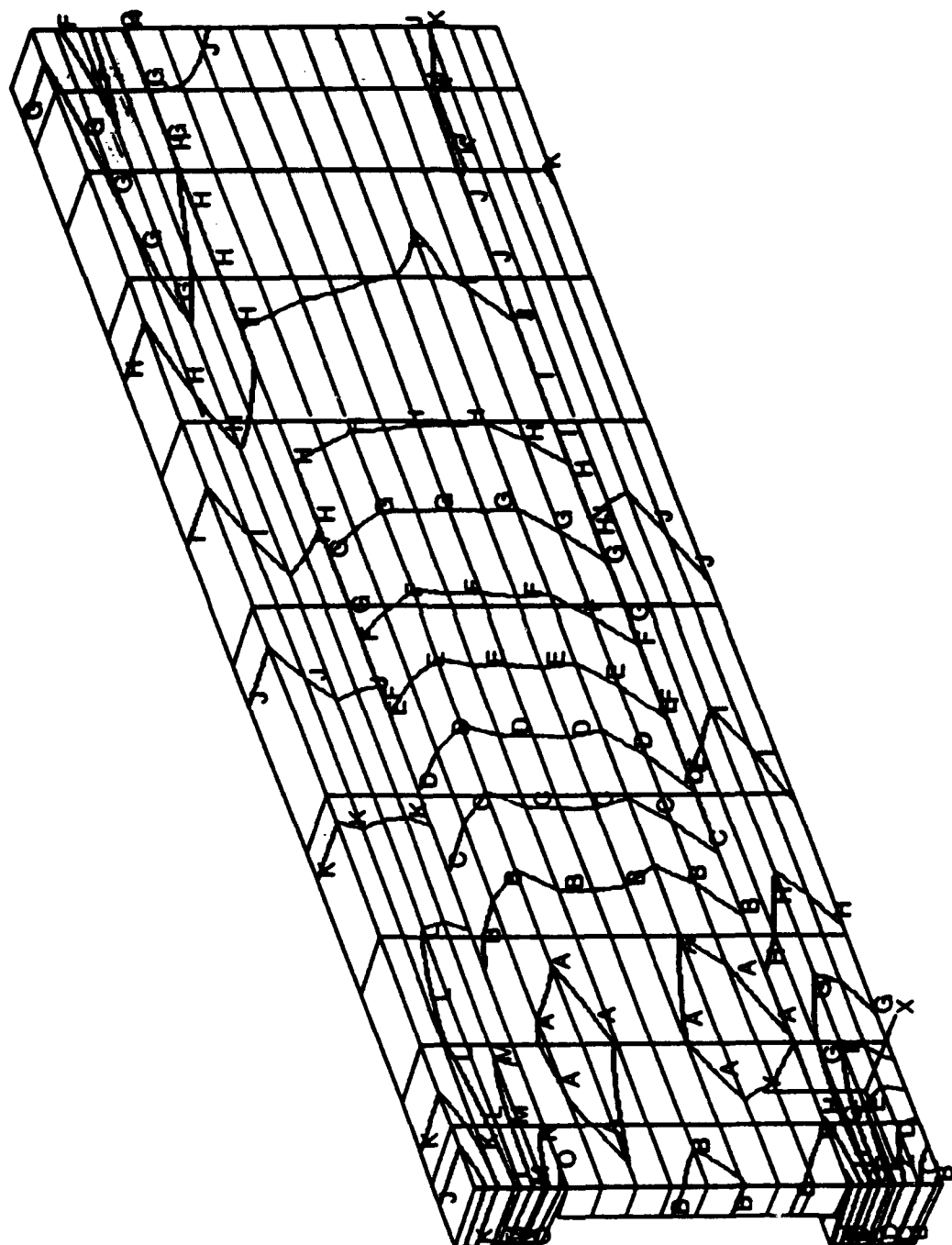


Figure 3.58. Contour plot of shear stress, τ_{yz} , of the side panel for Case I.

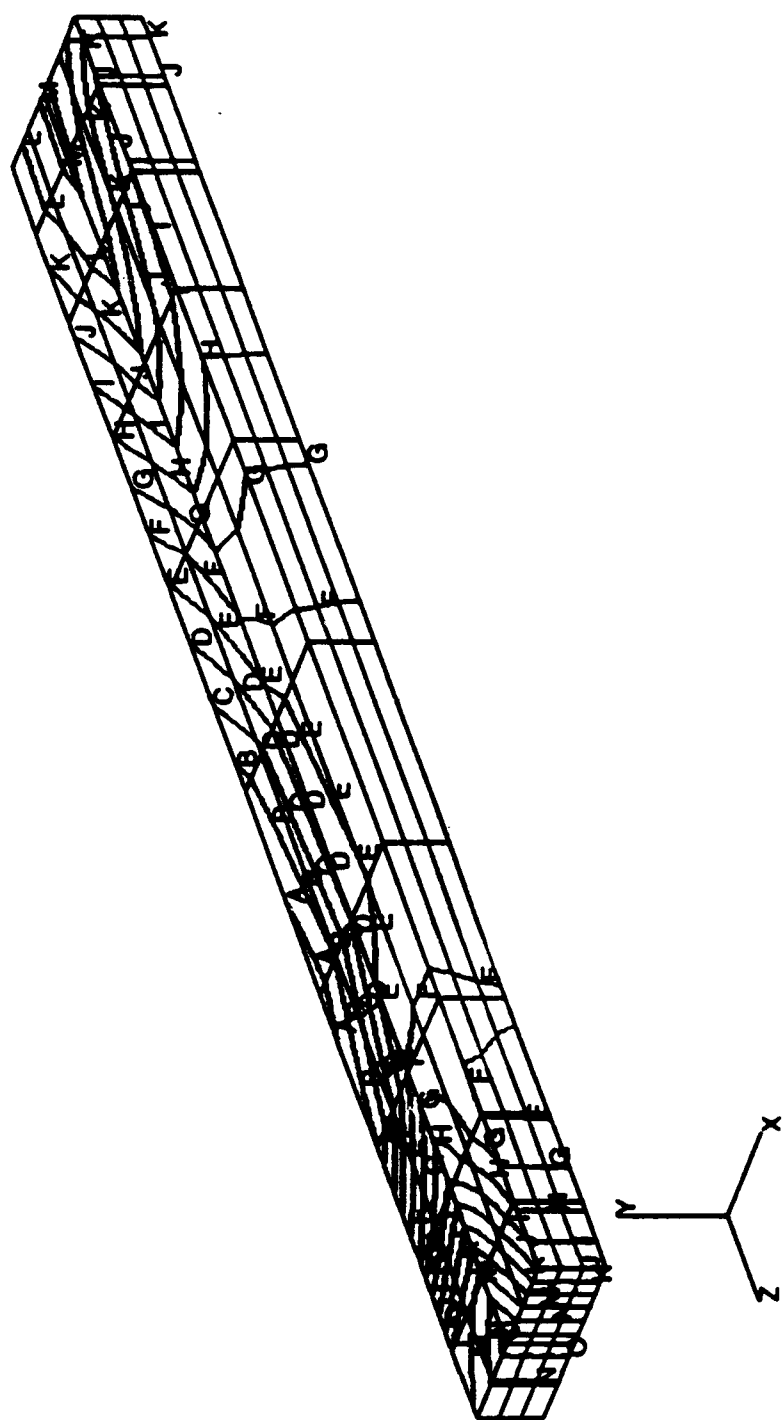
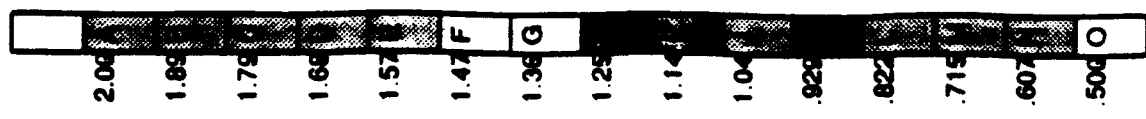
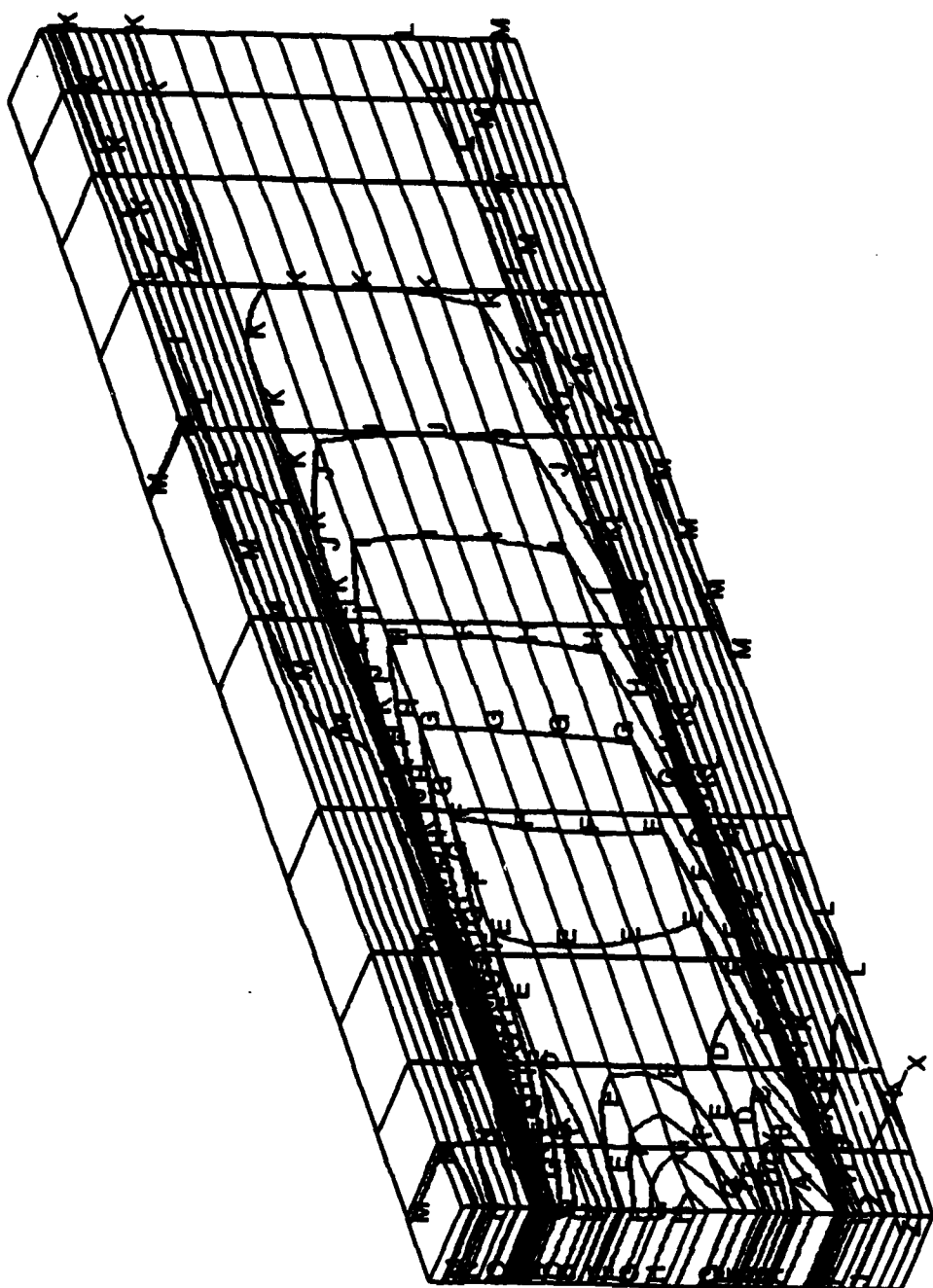
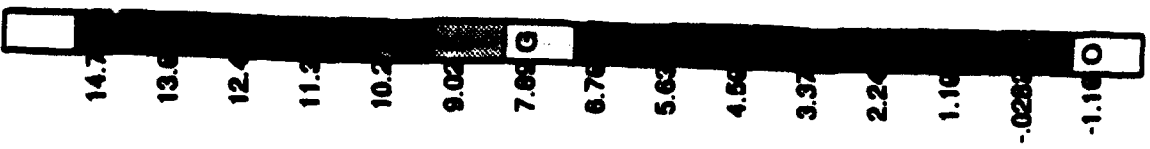


Figure 3.59. Contour plot of adhesive von Mises' stress in the "top" joint for Case I.



NEW BRIDGE (LOCAL, 2, LINEAR)
BRIDGE49_F12
LOAD STEP 1 - ITERATION 1

Figure 3.60. Contour plot of shear stress, τ_{yz} , of the side panel for Case II.

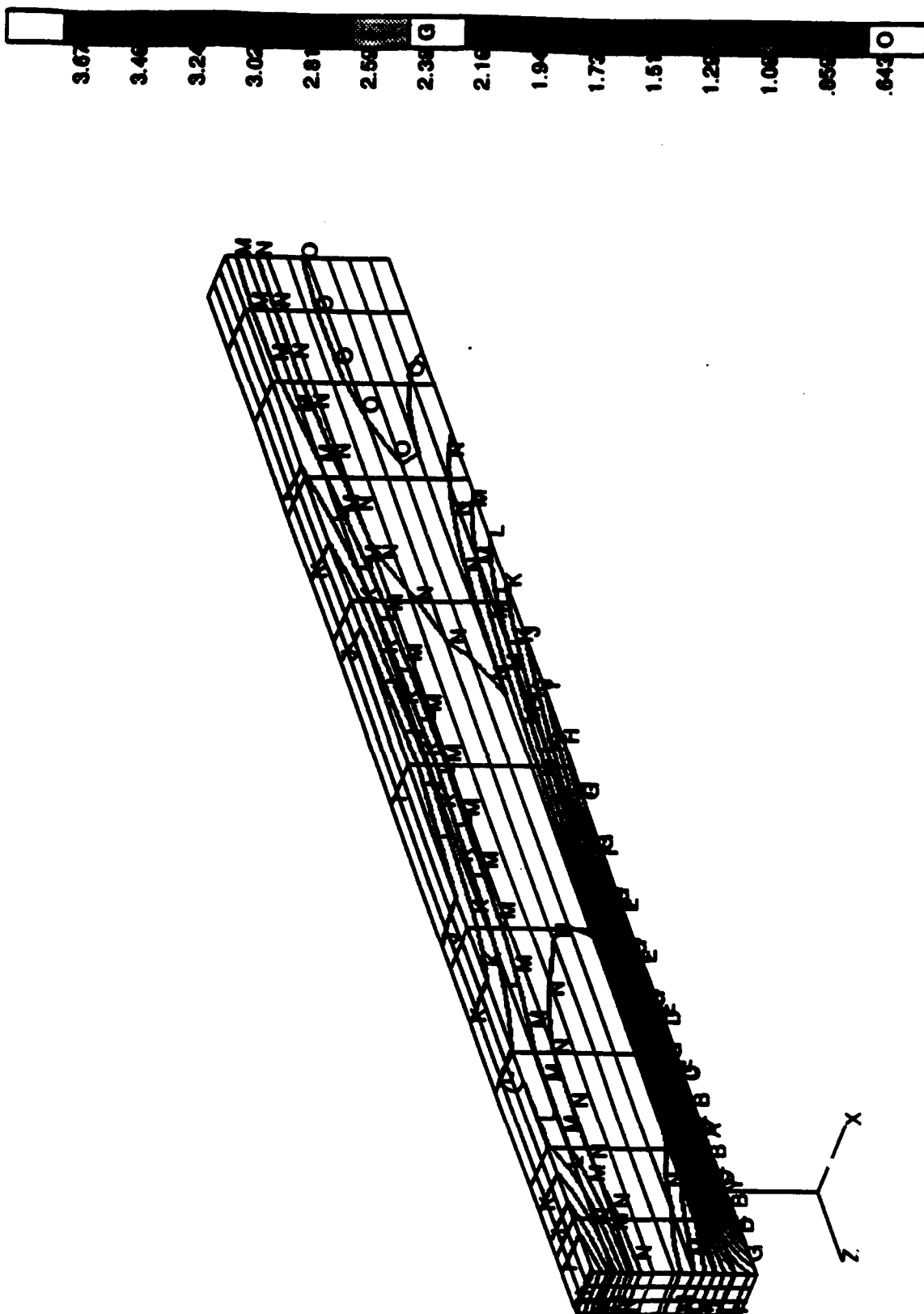


Figure 3.61. Contour plot of adhesive von Mises' stress in the "top" joint for Case II.

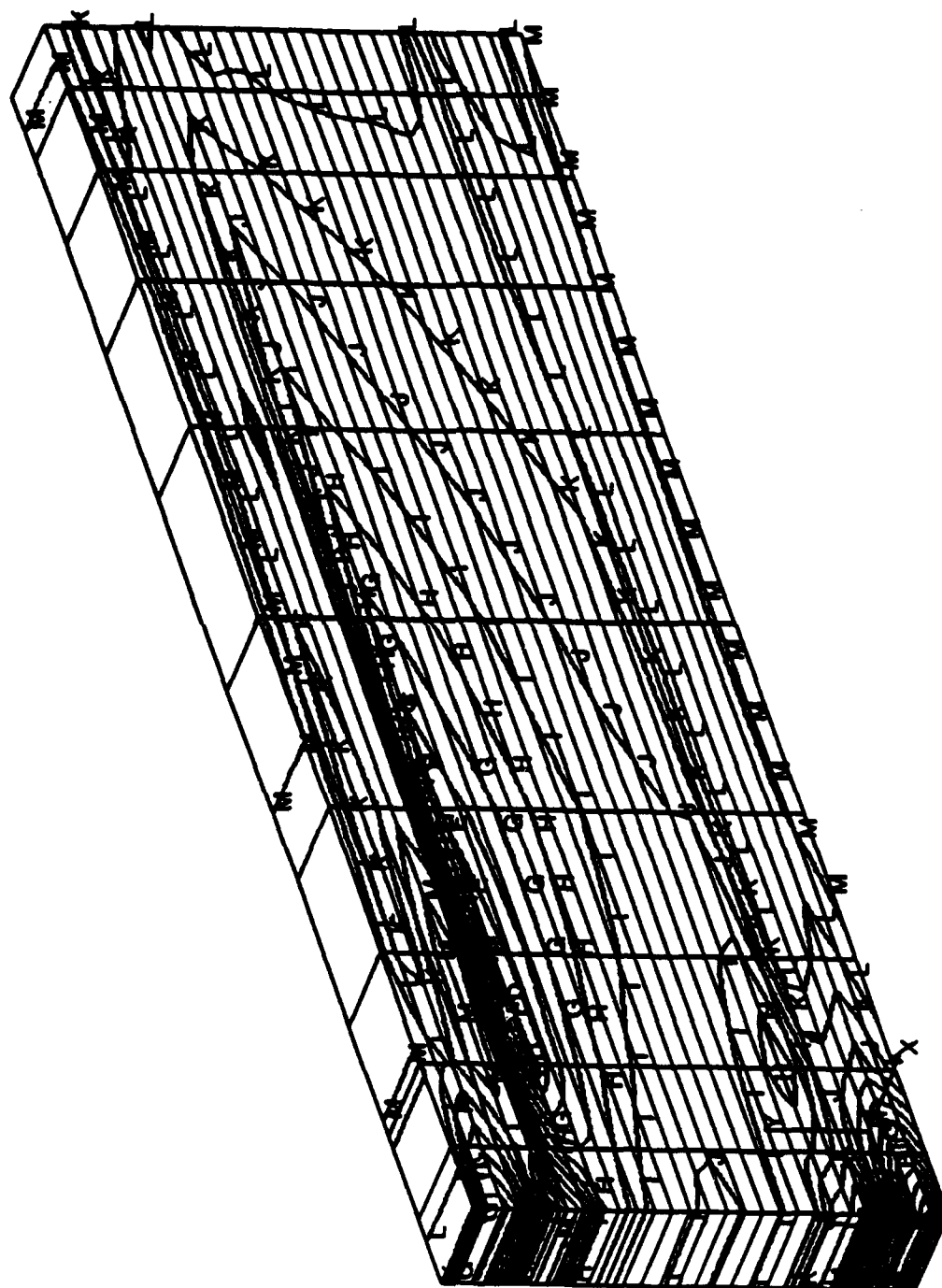


Figure 3.62. Contour plot of shear stress, τ_{yz} , of outer side panel in Case III.

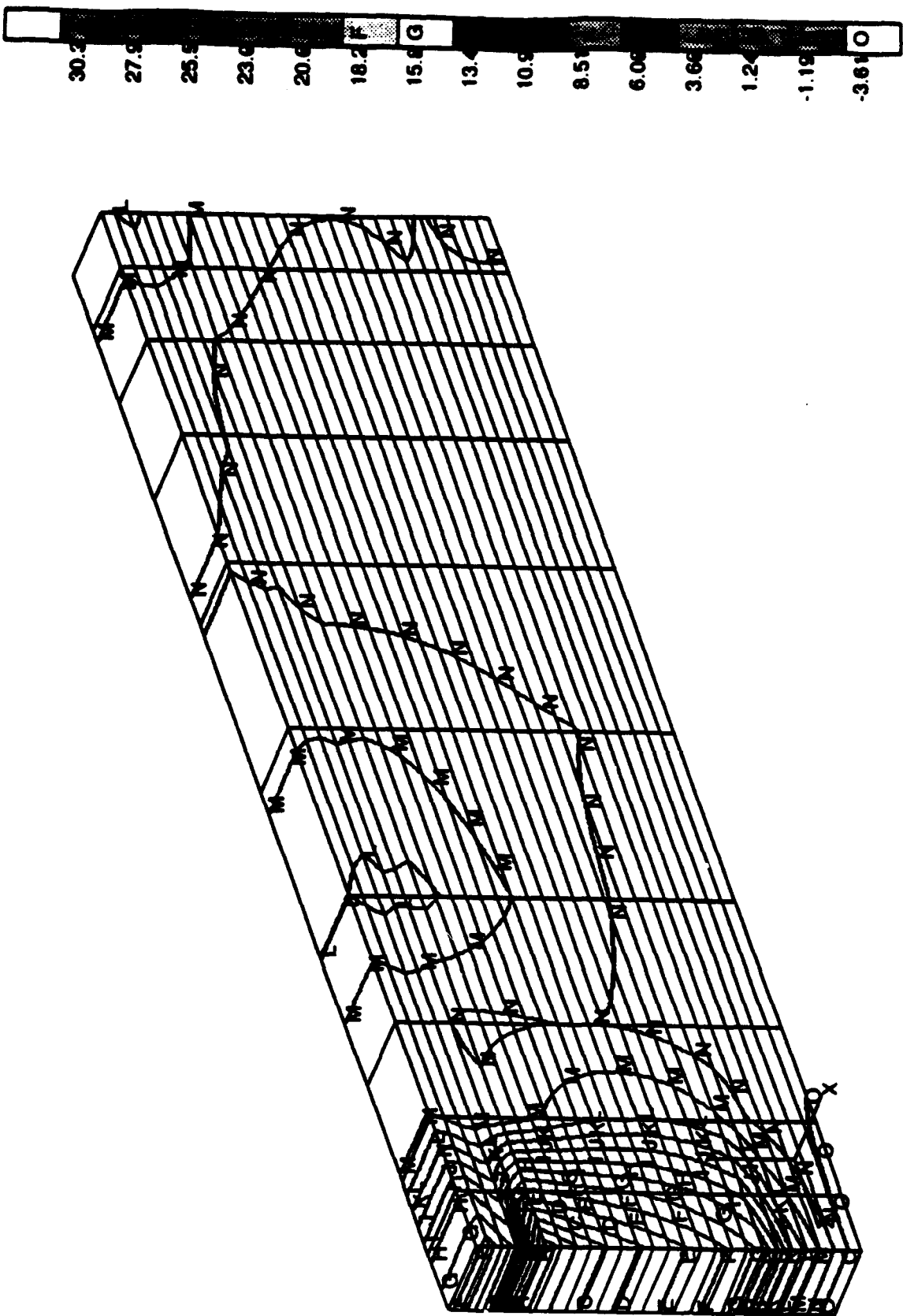


Figure 3.63. Contour plot of shear stress, τ_{yz} , of inner side panel in Case III.

3.8 Lessons Learned

Analysis of the quad lap joint allowed a direct comparison of FEM modeling and experimental results. Two important conclusions were reached as a result. One, the failure criteria was established so that subsequent modeling would rely upon a firm foundation, and would be tied to real world conditions. Second, that the full elastic/plastic analysis was not necessary to determine the critical behavior of the adhesive joints. This significantly reduced the amount of computer time required to examine a particular joint geometry, and allowed a much broader range of conditions to be examined.

The parametric studies of joint design proved that chamfers and stiffening rings were not effective ways to reduce stress concentrations on the joint. The taper results clearly showed that a "knife-edge" taper was necessary to achieve significant stress reduction at the ends of the joint. However, the taper need not be carried over the entire length of the joint to be fully effective, as shown by the type II taper studies.

The parametric studies of tubular overlap joints that took joint geometry into account had one striking conclusion: short overlap joints did not need taper. The extensive range of geometries studied were reduced to a few simple contour plots that provide an easy way for a designer to determine exactly what load the joint can be expected to carry for a given configuration. These design guidelines were completed for arbitrarily sized tubular joints composed of aluminum, or composites, or a mix of the two. In addition, we determined that the only significant adhesive variable was tensile strength, so that the guidelines were normalized as a function of adhesive strength, and therefore will apply to any adhesive.

The design concept studies for the LV/FB center span significantly influenced the design of the demonstration article. According to our modeling, the demonstration article should meet all design goals. The final examination of stiffeners indicated that such stiffening was not needed. Unfortunately this results was achieved only after the completion of the demonstration article.

4.0 ADHESIVE ENHANCEMENT AND REPAIR KIT DEVELOPMENT

The primary purpose of this task was to improve the properties of our low-temperature curing epoxy adhesive formulation 3H to make it suitable for use as a repair kit adhesive. This adhesive was produced under our previous program (#DAAK70-86-C-0084), but despite very attractive strength and fracture properties, it proved to be difficult to use due to its very high viscosity. A modified formulation was developed which retained the good properties of 3H but proved far easier to use, and prototype repair kits have been provided to BRDEC for evaluation. This adhesive was used to manufacture the demonstration article, in conjunction with repair kit style dispersing techniques.

4.1 Viscosity Improvements to Adhesive 3H

The low-temperature curing epoxy adhesive 3H, formulated in our previous program, has excellent strength and fracture characteristics. However, it is very difficult to mix and use. The main problem is the high viscosity of the resin and the need for heating when the resin is mixed with the curing agent. Potential use as a repair kit adhesive depended on improving the "user-friendliness" of the formulation. Therefore, we concentrated on reducing the effective viscosity of this adhesive in such a way that the attractive properties would not be sacrificed.

Our approach to reduce the viscosity of 3H was to reduce its epoxy equivalent weight (EEW) (i.e., the molecular weight of the constituents between each epoxy unit) from 250 to 215. To reduce the EEW, we added approximately one-half the normal amount of the chain extender molecule (bisazodiol) during the resin preparation. The result was a less viscous resin, which however was still very difficult to effectively mix with the curing agent at room temperature. With slight warming (to ~40-50°C by hot water bath or heat gun), the resin flowed sufficiently well to insure proper mixing. Once the curing agent was added, the resulting system was easily stirred at room temperature. A compact tension specimen was produced by casting a net shape test article from the neat adhesive resin (Figure 4.1), and tested for fracture properties via the unload-compliance method. The specimen snapped at a load of 25 lb and a crack length of 0.017 in. Since fracture was quite brittle, useful G and I values were not obtained.

Given this poor fracture performance, a number of other modifications were made to the 3H formulation to improve the fracture properties of the less viscous alternative (Table 4.1). For formulation no. 2 we eliminated Hycar 1872 rubber in addition to decreasing the EEW of the resin from 250 to 215. Eliminating the Hycar 1872 reduced resin viscosity considerably. The result was a room-temperature workable resin which was easily blended with curing agents ATBN 1300x16 and V40. A bulk compact tension specimen of this adhesive failed at 0.021 in. crack length and a maximum load of 35 lb. Again, useful G and I values were not obtained due to the brittle nature of the fracture.



Figure 4.1. Neat adhesive compact tension specimens.

The third formulation experiment used a reduced EEW resin (215) with Hycar CTBN 1872 being added with the curing agent, rather than the resin. The result was a very workable room-temperature adhesive resin. However, a bulk compact tension specimen experienced brittle failure at a crack extension of 0.01 in. and a load of 30 lb. The brittleness of failure for this system may be attributed to the possible incompatibility of unreacted Hycar CTBN 1872 rubber with other components. Normally, during the preparation of 3H resin, the carboxy end groups (-COOH) of 1872 react to open the epoxy ring to form a network of ester groups (-COOR). This reaction is thermodynamically favored at 160°C.

When 1872 is added as part of the curing agent, it may not react with the epoxy group at room temperature, and therefore will not enhance the fracture behavior of the resultant adhesive.

Further experiments were performed using lower quantities of Hycar in the 215 EEW resin. Table 4.1 shows the formulation details for all the trials. In all cases with reduced amounts of Hycar in the resin, the resultant formulations were all less viscous, and readily workable at room temperature. Results of fracture testing of bonded aluminum compact tension specimens are shown in Table 4.2. While fracture properties are somewhat reduced, compared with the original formulation, they are quite good for the entire range of Hycar additions (formulations nos. 4 and 7 being the extremes). In formulation no. 8, Jeffamine 400 was used in place of the normal curing agents. In the previous program this provided a very tough matrix, but poor moisture resistance.

Table 4.1. Adhesive 3H Viscosity and Property Enhancement

<u>Formulation</u>	<u>Resin</u>	<u>Extender/Toughener</u>	<u>Curatives/ Tougheners</u>	<u>Epoxy Equivalent Wt.</u>
Original	DER 331	13 pph bisazodiol/ 3 pph Hycar 1872	10 pph ATBN 1300 x 16 40 pph Epon V40	250
1	DER 331	6 pph bisazodiol/ 3 pph Hycar 1872	10 pph ATBN 1300 x 16 40 pph Epon V40	215
2	DER 331	6 pph bisazodiol/ 0 pph Hycar 1872	10 pph ATBN 1300 x 16 40 pph Epon V40	215
3	DER 331	6 pph bisazodiol/ 0 pph Hycar 1872	10 pph ATBN 1300 x 16 40 pph Epon V40 3 pph Hycar 1872	215
4	DER 331	6 pph bisazodiol/ 1.5 pph Hycar 1872	10 pph ATBN 1300 x 16 40 pph Epon V40	215
5	DER 331	6 pph bisazodiol/ 1.8 pph Hycar 1872	10 pph ATBN 1300 x 16 40 pph Epon V40	215
6	DER 331	6 pph bisazodiol/ 1.9 pph Hycar 1872	10 pph ATBN 1300 x 16 40 pph Epon V40	215
7	DER 331	8.8 pph bisazodiol/ 2.3 pph Hycar 1872	10 pph ATBN 1300 x 16 40 pph Epon V40	230
8	DER 331	6 pph bisazodiol/ 1 pph Hycar 1872	45 pph Jeffamine D400	215

Table 4.2. Fracture Testing of Lower Viscosity Formulations

Formulation	# Specimens	Peak Load (lb)	G	I (in.-lb)/in. ²	J
3H	10	165	5.8	11.9	8.7
#4	2	140	6.9	12.9	6.3
#7	3	135	4.0	12.7	6.2
#8	2	108	3.5	53.5	10.9

Decreasing the EEW of the 3H resin to 215 also reduces its viscosity. Reduction of Hycar CTBN 1872 rubber further reduces the viscosity, resulting in a very workable room-temperature resin. The formulations featuring reduced levels of Hycar all performed fairly well. Thus the decision was made to focus on formulation no. 4, featuring the lowest level of rubber addition, since it had the lowest working viscosity, and had good fracture properties.

4.2 Cure Acceleration Experiments

Another desirable property of a repair adhesive would be a rapid cure time to practical strength levels. We investigated additives to: 1) accelerate the room-temperature cure of adhesive 3H and 2) possibly increase 3H's moisture resistance without jeopardizing its fracture toughness. The literature suggested that imidazoles may accelerate epoxy room-temperature cure. We identified Curimid™ 2PIZ (2-phenyl-2-imidazole), manufactured by Polyorganix in Newport, Maine, as a candidate. Ten parts-per-hundred Curimide 2 PIZ were added to 3H in conjunction with the curing agents V40 and ATBN. DSC was run, and the Borchardt-Daniels kinetics program⁽²²⁾ used to calculate the theoretical cure time of the system at 50°C. The resultant time, 0.94 day, was somewhat less than that for 3H alone.

However, when we tested samples of this formulation by performing DSC tests after simulated cure periods, with and without Curimide, we saw no cure acceleration. As shown in Table 4.3, the formulations with PIZ have greater exotherms than plain 3H, indicating incomplete cure.

Table 4.3. DSC Results of Cure Acceleration Experiments

Sample	Cure Condition	DSC Analysis	
		Tg(°C)	Texo(°C)
3H + 10 pph 2 PIZ	50°C for 24 hr, 3 days R.T.	46.8	102.8
3H + 10 pph 2 PIZ	4 days R.T.	50.4	90.0
3H	50°C for 24 hr, 3 days R.T.	48.7	None
3H	4 days R.T.	41.9	83.4

Other candidates were considered, such as aliphatic aldehydes, which accelerate the cure of polyamines with epoxies, and low-molecular-weight polymercaptans, which are low-viscosity thioethers that can be utilized as epoxy adducts. These did not prove suitable, however, and no satisfactory means to reduce cure time was found. Of course, increasing temperature during cure will cause accelerated cure, down to very rapid (< five min) times.

4.3 Stress Relaxation of 3H-F4

The promising reduced-viscosity formulations (nos. 4 and 8) were subjected to a stress relaxation test to determine their resistance to degradation in high moisture environments. Stress-relaxation measurements were performed on 7-in. x 0.2-in. x 0.1-in. strips of cured adhesives. The strips were placed in a stress-relaxation jig in a humidity chamber set at 50°C and 95 percent relative humidity. (For a detailed description of the general test, see Page 27 of the Final Report, MML TR-90-26, February 1990.) Figure 4.2 is a plot of the stress relaxation curve for formulation 8. The equilibrium sustained stress of the bulk adhesive at 2 percent and 4 percent strain under 50 percent and 90 percent relative humidity is quite low. (The gauge length of the specimen in these tests was 5 in. Since the gauge length is so much larger than the other specimen dimensions, it is essentially a far-field test.) In essence, it has very little load-bearing capacity under severe environments. This is not too surprising, because we have previously shown (Final Report) that, although addition of Jeffamine D400 greatly increases fracture toughness, it severely reduces moisture resistance.

Figure 4.3 is a typical plot of the stress-relaxation curve for formulation no. 4 (which will subsequently be called 3H-F¹¹). The locus of points on the upper part of the curve represents the initial stresses when the adhesive strip is immediately strained. The locus of lower points represents the equilibrium stress on the adhesive strip when it relaxes fully. The last three points on the curve represent the stress on the adhesive strip as it is strained to failure (past 6

percent strain). This plot demonstrates that in addition to its dead load capacity, adhesive 3H-F4 can tolerate rapid loading, even under equilibrium high humidity conditions. In this instance, the failure occurred at approximately 70 percent of its ultimate tensile strength despite considerable elongation under high-humidity loading.

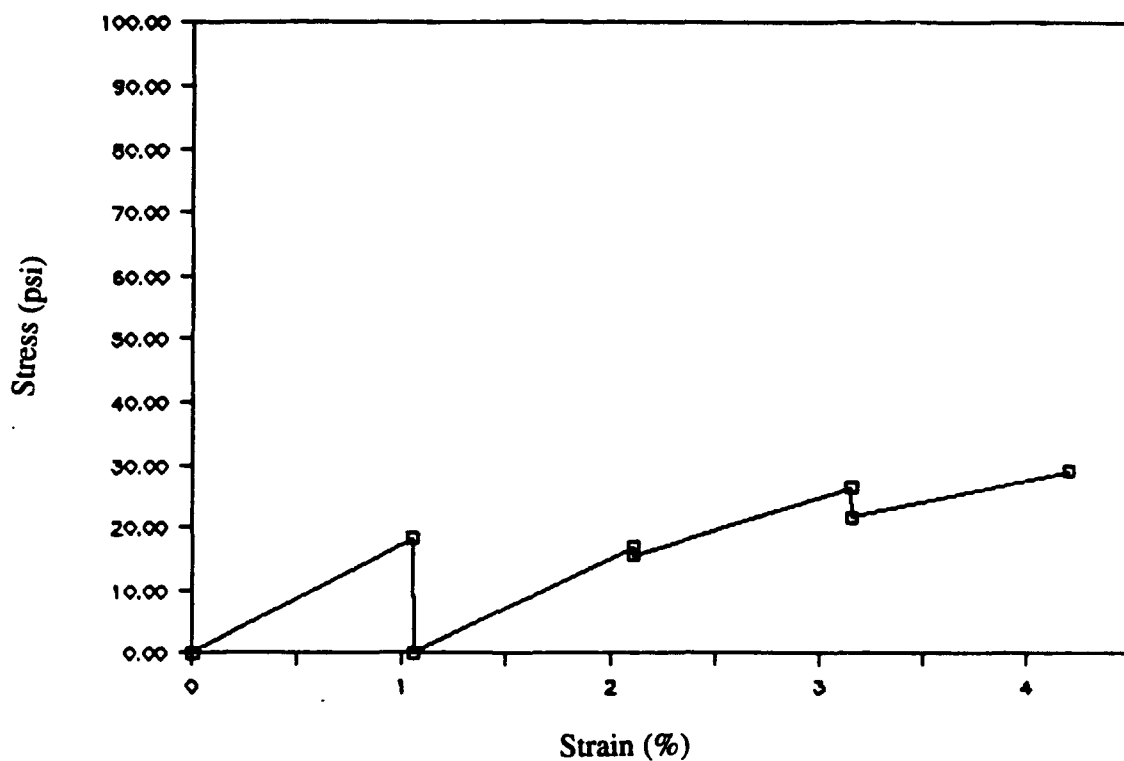


Figure 4.2. Stress relaxation plot for formulation no. 8, with Jeffamine 400 curative.

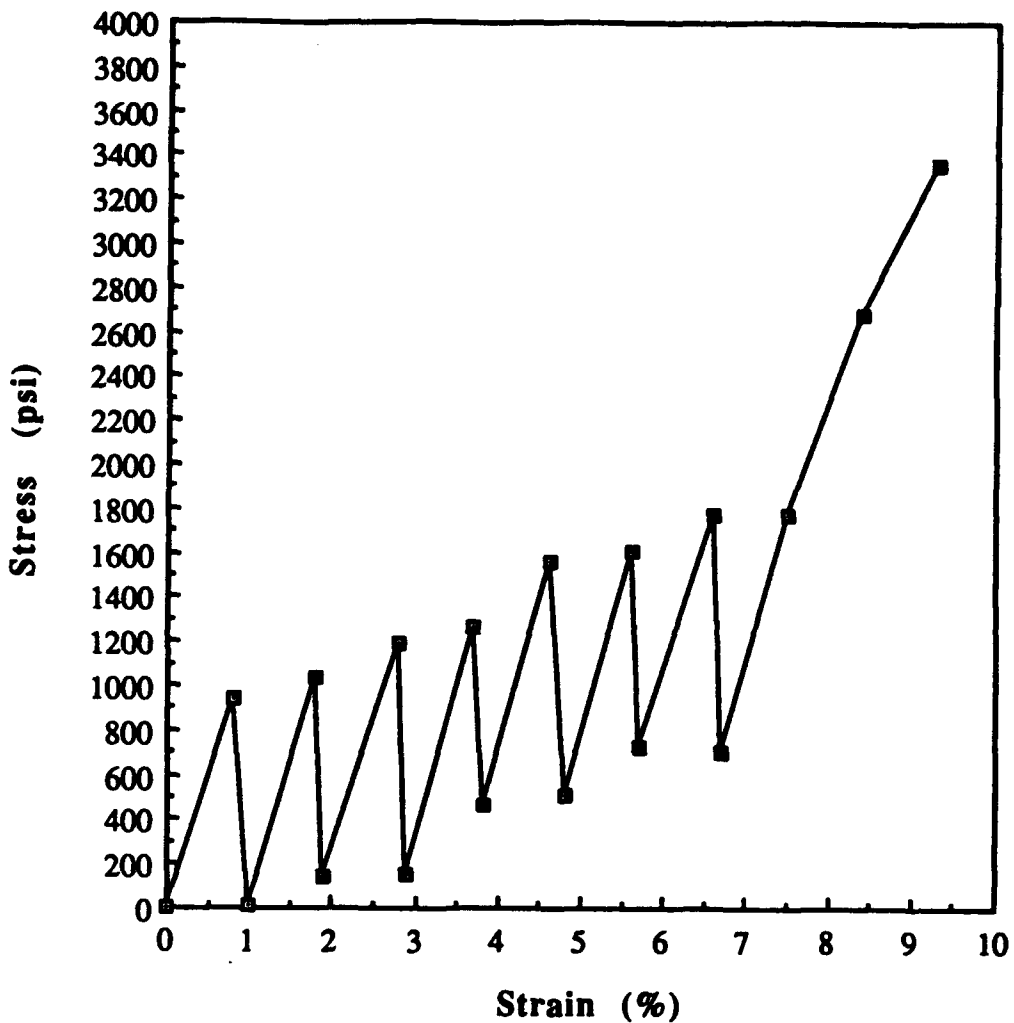


Figure 4.3. Stress-relaxation plot for adhesive 3H-F4.

Table 4.4 shows the stress-relaxation results for adhesive 3H-F4. Also shown for comparison are the results reported for adhesive 3H. The initial stress and equilibrium stresses are reported at 2 percent, 4 percent, and 6 percent strain.

Table 4.4. Stress-Relaxation Results for 3H-F4 and 3H.

Formulation	Initial Stress/Equilibrium Stress		
	2% Strain	4% Strain	6% Strain
3H-F4	950/140	1180/440	1500/690
3H	1220/230	1400/385	1600/520
Hysol 9394	2500/500	2900/1600	3800/2300

The equilibrium stresses for each system are comparable. In fact, at 6 percent strain the equilibrium stress for 3H-F4 is ~30 percent greater than adhesive 3H. More significantly, the results show that we can modify adhesive 3H to lower its viscosity without compromising its dead load strength in a humid environment.

4.4 Tensile Testing of 3H-F4

Tensile testing was performed on 7-in. by 0.2-in. by 0.01-in. cured strips of adhesive 3H-F4. The adhesive films were prepared and tested using the methods described in Semi-Annual Report #4, page 27. Figure 4.4 shows a plot of stress vs. strain for a typical specimen of adhesive 3H-F4. The plot is representative of a moderately strong, ductile adhesive system. The points on the curve represent the stress at each increment of strain applied by the jig. The curve is fairly linear up to 3.5 percent strain where yielding occurs due to plasticity of the adhesive until finally the adhesive strip is shown to fail at >5000 psi and 5 percent strain.

Table 4.5 shows the results for the tensile testing performed on strips of adhesive 3H-F4. Values for Ultimate Tensile Strength (UTS), Elongation, and Young's modulus are reported. Results were based on an average of the test results of five specimens. Results for adhesive 3H are shown for comparison.

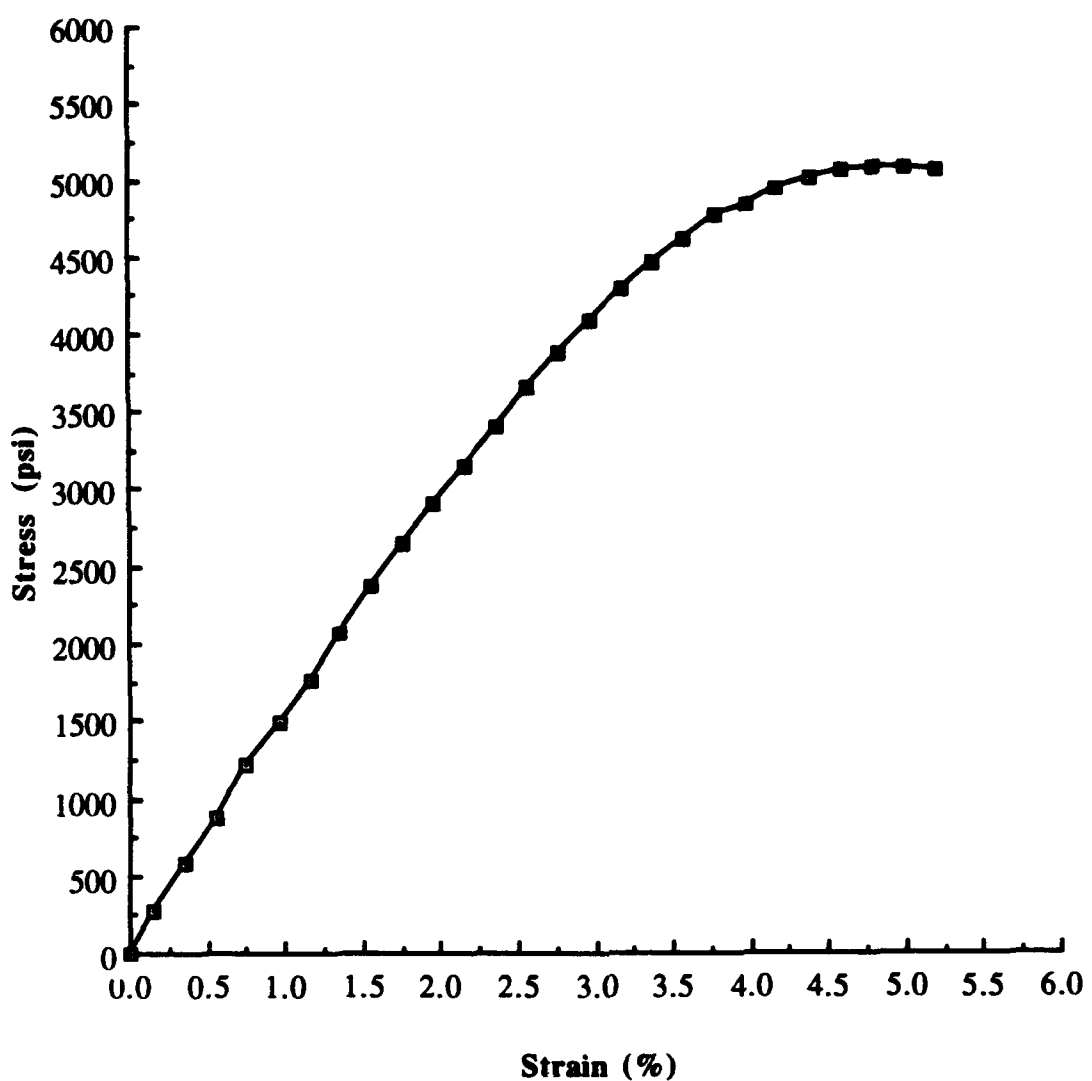


Figure 4.4. Stress-strain plot for neat adhesive 3H-F4 specimen.

Table 4.5. Tensile Testing Results of 3H-F4 and 3H

Formulation	UTS (psi)	Elongation (%)	Modulus (ksi)
3H-F4	5010	4.3	175
3H	6140	5.6	204
Hysol 9394	8970	3.1	495

It is apparent from the table above that reducing the viscosity of adhesive 3H causes a moderate reduction in its strength. As can be seen, the average tensile strength of adhesive 3H-F4 (EEW=215) is 1130 psi less than the average value of adhesive 3H (EEW=250). Elongation to failure and modulus are also lower for 3H-F4 when compared with 3H.

4.5 Lap Shear Testing of 3H-F4

Testing was performed on double lap specimens of 6061 T6 aluminum bonded with adhesive 3H-F4. The aluminum adherends were prepared in the usual manner: 1) Turco degreaser, 2) FPL etch, 3) phosphoric acid anodization. (For more information on surface preparation, see Final Report, Contract DAAK70-86-C-0084, page 24.) Adhesive 3H-F4 was applied to the adherend surfaces using two techniques: 1) The adhesive and curing agents were weighed into a cup, hand mixed and manually applied onto adherends, and 2) an adhesive mixing "gun" was used to dispense the adhesive directly on the adherends. In the second case, the epoxy resin was placed in the larger cartridge and the curing agents were placed into the smaller cartridge on a Ratio-Pak model PPM-300HT adhesive gun containing a static mixer; then the adhesive was pushed out of the gun at a volume ratio of 4:1 (3H-F4 resin:curing agent), mixed together during travel along the six in. "motionless mixer" tube, and directly applied to the adherend. The gun applicator and the application technique are shown in Figures 4.5 and 4.6. The specimens were cured for 16 hr at ambient temperature and 7 hr at 70°C. Double lap shear testing was performed on an Instron model 1125 mechanical tester. The crosshead speed was constant at 0.05 in./min until the specimens failed.

Table 4.6 shows the results for double lap shear testing of adhesive 3H-F4 and 3H-F4 when applied with the applicator gun. Also shown for comparison is the result for adhesive 3H. Note that the aluminum adherends begin to yield at 5500 psi, and test values above this point could be higher with stiffer adherends.

Table 4.6. Double Lap Shear Results

Formulation	Shear Strength	# Test Specimens	Failure
3H-F4	4950	10	Adhesive/Cohesive
3H-F4 (applicator gun)	5720	4	Adhesive/Cohesive
3H	5600	5	Adhesive/Cohesive
Hysol 9394	6100	5	Adhesive/Cohesive

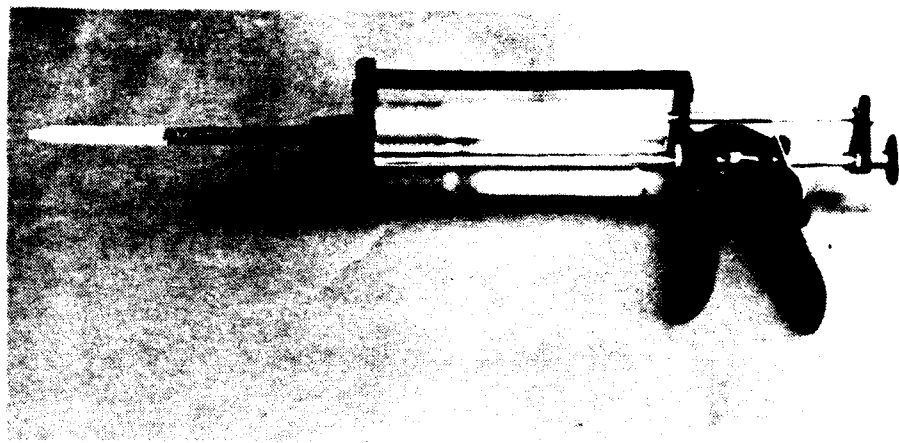


Figure 4.5. Adhesive applicator gun.

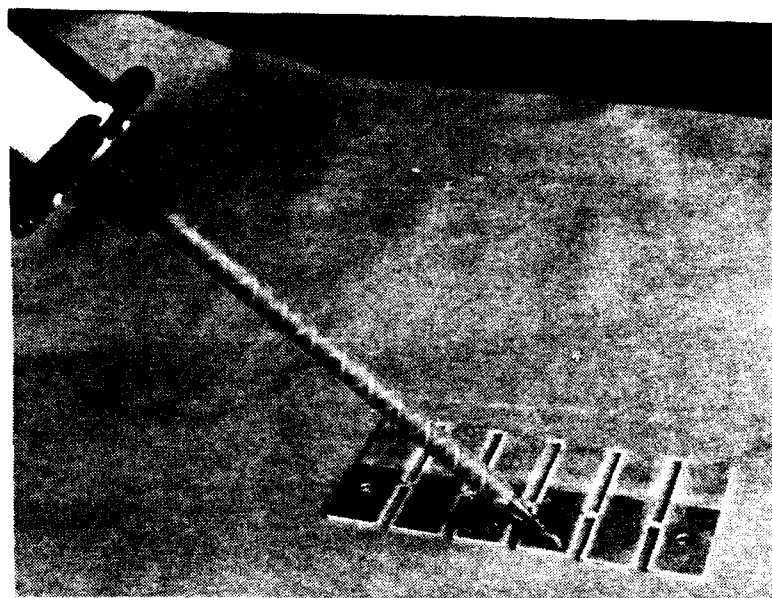


Figure 4.6. Applying 3H-F4 adhesive to double lap shear specimens.

The hand-mixed neat tensile specimen results (5010 psi) correlate very well with the aluminum double-lap shear test value (4950 psi). However, the double lap shear specimens prepared using a gun applicator had a higher strength than the neat adhesive (5720 psi). We suspected that there might have been a difference in mixing ratio of part A to part B between the hand mixed and adhesive gun-applied cases.

The hand-applied material was mixed by weight, 2 parts of part A to 1 of part B. The gun applicator dispenses by volume. The volume ratio used for the lap shear specimens was 4:1. Our best efforts to accurately measure the densities of the two parts did not yield a sufficiently good result to determine the exact densities of the two components; therefore we cannot determine how closely comparable the two mixing techniques are. The difficulty in measurement is removing all air bubbles in an accurately measured volume. Both parts have an apparent density between 0.75 and 0.90 gm/cc, and the two parts do not appear to significantly differ in density, so that 2:1 by weight or volume should be essentially the same.

We prepared thin neat adhesive films of cured 3H-F4 using various mixing ratios (by weight) for tensile testing, in the same manner reported in "Semi-Annual Report #4, MML TR 92-40C." Thin films of each ratio were cured between release-film-covered aluminum plates. Roughly 1-cm-wide test strips of the cured adhesive were cut out and tested in an Instron test machine. The average results for three specimens for each mixing ratio are shown in Table 4.7.

Table 4.7. Neat Adhesive Strip Tensile Strengths as a Function of Mixing Ratio

Adhesive Mixing Ratio (by weight)	Tensile Strength (psi)	Standard Deviation (psi)
2:1	5840	+690
3:1	4320	+550
4:1	3880	+570
5:1	5870	+470

Both the 3:1 and 4:1 films broke mostly at the edge of the sample grips, rather than in the gauge section of the test specimen. Thus the quoted tensile strength values for these ratios are lower than the actual strength of the adhesive material. The 2:1 and 5:1 ratio films did provide good values. Their apparent strengths, ~5850 psi, match the gun applicator applied lap shear strengths. In addition, the films prepared with these widely different mixing ratios

had very similar strengths, essentially eliminating mixing ratio as a critical factor in achieving high strength. In fact, it appears that there is a wide latitude in allowable mixing ratio. This is an attractive feature of a repair kit adhesive that would be applied under less-than-ideal conditions.

4.6 3H-F4 Adhesive Preparation

Given its excellent mix of basic properties, including relative ease of mixing and application, good strength and moisture resistance, and outstanding fracture toughness, the 3H-F4 formulation was chosen as the optimized low temperature curing adhesive to be used for the demonstration article. We developed a larger batch preparation procedure to facilitate producing sufficient quantities of the adhesive for this purpose. The following procedure was used to manufacture 1 liter batches.

Adhesive manufacture is completed in four stages. First, to ensure chemical purity, terephthaldehyde is recrystallized from terephthalidicarboxaldehyde (obtained from Aldrich, #T220-7). Secondly, the 4,4'-dihydroxyphenyl-p-iminobenzene (bisazodiol) monomer is prepared. The part A resin is processed, combining these precursors with DER 331 epoxy resin. Finally, the part B resin is mixed together. These processing steps are described in the following sections.

4.6.1 The Bisazodiol Monomer Reaction

Reagent grade ethanol (500 ml) is added to a three-neck flask and subjected to a nitrogen purge via bubbled gas for one hour. While stirring with a magnetic stir bar, 25.0g (0.186 moles) of terephthaldehyde is poured into the three-neck flask. With continued mixing and purge, 40.7g (0.372 moles) 4-aminophenol is slowly added. The mixture changes color from white to yellow upon reaction, and with continued stirring a fine yellow precipitate is formed. Total mixing time of the reactant with purge is two hours. The mixture is then filtered, using qualitative filter paper and a buchner funnel, and washed with 1000-ml ethanol. The solids are placed in a vacuum oven at 50°C for four hr at roughing pump pressure (~ 50-150 microns) in order to dry them. Upon cooling, the bisazodiol monomer is ground to a fine yellow powder with mortar and pestle.

4.6.2 Part A Production

Hycar 1872 (50.0 g, B.F. Goodrich) is placed into a one-neck flask, and dissolved in 450.0 g reagent grade methylene chloride (CH_2Cl_2). The Hycar- CH_2Cl_2 mixture is then stirred a minimum of 24 hr prior to the manufacture of 3H-F4 resin to ensure homogeneity. When the Hycar- CH_2Cl_2 mixture is homogenous, i.e., there are no solids visible, 1000g of DER 331 resin is poured into a 5000-ml three-neck flask. Then a specified weight of the Hycar- CH_2Cl_2 mixture is added to the DER 331 resin. The amount of Hycar- CH_2Cl_2 mixture added to the DER 331 resin is calculated as follows:

$$\text{wt Hycar-CH}_2\text{Cl}_2 \text{ mixture} = (0.15) (\text{wt DER 331}), \text{ i.e., } 150 \text{ gm}$$

The DER 331 resin - Hycar mixture is then heated via an oil bath to 80°C and stirred under roughing pump vacuum, such that the reduced pressure insures the removal of methylene chloride from the mixture. After approximately 2 hr at 80°C, the mixture should be an off white color and bubble free.

At this time the temperature is raised to slightly greater than 120°C and stabilized. The vacuum is then removed and a triphenylenphosphine ($\Phi_3\text{P}$) catalyst (Aldrich #T8,440-9) is poured into the flask. The vacuum is then reapplied. The amount of triphenylphosphine added is calculated as follows:

$$\text{wt } \Phi_3\text{P} = (0.002) (\text{wt DER 331}), \text{ i.e., } 2 \text{ gm}$$

After approximately 20 minutes, the vacuum is removed, and the bisazodiol monomer is poured into the reaction flask. The amount of monomer added is calculated by solving:

$$\text{wt bisazodiol} = (0.058) (\text{wt DER 331}), \text{ i.e., } 58 \text{ gm}$$

The vacuum is then reapplied and the temperature is increased to 155 to 160°C and held for 2 hr. The color change associated with the reaction is from reddish brown to yellow. If the temperature exceeds 170°C, the mixture may become overheated and the color will change back to reddish brown. Preliminary screening indicates that the color change back to reddish-brown does not effect the final properties, but the number and type of tests completed with

the adhesive in this condition is limited. Subsequently, use of adhesive 3H-F4 in the "burnt" condition has been rejected.

After the 2-hr mixing time, both heat and vacuum are removed. Once the temperature has decreased to approximately 130°C, the adhesive can be poured into a storage container. The adhesive does not require stirring during the cooling period. Furthermore, tests suggest that if stirring is omitted during cooling, the amount of residual air bubbles remaining in the final product are reduced.

4.6.3 Part B Production

Part B of 3H-F4 is a simple mixture of two commercial components. one part (by weight) of B.F. Goodrich ATBN rubber, "Hycar 1300X16", is added to four parts of Miller Stephenson Chemical Company's "Shell Epon curing agent V40". Since the rubber is quite viscous, mixing is facilitated by heating the components in a water bath to 50° to 60°C. After thorough mixing, the Part B material can be poured in an applicator cartridge or storage container.

The adhesive should be used in a 2:1 to 3:1 volume ratio, part A to part B. Some heating facilitates mixing. We have had good success immersing applicator cartridges in hot tap water baths, ~40°C, which improves flow characteristics and reduces the pressure required to dispense the adhesive through the mixing tube applicators.

4.7 Vinyl Functional Additions - 3HVT

We investigated modifying the basic 3H formulation with a vinyl additive to hopefully improve moisture resistance and workability of the adhesive.

The first part of the modification was a chain advancement reaction in which 4,4'-dihydroxyphenyl-p-iminobenzene (bisazodiol) reacts and opens the epoxy ring in what is called an etherification reaction. This reaction increases the effective EEW of the resin to 215. A 500-ml reaction flask equipped with a mechanical stirrer was charged with 105.9 g DER-331, 0.2 g triphenylphosphine, and 2.5 g of bisazodiol. The triphenylphosphine was used as a catalyst for the etherification reaction. Under argon sweep the flask was heated in an oil bath to 160°C with stirring and was maintained at that temperature for 2 hr, then decreased to 80°C. The color of the reaction mixture was clear yellow.

The second part of the modification was the addition reaction, wherein 4-pentenoic acid reacts and opens the epoxy ring thus forming an unsaturated ester side chain. Ten ml (0.1 mole) of 4-pentenoic acid was added to the bisazodiol advanced resin under an argon sweep. The reaction mixture was stirred at 80°C for 26 hr, whereupon the vessel was removed from the heat and the resulting clear yellow resin was transferred to a glass container. Infrared spectra of 4-pentenoic acid and of the resulting resin were recorded that indicated that the esterification reaction had gone to completion.

4.7.1 Curing of Resin and Film Preparation

The curing step was initiated with the addition of 10 parts ATBN 1300 X 16 (rubber) and 40 parts Epon 40 polyamide curing agent to 100 parts modified 3H resin. After thorough mixing a small amount of the sample (0.005 g) was placed in a disc sample pan, hermetically sealed, and then heated from room temperature to 250°C under an argon atmosphere in a TA Instruments model 2910 differential scan calorimeter, in order to study the curing reaction. A small amount of the resin was also smeared onto an NaCl disc and then placed in a Nicolet 5SXC Fourier Transform Infrared Spectrometer. Spectra were recorded initially, after curing at 16 hr in ambient environment, and after the disc was postcured at 70°C for 7 hr.

The data obtained from the DSC thermogram of modified 3H were transferred to a software program "Borchardt and Daniels Kinetics Data Analysis Program," which calculates the following kinetic parameters: reaction order, heat of reaction, activation energy, and Arrhenius frequency factor. From these parameters, we were able to plot the conversion time at various temperatures and approximate the amount of time needed to cure the resin at the temperature of choice. The results of this analysis indicated that cure would reach completion in 17 hr at 30°C, 8 hr at 40°C, and 5 hr at 50°C.

The cure state of the adhesive was also monitored by examining the infrared absorption peak for the epoxide unit, seen at approximately 915 cm^{-1} . As the resin is curing, the ring opening reaction can be monitored by observing the decreasing absorbance of the 915 cm^{-1} peak.. After 16 hr at ambient temperature, the epoxide absorption decreased by more than 50 percent, and after a post-cure for 7 hr at 70°C the reduction was close to 90 percent.

4.7.2 Mechanical Testing

An adhesive film was cast by pouring approximately 30 g of the modified resin/curing agent mixture onto a silicone release sheet on top of a 12 in. x 5 in. x 1 in. aluminum block. A second release sheet was placed on top of the resin then the adhesive pool was then spread evenly across the area of the block by using a glass rod. Another 12 in. x 5 in. x 1-in. block containing 0.010-in. shims was placed on top of the resin and the entire system was clamped and the adhesive allowed to cure for 16 hr at room temperature and then was postcured for 7 hr at 70°C. The adhesive film was then removed and cut into 7 in. x 0.2 in. x 0.01 in. strips for tensile and stress relaxation testing.

Tensile testing of 3HVT strips was performed on the stress fixture described in Section 4.3. The strips were clamped into place within the jig and then strained (by hand) at a quasi-constant speed to failure.

Table 4.8 gives the results of the tensile testing performed on 3HVT. The results are based on an average of six specimens. Also shown for comparison are the tensile results for the original 3H formulation. Overall, 3HVT's tensile properties were reduced 30 percent over the original formulation. We hypothesize that the reduction in mechanical performance is a product of the uncured vinyl end groups of the ester unit of the 4-pentenoic acid.

Table 4.8. Tensile Results for Adhesive 3HVT

Specimen	UTS (psi)	Elongation (%)	Modulus (ksi)
1	4550	4.2	164.6
2	4500	4.8	148.6
3	4165	3.5	156.0
4	3680	3.5	137.7
5	3890	4.5	135.1
6	4250	3.7	152.9
avg	4170 ± 0.5	4.0 ± 0.5	149.1 ± 11.2
Original 3H	6140	5.6	204.3

DSC and infrared analysis shows that the curing mechanism for the epoxide groups in 3HVT is thermodynamically favorable at, or slightly above, ambient temperature. However, no evidence can be seen that supports the polymerization involving the unsaturated unit of the modified resin. For the vinyl-terminated groups attached to this unit, an elevated

temperature is most likely needed to effectively react the double bonds in what is called a Michael addition. If left uncured, the unsaturated ester groups most probably act as a plasticizer, which effectively reduces the overall tensile properties of the cured adhesive. Given the lack of a practical way to ensure this reaction at low temperatures, further development on this formulation was canceled.

4.8 Field Repair Technology

In order to deliver a readily applied repair kit adhesive, we have investigated two companies that manufacture adhesive application guns and cartridges: 1) Lord and 2) Techon Systems, Inc. Both systems feature a two-cartridge gun system, with a mixing applicator tip so the operator merely needs to squeeze the handle (or trigger on pneumatically operated guns) to dispense ready mixed adhesive in a precisely controlled fashion. Techon supplies a variety of manual and pneumatically operated cartridge guns which can handle a wide range of viscosities from 5,000 to 200,000 centipoise (cps). This system handles large (700 ml) caulking gun-sized containers, and would be most suitable for manufacturing and depot repair operations. The Lord system is designed for small quantities, is hand operated, and is inexpensive. This system is better suited for field use.

The Lord PAK 50 hand applicator (Figure 4.7) consists of three parts: the dispensing gun, the mixing tube tip, and the dual-chamber storage cylinder. The storage cylinder clips into the dispensing gun, and the mixing tip replaces a blank storage tip. The cross section of one storage chamber is one half that of the other, and the dispensing gun ensures equal displacements of material in the two chambers. Thus, the correct mixing ratio is maintained as the applicator squeezes out the desired volume of adhesive. The mixing tip automatically causes thorough mixing, and the adhesive that emerges can be directly applied to the bonding area. This packaging guarantees successful use of the adhesive. The reusable dispensing gun costs \$31 in single unit quantities, and the storage cylinder mixing tip cost \$3.50. The entire package fits in a 6-in. x 3-in. x 2-in. space, and can be utilized as easily in the field as in an assembly area. Pneumatically operated dispensing guns are also available for production line use. A gun system with spare parts and loaded adhesive tubes has been delivered to Belvoir RDEC for evaluation. Note that placing tubes in a hot water bath (~40 °C) prior to use in the applicator gun facilitates resin flow and mixing.

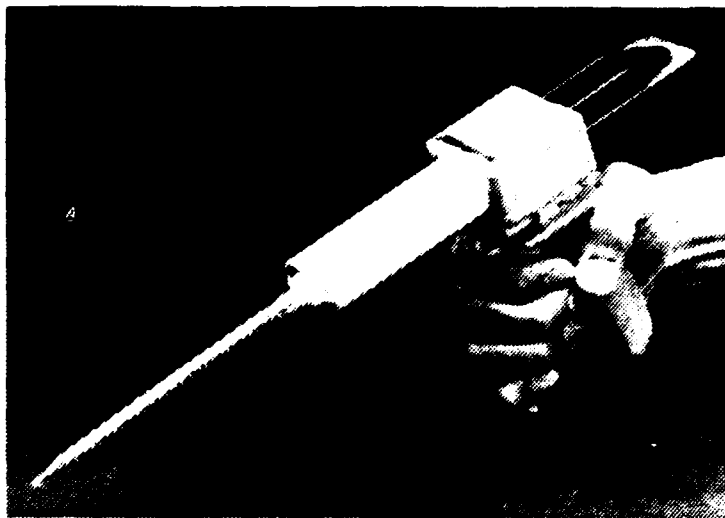


Figure 4.7. Lord PAK 50 dispensing and mixing adhesive gun.

4.9 Sealant Investigation

A number of sealants were tested to determine if they would permit a nonmoisture-resistant adhesive system to perform better in warm-humid environments. Theoretically, if the sealant prevented the penetration of moisture into the adhesive, the adhesive's load bearing capacity would be retained when subjected to stress relaxation under high humidity conditions.

Film strips of MML 3H and Hysol 9394 adhesives were prepared as for stress strain jig testing and then painted with each sealant. Care was taken to paint the front, back, and sides of each strip for a complete seal. The strips were allowed to cure at ambient temperature for 16 hrs then post-cured for 7 hrs at 70°C. Stress-relaxation measurements were performed at 50°C and 90 percent relative humidity.

Moisture absorption testing was also performed on candidate sealants and sealant coated adhesive test strips to determine their usefulness in field applications where moisture-induced deformation is needed to retain maximum bond strength of the adhesives. The sealants tested included Shin Etsu's silicones KE-44W, KE-45T, and KE-348T, and

fluorsilicone FE-125; Uniroyal Silaprene M6792, and Dow Corning's silicones 3140 and 3145.

4.9.1 Preparation of Sealant Films

Film specimens of the sealants alone and of adhesives 3H and Hysol 9394 coated with the sealants for moisture absorption and stress-relaxation testing were prepared in the same manner as previously. For the sealant-coated adhesive preparation, 10-mil-thick films of adhesive 3H and 9394 were cast and cured for 16 hrs at room temperature, then postcured for 7 hrs at 70°C. Sealant was applied to one side of the adhesive film, and allowed to cure for 16 hrs at ambient temperature. Sealant was then applied to the second side and also cured at ambient for 16 hrs. The strips were then cut to testing size. For moisture absorption, the strips were cut to 3 in. x 1 in. x 0.010 in. strips; for stress-relaxation they were cut to 10 in. x 0.200 in. x 0.010 in. The sides of the strips were then sealed and cured for 72 hrs at ambient temperature. The strips used for moisture and stress-relaxation testing are shown in Figure 4.8.

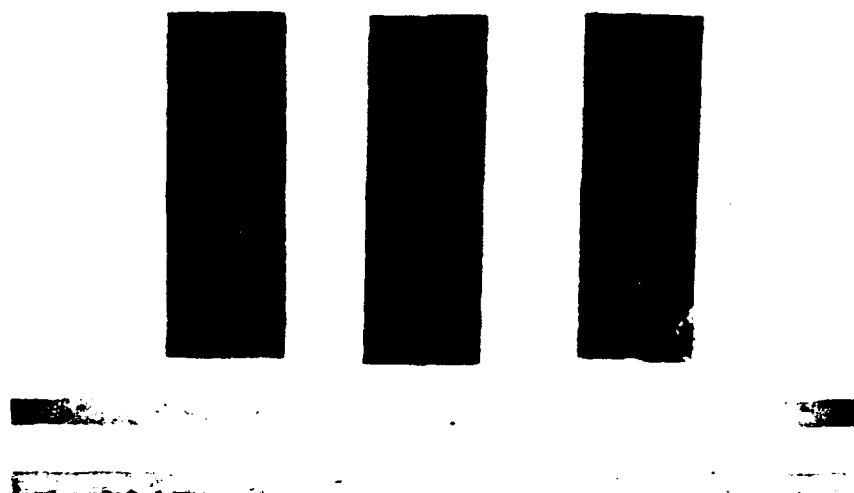


Figure 4.8. Optical macrograph of test strips used for moisture pickup (top) and stress relaxation (bottom) testing.

4.9.2 Moisture Absorption

Moisture uptake in the test specimens was measured by direct water immersion according to ASTM D570-81, "Standard Test Method for Water Absorption of Plastics." Each specimen was fully immersed in separate water-filled containers at ambient temperature. Prior to immersion, the specimens were weighed on a Mettler H31 Ar analytical balance to the nearest 0.0001 g and their initial weights recorded. The weight of the glass slide was subtracted so that a proper percentage weight gain could be determined. After various exposure times, the specimens were removed from their separate containers one at a time, towel dried, immediately weighed, and then returned to their containers. The percent weight gain was calculated and recorded as a function of immersion time.

Figure 4.9 shows water absorption plots of the direct water immersion experiment for the sealant films. Dow Corning 3140 and Shin Etsu FE-125, KE-44W, KE-348T, and KE-45T sealants are included. The Dow Corning 3145 sealant absorbed no moisture and has not been included. With the exception of KE-348T, all the sealants tested have reached apparent equilibrium.

The best performers are sealant 3145, which gained 0 percent over 480 hrs, and 3140, KE-44W, and KE-125 which gained ~ 0.2 percent water. KE-45T absorbed approximately 0.5 percent moisture and KE-348T, which had not reached equilibrium, absorbed up to 1.6 percent water.

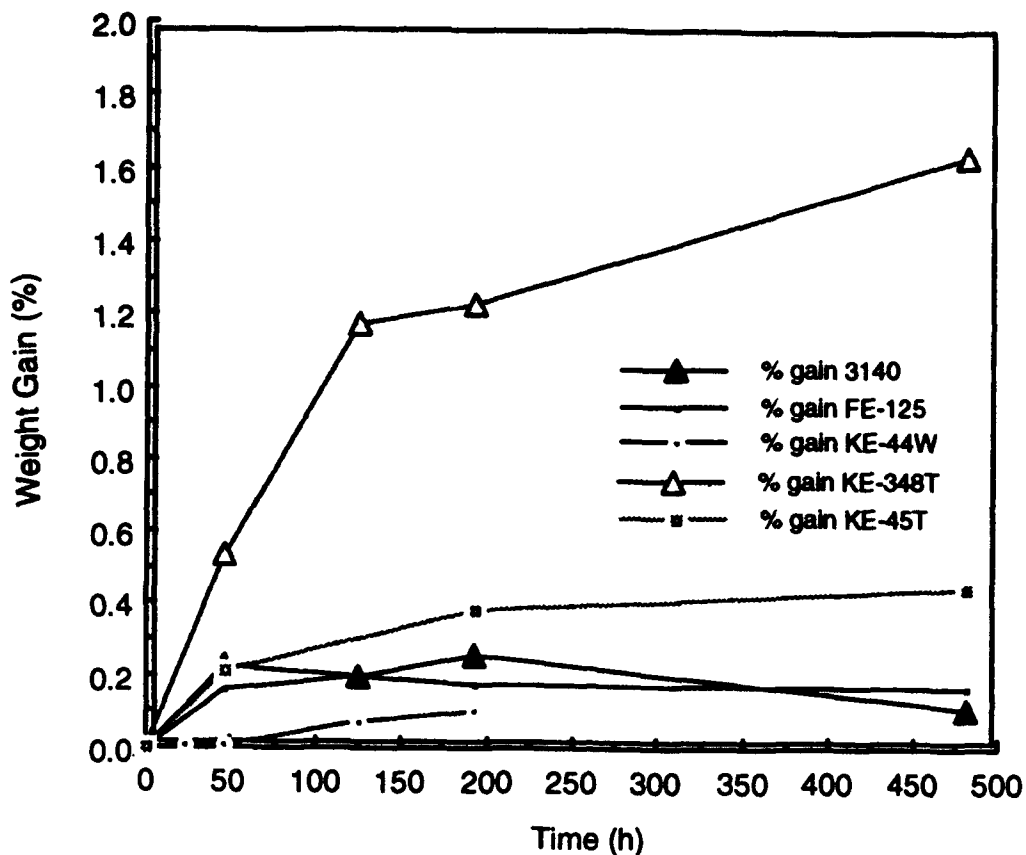


Figure 4.9. Water absorption weight gain for sealant materials alone.

4.9.3 Moisture Absorption of Coated Adhesives

Figure 4.10 contains water absorption plots of the direct water immersion experiment on films of adhesive 3H by itself and coated with Shin Etsu's KE-45T, KE-348T and KE-44W, and Product Research Corporation's P2 (polysulfide) sealant. With the exception of adhesive 3H coated by the polysulfide sealant, all specimens had reached apparent equilibrium, with the KE-44W specimen reaching apparent equilibrium in approximately half the time.

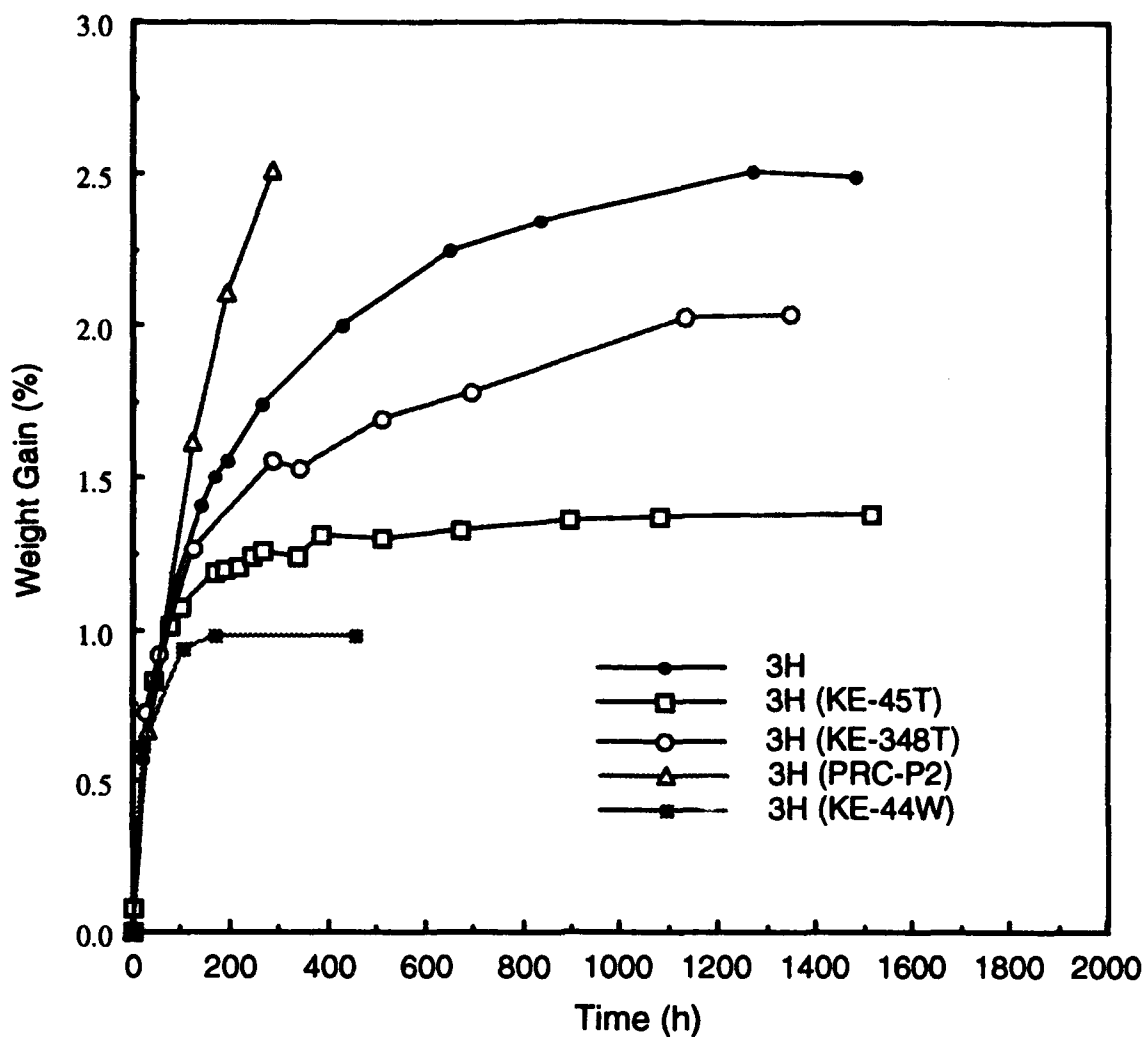


Figure 4.10. Water absorption weight gains for adhesive 3H alone and coated with sealants.

Figure 4.11 shows the water absorption plots for Hysol 9394 adhesive without sealant, coated with KE-45T sealant, and P2 sealant. The plots show that the addition of a sealant coating does provide some reduction in water uptake to the adhesive. The specimens coated with KE-45T sealant absorb approximately half the amount if no sealant were used. The P2 sealant again shows little promise. The specimens coated with this sealant already reached the water absorption threshold of the specimens coated with KE-45T sealant and are not even close to equilibrium.

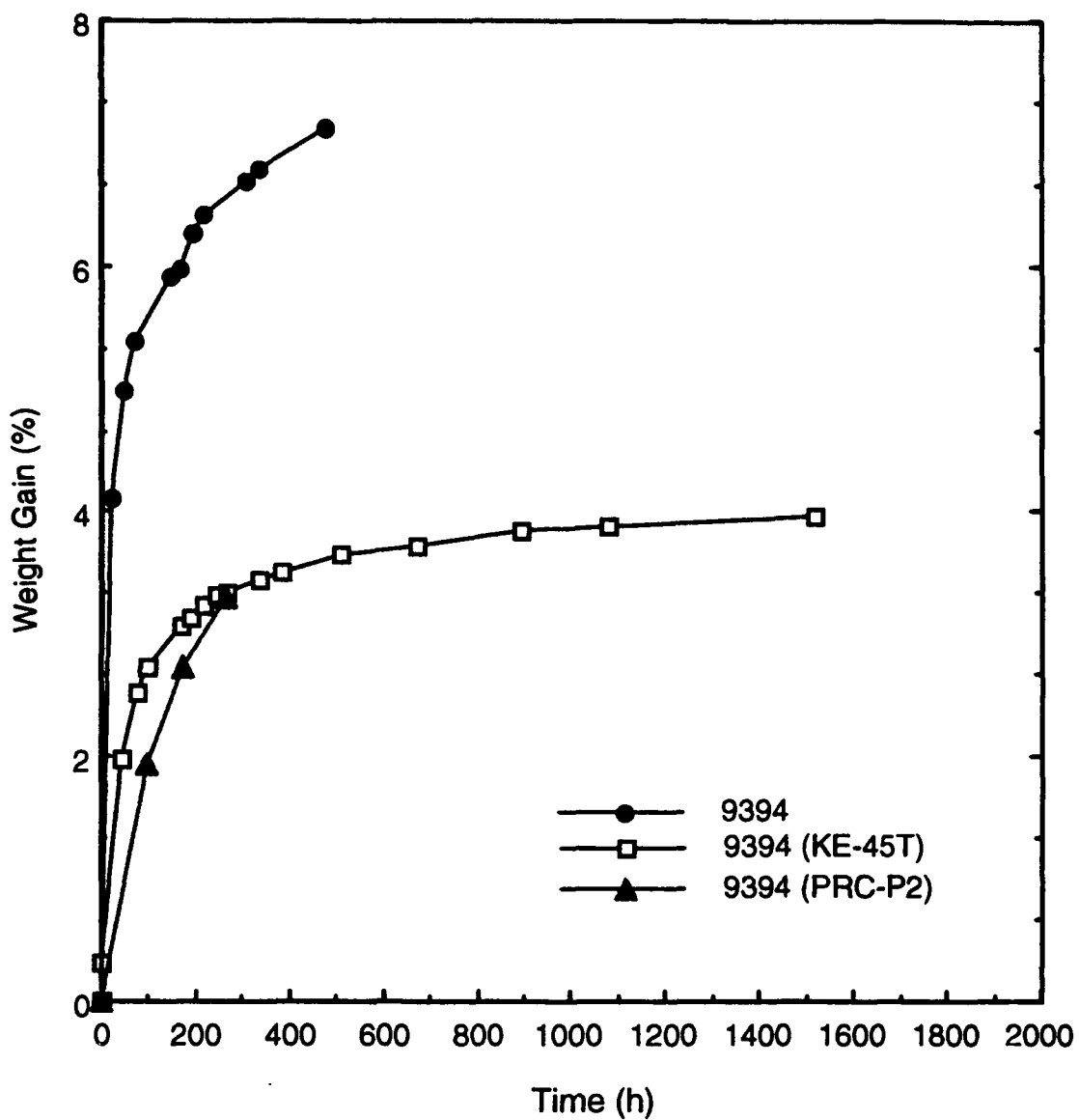


Figure 4.11. Water absorption weight gains for Hysol 9394 adhesive coated with sealants.

Interpreting the data from the sealant weight-gain experiments, one might conclude that most of the sealants studied would be viable candidates for protecting adhesively bonded joints from moisture ingress. The results from the sealant-coated adhesive experiments, however, tell a different story. The results of the sealed 3H film experiments show that all specimens gain at least 1 percent moisture. However, three out of the four sealants studied showed improvement over the unsealed film. KE-44W showed the best protection. The

results of the sealed 9394 film experiments also show that the two coated specimens still gain a substantial amount of water.

Results of the P-2 sealant-coated adhesive 3H and 9394 films tests indicate that this sealant gave no protection against water ingressoin. 3H film specimens coated with this sealant show a higher percentage water weight gain than 3H containing no sealant, possibly due to water absorption in the sealant. In theory, polysulfides could provide better moisture protection since the sulfur atom in the sealant does not hydrogen bond to water as well as the -OH constituent in the cured epoxide. However, the sulfur atoms in polysulfides are very large. When the sealant is fully cured, gaps may be created between the polymer chains that will allow water molecules to pass through and penetrate to the epoxide film, much the same way that holes in a screen allow smaller particles to pass. Moisture uptake alone is not a reliable indicator for determining mechanical performance, and therefore further testing in stress relaxation jigs was necessary to fully evaluate the sealants.

4.9.4 Stress Relaxation

Stress relaxation testing was performed on 10 in.x 0.2 in. x 0.01 in. strips of adhesive 3H coated with Shin Etsu's KE-45T, KE-348T, and KE-44W silicone sealants, Dow's 3145 silicone sealant, and PRC's P2 polysulfide sealant. The sealed 3H adhesive strips were placed in a self-contained stress jig positioned inside a humidity chamber controlled at 50°C and 95 percent relative humidity. After reaching equilibrium, the strips were placed under roughly 10 percent of their ultimate strain. The relaxation of the stress as the adhesive stretched was logarithmic; the measured stress level decreased until an equilibrium was reached after 8 to 16 hrs. At that point another increment of strain was applied and the adhesive allowed to relax again. The procedure was repeated until the strain level exceeded 6 percent. The results were a measure of sustainable stress as a function of strain for a sealed bulk adhesive system in equilibrium with its environment. After 6 percent strain, the specimens were loaded rapidly to failure and the stress at each increment of strain was recorded. Further information on the stress relaxation technique can be found in "Moisture-Resistant, Low-Temperature-Curing Adhesives Final Report", Contract #DAAK70-86-C-0084, Section 3.3.

Moisture absorption alone is not a discriminator of the mechanical performance of an adhesive that is placed under duress such as heat and humidity. The phenomenon of stress-relaxation in most instances is related to the amount of moisture absorbed and is a good

indication of how an adhesive will perform under these adverse conditions. When placed under strain, an adhesive will stress-relax much like a rubber band. In hot, humid environments its stress-relaxation is exorbitant. Hypothetically, adding a coating over the adhesive or adhesive joint should improve its mechanical behavior due to reduced ingress of moisture into the adhesive bond-line.

Figure 4.12 shows the stress relaxation curve for adhesive II-3HA coated with Silaprene M6792 sealant. The equilibrium-sustained-stress is quite low, which indicates that the sealant had no beneficial effect on the moisture resistance of II-3HA adhesive.

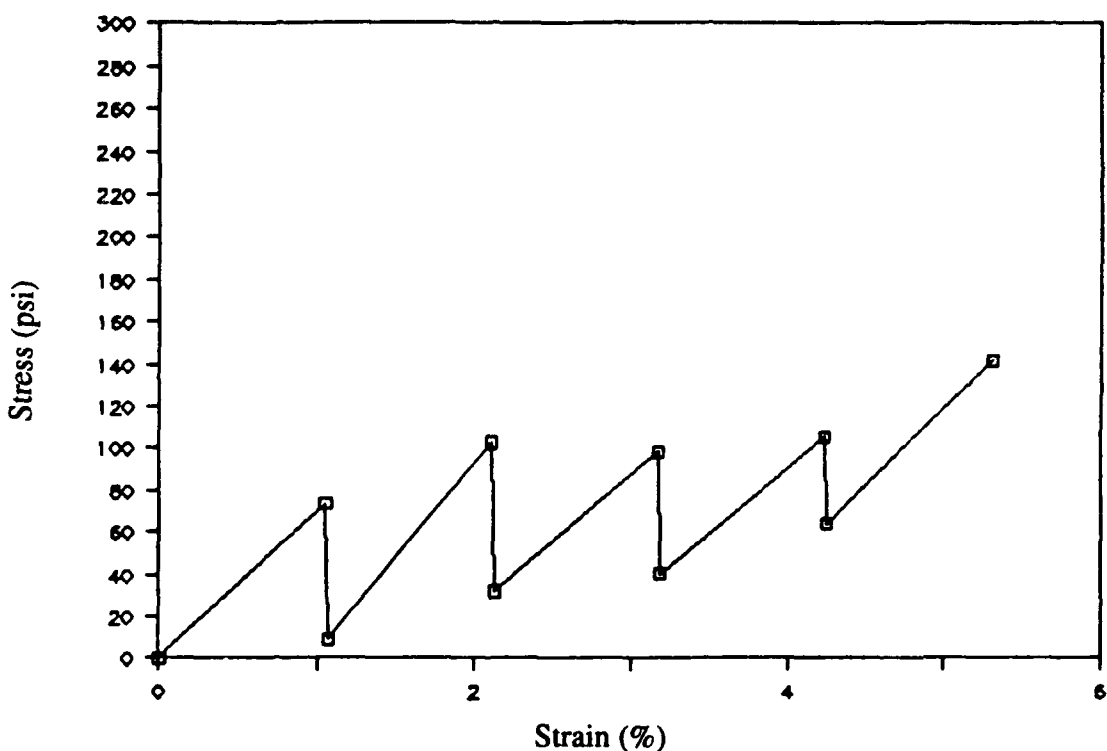


Figure 4.12. Stress relaxation curve for 3H adhesive coated with Silaprene M 6792.

Plots of the stress-relaxation behavior of adhesive 3H that has been coated with Dow's 3145 sealant, Shin Etsu's KE-348T, KE-45T and KE-44W sealants, and PRC's P2 sealant are shown in Figure 4.13. Shown for comparison is the stress relaxation of 3H containing no sealant. It can be seen that the sealants have no positive effect on the stress-relaxation behavior of adhesive 3H. Their equilibrium stresses at 6 percent strain appear to be equal or lower than that of uncoated 3H. Also shown for each sealant plot is its rapid

loading behavior at strains exceeding 6 percent. Each system has reserve energy to handle dynamic loading at levels above their dead load. However, the stress levels at failure are not better than the uncoated 3H system.

Table 4.9 gives the tabulated stress-relaxation results for 3H coated with the sealants. Shown are the initial stress and equilibrium stress at 2 percent, 4 percent, and 6 percent strain for each system. The results are consistent with the graphs shown on the previous page. The sealant-coated 3H systems retain less equilibrium stress at 6 percent strain than uncoated 3H. Furthermore, polysulfide-coated 3H gave considerably lower equilibrium stress values than the others. The fact that the polysulfide-sealed adhesive 3H gains far greater amounts of moisture would explain this behavior. Indeed water has an undesirable effect on the mechanical behavior of this sealant.

Table 4.9. Stress Relaxation Results: Adhesive 3H Coated with Various Sealants

Sealant	Initial Stress/Relaxation Stress (psi)		
	2% Strain	4% Strain	6% Strain
3H (No Sealant)	1110/30	1390/510	1570/730
Dow 3145	750/70	880/240	1050/450
KE-44W	1360/240	1600/470	1800/670
KE-348T	990/180	1400/470	1600/640
PRC-P2	830/65	900/160	1030/210

It is very apparent that the use of sealants on our adhesive 3H does very little to protect it from the detrimental effects of moisture. Although the sealants themselves absorb very little moisture (with the exception of PRC's P2) in static water immersion testing, the coated systems are shown to absorb moisture at a percentage that is only slightly lower than 3H with no coating. When an adhesive is strained, as in the stress relaxation experiment, the amount of moisture it absorbs is greater than if it were not strained. Since the stress-relaxation behavior of sealant-coated adhesive 3H is no better than uncoated 3H the sealants are not doing their intended job.

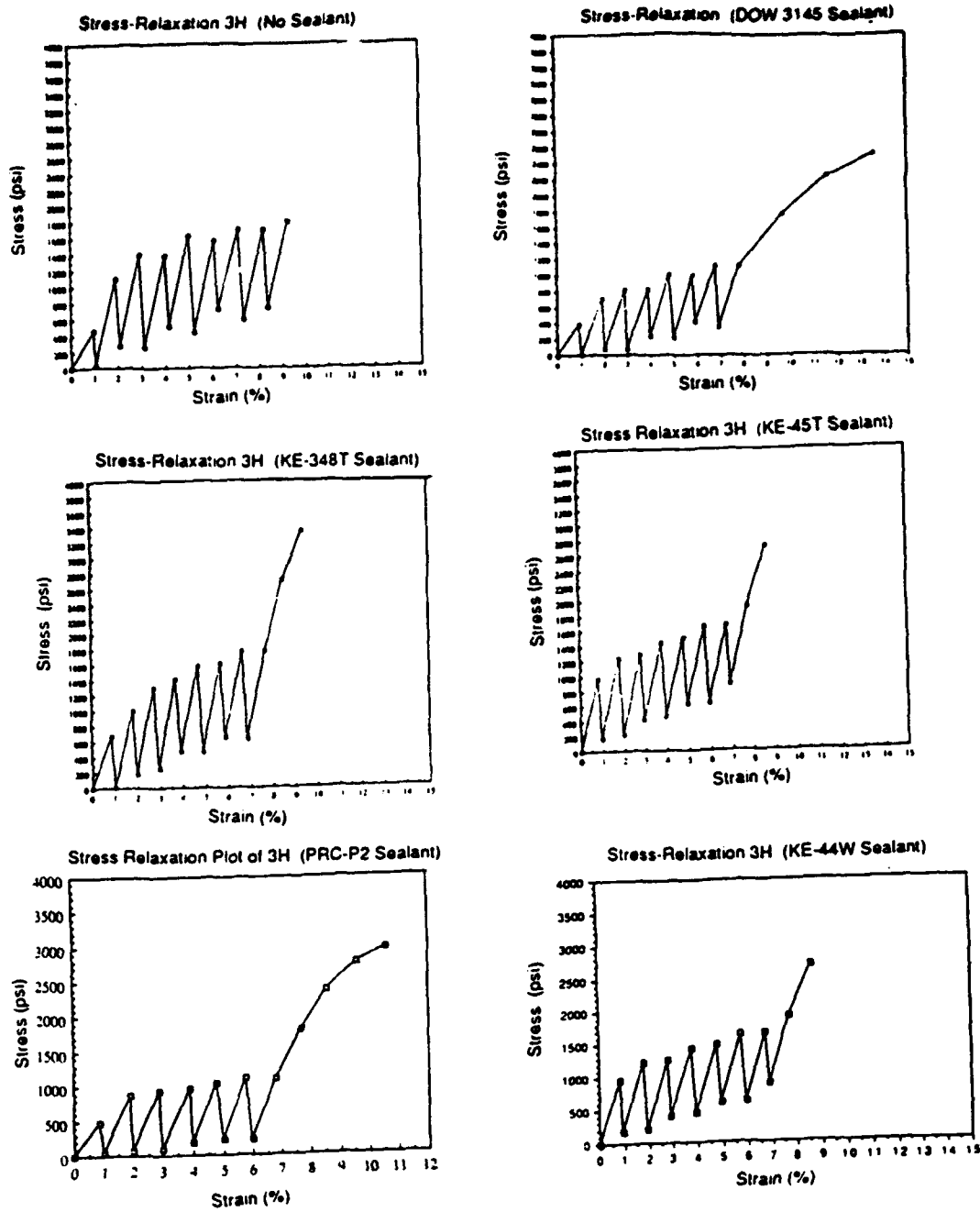


Figure 4.13. Stress-relaxation plots of sealant coated 3H.

It is apparent that the sealants do not significantly retard the passage of water molecules into the adhesive, particularly under strained conditions. As a result, we see no prospect of using sealants to improve the long-term performance of structural epoxies. Adhesives for long-term structural applications must rely on their inherent resistance to moisture degradation if they are to perform their intended task.

5.0 DEMONSTRATION MODEL

Our design concept studies focused on simple-to-construct solutions that use a minimum of material, for weight savings, as well as well-proven adhesive joint configurations, to minimize the chance of joint failure. These configurations are based on decades of aircraft construction experience. The basic principles are to 1) increase the bonded area as much as possible, 2) try to achieve pure shear loading, particularly at edges, and 3) reduce the area of exposed adhesive as much as possible to avoid environmental degradation.

5.1. Design Details

Figure 5.1 shows a simple box-beam design based on the use of four extruded box-with-lip shapes as the longitudinal load-bearing members used as the baseline in our design study. Thin skin side sections are bonded to two edges of each extrusion along their entire length. This configuration gives a large bonding area that is oriented in shear to the principal stress directions, including bending. The design utilizes top surface composite deck structures, bolted in place for easy replacement, as it is in the original welded LV/FB design.

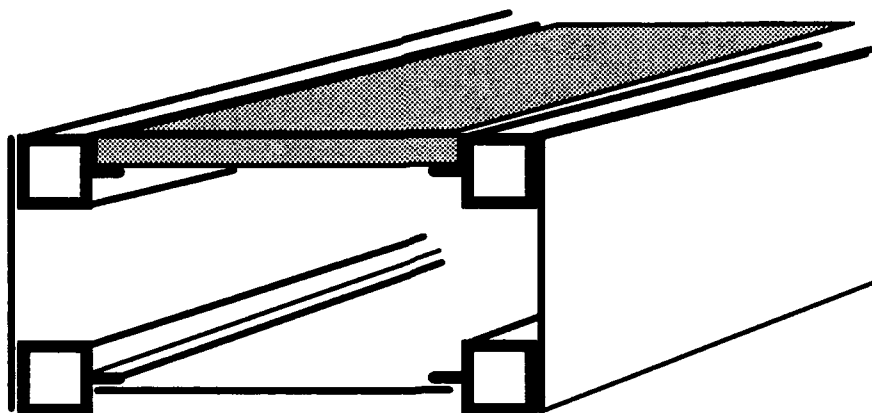


Figure 5.1. Box-section design concept for an adhesively bonded interior bay.

One significant change was made to the top deck mounting. Following examination of the prototype after testing and consultation with BRDEC engineers, the existing LV/FB center section and the composite deck-mounting arrangement (Figure 5.2), the design was modified to include support on both sides of the deck (see Figure 5.3). This design should reduce the tendency of the deck support to flex and crack, and should add to the rigidity of the beam structure.

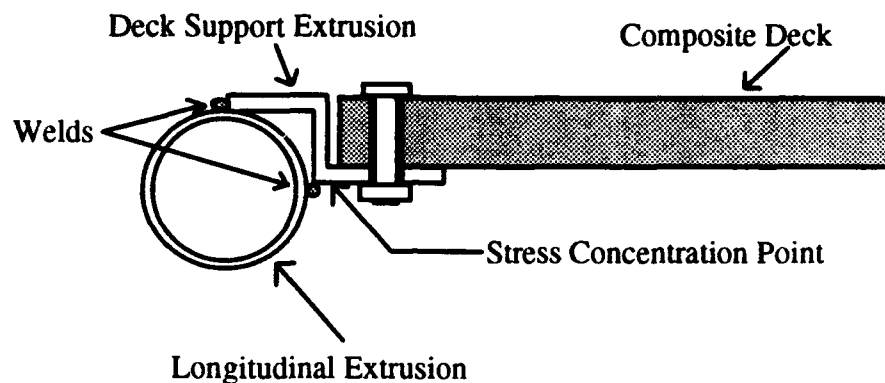


Figure 5.2. Cross section drawing of deck support structure, original design.

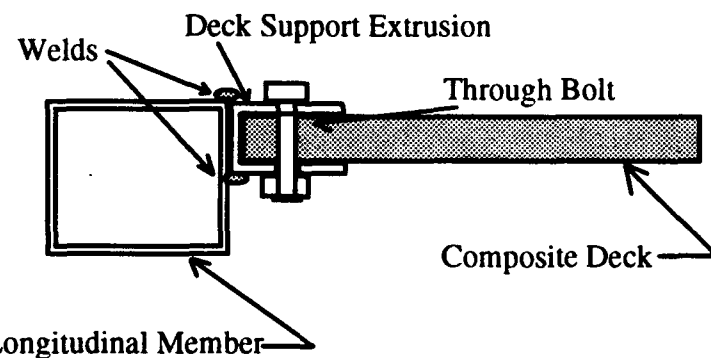


Figure 5.3. Cross section drawing of demonstration article deck support configuration.

Given the results of the computer modeling study, and the choice of flat aluminum plate side panels, the only further question was additional stiffening to reduce the possibility of side plate buckling. Buckling was the only area in which stress values appeared at all

questionable in the computer model. Stiffeners had to be designed without the benefit of detailed computer analysis due to time constraints. The general concept was to reduce the ability of the side plates to bend by adding internal stiffeners on the inside of the longitudinal extrusions. A U-shaped end plate design was chosen that acted as a doubler on the outside of the side plate at each end, wrapped around the end, and became a stiffener inside the bridge, where it was bonded to the inner edges of the extrusions. This not only added stiffness to the ends of the bridge, it also covered the sharp edge of the end plate, increasing user safety. Internal bracing was designed to span the gap between the upper and lower longitudinal extrusions to further stiffen the side plates. Flat 0.063-in. thick panels were bonded on the inside extrusion surfaces as shown in Figure 5.4. They were bonded along a 45° angle so that they would be oriented in the principal stress directions. The primary problem with the internal stiffeners is the limited bonding surface area along the upper extrusion, due to the deck support extrusion. In order to increase the bond surface area, and provide compression loading to compensate for the limited bonding area, the top edge of the stiffeners were bent to fit under the deck support extrusion, see Fig 5.5. The weld bead between the box and deck support extrusion forced the use of 45° bends, which again reduced the effective bond area.

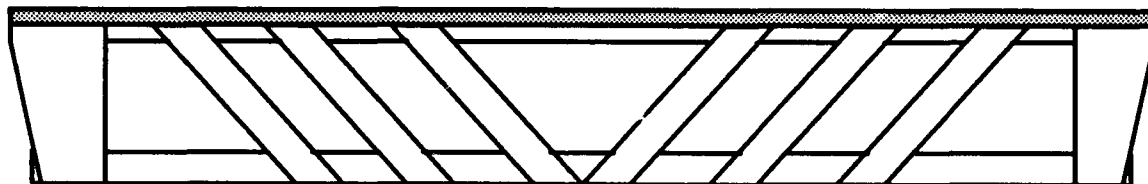


Figure 5.4. Layout of internal and end stiffeners.

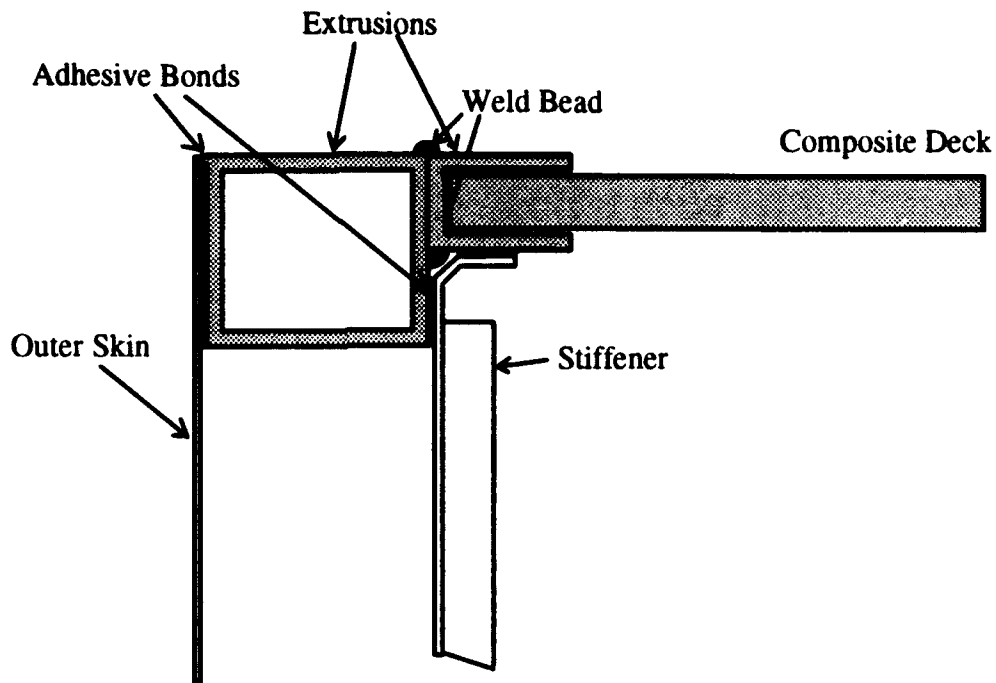


Figure 5.5. Inner stiffener bend detail to avoid weld bead.

5.2. Construction Details

Figure 5.6 shows a photograph of the completed demonstration article, as prepared for shipment to BRDEC. The overall box design is clearly evident. A close-up view of the end, Figure 5.7, shows the channel extrusions and the deck plates, as well as the hinge fittings and locator pins. Figure 5.8 shows the inner stiffeners and end plates as bonded between the longitudinal extrusions.

The highest adhesive loads in this design are between the lower hinge joints and the longitudinal extrusions. This joint is essentially the same as the tubular joint modeled in the parametric studies, and the design guidelines were used in its design, i.e., the joint length (five in.) was chosen based on the maximum untapered length from the design guideline plots for aluminum-to-aluminum bonds. In order to ensure long-term reliability of this joint, the best surface preparation was used, PAA. This process produces an aluminum oxide surface

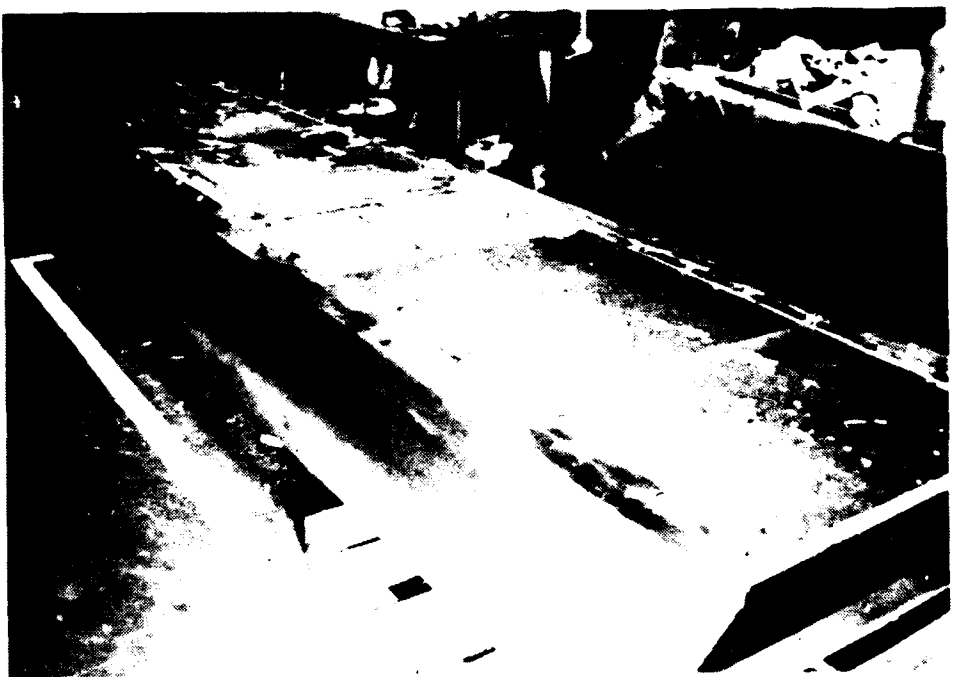


Figure 5.6. Photograph of the completed LV/FB center span demonstration article.

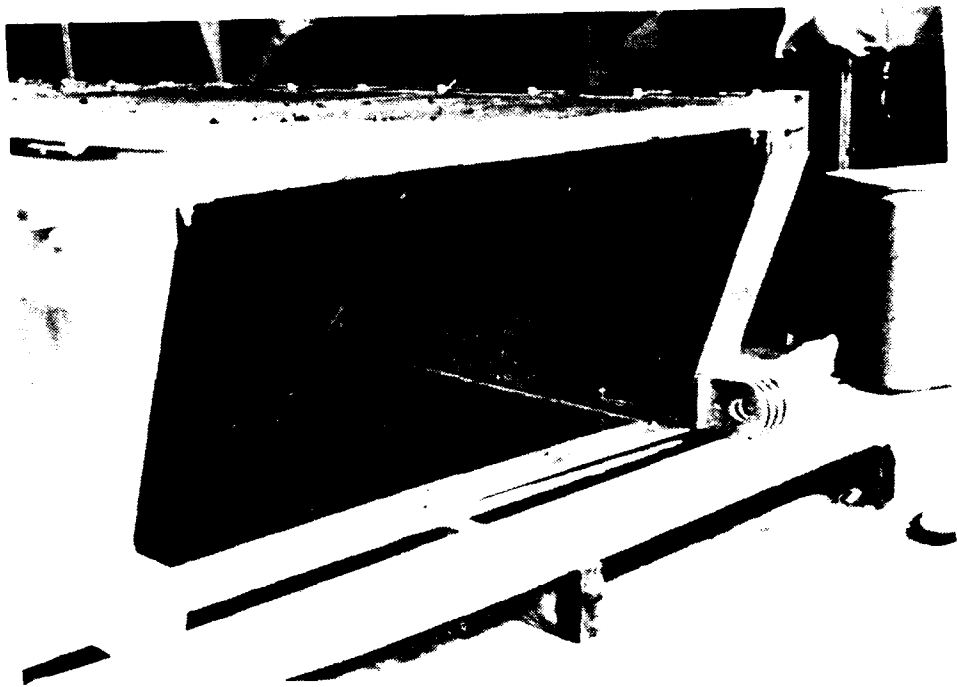


Figure 5.7. Close up view of the end of the span, showing the end doubler plate and hinge fittings.

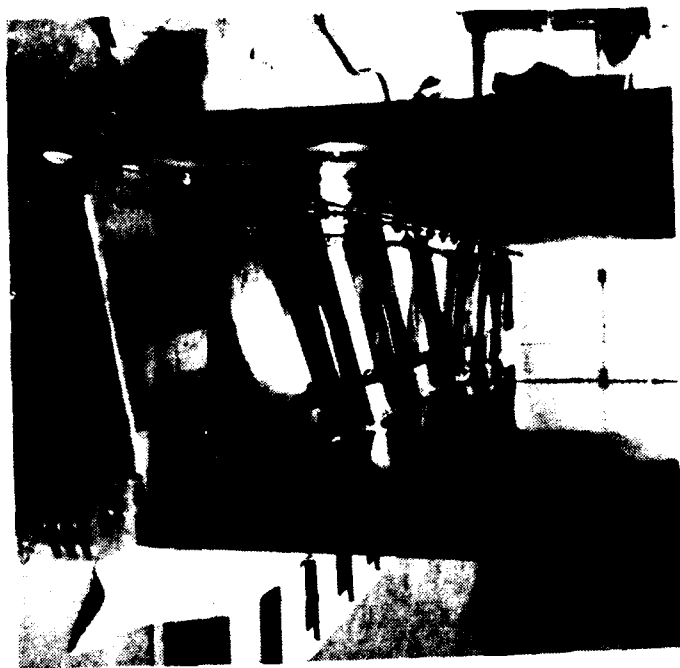


Figure 5.8. Interior view of demonstration article, showing internal stiffeners.

coating that has proven to have the ideal combination of porosity and thickness for epoxy adhesive bonding. In addition, adsorbed phosphate molecules retard degradation of the oxide interface when it comes in contact with moisture, enhancing the durability of the joint. Consult our reference discussing surface preparations (23) for further details of PAA, and the other treatments discussed in this section, FPL and P2.

We followed the treatment practice used at our production plants for this process. The aluminum surfaces to be treated were first cleaned in a commercial alkaline cleaner (TURCO 4215-S) to remove surface oils, then etched in Forest Products Laboratory (FPL) solution to remove any mill scale, and finally anodized in a 10 weight percent solution of phosphoric acid in water for 15 min at room temperature.

PAA treatments were applied to the bonding surfaces of all small parts, including the hinge fittings, the internal and end stiffeners, and to the ends of the lower longitudinal box extrusions.

5.3. P2 Etch

For large pieces that would not fit in our laboratory-scale processing tanks, we relied on another treatment method, P2 manual etch. The P2 solution was jointly developed by the U.S. Army and Bell Helicopter to provide a nontoxic replacement for FPL. As such, it was expected to be a direct replacement, i.e., it was to be used as an immersion solution at elevated temperatures. We have been investigating this approach at MML for possible application to the External Tank of the Space Shuttle. Our research showed that P2 produced a good bonding morphology at lower temperatures, and less concentrated solutions. By combining our modified chemical formulation with Cab-O-Sil thickening agent, we developed a way to apply P2 as a manual operation. This formulation is: 370 g/l concentrated sulfuric acid, 150 g/l ferric sulfate and 50 g/l grade EH-5 Cab-O-Sil in water.

We followed the following process for treating the aluminum surfaces. First, the aluminum is mechanically cleaned with Scotch-Brite pads and alcohols. Then the thickened P2 solution is painted on the surface to be cleaned, allowed to sit for 30 min, then thoroughly rinsed off, preferably with a forceful spray of deionized water to completely remove the etch solution. Treated surfaces should have a light, frosted appearance, and should be water-break free on rinsing. We prepared the edges of the side and bottom panels, and the long edges of the longitudinal extrusions for bonding in this manner.

5.4 Adhesive Application

Our epoxy adhesive 3H-F4 was applied using the applicator guns described in Section 4. The smaller Lord gun was used for the hinge fittings, and the larger gun for everything else. Working with this adhesive was greatly facilitated by the guns, allowing the amount to be easily controlled, and allowing the relative tacky, taffy-like adhesive to be placed exactly where desired with minimum waste.

A minimum of tooling was used for construction. C-clamps were used to secure the extrusions to the side panels during adhesive cure. Small pieces of 0.012-in. thick shim material were placed near the clamp region to control bond line thickness. Spacer blocks were used to obtain the correct spacing between the longitudinal extrusions when the side and bottom panels were bonded in place. In hindsight, better alignment techniques should

have been employed. The C-clamps were difficult to align so that the parts stayed in position during tightening. Alignment pins between the panels and extrusions would have maintained better dimensional tolerances.

Nevertheless, construction was straightforward, and no major difficulties were encountered. The only other lesson learned was that masking off surfaces where adhesive was not desired would have been useful. A great deal of effort was expended in removing unaesthetic adhesive drips and ridges from external surfaces of the article.

6.0 REFERENCES

1. J.D. Venables, *J. Mater. Sci.*, **19**, 1984, pp. 2431-2453.
2. J.D. Venable, D.K. McNamara, J.M. Chen, et all, Proc. 12th SAMPE Tech. Conf, Seattle, WA, October 1980 (SAMPE, Azusa CA), pp. 909-919.
3. C.O. Arah, Report MML-TR-90-26, February 1990, BRDEC Contract #DAAK70-86-C-0084.
4. T.A. DeVilbiss, D.S. Messick, D.J. Progar, and J.P. Wightman, "SEM/XPS Analysis of Fractured Adhesively Bonded Graphite Fiber-Reinforced Polyimide Composites," *Composites*, July 1985, pp. 207-219.
5. D.J.D. Moyer and J.P. Wightman, "The Role of Surface Pre-treatment and Surface Analysis in the Bondability of Carbon Fiber-Polyimide Matrix Composites," Report CASS/CHEM-89-8, November 1989.
6. J. Osterndorf, R. Rosty, and M.J. Bodner, "Adhesive Bond Strength and Durability Studies Using Three Different Engineering Plastics and Various Surface Preparations," *SAMPE Journal*, **25**(4), July/August 1989, pp. 15-19.
7. B.M. Parker and R.M. Waghorne, "Surface Pretreatment of Carbon Fibre-Reinforced Composites for Adhesive Bonding," *Composites*, **2**, 1982, pp. 280-288.
8. J.G. Dillard and I. Spinu, "Plasma Treatment of Composites for Adhesive Bonding," in How To Apply Advanced Composites Technology, Advanced Composites Conference, Dearborn, MI, ASM International, 1988, pp. 199-208.
9. J.G. Dillard, "Surface Preparation of Composites", in ASM Engineered Materials Handbook, ASM International, 1990, pp. 281-297.
10. G.K.A. Kodokian and A.J. Kinloch, "The Adhesive Fracture Energy of Bonded Thermoplastic Fibre-Composites," *J. Adhesion*, **19**, 1989, pp. 193-218.
11. S.I.Y. Wu, "Adhesive Bonding of Thermoplastic Composites, Surface Treatment Study," in Proc. 35th SAMPE Symposium, Anaheim, CA, April 1990, pp. 846-858.
12. A. Zebrauskas, R. Spirikaviciene, and M. Baranauskas, "Adhesion Improvement of Polymeric Substrates by the Application of a Copper Sulfide Coating," *J. Adhes. Sci. & Tech.*, **4**(1), 1990, pp. 25-33.
13. W.W. Wendlandt, *Thermal Analysis*, Wiley & Sons, New York, 1986, Chapter 5.

14. W.W. Wendlandt, *Thermal Analysis*, Wiley & Sons, New York, 1986, Chapter 11.
15. G.K.A. Kodokian and A.J. Kinloch, "Surface pretreatment and adhesion of thermoplastic fibre-composites" J. of Mat. Sci. Let. 7(1988), pp. 625-627.
16. J.W. Chin, J.P. Wightman, J. Adhesion, 1991, Vol 36, pp 25-37.
17. J.W. Chin, J.P. Wightman, "Surface Characterization of Plasma-Modified LaRC-TPI", 14th annual Adhesion Society Meeting, Clearwater, Florida, Feb 17-20, 1991.
18. A.S. Crasto, Interphase Modification in Carbon-Fiber Composites via Electrodeposition, PhD Thesis, Washington State University, 1986, Univ. Micro. Serv., Ann Arbor, MI, #8621984.
19. R. H. Olsen, "Implementation of Phosphoric Acid Anodization at Air Force Air Logistics Centers," in Proc. 11th National SAMPE Technical Conference, November 1979, pp. 770-779.
20. C.O. Arah, D.K. McNamara, H.M. Hand, and M.F. Mecklenburg, *J. Adhes. Sci. Tech.*, 3(4), 1989, pp. 261-275.
21. P. Albrecht, M.F. Mecklenburg, J. Wang, and W. Hong. Final Report, Office of Research, Development, and Technology, Fed. Highway Admin., Contract No.DTFH-61-84C-00027, Feb. 1987.
22. H.J. Borchardt & F. Daniels, *J. Am. Chem. Soc.*, 79 (1957), pp 41-6. Program supplied by Dupont (TA Instruments) as part of TA 9900 DSC analysis package.
23. H. C. Clearfield, D.K. McNamara and G.D. Davis, "The Surface Preparation of Metals," in *Adhesives and Sealants, Engineered Materials Handbook Volume 3*, ASM International, 1990. pp. 235-298.

Appendix A Prototype MSDS Forms.

Material Safety Data Sheet.....Experimental Epoxy Adhesive, Part A, Preliminary

Martin Marietta Laboratories 410 204-2250
1450 South Rolling Road,
Baltimore, MD 21227

Product Name: Epoxy Adhesive 3H-F4, part A- Resin Base

Part I. Ingredients

Reaction products of epichlorohydrin, bisphenol A and bisazodiol	98.3 wt %
CAS# 025085-99-8	
Triphenylphosphine	0.2 %
Copolymer of Butadiene and Acrylonitrile	1.5 %
CAS# 603-35-0	
CAS# 9003-18-3	

Part II. Physical Data

Boiling Point: decomposes Vapor Pressure: ND
Specific Gravity: 1.1 Solubility in Water: none
Appearance: Viscous yellow liquid/semi solid. Slight epoxy odor.

Part III. Fire and Explosion Hazard Data:

Flash Point: > 400 F (> 205 C) Flammability Limits: ND
Extinguishing Media: Foam, CO₂, Dry chemical
Fire and Explosion Hazards: none known
Fire-fighting Equipment: Wear positive pressure self-contained breathing apparatus (SCUBA).

Part IV. Reactivity Data

Stability: stable. Excess heating for long periods degrades the resin.
Incompatibility: Avoid bases, acids, amines and oxidizing materials.
Hazardous Decomposition Products: By-products of incomplete pyrolysis or combustion of epoxy resins are mainly phenolics, carbon monoxide and water. Thermal decomposition products should therefore be treated as potentially hazardous substances.
Hazardous Polymerization: None by itself. Large quantities of material mixed with amines will cause considerable heat buildup.

Part V. Environmental and Disposal Information:

Spills/Leaks: Soak up in absorbent material such as sand, and collect in suitable containers. Residual resin may be removed using steam or hot soapy water. Solvents, such as acetone, may be used if appropriate handling procedures are followed.

Disposal Method: Do not dump in sewers, on ground, or any body of water. The preferred disposal method is to send to a licensed recycler, reclaimer, or incinerator.

Part VI. Health Hazard Data:

Eye: May cause slight temporary eye irritation.

Skin Contact: Prolonged exposure may cause skin irritation. Has caused allergic skin reaction in humans.

Skin Absorption: A single prolonged exposure is not likely to result in the material being adsorbed through the skin in harmful quantities. The LD50 for skin absorption in rabbits is 20 g/kg.

Ingestion: Single dose oral toxicity is low. The oral LD50 for rats is > e.g. 5 g/kg.

Inhalation: Vapors are unlikely due to physical properties.

Cancer Information: Diglycidyl ether Bisphenol A show weak/uncertain carcinogenicity.

Reproductive Effects: None seen in animal studies.

Mutagenicity: None seen in animal studies, uncertain in vitro studies.

Part VII. First Aid

Eyes: Flush eyes with plenty of water.

Skin: Wash off in flowing water, and clean with soap and water.

Ingestion: No adverse effects anticipated for minor exposure incidental to proper industrial handling.

Inhalation: Remove to fresh air if effects occur. Consult a physician.

Note to physician: No specific antidote. Supportive care. Treatment based on judgement of physician in response to reactions of the patient.

Part VIII. Handling Precautions:

Exposure guideline: None established.

Ventilation: Good general ventilation should be sufficient.

Respiratory Protection: No respiratory protection should be needed.

Skin Protection: For brief contact, no precautions other than clean, body-covering clothing. Use impervious gloves when prolonged or repeated contact could occur.

Eye Protection: Use safety glasses. Where contact is likely, chemical goggles are recommended.

Part IX. Additional Information:

Practice good caution and personal cleanliness to avoid skin and eye contact. Avoid breathing vapors of heated material.

DOT Classification: not regulated

DOT Proper Shipping Name: not regulated

DOT ID Number: not regulated

Material Safety Data Sheet.....Experimental Epoxy Adhesive, Part B, preliminary

Martin Marietta Laboratories 410 204-2250
1450 South Rolling Road,
Baltimore, MD 21227

Product Name: Epoxy Adhesive 3H-F4, part B - Hardener and Tougheners

Part I. Ingredients

1	Fatty Acid Polyamides	proprietary	70-75 wt.%
2	Triethylenetriamine	CAS# 112-24-3	5-10 %
3	Butadiene Acrylonitrile Copolymer	CAS# 68891-46-3	8-12 %

Part II. Physical Data

Boiling Point: decomposes Vapor Pressure: negligible at 20°C
Specific Gravity: 0.96 Solubility in Water: slight
Appearance: Viscous amber liquid/semi solid. Slight ammoniacal odor.

Part III. Fire and Explosion Hazard Data:

Flash Point: > 230 F (> 110 C) Flammability Limits: ND
Extinguishing Media: Protein type Foam, CO₂, ABC Dry Chemical
Fire and Explosion Hazards: none known
Fire-fighting Equipment: Wear positive pressure self-contained breathing apparatus (SCUBA). In confined spaces wear SCUBA during cleanup immediately after a fire as well as during attack phase.
Unusual Fire and Explosion Hazards: May produce hazardous vapors under fire, causing nitrogen oxides and nitrogen containing organic compounds to be released.

Part IV. Reactivity Data

Stability: stable.
Incompatibility: Avoid contact with strong oxidizing agents.
Hazardous Decomposition Products: CO, CO₂, oxides of nitrogen, ammonia, and small amounts of aromatic and aliphatic hydrocarbons.
Hazardous Polymerization: Will not occur.

Part V. Environmental and Disposal Information:

Spills/Leaks: Soak up in absorbent material such as sand, and collect in suitable containers. Residual resin may be removed using steam or hot soapy water. Solvents, such as acetone, may be used if appropriate handling procedures are followed.

Disposal Method: Do not dump in sewers, on ground, or any body of water. These products are not designated as hazardous by current conditions of the Federal Resources Conservancy and Recovery Act. The preferred disposal method is to send to a licensed recycler, reclaimer, or incinerator.

Part VI. Health Hazard Data:

Effects: May cause eye and skin irritation. Vapors at elevated temperatures may cause lung irritation if inhaled.

TLV: none established

Eye: Product is extremely irritating to the eyes and may cause severe damage, including blindness.

Skin Contact: Prolonged exposure may cause skin irritation. May be toxic if adsorbed through the skin.

Skin Absorption: A single prolonged exposure is not likely to result in the material being absorbed through the skin in harmful quantities. The LD50 for skin absorption in rabbits is 0.80 g/kg.

Ingestion: Product may cause severe burns of mouth and throat and irritation of the gastrointestinal tract. Single dose oral toxicity is low. The oral LD50 for rats is > 5 g/kg.

Inhalation: Mists or vapors (at elevated temperatures) may produce severe respiratory irritation, producing severe inflammation including lung. Extreme cases may be fatal.

Cancer Information: Not determined.

Reproductive Effects: Not determined.

Mutagenicity: Component 2 has been found to be a direct acting mutagen in the Ames assay.

Part VII. First Aid

Eyes: Immediately flush eyes with plenty of water for at least 15 minutes while holding eyelid open. Rinse continually with water while on way to get medical attention.

Skin: Immediately remove contaminated clothing. Wipe excess from skin and flush with water for 15 minutes. Use soap if available or follow by cleaning with soap and water. Get medical attention. Do not reuse clothing until thoroughly cleaned.

Ingestion: Do not induce vomiting. Do not give liquids to drowsy, convulsing or unconscious person. Give large quantities of water. If vomiting occurs repeat liquid administration. Get medical help immediately.

Inhalation: Remove to fresh air and provide oxygen if difficulty breathing. Get medical attention.

Part VIII. Handling Precautions:

Exposure guideline: none established.

Ventilation: Good general ventilation should be sufficient.

Respiratory Protection: At elevated temperatures or if mists are created, inhalation exposure is possible. Use NIOSH-approved respirator to prevent overexposure. Use either a full-face atmosphere-supplying respirator or an air-purifying respirator for organic vapors.

Skin Protection: Use chemical-resistant gloves and clothing when contact could occur.

Eye Protection: Use safety glasses. Where contact is likely, chemical goggles are recommended.

Part IX. Additional Information:

Store in a cool dry place, with adequate ventilation. Keep away from open flames and high temperatures.

Warning: extremely irritating to the eyes. Potential sensitizer. Containers, even emptied, can contain hazardous product residues. Wash with soap and water before eating or drinking, applying cosmetics or using toilet facilities. Contaminated leather articles including shoes cannot be decontaminated, and should be destroyed.

Heating this curing agent in the presence of air may cause thermal and oxidative decomposition with some epoxy resins. It may produce exothermal reactions, which in large masses can cause runaway polymerization and charring. Fumes and vapors from these chemical and thermal decompositions should be avoided. Do not breath fumes. Use a NIOSH-approved respirator as required to prevent over exposure.

Part IX. Transportation Requirements:

DOT Classification: not regulated

DOT Proper Shipping Name: not regulated

DOT ID Number: not regulated